Shedding Light on the Biological Effects of Ionising Radiation on DNA Using Advanced Optical Microscopy

Sofia D'Abrantes

A thesis submitted to and awarded by

Oxford Brookes University

in partial fulfilment of the requirements of the award of

Doctor of Philosophy

July 2020

This is dedicated to the most important people in my life:

My mum and dad, Claudia and Walter D'Abrantes, for their constant support and belief in me. They have inspired and shaped me into who I am today. To my brothers Ramiro, Ignacio, Felipe and Pacha who kept me laughing and entertained. Lastly, to the love of my life, Samuel John Millington, whose patience, kindness and encouragement since the day we met has made this possible.

Declaration

I hereby declare that this submission is my own work under the supervision of Professor Munira Kadhim, Dr Mark Hill and Dr Jason Parsons and that, to the best of my knowledge and belief, it contains no material previously published or written by another person or material which has to a substantial extent been accepted for the award of any other degree or diploma at any university or other institute. No confidential information in intellectual property contained in this submission is proprietary to Amazon.com Inc nor derived from my internship at Amazon.com Inc.

Name: Sofia D'Abrantes

Signature: 

Date: 06/07/2020

Acknowledgements

I would like to express my sincere gratitude to my supervisor Dr Mark Hill for the opportunity to join his team and his immense support throughout my PhD. His patience, guidance and knowledge have driven this project forward. I would particularly like to thank Dr Jason Parsons who guided me so positively and whose insight steered me through this research project. Our meetings and discussions were vital in inspiring me to think outside the box. Thank you to Professor Munira Kadhim for her dedicated guidance and encouragement.

A special thanks to Dr Abdullah Ahmed who has taken much time to discuss this work and for his advice and friendship throughout these four years. I would like to thank Dr Rhodri Wilson for microscopy access and his help with data analysis. Thank you to Dr James Thompson and Amy Elliott for their laboratory expertise (particularly for making all those dishes!). Special thanks to Dr Dave Carter for his encouragement and support throughout the PhD. Thank you to the BBSRC for an Interdisciplinary Bioscience Doctoral Training Partnership (DTP) studentship, STFC for access to the Central Laser Facility and everyone at the DTP for their support.

Lastly, a special thank you to all my family and friends for their support and motivation throughout the last four years.

Abstract

Detrimental effects of ionising radiation (IR) stem from its unique ability to produce clustered DNA damage (CDD) and double-strand breaks (DSBs). CDD consists of two or more lesions in close proximity, including DSBs, single-strand breaks and/or base damages. CDD complexity increases with rising linear energy transfer (LET) of radiation, while repairability decreases. This makes high-LET IR more biologically effective than low-LET. Understanding DNA repair mechanisms and associated signalling with radiation quality, may be useful in assessing exposure risks and also optimising radiotherapy. Despite this, CDD recognition and processing induced by different radiation qualities are currently unclear.

In this study, kinetics, morphology and localisation of DSB (γH2AX) and non-DSB (OGG1) clusters were measured at CDD sites using immunofluorescence and confocal microscopy (CM). Slower repair kinetics were observed for high-LET α-particles compared to low-LET γ-rays. Additionally, PARP inhibitor Olaparib in combination with IR resulted in increased foci persistence.

Although Ku70/Ku80 are known as major effectors in DSB repair and genome integrity, their interaction in relation to DSB repair has not been detected in living cells. Using GFP technology and advanced imaging,

Ku70-80 interaction was shown for the first time in live cells, with the Ku heterodimer pre-formed in the absence of DNA damage.

Most foci studies are performed using standard CM, but the resulting data is limited by their resolution. Emerging evidence suggests these foci are sub-divided in structural domains. Furthermore, there are discrepancies in DSB foci yields among different methods. To assess this, super-resolution microscopy was employed to compare foci kinetics and structure with CM. CM underestimated the number of X-ray-induced γH2AX and 53BP1 foci by a factor of 2-5 and overestimated their colocalisation. Therefore, super-resolution is not only useful in investigating foci structure, but will provide significant improvements in identifying the spatial distribution of correlated damage sites along high-LET tracks.

List of publications

D'Abrantes, S., Gratton, S., Reynolds, P., Kriechbaumer, V., McKenna, J., Barnard, S., Clarke, D.T., Botchway, S.W. (2017). Super-Resolution Nanoscopy Imaging Applied to DNA Double-Strand Breaks. Radiation Research. https://doi.org/10.1667/rr14594.1

Thompson, J.M., Elliott, A., **D'Abrantes, S**., Sawakuchi, G.O., Hill, M.A. (2019). Tracking down alpha-particles: the design, characterisation and testing of a shallow-angled alpha-particle irradiator. Radiation Protection Dosimetry. https://doi.org/10.1093/rpd/ncy300

Ahmed, A.R, Candeo, A., **D'Abrantes, S**., Needham, S.R., Yadav, R.B., Botchway, S.W., Parker, A.W. (2020). Directly imaging the localisation and photosensitization properties of the pan-mTOR inhibitor, AZD2014, in living cancer cells. Manuscript under peer-review in Photochemistry B.

Contents

List of Figures

LIST OF FIGURES

LIST OF FIGURES

LIST OF FIGURES

Abbreviations

2D 2-dimensional

3D 3-dimensional

53BP1 p53 Binding Protein 1

a-NHEJ alternative Non-homologous End-joining

AA Amino Acid

Alt-Ej Alternative End-oining

AP Apurinic/Apyrimidinic site

APLF Aprataxin-and-PNK-like Factor

ATM Ataxia Telangiectasia Mutated

ATR ATM and Rad3-related

BER Base Excision Repair

BiFC Bimolecular Fluorescence Complementation

bp base pairs

BRCA1 Breast Cancer susceptibility gene 1

BSA Bovine Serum Albumin

c-NHEJ classical Non-homologous End-joining

CDD Complex DNA Damage

CHO Chinese Hamster Ovary

ABBREVIATIONS

DAPI 4-6-Diamidino-2-phenylindole

DMSO Dimethyl Sulfoxide

DNA Deoxyribonucleic Acid

DNA PKcs DNA-dependent Protein Kinase, catalytic subunit

DSB Double-strand Break

dSTORM direct STochastic Optical Reconstruction Microscopy

ECL Enhanced Chemiluminescence

EDTA Ethylenediaminetetraacetic Acid

EGFP Enhanced Green Fluorescent Protein

FACS Fluorescence Activated Cell Sorting

FBS Foetal Bovine Serum

FLIM Fluorescence Lifetime Imaging Microscopy

FNTD Fluorescence Nuclear Track Detectors

FRET Förster Resonance Energy Transfer

FWHM Full-width at Half Maximum

GaAsP Gallium Arsenide Phosphid

GSDIM Ground-state Depletion Microscopy followed by Individual Molecule return

H2AX H2A Histone family member X

$H2B_{ub}$ Ubiquitination of Histone H2B

HeLa Henrietta Lacks

HPV Human Papillomavirus

HR Homologous Recombination

HRP Horseradish Peroxidase

HEK293 Human Embryonic Kidney 293

IR Ionising Radiation

IRIF Ionising Radiation Induced Foci

kb kilobase

LB Luria Broth

LDS Lithium Dodecyl Sulfate

LET Linear Energy Transfer

LIG DNA Ligase

LN Liquid Nitrogen

MDC1 Mediator of DNA Damage Checkpoint Protein 1

MEM Minimum Essential Medium

MES 2-(N-morpholino)ethanesulfonic acid

MRN Mre11/Rad50/Nbs1

NER Nucleotide Excision Repair

NHEJ Non-homologous End-joining

OGG1 8-Oxoguanine Glycosylase

OPSCC Oropharyngeal Squamous Cell Carcinoma

PA-FP Photoactivatable Fluorophore

PARP Poly(ADP-ribose) Polymerase-1

PBS Phosphate Buffered Saline

PCC Pearson's Correlation Coefficient

PCR Polymerase Chain Reaction

PDB Protein Data Bank

PFGE Pulsed-field Gel Electrophoresis

PMT Photomultiplier Tube

Pol β Polymerase *beta*

PVDF Polyvinylidene Difluoride

ABBREVIATIONS

RBE Relative Biological Effectiveness

RING Really Interesting New Gene

RNF20/40 RING Finger Protein 20/40

ROI Region Of Interest

RPA Replication Protein A

RT Room Temperature

SDS Sodium Dodecyl Sulfate

SIM Structured Illumination Microscopy

SMLM Single Molecule Localisation Microscopy

SNR Signal-to-noise Ratio

SR Super-resolution

SSB Single-strand Break

STED Stimulated Emission Depletion

TBE Tris-borate-EDTA

TBST Tris Buffered Saline with Tween-20

TIRF Total Internal Reflection Fluorescence

UMSCC74A University of Michigan-squamous Cell Carcinoma-74A

UV Ultraviolet Light

WWL White Light Laser

XLF XRCC4-like factor

XRCC1 X-ray Cross Complementing Factor 1

YFP Yellow Fluorescent Protein

γ**H2AX** Phosphorylation of Histone H2AX at Ser139

Chapter 1

Introduction

Ionising radiation (IR) arises from natural sources (such as cosmic-rays, soil, food and water), as well as man-made sources (including medical diagnostic and therapeutic exposures). DNA (deoxyribonucleic acid) has been identified as the principle sub-cellular target of IR (Hutchinson, 1966; UNSCEAR, 1993). Abundant evidence has revealed that cells with a deficiency in the DNA damage response show increased radiosensitivity (ICRP, 1998; National Research Council USA, 2006; UNSCEAR, 1993), chromosomal rearrangements (Peterson *et al.*, 1995; Ward *et al.*, 2001), and rates of mutation (ICRP, 2005; Lehnert, 2008) and carcinogenesis (Sarasin *et al.*, 1997). As a result, the characterisation of DNA damage induction, repair and mis-repair impacts clinical radiation oncology, as well as radiation protection and risk assessment from occupational, medical, environmental and space travel exposures.

It is estimated that mammalian DNA is subject to ~100,000 lesions/cell/day as a result from exogenous and endogenous agents (Lindahl *et al.*, 2000). These lesions are largely in the form of simple damage such as base lesions or single-strand breaks (SSBs). Endogenous damage can arise from normal cell processes, such as DNA replication

during cell division and oxidative damage during metabolism. Exogenous damage can occur from exposure to IR and chemicals such as those found in tobacco smoke. While endogenous lesions are typically repaired with high fidelity, those arising from exogenous IR are more complex and thus more difficult to repair.

1.1 Ionising Radiation

IR has a unique characteristic that differentiates it from any other type of cellular stressor, that is the ability to produce clustered DNA damage (CDD), where two or more lesions occur within one or two helical turns of DNA (originally named locally multiply damaged sites) (Ward, 1988). These include not only double-strand breaks (DSBs) but also complex DSBs, which have additional strand-breaks and/or base damage within a few base pairs (Goodhead *et al.*, 1993). The increased complexity of the lesions results in decreased efficiency and fidelity of repair. Failure to accurately repair such damage may result in mutations, chromosome aberrations, cell-cycle arrest, apoptosis and carcinogenesis (Bonassi *et al.*, 2008; Durante *et al.*, 2013; Hartwell *et al.*, 1989; Kastan *et al.*, 2004; Lea, 1946; Roos *et al.*, 2006; Shaltiel *et al.*, 2015).

The complex nature of IR-induced damage stems directly from its interaction with matter. IR deposits energy in highly structured tracks of ionisation events along the trajectories of the charged particles, which vary significantly depending on the type of radiation, the so-called radiation quality. As shown in **Figure 1.1**, IR may interact directly with critical targets within the cell (such as DNA), readily ionising or exciting the atoms it traverses. It may also interact with surrounding water molecules producing free radicals, most notably hydroxyl radicals, that can diffuse (∼6 nm) and react with DNA, resulting in indirect damage (Fielden *et al.*, 1992). ∼30% of the damage

caused by low-LET IR is direct, while the remaining ~70% are indirect effects (Nikjoo *et al.*, 1998). Incident photons (γ-rays and X-rays) interact with matter, producing fast electrons which may ionise water molecules ($H_2O \longrightarrow H_2O^+ + e^-$). Some excited water molecules (H_2O^*) may also dissociate ($H_2O^* \longrightarrow H + OH\cdot$), resulting in $OH\cdot$ and hydrogen atoms. The ion H_2O^+ can react with other water molecules ($H_2O^+ + H_2O \longrightarrow H_3O^+ + OH\cdot$) to form a hydronium ion (H_3O^+) and the highly reactive hydroxyl radical ($OH\cdot$). These reactive species can subsequently diffuse to DNA, causing breakage of bonds and chemical changes.

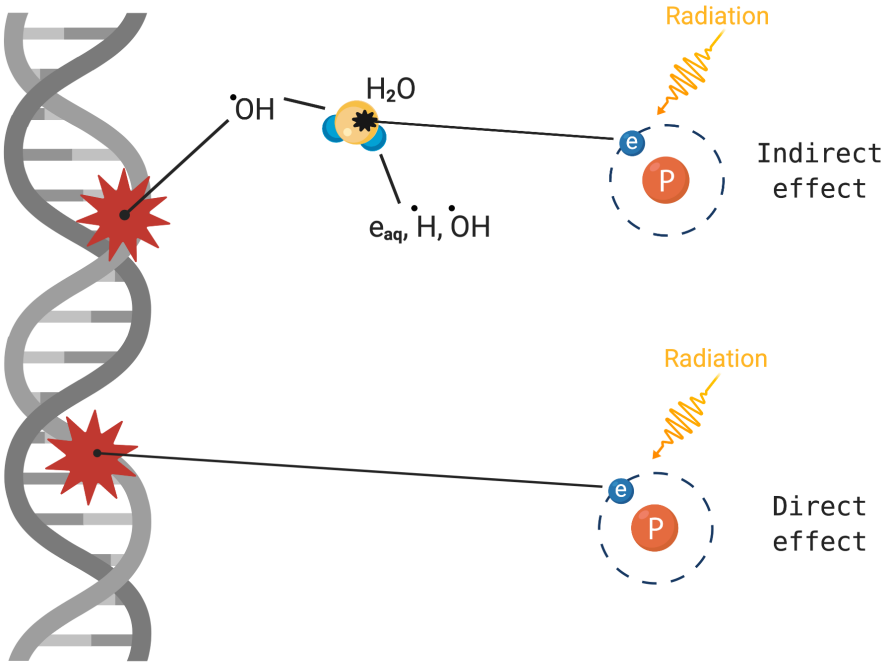

Figure 1.1: Direct and indirect effects of radiation on the DNA macromolecule - DNA damage may be induced through the direct ionisation of the DNA molecule, or indirectly from interactions with free radicals. Adapted from (Hall *et al.*, 2012).

The effects shown in **Figure 1.1** are said to occur in 'hit' or 'targeted' cells. In addition to these targeted effects, the non-targeted effects of IR have been well documented, and include genomic instability, adaptive response and a variety of bystander effects (Iyer *et al.*, 2000; Ward, 1999; Wolff, 1998; Wright, 1998). These effects are thought to be particularly significant at low radiation doses (Kadhim *et al.*, 2013).

1.2 Low- and High-LET Induced DNA Damage

Linear energy transfer (LET) is used to describe the average energy loss per unit distance along the path of an ionising particle (ICRU, 1970). Low-LET radiation sources (such as γ-rays and X-rays) are sparsely ionising, with energy in the region of 0.2-3 keV/μm, while high-LET radiation sources (such as α-particles with LET of $\sim$80-240 keV/μm) are densely ionising (Hall *et al.*, 2012). Many studies have shown the relationship between the LET and relative biological effectiveness (RBE) of radiation. In mammalian cells, RBE is often observed to rise with increasing LET, peaking at $\sim$100-200 keV/μm for a range of biological endpoints (Barendsen *et al.*, 1963; Cox *et al.*, 1979; ICRU, 1970; Miller *et al.*, 1995; Thacker *et al.*, 1979; Tracy *et al.*, 2015).

Particle beams (including protons, α-particles and ion rays) are characterised by a low entrance dose, whereby they lose energy along the track and immediately prior to the particle coming to a complete stop, the dose peaks in depth at a narrow and well-defined range called the Bragg peak (Durante *et al.*, 2010). The energy deposition drops shortly after this peak. This is because the energy lost is inversely proportional to the square of the particle's velocity (Durante *et al.*, 2010). The Bragg peak is exploited in particle radiotherapy to focus the effects of radiation on the tumour, while minimising irradiation of surrounding healthy tissues and organs. As the particles slow

down and lose energy, their LET increases and becomes maximal at around the Bragg peak (Durante *et al.*, 2010). Thus, high-LET radiation allows for the greatest RBE at the Bragg peak, which is of particular interest for radiotherapy.

The complexity and frequency of IR-induced lesions is dependent on radiation quality and the spatial distribution of energy deposition (**Figure 1.2A**). Approximately 30% of DSBs produced by low-LET radiation are complex, increasing to ∼90% for high-LET α-particles (Nikjoo *et al.*, 1998). Substantial evidence shows that complex damage is harder to repair than isolated lesions, with some being irreparable (Asaithamby *et al.*, 2011c). Indeed, many of the DSBs produced by high-LET α-particles persist for longer compared to the DSBs induced by low-LET γ-rays, and result in higher levels of chromosome aberrations, mutagenesis, cell death and carcinogenesis (Asaithamby *et al.*, 2011b,c; Blöcher, 1988; Brenner *et al.*, 1992; Jenner *et al.*, 1993; Kraemer *et al.*, 2003; Prise *et al.*, 1998).

As shown in **Figure 1.2B**, in addition to complex DSBs, IR is able to induce non-DSB clustered lesions. These have also been shown to have a decrease in repairability, resulting in an increase in lifetime and potentially producing a stalled replication fork (Asaithamby *et al.*, 2008; Dobbs *et al.*, 2008; Gulston *et al.*, 2004; Nikjoo *et al.*, 2001). The formation of stalled replication forks have a higher probability of producing DSBs. The increased chance of damage being present during replication can lead to enhanced mutation frequencies (Georgakilas *et al.*, 2013; Gulston *et al.*, 2002; Malyarchuk *et al.*, 2009). IR may also induce CDD, where two or more lesions occur within one or two helical turns of DNA.

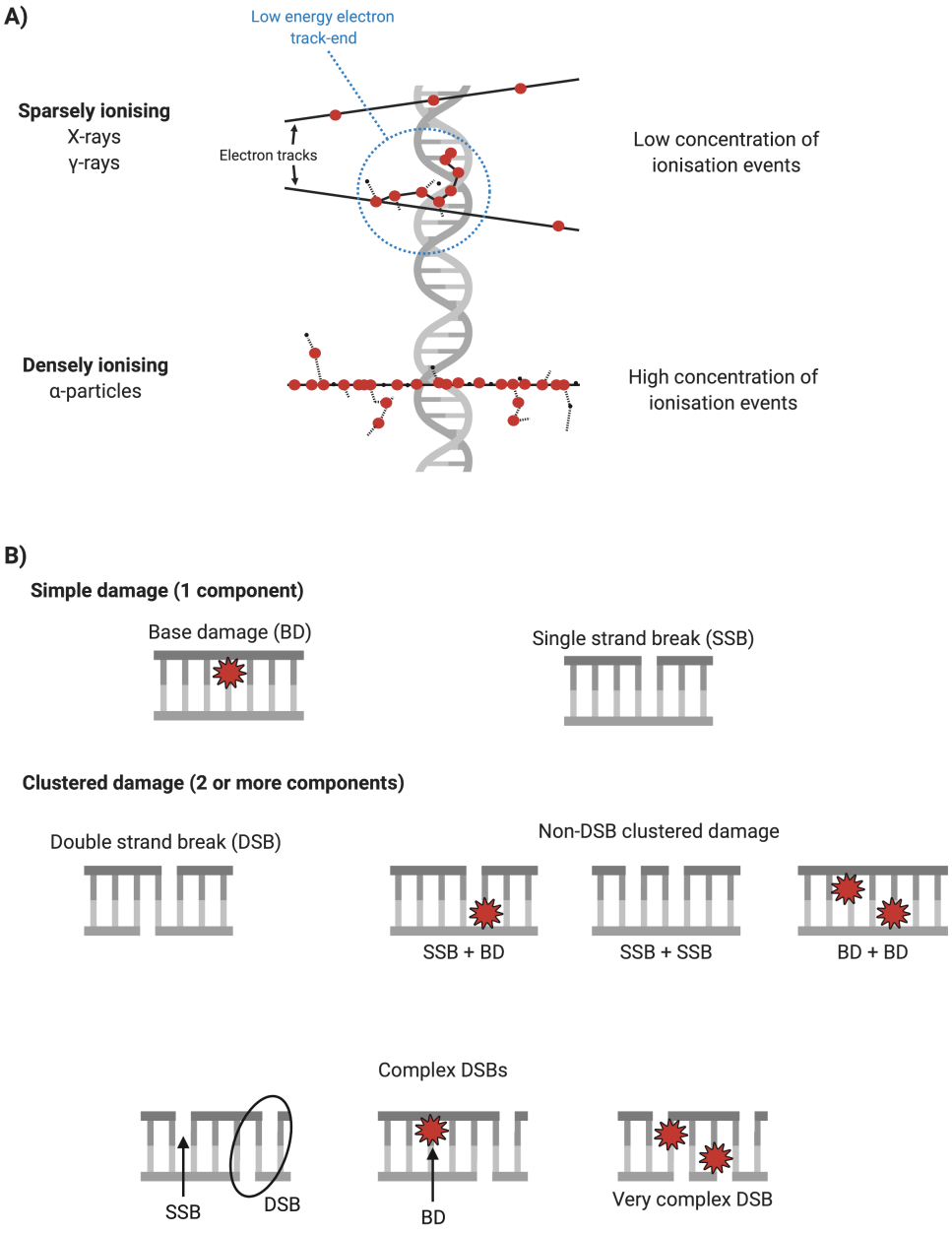

Figure 1.2: Ionising radiation produces a wide spectrum of DNA damage dependent on radiation quality - A) Illustration of low- and high-LET radiation tracks. **B)** Schematic of the types of lesions that can be induced by IR: simple damage such as base damage or SSBs; DSBs, complex DSBs and non-DSB clusters of SSBs and/or base damage. Adapted from Hill (2020).

1.3 DNA Damage Signalling

The induction of DSBs by IR leads to a cascade of signalling events (**Figure 1.3**). Following chromatin relaxation and nucleosome disruption at the damage site, the MRN complex (composed of Mre11/Rad50/Nbs1) recognises the DSB and binds to the site to tether the ends (Mimitou *et al.*, 2008; Petrini *et al.*, 2003; Zhu *et al.*, 2008). This complex is also required for signalling cell cycle checkpoints (Zhou *et al.*, 2000). Next, kinases ATM (ataxia telangiectasia mutated) and ATR (ATM and Rad3-related) are recruited to the damage site, phosphorylating the MRN complex (**Figure 1.3**) (Adams *et al.*, 2006; Bakkenist *et al.*, 2003; Carson *et al.*, 2003; Myers *et al.*, 2006). In response to IR, ATM phosphorylates histone H2AX, p53 binding protein 1 (53BP1) and many others (Banin *et al.*, 1998; Burma *et al.*, 2001; Czornak *et al.*, 2008).

The phosphorylation of core histone H2AX on carboxyl terminal serine 139 (termed γH2AX) is a critical component in DSB signalling and repair (Burma *et al.*, 2001; Stiff *et al.*, 2004). γH2AX formation leads to the recruitment of MDC1 (mediator of DNA damage checkpoint protein 1), which recruits more ATM proteins to amplify the signal and phosphorylate more H2AX (Stucki *et al.*, 2005). γH2AX formation over megabases of DNA triggers nucleosome conformational changes which signal the recruitment of 53BP1 and other proteins. These play a crucial role in determining the repair pathway of choice, homologous recombination (HR) or non-homologous end-joining (NHEJ) (**Figure 1.3**) (Paull *et al.*, 2000; Schultz *et al.*, 2000; Ward *et al.*, 2003).

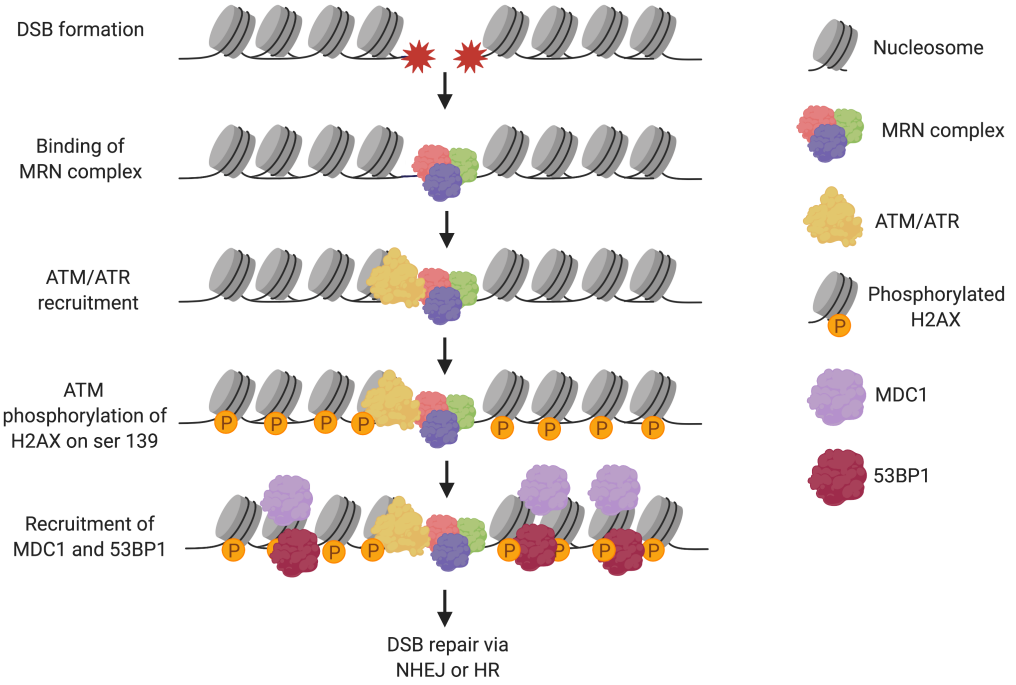

Figure 1.3: Illustration showing the signalling of DSB formation and recruitment of repair proteins - Upon DSB formation, the MRN complex binds to the site of damage, followed by the recruitment of ATM and/or ATR. These kinases phosphorylate and activate the MRN complex, as well as histone H2AX, forming γH2AX. This results in the recruitment of repair proteins MDC1 and 53BP1, leading to the activation of repair pathways NHEJ or HR.

1.4 DNA Repair Pathways

Cells have developed five major mechanisms to effectively repair the various types of DNA lesions, and ultimately maintain genome stability. These are discussed below and include base excision repair (BER), NHEJ, HR, nucleotide excision repair and mismatch repair.

1.4.1 Base Excision Repair

BER is the primary repair mechanism for eliminating SSBs including single base or nucleotide damage (Abbotts *et al.*, 2017; Chaudhry, 2007). DNA glycosylases (such as OGG1, 8-Oxoguanine glycosylase) recognise and remove the damaged base by cleaving the N-glycosidic bond that connects the base and deoxyribose sugars, leaving an abasic (also termed AP) site (Fromme *et al.*, 2004; Krokan *et al.*, 1997). As shown in **Figure 1.4A**, AP endonucleases (APE1 or APE2) nick the backbone by removing the sugar residue (Demple *et al.*, 1991). Consequently, DNA polymerases (such as Pol β) catalyse the addition of a new nucleotide (Singhal *et al.*, 1995; Sobol *et al.*, 1996) and DNA ligase III (along with XRCC1, X-ray cross complementing factor 1) seals the final nick on the strand (Caldecott *et al.*, 1995; Prasad *et al.*, 1996; Tomkinson *et al.*, 2001).

1.4.2 Non-homologous End-joining

NHEJ is used to repair DSBs during any mammalian cell cycle phase. It is referred to as 'non-homologous' as the broken ends are simply re-ligated back together without the need for a homologous template to guide repair (Moore *et al.*, 1996). There are two types of NHEJ, namely classical NHEJ (c-NHEJ, **Figure 1.4B**) and alternative

NHEJ (a-NHEJ, **Figure 1.4C**). During c-NHEJ, the Ku protein (composed of Ku70 and Ku80) recognises and binds to the damage site, protecting the DNA ends from non-specific processing (Mari *et al.*, 2006; Uematsu *et al.*, 2007). Ku also acts as a scaffold to recruit proteins including DNA-PKcs (DNA-dependent protein kinase catalytic subunit), XRCC4 (X-ray cross complementing protein 4), XLF (XRCC4-like factor), DNA ligase IV and APLF (Aprataxin-and-PNK-like factor) (Costantini *et al.*, 2007; Kanno *et al.*, 2007; Mari *et al.*, 2006; Nick McElhinny *et al.*, 2000; Uematsu *et al.*, 2007; Yano *et al.*, 2008).

The binding of Ku and DNA-PKcs leads to the translocation of Ku inward on the DNA strand and DNA-PKcs activation, forming a complex that holds the ends of the broken DNA together (Cary *et al.*, 1997; Gell *et al.*, 1999). If necessary, the DNA ends are processed by enzymes including Artemis (for end trimming) (Ma *et al.*, 2002; Povirk *et al.*, 2007) and Polymerases μ and λ (for end-filling) (Nick McElhinny *et al.*, 2005; Ramadan *et al.*, 2004). The broken ends are ligated by DNA Ligase IV (LIG4) and XRCC4 (Grawunder *et al.*, 1997).

a-NHEJ is used for 10% of DSB repair, typically when the DSB is resected but a sister chromatid is not available for HR (Bennardo *et al.*, 2008; Truong *et al.*, 2013). During a-NHEJ (**Figure 1.4C**), the MRN complex carries out DNA end resection, and is followed by the binding of PARP-1 (poly(ADP-ribose) polymerase-1) to the DNA ends (Bennardo *et al.*, 2008; Mansour *et al.*, 2010; Zhang *et al.*, 2005). Finally, DNA ligase I (LIG1) or XRCC1-Lig IIIα ligate the DSB (Audebert *et al.*, 2004; Bennardo *et al.*, 2008; Wang *et al.*, 2005).

1.4.3 Homologous Recombination

HR is the main repair pathway for DSBs during S and G2 phases of the cell cycle as it relies on using sister chromatids to guide repair (Escribano-Díaz *et al.*, 2013; Ira *et al.*, 2004). As seen in **Figure 1.4D**, nucleases carry out a resection in which one strand of the DNA is cut back in the 5' to 3' direction, creating 3' overhangs (Kass *et al.*, 2010; Symington *et al.*, 2011). A group of proteins including Rad51 (a DNA-dependent ATPase) form a filament of nucleic acid and protein on the single strand of DNA, and begin to search for DNA sequences which are identical to the overhang (Chen *et al.*, 2008; Sung, 1994). Once that sequence is found, the single-stranded filament moves into (invades) the recipient sister chromatid (Sung, 1994). Subsequently, a displacement loop (D-loop) is formed (Ferguson *et al.*, 1996). A DNA polymerase elongates the single strand of DNA using the sister chromatid as a template, changing the D-loop to a cross-shaped structure (termed holliday junction) (Lilley, 2000). Next, the newly synthesised DNA strand dissociates from the junction to anneal to the remaining 3' overhang (Sung *et al.*, 2006). Ligating enzymes reseal any remaining single stranded gaps, restoring the double helix (Lin *et al.*, 1984).

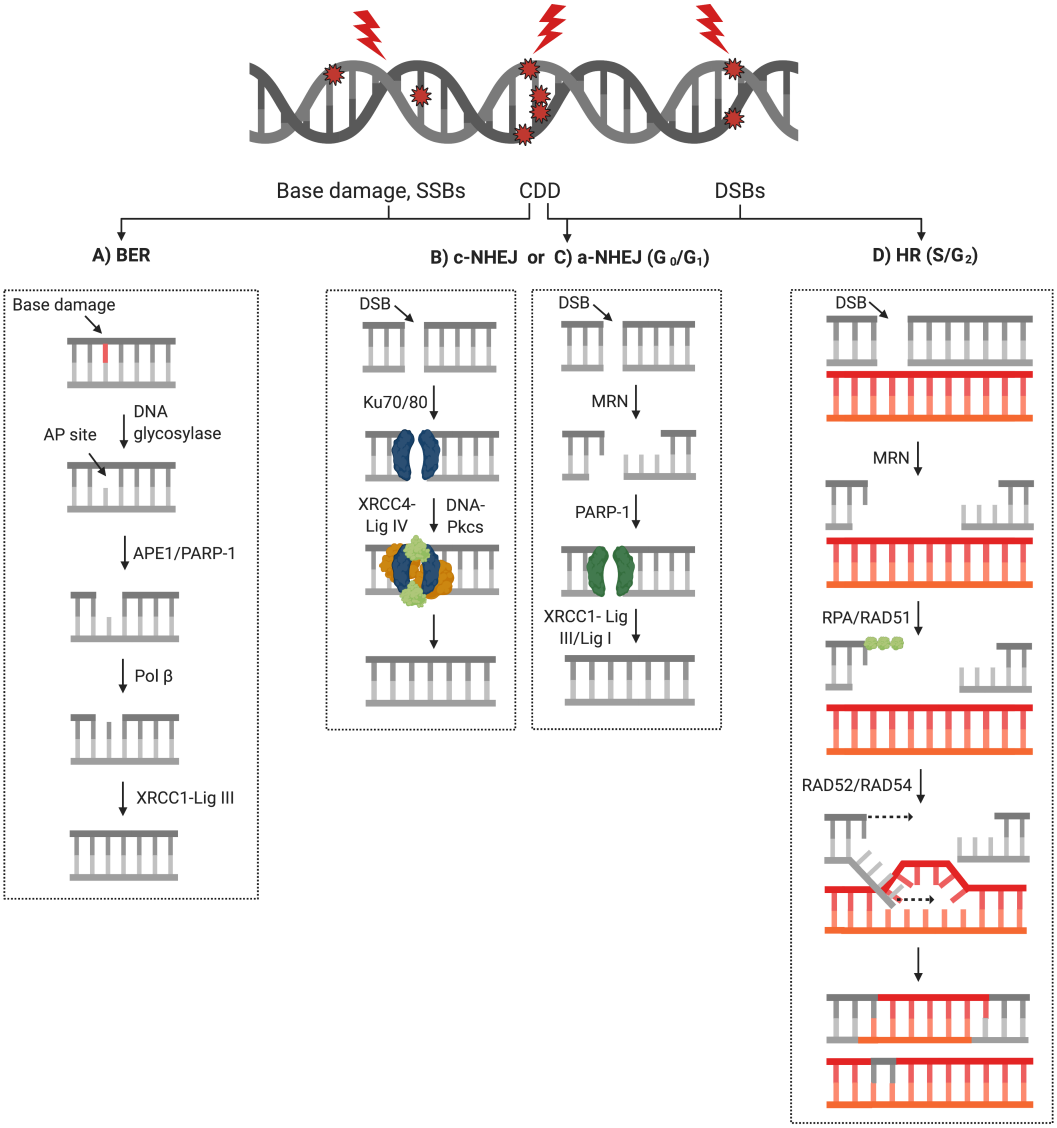

Figure 1.4: Schematic diagram of the most prominent DNA repair pathways in mammalian cells - IR generates a variety of lesions including SSBs, base damage and abasic sites which are predominantly repaired by **A)** BER. DSBs can be repaired by **B)** c-NHEJ (classical NHEJ) or **C)** a-NHEJ (alternative NHEJ) during G_0/G_1 phases, and by **D)** HR through S/G_2 cell-cycle phases. CDD is likely repaired by a combination of pathways. Adapted from (Vitti *et al.*, 2019).

1.4.4 Other Repair Pathways

Nucleotide excision repair is employed by the cell to repair bulky DNA adduct lesions induced by ultraviolet (UV) light (such as thymine dimers and 6,4-photoproducts (Rasmussen *et al.*, 1964; Setlow *et al.*, 1964). Mismatch repair is used to mend incorrect insertions and deletions of bases that arise during DNA replication and recombination (Buermeyer *et al.*, 1999; Lyer *et al.*, 2006; Shah *et al.*, 2010).

1.5 Concepts of Confocal and Multiphoton Microscopy

Optical imaging methods, such as confocal and widefield microscopy, are widely used for investigating DNA damage signalling and repair proteins. In particular, these techniques are known to benefit the quantification of complex lesions (Desai *et al.*, 2005). Confocal microscopy offers several advantages over widefield microscopy, including the ability to collect optical sections, elimination of out-of-focus light and improvements to image contrast (Wilson *et al.*, 1984). These enhancements are primarily due to the implementation of a pinhole aperture before the excitation source and detector (Wilson *et al.*, 1984).

The development of multiphoton microscopy allowed improvements in optical sectioning. Unlike one-photon excitation, this technique relies on the simultaneous absorption of multiple photons. During two-photon excitation, two photons (each with half the energy of a single photon) are absorbed at a single point in the focal plane (Ustione *et al.*, 2011). Since the energy of a photon is inversely proportional to its wavelength, the two absorbed photons have a wavelength double that required for one-photon excitation (Ustione *et al.*, 2011). For example, a fluorophore that usually absorbs ultraviolet light

(∼350 nm wavelength) can also be excited by two photons of near-infrared light (∼700 nm wavelength) if both reach the fluorophore at the same time. Most importantly, multiphoton microscopy makes use of the same scanning system as confocal but does not require a pinhole at the detector as fluorophores are only excited at the focal point. This results in a smaller excitation volume above and below the plane of focus, leading to reduced photobleaching, phototoxicity and cytotoxicity, as well as increased depth penetration (Ustione *et al.*, 2011).

Laser micro-irradiations are a well-established tool to investigate DNA damage signalling and repair in real time (Holton *et al.*, 2017). They allow the generation of highly localised tracks of DNA damage, permitting assessment of base lesions, SSBs or DSBs with some specificity, depending on the laser dose and wavelength applied (Holton *et al.*, 2017). For example, 405 nm micro-irradiations have been shown to induce DSBs (Holton *et al.*, 2017; Mortusewicz *et al.*, 2007). Upon damage induction, the spatial, temporal and coordinated dynamics of proteins may be detected within individual cells.

1.6 Advanced Microscopy Techniques

1.6.1 Förster Resonance Energy Transfer (FRET) and Fluorescence Lifetime Imaging Microscopy (FLIM)

FRET is a powerful technique to detect direct protein-protein interactions as it only occurs when two fluorophores are <10 nm apart. The mechanism behind fluorescence is shown in **Figure 1.5A** using a Jablonski diagram. Upon absorption of a photon (of energy hv) by a fluorophore, an electron is raised to an excited singlet energy state (S_1). After a few nanoseconds, the electron relaxes back to the ground state

(S_0) by vibrational relaxation while emitting a photon (with a wavelength longer than the absorbed wavelength). In contrast, as observed in **Figure 1.5B**, upon FRET the energy that is released from the relaxation of the donor fluorophore (e.g. EGFP, enhanced green fluorescent protein) is absorbed by a suitable acceptor (e.g. mCherry) in close proximity (<10 nm) (Selvin, 2000). This results in the excitation of one of its electrons, and the release of a photon by the acceptor fluorophore (rather than the donor). Proteins of interest may be tagged with appropriate fluorophores so that upon their interaction, FRET leads to a decreased donor emission and increased acceptor emission. By monitoring donor-acceptor emission ratio changes, protein interactions may be revealed (Selvin, 2000).

Although FRET may appear as a simple approach, it is highly dependent on emission intensity and signal-to-noise ratio (SNR). Furthermore, effects from photobleaching or spectral bleed-through make interpretation of FRET results challenging and open to misinterpretation. A more robust way of quantifying FRET is to measure the natural fluorescence lifetime τ (the average time the molecule spends in the excited state) of donor molecules using FLIM, in the presence and absence of an acceptor. This provides measurements which are less dependent on fluorophore concentrations (Gerritsen *et al.*, 2002). Simply, in the presence of an acceptor, the donor lifetime is quenched, indicating a direct physical interaction. The lifetime of molecules is recorded and displayed as pseudocoloured FLIM images, where the colour of each pixel represents a lifetime value. Long lifetimes are shown in blue, while short lifetimes are in red. If the donor lifetime is quenched or shortened in the presence of an acceptor, this will be reflected by a change in colour of the image pixels.

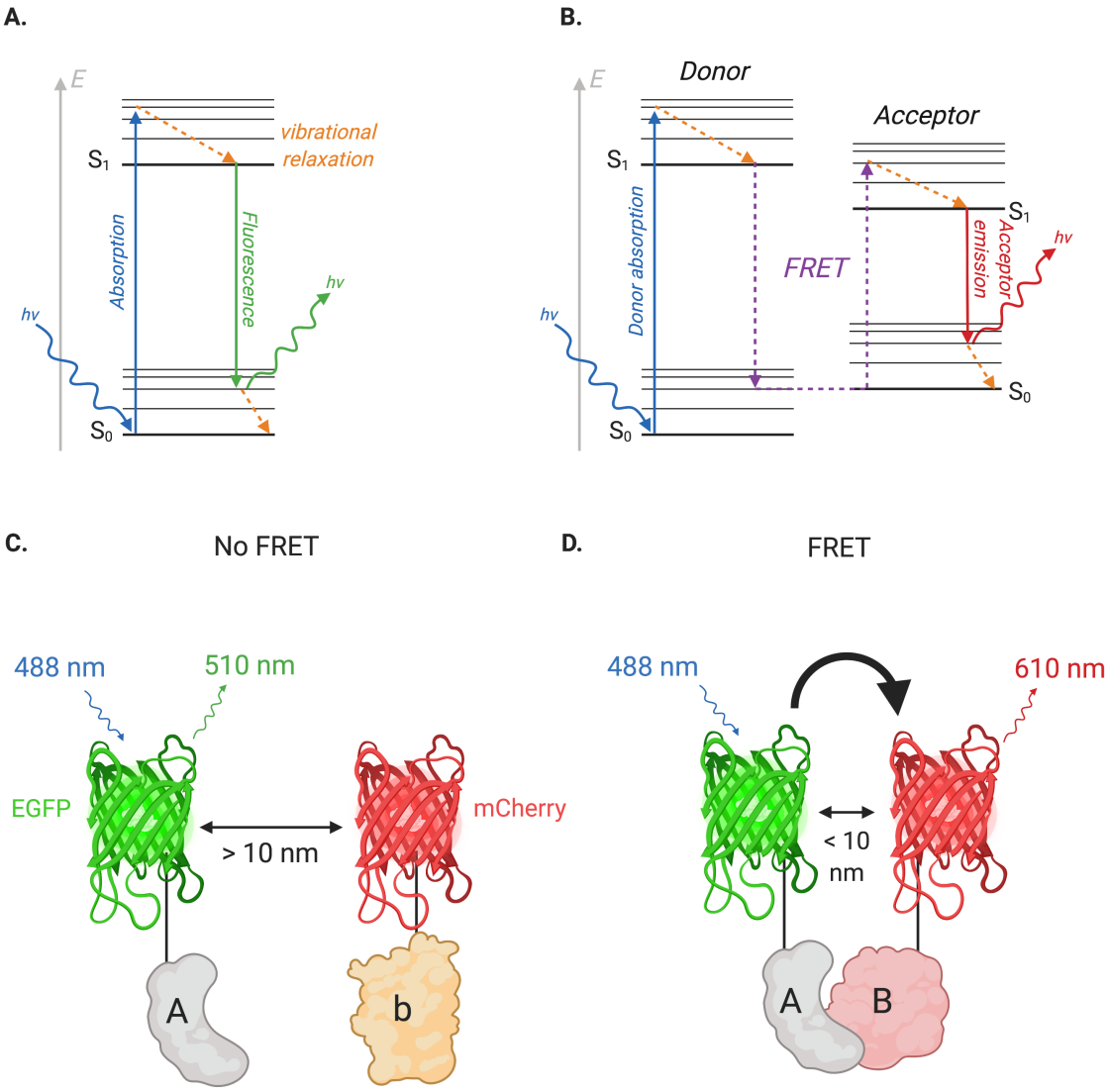

Figure 1.5: Basic principles of fluorescence and FRET - Jablonski diagrams describing **A.** fluorescence and **B.** FRET. **C.** Schematic showing lack of energy transfer between the donor and acceptor as the distance between them is too far >10 nm. **D.** When the distance between the donor and acceptor is <10 nm, energy transfer (FRET) may occur, indicative of a protein-protein interaction.

1.6.2 Bimolecular Fluorescence Complementation (BiFC)

BiFC assays are commonly used to visualise protein interactions in living cells (**Figure 1.6**) (Hu *et al.*, 2002). In this method, a fluorescent protein (e.g. Venus, a YFP - yellow fluorescent protein - variant), is split into two halves. The non-fluorescent N- and C-terminal fragments (namely VN and VC) are each fused to a protein of interest (A and B). The interaction between A and B brings the fluorescent fragments within close proximity, allowing the Venus to reform and emit fluorescence which can be detected using a fluorescent microscope. In contrast, b (a non-binding protein or a mutant form of B) is unable to form a complex with A, resulting in no fluorescence (**Figure 1.6**) (Hu *et al.*, 2002).

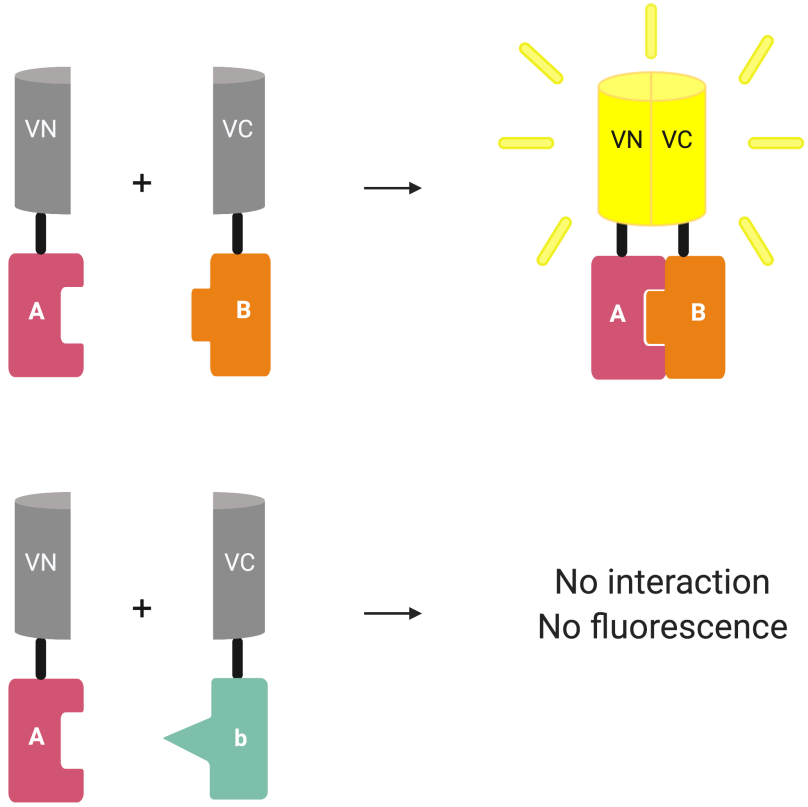

Figure 1.6: Illustration of the BiFC assay - The N- and C-terminal fragments (VN and VC, respectively) of Venus, a YFP variant, are fused to two proteins of interest (A and B). The interaction between A and B brings the fluorescent fragments within close proximity, allowing the Venus to reform and emit fluorescence. In contrast, b (a non-binding protein or a mutant form of B) is unable to form a complex with A, resulting in no fluorescence.

1.6.3 High-resolution Imaging

Despite the advantages of standard confocal and widefield microscopy, these techniques are hampered by a lateral resolution limit of ~250 nm (Abbe, 1873), restricting the amount of information that can be captured. In recent years, several techniques have

been developed to circumvent the diffraction limit and improve resolution, including pixel reassignment (such as Airyscan and Hyvolution) and super-resolution (SR) methods.

1.6.3.1 Pixel Reassignment Methods

As mentioned in **section 1.5**, the resolution of confocal microscopy relies on a pinhole. A small pinhole diameter rejects unwanted out-of-focus light, leading to a higher resolution (Sheppard *et al.*, 1977). However, this also results in low SNR, which in turn deteriorates the spatial resolution. As fluorescence signal from biological samples is often weak, a relatively large pinhole is typically chosen to improve SNR. To achieve higher resolution, a small pinhole array (instead of a single pinhole) would be needed. This problem is overcome by Airyscan microscopy. Airyscan makes use of the same scanning system as confocal, as well as a unique detector which enables a resolution of ∼140 nm (a ∼2-fold improvement compared to confocal) without the need of a pinhole (Huff, 2015). The Airyscan detector consists of a Gallium Arsenide Phosphid (GaAsP) photomultiplier tube (PMT) array of 32 elements. As the sample is scanned, each detector element records the whole image, and the contribution of each detector is determined by deconvolution, reassigning the pixels to their correct positions. This enables the summing of signals from all 32 detector elements that would otherwise be rejected by the confocal pinhole. Most importantly, this results in increased signal levels and SNR ratio in both the lateral and axial direction (Huff, 2015).

Hyvolution is another pixel reassignment method. Unlike Airyscan, Hyvolution does not provide any hardware improvements but instead relies on a standard confocal system (customised with a small pinhole and high sensitivity detector) coupled with de-

convolution (Borlinghaus *et al.*, 2016). The deconvolution uses an iterative algorithm to deblur and reassign the pixels, leading to improved SNR and resolution down to ∼140 nm (Borlinghaus *et al.*, 2016).

The key advantage of pixel reassignment methods is the resolution improvement down to ∼140 nm with high SNR. In addition, most fluorophores are compatible, images can be recorded with multiple channels in parallel, and fast imaging reduces photobleaching and cytotoxicity effects. As these methods are readily available extensions to existing systems, they are low cost and user friendly.

1.6.3.2 Super-resolution Imaging

There are three major SR techniques, namely SIM (structured illumination microscopy), STED (stimulated emission depletion) and SMLM (single molecule localisation microscopy). A comparison of the different imaging techniques can be found below in **Table 1**.

SIM enhances resolution by illuminating the sample with a striped pattern to generate frequency shifting (Gustafsson, 2000). Nine raw images are acquired at different orientations by moving the diffraction grating. Specialist software is required to reconstruct the SR image, reaching ∼110 nm lateral resolution (2-fold improvement compared to widefield). This technique allows the use of simultaneous colour imaging and conventional fluorophores, is live-cell compatible and can be upgraded for 3D imaging (Gustafsson, 2000; Shao *et al.*, 2011). However, SIM also has some drawbacks including sensitivity to out-of-focus light, modest resolution improvement, long processing times and a high risk of artefacts generated during image reconstruction (Demmerle *et al.*, 2017).

STED achieves 60-120 nm resolution by selective deactivation of fluorophores using a confocal excitation beam and a smaller depletion laser beam to scan the sample simultaneously (Eggeling *et al.*, 2015). The confocal beam is used to excite the fluorophores, while the depletion beam is used to inhibit them, preventing fluorescence. By switching off the fluorescence emission in the outer regions of the diffraction-limited excitation focus, only the emission from molecules in the centre are detected and used to form sub-diffraction images (Eggeling *et al.*, 2015). STED offers substantial lateral resolution improvements, does not require reconstruction algorithms and allows multi-colour imaging. On the downside, it requires expensive optics and special dyes, the systems are difficult to maintain, and vast laser powers are needed, making it generally incompatible with live-cell imaging (Bottanelli *et al.*, 2016; Göttfert *et al.*, 2013).

SMLM encompasses techniques that achieve SR by using isolating emitting fluorophores and determining their position. The single molecule signals are collected over several thousand camera frames and algorithms are used to detect their positions depending on the number of photons measured from each individual fluorophore. The images are then superimposed into a single-plane image, achieving ∼20 nm lateral resolution. There are many types of SMLM approaches, dependent on the on/off switching of fluorophores. Direct STochastic Optical Reconstruction Microscopy (dSTORM), also referred to as GSDIM (ground-state depletion microscopy followed by individual molecule return) employs conventional fluorescent probes, along with thiols, to transfer fluorophores into long-lived and reversible off-states (non-fluorescent) (Van De Linde *et al.*, 2011a). The stochastic return to the on-state leads to fluorescence signals being emitted for a short time, before returning back to the off-state. The fluorescence produced by these molecules is recorded over time and a SR image is reconstructed from the thousands of

images (Van De Linde *et al.*, 2011b). GSDIM allows the use of some conventional fluorophores which act as reversible photo-switches, unlike other SMLM techniques which require specialist photoactivatable fluorophores (PA-FPs) that can be localised only once. Additionally, standard fluorophores have been shown to have higher photostability and brightness than PA-FPs (Shaner *et al.*, 2008). Drawbacks include cost, the need for specialised buffers, image acquisition and processing takes hours to acquire, high laser powers are typically incompatible with live-cell imaging and the localisation algorithms are prone to artefacts.

	SIM	**STED**	**GSDIM**
Concept	Structured illumination	Stimulated emission depletion	Localisation with photoswitching
Best lateral resolution	100 nm	60 nm	20 nm
Advantages	Conventional fluorophores Multi-colour imaging Mostly live-cell compatible	High lateral resolution No processing algorithm required Multi-colour imaging	Very high lateral resolution Some standard fluorophores Conventional staining protocols
Disadvantages	Modest resolution improvement Long processing times Sensitivity to out-of-focus light Processing algorithms may lead to artefacts Incompatible with fast live cell experiments	System complexity High cost Phototoxicity and photobleaching Poor axial resolution Generally live cell incompatible	System complexity High cost Resolution depends on embedding media Image acquisition and processing takes hours to acquire Live cell incompatible

Table 1: Comparison table of different SR imaging techniques.

1.7 Objectives and Outline

The purpose of this research project is to contribute to the understanding of DNA damage and the underlying mechanisms of subsequent signalling and repair kinetics, including how this varies with dose delivered and, importantly, the quality of radiation

used. The research in this work is composed of three parts. The first investigates the mechanism of recognition and processing of CDD after high-LET radiation and is compared with low-LET. Recent studies have shown that the binding ability of Ku70 and Ku80 is crucial in determining whether DSB repair will occur via NHEJ or an alternative end-joining repair pathway. Thus, the second part of this project explores the interaction of Ku70-Ku80 using live-cell microscopy. To date, current work has failed to provide conclusive evidence of such interaction. The final part of this project investigates the early effects caused by IR using γH2AX and 53BP1 as markers of DSBs using SR microscopy. Due to limitations in the resolution of confocal microscopes, less is known about the localised effects of IR at the nanometre scale, where IR is expected to be most efficient at producing correlated damage. Details of each section are outlined below.

Radiation therapy relies on IR to kill cancer cells. This ability of IR, particularly charged particles, is based on the induction of CDD resulting from the high density of ionisation events along their track. Due to the difficult nature of their repair, CDD contributes significantly to cell killing. Studies have shown the delay in processing and repair of these lesions by the persistence in DNA repair foci. High-LET radiation, such as α-particles, has an elevated propensity to form CDD in contrast to low-LET γ-rays or X-rays. Additionally, cluster complexity (number of lesions within one cluster), as well as multiple correlated CDD events (at distances of >10 nm) also rise with increasing LET. This may be an advantage for dose delivered to cancer cells, but a disadvantage for dose absorbed in normal tissues. In addition to improvements to the absorbed dose distribution, high-LET has other clinical biological advantages. Unlike well oxygenated normal tissues, most tumours have hypoxic regions which are more

resistant to the effects of IR (Höckel *et al.*, 1996). High-LET radiation therapy against hypoxic tumours is highly effective due to the reduced dependence on the presence of oxygen in the tumour (Furusawa *et al.*, 2000). Radiosensitivity also varies with the phase of the cell cycle; it is lowest in G1 and early S stages, and highest in M and G2 (Pawlik *et al.*, 2004). High-LET radiation is less sensitive to cell cycle variations, which may be beneficial in the treatment of slow growing tumours (Bird *et al.*, 1975). Thus, high-LET radiotherapy is expected to have greater therapeutic effectiveness and represents a promising alternative for radioresistant tumours.

Despite this, the differences in signalling and repair mechanisms involved in the recognition and processing of CDD are currently unclear. Recent studies have identified proteins OGG1 (Nikitaki *et al.*, 2016a), PARP-1 (Carter *et al.*, 2019), RNF20/40 and $H2B_{ub}$ (Carter *et al.*, 2018) as essential components for CDD repair. Briefly, OGG1 is a DNA glycosylase involved in BER which cleaves glycosidic bonds and causes a strand break (Aburatani *et al.*, 1997). Its main role involves removing oxidised purines from DNA, in particular 8-oxo-guanine lesions which account for 30% of base damage caused by IR (Burrows *et al.*, 1998). RNF20/40 is an E3 ubiquitin protein ligase needed for ubiquitination of histone H2B and methylation of H3 (Carter *et al.*, 2018). H2B is one of the four histone proteins involved in condensing chromatin, and has been shown to maintain chromosomes and regulate transcription, replication and DNA repair (Carter *et al.*, 2018). H2B lysine 120 monoubiquitination is required for the activation of transcription, forming $H2B_{ub}$ (Carter *et al.*, 2018).

To investigate their localisation to CDD sites, HeLa and oropharyngeal squamous cell carcinoma (UMSCC74A) cells were exposed to low-LET (protons and γ-rays) and high-LET radiation (perpendicular and angled α-particles, and protons). Foci kinetics were

measured and compared following different radiation qualities and visualised using confocal imaging. Foci persistence, area, clustering and colocalisation were also evaluated. Additionally, the synergistic effect of IR in combination with PARP inhibitor Olaparib was also investigated.

Recent studies have shown inaccurate DNA repair after Olaparib and IR exposure (Hirai *et al.*, 2012; Kötter *et al.*, 2014). This is thought to be due to a disruption in the binding ability of DNA repair proteins Ku70 and Ku80, which determine the pathway of choice for DSB repair (Mansour *et al.*, 2013). This protein-protein interaction is impaired more frequently in tumours compared to normal tissues (Costantini *et al.*, 2007; Parrella *et al.*, 2006; Pucci *et al.*, 2001). So far, Ku70-80 binding has been studied using *in vitro* pull-down techniques, which lack information about their spatiotemporal dynamics in live cells. Despite current knowledge of Ku function as a major effector in genome integrity and proper cellular development, live cell studies are lacking. To understand Ku70-80 interactions and regulation in relation to DNA repair, Ku70 and Ku80 were tagged with fluorescent proteins (EGFP and mCherry). Their interaction was then evaluated using two independent microscopy techniques, FRET-FLIM and BiFC, in live HEK293 cells. Different N- and C-terminal tagging combinations were tested to investigate whether the position of the fluorescence tag affected the localisation and interaction of the proteins. Laser micro-irradiations were used to induce DNA damage in single cells.

Much progress has been made in uncovering the basic IR-induced responses and mechanisms. However, due to limitations in the resolution of conventional confocal microscopes, less is known about the localised IR effects at the nanometre spatial scale. This is where IR is expected to be most efficient at producing correlated damage due to

spatial pattern of energy deposition along the radiation tracks. The limited resolution of confocal microscopy restricts insights into the fine structure of foci, particularly the discrimination of clustered damage after IR (Böcker *et al.*, 2006; Costes *et al.*, 2010; Perez *et al.*, 2016). The development of SR techniques such as STED, SIM and GSDIM offer the possibility to visualise foci at almost ten times the resolution of confocal microscopes (Betzig *et al.*, 2006; Dickson *et al.*, 1997; Gustafsson, 2000; Hell *et al.*, 1994; Rust *et al.*, 2006). For the final part of this research project, these SR methods, along with high-resolution Airyscan and Hyvolution, were employed to investigate the early effects of X-ray radiation at the nanometre scale in HeLa cells. The induction of γH2AX and 53BP1 foci was measured using immunofluorescence. Results from confocal and SR microscopy techniques were compared to highlight the differences in foci quantification, structure and colocalisation due to technical limitations related to the detection systems.

Chapter 2

Materials and Methods

2.1 Materials

2.1.1 DNA Plasmids and Vectors

pOPINE-3C-EGFP	Plasmid #41125, Addgene
pOPINE-3C-mCherry	Oxford Protein Production Facility
pOPINEneo-3C-GFP	Plasmid #53534, Addgene
pEGFP-C1-FLAG-Ku70	Plasmid #46957, Addgene
pEGFP-C1-FLAG-Ku80	Plasmid #46958, Addgene
pBiFC-bFosVC155	Plasmid #22013, Addgene
pBiFC-bJunVN155(I152L)	Plasmid #27098, Addgene

2.1.2 Cell Lines and Culture Reagents

Immortalised Henrietta Lacks (HeLa), Human Embryonic Kidney (HEK293) and Chinese Hamster Ovary (CHO) cells were purchased from ATCC (USA) and tested for mycoplasma contamination. UMSCC74A were kindly provided by Prof T. Carey, University of Michigan, USA. All cell culture reagents were purchased from Thermofisher Scientific including: Minimum Essential Medium (MEM), Foetal Bovine Serum (FBS),

L-glutamine (200 mM), 100 U penicillin, 0.1 mg streptomycin, 1X Phosphate Buffered Saline (PBS) and 0.25% Trypsin-EDTA (1X, 2.5 g porcine trypsin and 0.2g EDTA 4Na per litre in Hank's Balanced Salt Solution). Dimethyl sulfoxide (DMSO) was purchased from Sigma-Aldrich.

See **Appendix A1-A2** for details on labelling and cloning reagents.

2.2 Methods

2.2.1 DNA Amplification by Polymerase Chain Reaction (PCR)

PCR amplification was performed in a 50 μl reaction (containing 1 μl template DNA (100 ng), 25 μl Phusion Flash Master Mix, 1.5 μl forward and reverse primers each (10 μM) and 21 μl water) using a Veriti Thermal Cycler and the previously described cycling protocol (Bird, 2011): 1 cycle of initial denaturation was used for 10 s at 98°C, this was then followed by 29 cycles of denaturation at 98°C for 1 s, annealing at 60°C for 5 s and extension at 72°C for 15 s/Kb. After this cycling, there was a final extension step at 72°C for 2 min.

2.2.2 Isolation of DNA Fragments Using Agarose Gel Electrophoresis

PCR products were isolated by agarose gel electrophoresis, followed by band purification. Upon completion of the PCR reaction, 10 μl DNA Gel Loading Buffer (0.25% w/v bromophenol with 30% v/v glycerol) was added to each sample and mixed gently. 40 μl dye-PCR mix was loaded into a pre-cast 1.0% agarose/Tris-borate-EDTA (TBE) gel containing 0.5 g agarose, 50 ml TBE (1X) and 5 μl SYBRSafe. 5 μl Hyperladder 1 kb was loaded adjacent to the samples. The gel tank was filled with 1X TBE and

subjected to electrophoresis at 70 Volts for 1-2 h using a PowerPac Basic Power Supply until the markers were sufficiently separated.

After marker bands were sufficiently separated, the gel was illuminated with UV (302 nm) excitation (Bio-Rad Chemidoc MP Imaging) to verify the PCR band sizes. Bands of correct bp lengths were excised using a scalpel and the DNA was extracted using a NucleoSpin Gel and PCR clean-up kit (see **Appendix A3**). The excised bands were placed in a microcentrifuge tube and weighed. For every 100 mg of agarose gel, 200 μl NTI buffer was added. The agarose was dissolved and 700 μl of the solution was loaded into a NucleoSpin Gel and PCR Clean-up column with a 2 ml collection tube and centrifuged for 30 s at 17,900 x g in a microcentrifuge. The flow-through was discarded from the collection tube. Next, 700 μl NT3 buffer was added to the column, and the centrifugation and discarding was repeated. The column was further centrifuged for 1 min and placed on a heating block at 70°C for 5 min to completely remove any excess buffer. Next, it was incubated with 12 μl NE elution buffer for 1 min and placed into a new microcentrifuge tube before performing a final centrifugation. The eluted sample was stored at -20°C until needed.

2.2.3 Fusion Cloning Reaction

A Quick-Fusion Cloning Kit (see **Appendix A3**) was used to clone a PCR DNA fragment into a linearised pOPINE vector. Two-way fusion (involving one DNA insert), was performed in a 10 μl reaction containing 1 μl linerarised vector (20-100 ng), 2 μl PCR product insert (10-100 ng), 1 μl fusion enzyme, 2 μl fusion buffer (5X) and 4 μl sterile water. For three-way fusion reactions (involving two DNA inserts), 2 μl of each insert, 2 μl vector, 1 μl fusion enzyme, 2 μl fusion buffer (5X) and 1 μl sterile water

were used. Tubes were incubated for 30 min at 37°C and then placed on ice.

2.2.4 Plasmid Transformation Using Escherichia Coli

100 μl One Shot OmniMAX (Invitogen) chemically competent cells were thawed on ice for each transformation, as described previously (Bird, 2011). Briefly, after addition of 100 ng plasmid DNA, the solution was mixed gently and placed on ice for 30 min followed by 30 sec heat-shock at 42°C. Cells were returned to ice for 2 min and 250 μl S.O.C medium was added to each vial. Tubes were incubated with shaking for 1 h at 37°C. 100 μl transformation mix was spread on a selective LB (Luria Broth) agar plate. After drying, plates were inverted and incubated at 37°C overnight. To prepare selective agar plates, all work was performed inside a Class II biological safety cabinet (Nuaire) to prevent airborne contamination. LB agar plates were prepared as follows: 25 ml LB agar supplemented with the appropriate antibody (1/1000 dilution, 50 μg/ml carbenicillin or 35 μg/ml kanamycin) was mixed gently, poured into a sterile petri dish and left to set. See **Appendix A4** for details on LB and LB agar protocols.

2.2.5 Colony Selection and Starting Culture

The blue-white colony screen was used to detect successful DNA ligation into the vector (Rüther, 1980). The formation of white colonies on the agar plate was indicative of successful ligation, while blue colonies indicated no DNA insert. 5 ml LB containing the appropriate antibiotic was inoculated with a single white colony of transformed bacteria and incubated overnight at 37°C in a shaker.

2.2.6 Small Scale Plasmid Preparation

Small quantities of plasmid DNA (0.5-1 μg) were prepared using a QIAprep Spin Miniprep Kit (see **Appendix A3**) by purifying DNA from the starting culture following the standard manufacturer protocol. Briefly, 5 ml bacterial culture was spun down at 6,800 x g for 3 min at room temperature (RT). The supernatant was removed, and the pellet resuspended in 250 μl P1 buffer, LyseBlue and RNAse A. 250 μl P2 buffer was added and the tube was inverted several times until the solution turned blue to lyse the cells. 350 μl N3 buffer was added to halt the lysis reaction, and inverted until the solution turned white. The tube was then centrifuged at 17,900 x g for 10 min. The supernatant was transferred to a QIAprep spin column (attached to a collection tube) and centrifuged for 30 sec. 500 μl PB buffer was added to the column, followed by another centrifugation. The column was washed with 750 μl PE buffer with ethanol to precipitate the plasmid DNA, and centrifuged for 30 sec, and a further minute to remove any residual buffer. The column was transferred to a fresh microcentrifuge tube and then resuspended in 25 μl EB buffer for 1 min, before a final 2 min centrifugation to elute the DNA. The resulting DNA concentration and purity (260/280 nm ratio) were determined using a NanoDrop 8000 Spectrophotometer.

2.2.7 Construct Verification

2.2.7.1 PCR Screening

PCR verification was carried out using a construct-specific reverse primer and a vector-specific forward primer, as outlined previously (Bird, 2011). Briefly, reactions were set-up in PCR tubes on ice containing Phusion Flash master mix (2X), 10 μM pOPINE

forward primer and gene-specific reverse primers, 100 ng DNA plasmid and made up with sterile water to 25 μl. DNA was amplified using the PCR protocol described in **section 2.2.1** and the products were isolated by agarose gel electrophoresis, as outlined in **section 2.2.2**, with the following modifications: upon completion of the PCR reaction, 5 μl filtered DNA loading buffer was added to each sample (rather than 10 μl), and 20 μl PCR-dye mix was loaded into the gel (rather than 40 μl).

2.2.7.2 Sanger Sequencing

Construct sequences were confirmed by Sanger sequencing (Source BioScience Sanger Sequencing Service, UK) using T7F or custom primers. Results were analysed using SnapGene software and ran through BLAST (Basic Local Alignment Search Tool, NCBI) to match the insert with the original cDNA sequence.

2.2.8 Cloning Details of FRET-FLIM Plasmids

2.2.8.1 C-terminal Tagged Ku70 and Ku80 Constructs

Human Ku70 and Ku80 DNA sequences were amplified from human-tagged open reading frame clones (OriGene, USA) by PCR. Ku70-EGFP and Ku80-EGFP constructs were made by in-fusion of full length Ku70 and Ku80 PCR products into a cut pOPINE-3C-EGFP vector using the primers in **Figure 2.1A**. Full vector maps are shown in **Figures 2.1B-D**. All vector maps were generated using SnapGene software (version 5.0.4). Similarly, Ku70-mCherry and Ku80-mCherry constructs were made by in-fusion of full length Ku70 and Ku80 PCR products into a cut pOPINE-3C-mCherry vector using the same primers in **Figure 2.1A**. pOPINE-3C-mCherry originated from the

pOPINE-3C-EGFP vector (Bird *et al.*, 2015) and thus contained the same primer overhangs. Full vector maps are shown in **Figure 2.2**.

A)

Ku70-EGFP Fwd	aggagatataccatgTCAGGGTGGGAGTCATATTACAAAAC
Ku70-EGFP Rev	cagaacttccagtttGTCCTGGAAGTGCTTGGTGAG
Ku80-EGFP Fwd	aggagatataccatgGTGCGGTCGGGGAATAAGG
Ku80-EGFP Rev	cagaacttccagtttTATCATGTCCAATAAATCGTCCAC

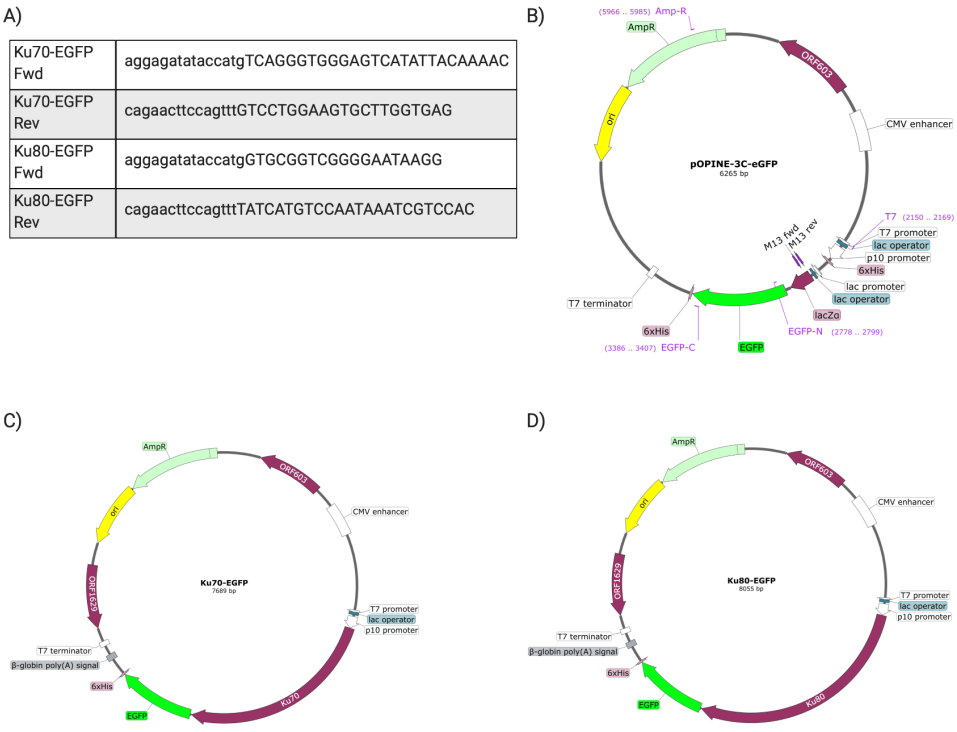

Figure 2.1: Cloning of Ku70/80-EGFP and Ku80-EGFP - A) Primers for cloning Ku70-EGFP and Ku80-EGFP (5' ⟶ 3'). Full vector maps of **B)** pOPINE-3C-EGFP, **C)** Ku70-EGFP and **D)** Ku80-EGFP.

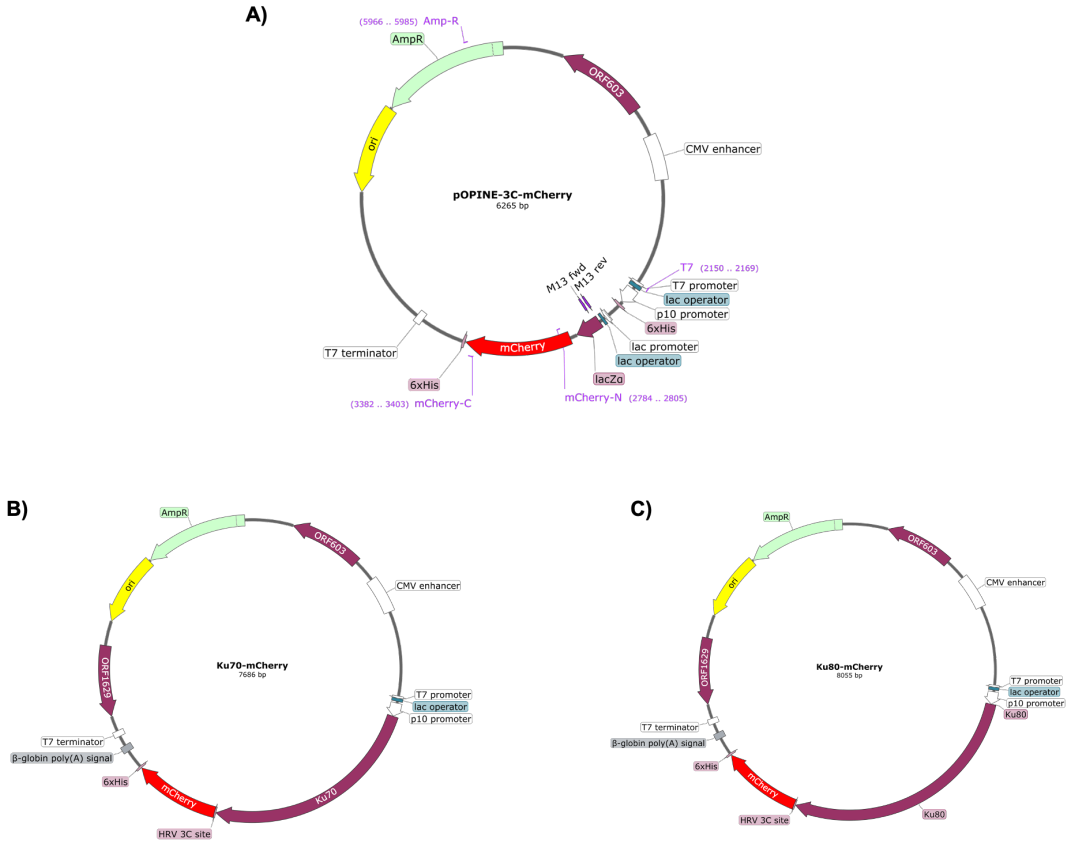

Figure 2.2: Cloning of Ku70-mCherry and Ku80-mCherry - Full vector maps of **A)** pOPINE-3C-mCherry, **B)** Ku70-mCherry and **C)** Ku80-mCherry.

2.2.8.2 N-terminal Tagged Ku70 and Ku80 Constructs

mCherry-Ku70 and mCherry-Ku80 constructs were made by two-way in-fusion of full length Ku70 and Ku80 PCR products (from the Ku70-EGFP and Ku80-EGFP plasmids) with mCherry from mCherry-S6K1 (Ahmed, 2018) into a cut pOPINE vector using the primers in **Figure 2.3A**. Vector maps are shown in **Figures 2.3B-D**. EGFP-Ku70 and EGFP-Ku80 constructs were a gift from Steve Jackson (Britton *et al.*, 2013).

A)

mCherry-Ku70 Fwd	gagctgtacaagTCAGGGTGGGAGTCATAT
mCherry-Ku70 Rev	ctcccaccctgaCTTGTACAGCTCGTCC
mCherry-Ku70 pOPINE Fwd	aggagatataccatgGTGAGCAAGGGCGAGGAG
mCherry-Ku70 pOPINE Rev	gtgatggtgatgtttGTCCTGGAAGTGCTTGGTG

mCherry-Ku80 Fwd	gagctgtacaagGTGCGGTCGGGGAATAAG
mCherry-Ku80 Rev	ccgaccgcacCTTGTACAGCTCGTC
mCherry-Ku80 pOPINE Fwd	aggagatataccatgGTGAGCAAGGGCGAGGAG
mCherry-Ku80 pOPINE Rev	gtgatggtgatgtttTATCATGTCCAATAAATCGTCC

B)

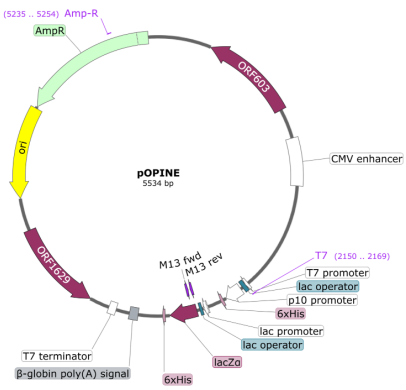

C)

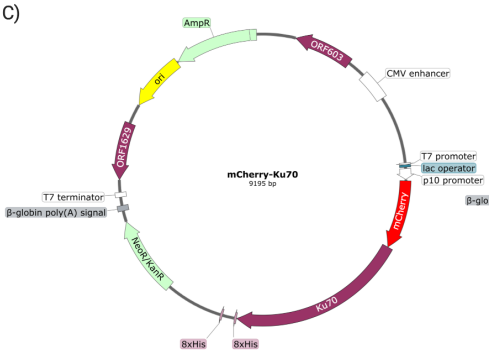

D)

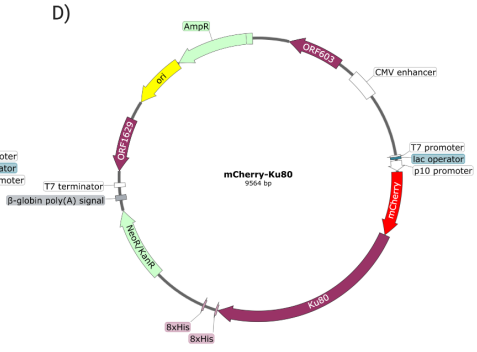

Figure 2.3: Cloning of mCherry-Ku70 and mCherry-Ku80 - A) Primers for cloning mCherry-Ku70 and mCherry-Ku80 (5' ⟶ 3'). Full plasmid maps of **B)** pOPINE vector, **C)** mCherry-Ku70 and **D)** mCherry-Ku80.

2.2.9 Cloning Details of BiFC Plasmids

Venus, a YFP variant, was split into two fragments, namely VN155(I152L) and VC155 (Kodama *et al.*, 2010). The VN155(I152L) fragment was attached to Ku70 and VC155 was fused to Ku80. Ku70-VN155(I152L) and Ku80-VC155 constructs were made by in-fusing full-length Ku70 and Ku80 PCR products (from the Ku70-mCherry and Ku80-mCherry plasmids) with VN155(I152L) from bJun-VN155(I152L) and bFos-VC155 (Kodama *et al.*, 2010) into a cut pOPINEneo-3C-GFP vector using the primers in **Figure 2.4A**. Full vector maps are shown in **Figure 2.4B-D**. The Ku80 binding motif of Ku70 was mutated by altering leucine at position 385 to arginine in the Ku70-VN155(I152L) construct using the primers in **Figure 2.4E**.

A)

Ku70-VN Fwd	aagcacttccaggACGGTACCGGAGGTGGCGGG
Ku70-VN Rev	gccacctccggtaccgtCCTGGAAGTGCTTGGT
Ku70-VN pOPINE Fwd	aggagatataccatgTCAGGGTGGGAGTCATATTACA
Ku70-VN pOPINE Rev	gtgatggtgatgtttGGCGGTGAGATAGACGTTGTG

mCherry-Ku80 Fwd	ttattggacatgataGGTACCCGTCCGGCGTGC
mCherry-Ku80 Rev	cgccggacgggtaccTATCATGTCCAATAAATC
mCherry-Ku80 pOPINE Fwd	aggagatataccatgGTGCGGTCGGGGAATAAGGC
mCherry-Ku80 pOPINE Rev	gtgatggtgatgtttCTTGTACAGCTCGTCCATGCC

B)

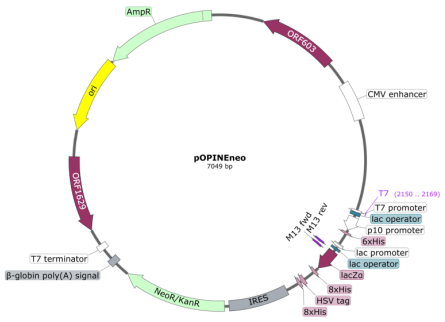

C)

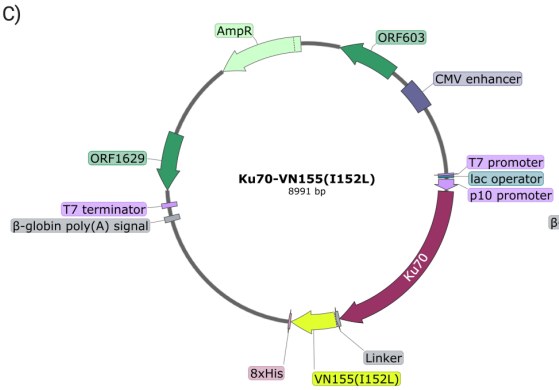

D)

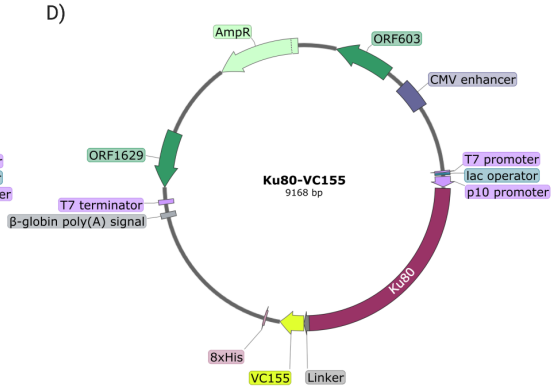

E)

Ku70-L385R-VC Fwd	ACCCTGTTCAGTGCT **CGG**CTCATCAAGTGTCTG
Ku70-L385R-VC Rev	CAGACACTTGATGA **GCC**GAGCACTGAACAGGGT

Figure 2.4: Cloning of Ku70-VN and Ku80-VC - **A)** Primers for cloning Ku70-VN and Ku80-VN (5' ⟶ 3'). Full plasmid maps of **B)** pOPINEneo-3C-GFP vector, **C)** Ku70-VN155(I152L) and **D)** Ku80-VC155 constructs. **E)** Primers for generating *Ku70-L385R-VN* (Ku70-VN mutant) (5' ⟶ 3').

2.2.10 Cell Culture

All tissue culture work was carried out in a class II hood with laminar flow and using aseptic technique. HeLa, CHO and HEK293 cells were cultured in MEM supplemented with 10% FBS, 1% Penicillin-Streptomycin and 1% L-Glutamine. Cells were maintained in an incubator (Binder) at 37°C with 5% CO_2 humidified air in T75 culture flasks. For routine cell passage (every two days), the medium was aspirated, and cells were washed in PBS. To detach cells, 2 ml trypsin-EDTA (1X, ethylenediaminetetraacetic acid) was added for ∼2 min (until cells had detached) and diluted 1:20 with medium. Cell number was determined using a haemocytometer.

2.2.11 Long-term Cell Storage

Cells were detached as described in **section 2.2.10** and then centrifuged at 200 x g for 5 min. The cell pellet was re-suspended in 10 ml freezing mix (90% FBS, 10% DMSO). Aliquots containing $1x10^6$ cells/ml were added to sterile cryotubes and placed in a CoolCell freezing container (BioCision). Cells were stored overnight at -80°C before being transferred into liquid nitrogen (LN) for long-term storage. To thaw cells from LN, cryovials were placed in a 37°C water bath for 1 min and pipetted to a flask with pre-warmed medium.

2.2.12 Cell Seeding

For α-particle irradiations (α-IR), cells were plated at $1.5x10^5$ cells/ml in glass-wall dishes (30 mm internal diameter) containing 2 ml medium as outlined previously (Thompson *et al.*, 2019). These dishes were custom-made with a thin PET (polyethy-

lene terephthalate) base also known as Mylar (DuPont Teijin films, Dumfries, UK) to minimise energy loss during α-IR. Following plating, cells were incubated at 37°C for 24 h to form a monolayer. For angled α-IR, cells were plated on 0.9 μm thick Mylar-based dishes while for perpendicular α-IR, 2.5 μm thick Mylar-based dishes were used. For γ-ray irradiations, similar custom-made glass-wall dishes were employed, but with a coverslip fixed to the base. For X-ray irradiations and experiments that did not involve irradiation, cells were plated on commercial glass-bottom dishes (35 mm diameter) (MatTek Corp, Ashland, MA). For experiments involving Olaparib, 100 nM Olaparib dissolved in DMSO was added to cells ∼16 h prior to irradiation.

2.2.13 Cell Transfection

For experiments requiring cell transfection (**Chapter 4**), cells were transiently transfected using FuGENE HD (Promega), 24 h after seeding. A solution containing 500 ng DNA plasmid, 6 μl FuGENE HD and opti-MEM for a final volume of 100 μl was prepared in a sterile microcentrifuge tube and mixed gently. For co-transfections with two plasmids, two quantities of DNA were added (one for each plasmid) and the rest remained the same. Following a 15 min incubation at RT, the transfection mixture was added dropwise to the seeded cells.

2.2.14 Cell Irradiations with IR

Cells were plated, incubated at 37°C for 24 h and irradiated with low- or high-LET radiation. After irradiation, cells were placed back in the incubator to allow for repair at different time-points before fixing and immunofluorescent staining (**section 2.2.15**).

2.2.14.1 Low-LET X-rays

Low-LET X-ray irradiations were performed at Public Health England (Didcot, UK), using a 250 kVp X-ray source (13.0 mA at 500 mGy/min with both 1 mm copper and 1 mm aluminium filtering; AGO X-Ray Ltd., West Coker, UK), as previously described (D'Abrantes *et al.*, 2017). On the day of irradiation, seeded cells were removed from the incubator and exposed to IR on ice to prevent DNA repair while being transported back to the laboratory for processing.

2.2.14.2 Low-LET γ-rays

γ-ray irradiations were performed using a caesium-137 sealed-source irradiator (GSR D1, Gamma-Service Medical GmbH) at a dose rate of ∼1.6 Gy/min (incident LET 0.3 keV/μm). Cells were irradiated at RT before being incubated at 37°C.

2.2.14.3 High-LET α-particles

High-LET α-IR was performed as previously described (Thompson *et al.*, 2019). Briefly, cells were irradiated with 3.26 MeV α-particles (incident LET 121 keV/μm) using a ^{238}Pu α-particle irradiator. In addition to conventional perpendicular irradiations, a novel technique was used to irradiate at 70° to the normal by scanning the dish across a collimated α-particle beam (approximately 4 mm x 30 mm) (Thompson *et al.*, 2019).

Absorbed dose is defined as the energy deposited by ionizing radiation to matter per unit of mass (J/kg or Gy). Dose D (Gy) at a incident surface of the cells is given by:

$$D = \frac{\phi L}{\rho} \tag{1}$$

where ϕ is the density, ρ is the particle fluence (particles μm^{-2}) and L is the LET (keVμm^{-1}). For the angled irradiations, ρ was multiplied by cos θ. This corresponds to:

$$D = 0.16 \times \phi \times L \tag{2}$$

assuming a cell density of 1 gcm^{-3}. An estimate of the average number of hits per cell nucleus was calculated by multiplying the nuclear area (in μm^2) by the dose and obtaining ϕ.

The fluence of α-particles across the scanned dish was determined using 25 mm diameter fluorescence nuclear track detector (FNTD) discs (Landauer Inc., Stillwater, OK, USA) (McFadden *et al.*, 2016) placed directly on the mylar-based dish. The FNTDs were exposed to perpendicular and angled α-particles. For the angled irradiations, FNTDs were exposed by traversing the dish over a 7.5 mm collimating slit five times. Following irradiation, the resulting tracks were imaged with a Zeiss LSM 710 confocal microscope, see **Methods 2.2.17.3** for imaging details.

2.2.14.4 Low and High Energy Protons

Irradiations with protons were performed using a horizontal, passive-scattered beam line of 60 MeV maximal energy at the Clatterbridge Cancer Centre as previously described (Carter *et al.*, 2018; Kacperek, 2009). Cells seeded in 35 mm dishes were placed

at the isocenter 70 mm from a brass collimator of 43 mm diameter and irradiated with 4 Gy (dose rate ∼5 Gy/min). For high energy protons, cells were exposed directly to a ∼1 keV/μm pristine beam of 58 MeV effective energy. For low energy protons, cells were exposed to 11 MeV mean energy and a corresponding average LET ∼12 keV/μm, using a modulator to generate a 27 mm spread-out Bragg peak (SOBP). A 24.4 mm Perspex absorber was used to position the cells at the distal edge of the SOBP. Cells were kept at 37°C until being irradiated at RT and brought back up to 37°C after irradiation.

2.2.15 Cell Fixation and Immunofluorescent Labelling

Fixation and labelling protocols were performed as described previously (Thompson *et al.*, 2019). Cells were washed with 1X PBS and fixed in 1 ml 4% paraformaldehyde in PBS for 30 min at 4°C. After fixation, cells were washed three times in PBS and permeabilised with 1 ml permeabilising buffer (0.25% Triton X-100 in PBS) for 5 min at RT. Cells were then washed three times with PBS for 5 min and incubated with 1 ml blocking buffer (1% BSA in PBS) for 15 min at RT. This was followed by a 45 min incubation with 500 μl primary antibody solution (1 μg primary antibody in 500 μl blocking buffer) at RT. Samples were then washed three times with PBS, before incubating with 500 μl secondary antibody solution (1 μg secondary antibody in 500 μl blocking buffer) for 30 min, in the dark and at RT. This was followed by three washes with PBS, addition of mounting medium ProLong Gold Antifade Mountant with DAPI and covering with a 22 mm diameter glass coverslip. Dishes were stored in the dark at 4°C until ready for imaging.

2.2.16 Western Blot Analysis

24 h post-transfection, cells were detached as described in **section 2.2.10**. Trypsinised cells were centrifuged for 4 min at 13,000 x g. Cell pellets were re-suspended in 50 μl Cellytic M lysis buffer (consisting of 150 mM NaCl, bicine and dialyzable mild detergent) and vortexed for 2 min before incubating them on ice for 20 min. NuPAGE LDS Sample Buffer (4X, containing glycerol, lithium dodecyl sulfate (LDS), 0.8 M triethanolamine-Cl pH 7.6, 4% Ficoll -400, 0.025% phenol red, 0.025% coomassie G250, 2 mM EDTA disodium) was added to each sample and boiled in a heating block (95°C) for 5 min. 5 μl Novex Sharp pre-stained protein standard was loaded onto the first well of a NuPAGE 4-12% Bis-Tris protein gel. 10 μl sample was loaded into each succeeding well and ran with NuPAGE MES SDS (2-(N-morpholino)ethanesulfonic acid sodium dodecyl sulfate) Running Buffer (1X, containing 50 mM MES, 50 mM Tris Base, 0.1% SDS and 1mM EDTA) for 35 min at 200 V in an XCell SureLock Mini-Cell Electrophoresis System. Gels were transferred to PVDF membranes using an iBlot Gel Transfer device (Thermofisher Scientific). Membranes were placed into plastic containers and incubated with 10 ml blocking buffer (5% milk powder in 1X TBST, tris buffered saline with tween-20, for 1 h. Next, primary anti-Ku70 antibody (1:1000 in blocking buffer) was added and incubated at 4°C overnight on a rocker. Membranes were washed three times for 5 min with 10 ml 1X TBST buffer and incubated with horseradish peroxidase (HRP)-linked secondary antibody (1:2000 in blocking buffer) in plastic containers for 1 h at RT. Following three washes with TBST, membranes were washed in deionising water, blots were developed in a final volume of 10 ml Pierce ECL (Enhanced chemiluminescence) Western Blotting Substrate (containing HRP substrate) for 5 min prior to chemiluminescent imaging on a ChemiDoc MP Imaging System.

The blot was 'stripped' using Restore Western Blot Stripping Buffer (containing Tris-HCl, SDS and β-mercaptoethanol) at 37°C for 15 min and re-blotted using a vinculin antibody to determine protein loading for normalisation. Bands were quantified using Fiji (ImageJ; NIH (Schindelin *et al.*, 2012)). See **Appendix A5** for TBS and TBST buffer composition.

2.2.17 Imaging Methods

2.2.17.1 Live Confocal and FRET-FLIM Imaging of Ku70/80

HEK293 cells were imaged 48 h after transient transfection with Ku70/80 constructs. Imaging and micro-irradiation experiments were performed at 37°C using an inverted Nikon TE2000-U microscope connected to a Nikon C2 scanning system with an mCherry (561 nm excitation) and EGFP (488 nm excitation) filter set. A computer-controlled microscope stage (Marzhauser Wetzlar GmbH & Co., Germany), a Nikon 60x/1.27 numerical aperture (NA) plan-apochromat (PlanApo) water immersion objective, and a standard photomultiplier tube (PMT) were used to record single-plane 2D images. For laser micro-irradiations, an 8 μm line within the cell nucleus was generated for 10 sec with a 405 nm laser set to 100% (single-photon excitation, 1 mW. Illumination power at the objective was 24 μW). The laser was scanned once over the respective cell. Images were obtained before and immediately after irradiation and analysed in Fiji.

The FRET-FLIM settings and microscope setup used have been previously described (Yadav *et al.*, 2013). Briefly, fluorophores were excited using a pulsed titanium sapphire laser system (Mira 900, Coherent Lasers, UK) pumped by a 532 nm solid-state laser source (Verdi V18, Coherent Lasers, UK), tuned to 910 nm (180 fs pulses at 76 MHz)

and emitted through a Comar BG39 bandpass filter (to reject laser excitation light and collect EGFP emission). Photons were counted using a Becker-Hickl (B&H) high speed hybrid detector (HPM-100) and SPCM64 software package for time-correlated single photon counting, used to measure highly accurate lifetimes. Single-plane 2D images were acquired (until >100 counts/pixel were collected) and analysed with SPC Image B&H software (version 6.0). Each pixel on a FLIM image was colour-coded according to its lifetime.

2.2.17.2 Live Confocal BiFC Imaging of Ku70/80

24 h after HEK293 cell transfection with the respective BiFC constructs, cells were imaged using an inverted Nikon TE2000-U microscope connected to a Nikon C2 scanning system with a SuperK-FIANIUM supercontinuum white light laser (WLL) and a Nikon 60x/1.27 NA PlanApo water immersion objective. Venus fluorophores were excited using 515 nm. Single-plane 2D images were recorded and detected using a standard PMT. Fluorescence intensity was quantified in >100 cells for each experiment using Fiji.

2.2.17.3 Confocal Imaging of Fixed Samples and FNTDs

Following fixation, HeLa cells were imaged using a confocal microscope (LSM 710, Carl Zeiss, Inc.) equipped with a Zeiss 63x/1.4 NA PlanApo oil immersion objective and a standard PMT. AlexaFluor488 was excited with 488 nm and Aberrior STAR635P (StarRed) with 633 nm. Individual confocal slices (obtained with a z-step size of 0.66 μm) were recorded and compressed into 2D maximum intensity projections using Fiji. FNTDs were excited with 633 nm. Eight individual confocal slices were obtained per

image and compressed into 2D maximum intensity projections using Fiji.

2.2.17.4 Airyscan Microscopy

Airyscan microscopy was carried out using a Zeiss LSM 880-Elyra PS1 system (Carl Zeiss, Inc.) with a Zeiss 100X/1.46 NA PlanApo oil immersion objective and a GaAsP detector. AlexaFluor488 and Silicon Rhodamine (SiR) were excited using 488 nm and 633 nm laser lines, respectively. Single-plane 2D images were processed in Zeiss ZEN software and analysed using Fiji. The strength of the Wiener filter to determine the deconvolution parameters was automatically set by the software from the image SNR.

2.2.17.5 Super-resolution SIM

2D SIM was executed using an ELYRA PS1 (Carl Zeiss, Inc) microscope equipped with 488 nm and 561 nm laser lines, a Zeiss 100X/1.46 NA oil PlanApo objective and a PCO Edge scientific CMOS (sCMOS) camera.

2.2.17.6 Super-resolution STED

2D single- and dual-colour STED microscopy was performed using a Leica SP8 3X STED SMD confocal microscope (Leica Microsystems, Manheim, Germany), equipped with a pulsed super-continuum WLL and a Leica 100X/1.4 NA PlanApo oil immersion objective. Notch filters were used to reject laser excitation light. AlexaFluor488 was excited with 488 nm and STED-depleted with 592 nm. SiR was excited with 652 nm and STED-depleted with 775 nm.

2.2.17.7 Super-resolution GSDIM

GSDIM was carried out as previously described (Van De Linde *et al.*, 2011b) on a Nikon N-STORM microscope equipped with a 100X/1.49 NA Apo TIRF (total internal reflection fluorescence) oil lens. Cells were excited by 488 nm laser light under TIRF illumination. Emitted fluorescence was detected using an Andor iXon DU-897E EM-CCD camera. The resulting single-plane 2D images were analysed using a previously described algorithm (Yang *et al.*, 2012) and processed using Fiji.

2.2.18 Image Processing and Foci Analysis

Image processing and analysis was performed using Fiji. All plots were created using the Python library Plotly (Plotly Technologies Inc., 2015). Z-tools such as maximum intensity Z-projection (where individual confocal slices are merged into a single plane) and orthogonal views (where the XZ and YZ planes at a given point in the 3D image are shown) were used to visualise 3D stacks. Unless stated, analysis was performed using 2D maximum intensity projections of 3D confocal slices obtained with a z-step size of 0.66 μm.

Foci were counted using an in-house macro built on Fiji as described previously (Rodriguez-Berriguete *et al.*, 2018). The flow diagram shown in **Figure 2.5** outlines the steps taken. Firstly, images were split into three different channels (green, red and blue). The recognition of the regions of interest (ROIs), blue DAPI staining within the cell nucleus, relied on conventional image processing steps including a histogram-based binerisation (conversion in black and white to distinguish objects from the background) by applying 'Huang dark' thresholding (Huang *et al.*, 1995), which was manually ad-

justed to select the nuclei. Next, a smoothing mask was used to reduce noise. A number of steps were applied to refine the reconstruction of the nuclei (including hole filling and watershed segmentation to separate overlapping objects). Using the 'Analyse Particles' tool, a size filter was used to avoid particles outside the size of a typical nucleus (100-300 pixel^2). ROIs were stored to use in the next step, to extract parameters such as nuclei size and determine the number of foci/nucleus.

For the selection of foci, a smoothing mask was applied and the 'Find Maxima' tool was used. This searches for local maxima in an image and ignores pixels with a level below a user-defined threshold (Schindelin *et al.*, 2012). The threshold used for the maxima was defined visually to discriminate foci from background signals (shown in **Figure 3.4**). The output of the script was an image showing the foci within each cell nucleus and a table with area and number of foci/nucleus. The average foci yield/nucleus and standard deviation were calculated for each image and consequently each sample. All steps were optimised by manually adjusting the criteria and comparing the results with manual scoring. Once optimised, the criteria was kept fixed. Visual checks were performed on all images from every data set after processing for quality assurance.

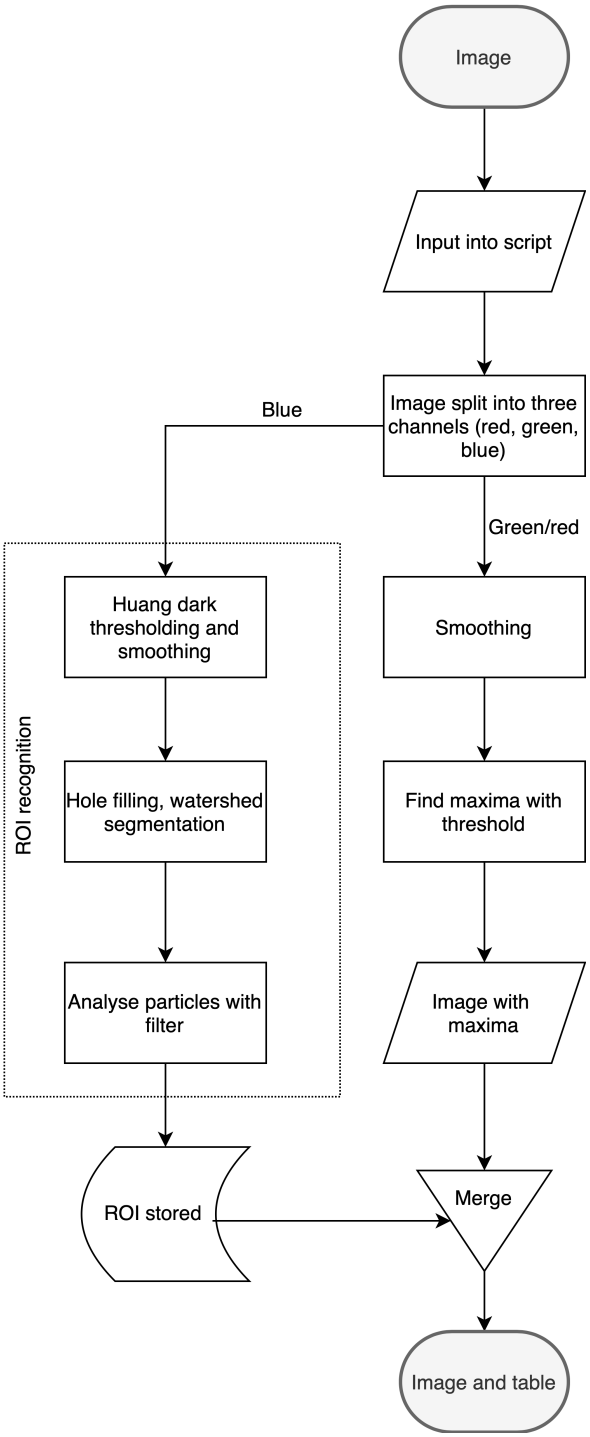

Figure 2.5: Image processing flow chart - Flow chart showing the steps for foci recognition.

Foci area was measured with the FociPicker plugin using automatic parameters (Du *et al.*, 2011) and visually inspected for quality assurance. Foci co-localisation was quantified using the JaCoP plugin (Bolte *et al.*, 2006). Pearson's correlation coefficient and Mander's overlap coefficients M1 and M2 were employed. Coste's automatic thresholding was used to eliminate bias and improve SNR (Costes *et al.*, 2004; Wu *et al.*, 2012). Foci intensity profiles were measured in Fiji. Several custom-made macros were designed to efficiently make use of these tools by batch processing.

Chapter 3

Investigating OGG1 Recruitment to Complex DNA Damage Sites

3.1 Brief Introduction

As outlined in the **Introduction**, radiation therapy relies on ionising radiation (IR) to kill cancer cells. This ability of IR, particularly charged particles, is based on the hallmark induction of highly localised ionisation events resulting in closely spaced DNA lesions, termed clustered or complex DNA damage (CDD). This not only includes DSBs and complex DSBs, but also non-DSB clusters. CDD is more difficult to repair and thus plays a significant role in cancer cell killing. Studies have shown the delay in processing and repair of CDD by the persistence in DNA repair protein foci. High-LET radiation (such as α-particles and carbon ions) has an elevated propensity to form CDD in comparison with low-LET X-rays and γ-rays. This is one of the reasons why high-LET radiotherapy is expected to have greater therapeutic effectiveness and represents a promising alternative for radioresistant tumours. Despite this, the recognition and processing of CDD produced by different radiation qualities are currently unclear, particularly those produced by α-particles and protons (at and around the Bragg peak).

3. OGG1 RECRUITMENT TO COMPLEX DNA DAMAGE SITES

Recent studies have identified proteins OGG1 (Nikitaki *et al.*, 2016a), PARP-1 (Carter *et al.*, 2019), RNF20/40 and $H2B_{ub}$ (Carter *et al.*, 2018) as essential components for CDD repair. The working hypothesis of this chapter is the following:

- High-LET IR enhances foci persistence of OGG1, γH2AX, PARP1, RNF20 and $H2B_{ub}$ at sites of complex DNA damage, compared to low-LET IR. PARP inhibition with Olaparib further increases foci persistence after high-LET IR. The structure and spatial distribution of foci can be used as an indicator of low- or high-LET IR exposure.

Methods

UMSCC74A (oropharyngeal squamous cell carcinoma) and HeLa cells were irradiated with 4 Gy low-LET protons and gamma-rays (γ-rays), and comparing the response to high-LET alpha-particles (α-particles) and protons (**Methods 2.2.14**). At various time-points post-IR, DNA damage induction and repair were measured by quantitative imaging (**Methods 2.2.17-18**). 4 Gy was chosen to enable comparison with ongoing studies by collaborators (Carter *et al.*, 2018).

Publications for this chapter:

Thompson, J.M., Elliott, A., **D'Abrantes, S.**, Sawakuchi, G.O., Hill, M.A. Tracking down alpha-particles: the design, characterisation and testing of a shallow-angled alpha-particle irradiator. *Radiation Protection Dosimetry.* (2019).

3.2 Results

3.2.1 PARP1, $H2B_{ub}$ and RNF20 Expression Following IR

To begin with, the recruitment of PARP1 to DNA damage sites was investigated. HeLa cells were irradiated with 4 Gy γ-rays, fixed 1 h post-IR, labelled with PARP1-AlexaFluor488 and imaged using confocal microscopy. **Figure 3.1A** shows there was no difference in specific foci formation between the control and irradiated samples. Staining outside the nucleus indicated non-specific antibody binding. Next, to evaluate $H2B_{ub}$ recruitment, HeLa cells were irradiated with 1 Gy perpendicular α-particles, fixed 1 h post-IR, stained with $H2B_{ub}$-AlexaFluor488 and DAPI, and visualised using confocal imaging. **Figure 3.1B** shows there was abundant cytoplasmic $H2B_{ub}$ staining, also suggesting non-specific antibody binding. Thus, these particular anti-$H2B_{ub}$ and anti-PARP1 antibodies were unsuitable for immunofluorescence (IF) studies.

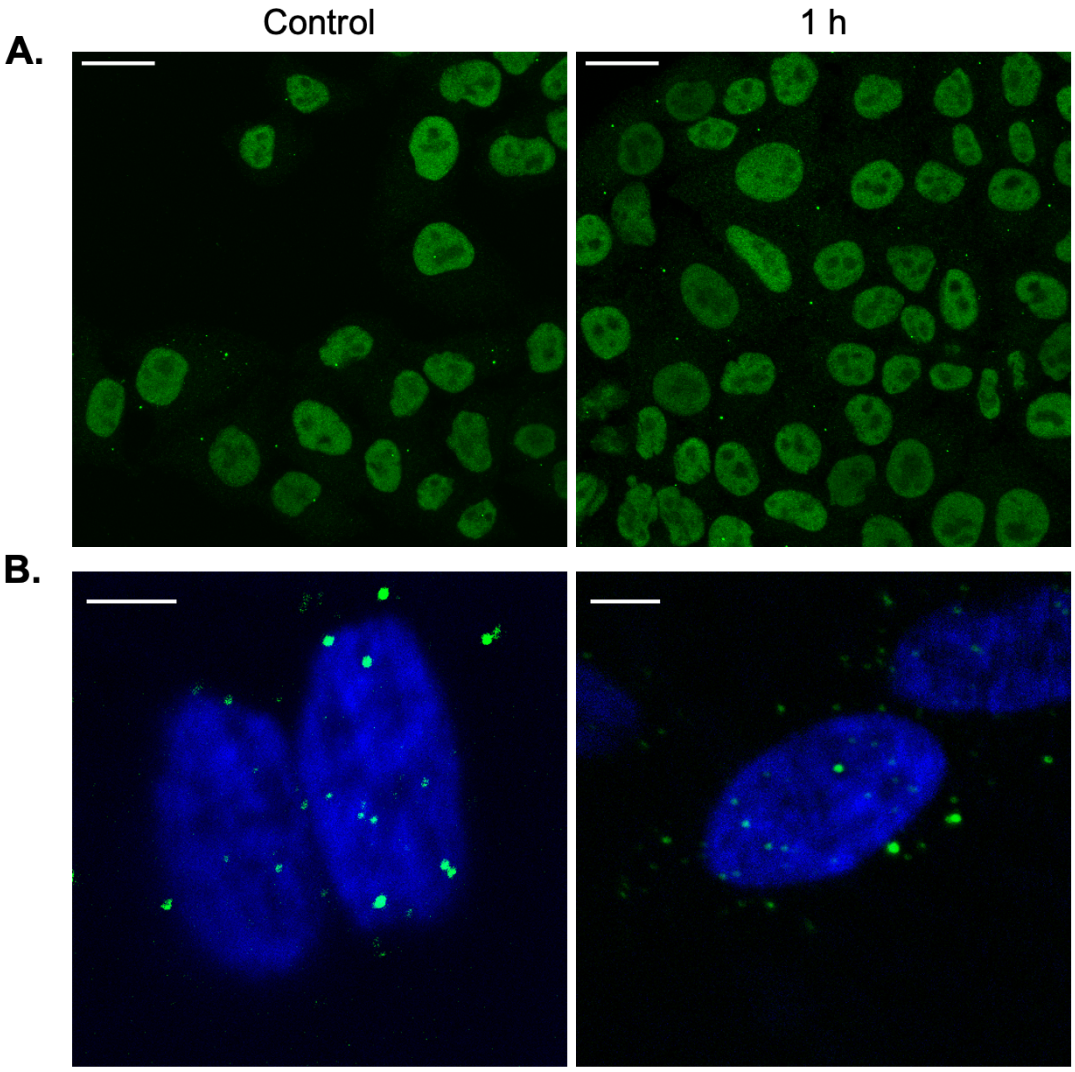

Figure 3.1: PARP1 and $H2B_{ub}$ labelling in HeLa cells - A) PARP1-AlexaFluor488 expression in unirradiated (left) and irradiated (right) cells with 4 Gy γ-rays. **B)** $H2B_{ub}$-AlexaFluor488 and DAPI expression in unirradiated and irradiated cells with 1 Gy perpendicular α-particles. Cells were fixed 1 h post-IR and imaged using confocal microscopy. Representative data from three independent experiments. Scale bars, **A)** 20 μm, **B)** 10 μm.

RNF20 recruitment to DNA damage sites was investigated next. **Figure 3.2A** shows unirradiated and irradiated HeLa cells left to repair for 30 min and labelled with $H2B_{ub}$-AlexaFluor488 and RNF20-StarRed. $H2B_{ub}$ foci did not appear to be irradiation dependent. Several foci, which were largely outside the nucleus, were observed in the control sample. The predominantly nuclear localisation of RNF20 was in agreement with other studies (Nakamura *et al.*, 2011), however no foci were observed 30 min post-IR. To exclude this was associated with transcription and to largely examine possible DNA damage-dependent foci formation, cells were preincubated with 1μg/ml transcription inhibitor actinomycin D for 1 h prior to irradiation (**Figure 3.2B**). Using DMSO as a control, there were still no RNF20 foci observed upon IR, suggesting that this specific anti-RNF20 antibody was unsuitable for investigating IR-induced effects. Levels of $H2B_{ub}$ appeared to be somewhat suppressed following actinomycin D incubation, while the levels of RNF20 looked unaffected.

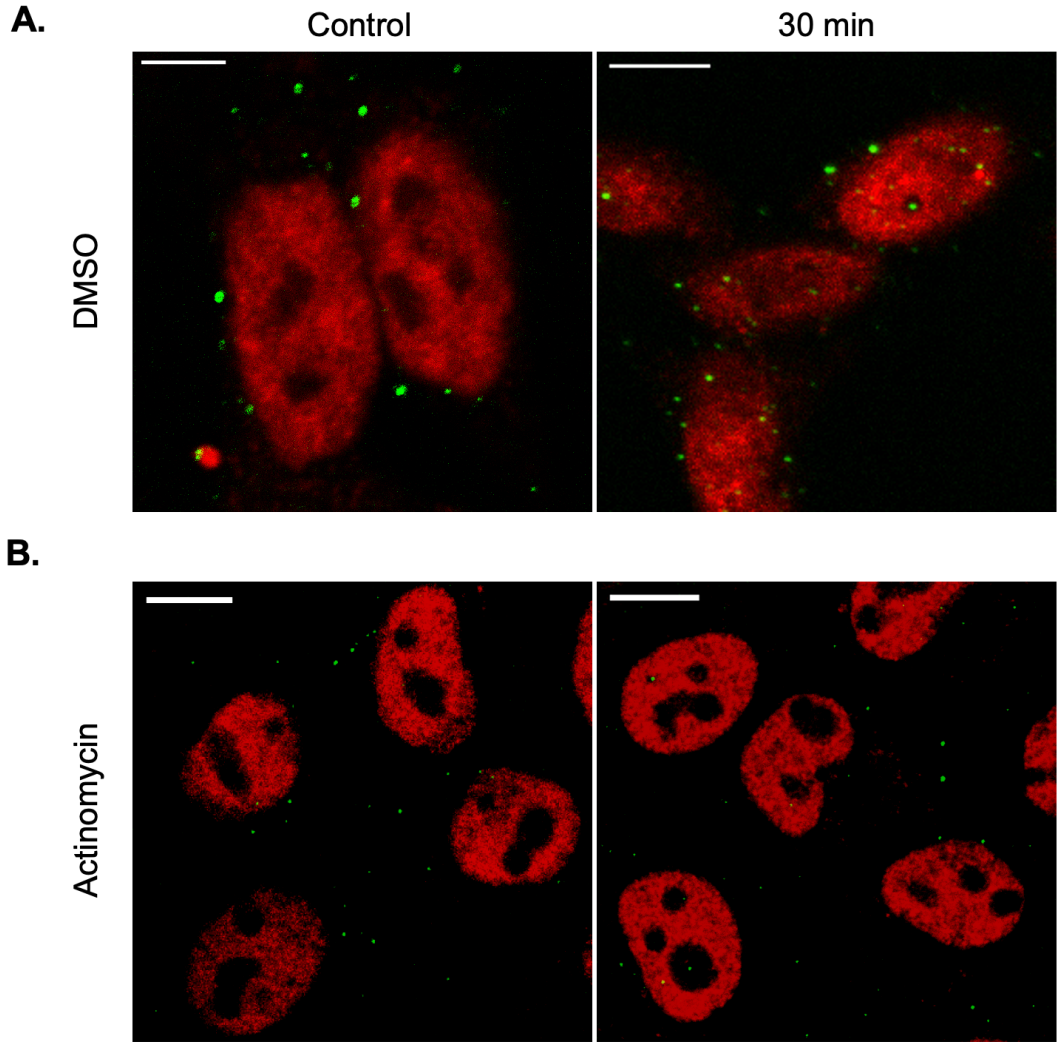

Figure 3.2: RNF20 and $H2B_{ub}$ labelling in HeLa cells - $H2B_{ub}$-AlexaFluor488 and RNF20-StarRed expression in unirradiated (left) and irradiated (right) cells incubated for 1 h with **(A)** DMSO or **(B)** 1 μg/ml actinomycin D prior to irradiation. Cells were irradiated with 1 Gy perpendicular α-particles, fixed after 30 min and imaged using confocal microscopy. Representative data from three independent experiments. Scale bars, 10 μm.

3.2.2 OGG1 and γH2AX Expression Following Low- and High-LET IR

Next, the recruitment of OGG1 and γH2AX to DNA damage sites was evaluated. HeLa cells were irradiated with low-LET γ-rays (γ-IR) or high-LET perpendicular or angled α-particles (α-IR). Cells were fixed 1 h post-IR, labelled with γH2AX-AlexaFluor488, OGG1-StarRed and DAPI, and imaged using a confocal microscope. **Figure 3.3A** reveals the 2D and 3D visualisation of OGG1 and γH2AX foci following γ-IR, which enabled efficient discrimination between individual foci. As highlighted by the white dotted circle on the right-hand side, at least three closely spaced foci could be distinguished in the y-z and x-z axis, which overlapped as one focus in the x-y. This was also observed after perpendicular and angled α-IR in **Figures 3.3B-C**. It was difficult to resolve individual foci along the perpendicular particle track in **Figure 3.3B**, as several foci appeared extended along the z axis. This stems from the microscope ∼500 nm axial resolution limit. In contrast, cells in **Figure 3.3C** clearly showed multiple foci along the path of the angled α-particles traversing the nucleus, providing an improved way to distinguish foci.

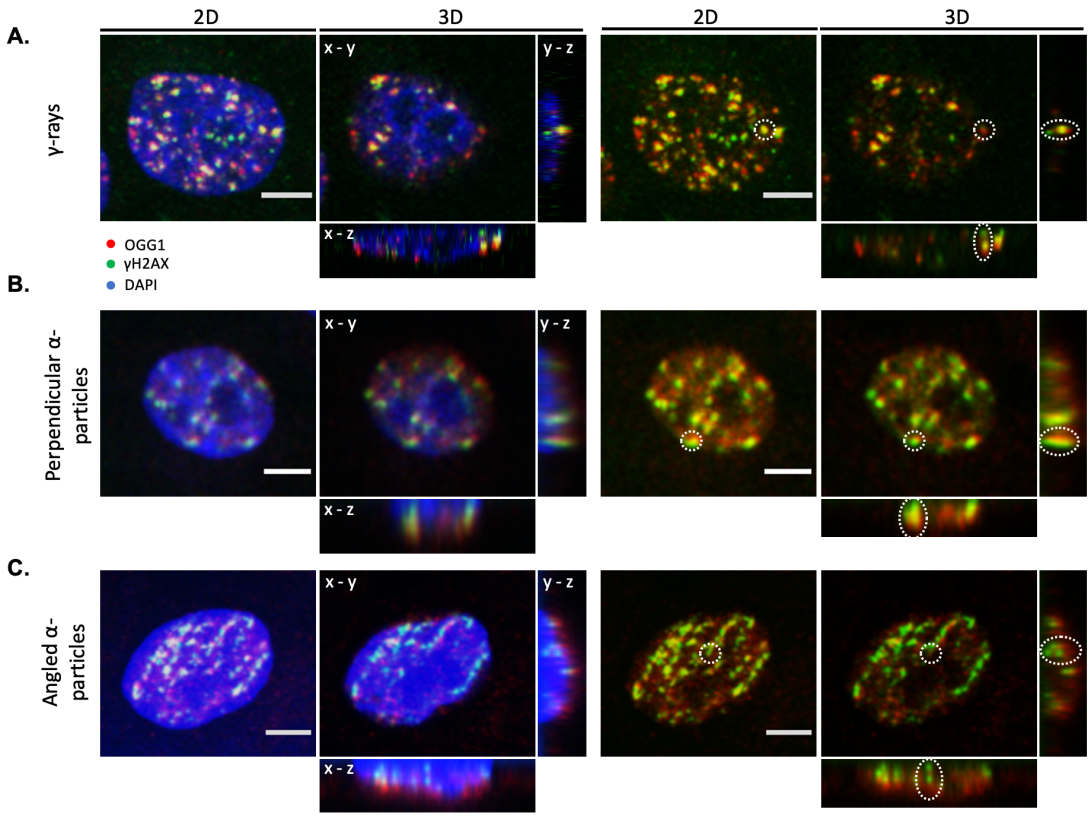

Figure 3.3: 2D and 3D visualisation of OGG1 and γH2AX foci following low- and high-LET IR - OGG10-StarRed, γH2AX-AlexaFluor488 and DAPI were visualised in HeLa cells 1 h after 4 Gy **A)** γ-rays, **B)** perpendicular α-particle and **C)** angled α-particle irradiation. White dotted circles highlight where several foci that overlap in the 2D image were well separated in the 3D orthographic projection. Representative data from three independent experiments. Scale bars, 5 μm.

3.2.3 Threshold Comparison and Manual Validation for γH2AX and OGG1 Foci Quantification

Once it was established that OGG1 and γH2AX foci could be visualised, their quantification after low- and high-LET IR was investigated. Foci were counted using an in-house macro built on ImageJ with an adjustable threshold to discriminate foci from background signals (see **Methods 2.2.18**). The macro was calibrated by testing several thresholds and comparing them by eye. **Figure 3.4** shows three of several thresholds that were tested. To account for the presence of DNA damage on different planes, 3D image stacks were recorded and reconstructed as a 2D image.

HeLa cells were irradiated with 4 Gy γ-IR and labelled with γH2AX-AlexaFluor488 and OGG1-StarRed 1 h post-IR. **Figure 3.4A** shows several discrete γH2AX foci and a low background signal in the original image. The 750 and 500 thresholds did not identify sufficient foci, while the 250 threshold allowed the recognition of most foci in the nucleus. This is particularly clear in the expanded views (**Figure 3.4Ai**). Similarly, OGG1 foci were best identified by the 250 threshold, as shown in **Figure 3.4B**. The higher background signal of OGG1 led to the false recognition of foci outside the cell nucleus. This did not interfere with the foci quantification, as the macro segregated each nucleus from their DAPI signal prior to obtaining the number of foci/cell, excluding any signal outside the cell nucleus.

The 250 threshold was then applied and tested on several more images. After confirming it was suitable, it was used throughout this study. Several visual checks were performed between data sets to make sure this threshold remained appropriate. While the absolute number of foci may vary with scoring criteria, as the same criteria was used across all samples the general trends remained the same.

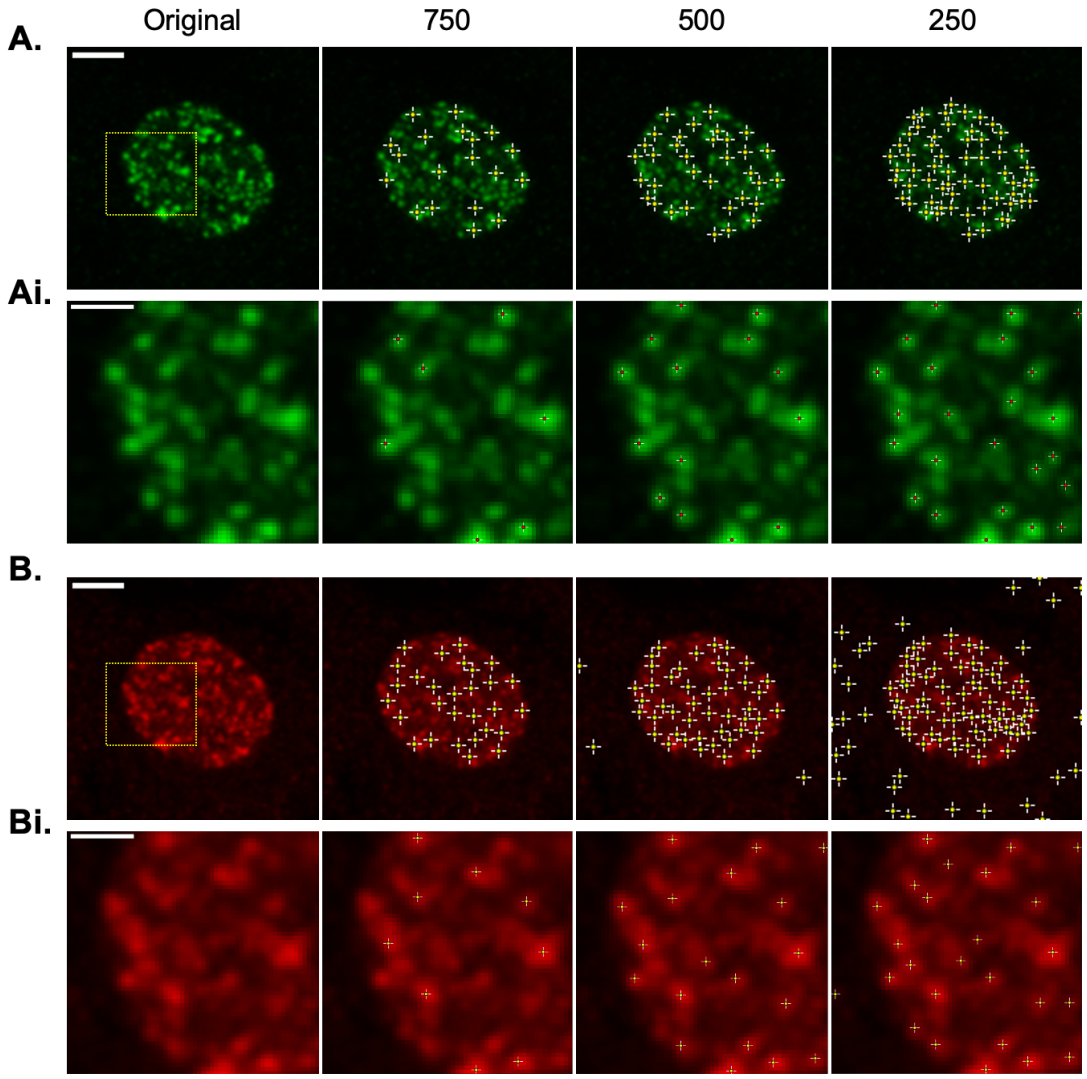

Figure 3.4: Threshold comparison for γH2AX and 53BP1 foci quantification - Irradiated HeLa cells labelled with **A.** γH2AX-AlexaFluor488 or **B.** OGG10-StarRed 1 h following 4 Gy γ-IR, and imaged using confocal microscopy. Foci were counted with an automated ImageJ script which used a threshold to count foci. From left to right: original image, and 750, 500 and 250 thresholds (scale bars 5 μm). **Ai./Bi.** Expanded views of the yellow-boxed region (scale bars, 2 μm). Representative data from three independent experiments.

3.2.4 OGG1 and γH2AX Foci Kinetics Following Low-LET γ-rays and High-LET α-particles

To investigate OGG1 and γH2AX foci kinetics, HeLa and UMSCC74A cells were irradiated with γ-IR or α-IR known to generate CDD in different proportions. The yields of OGG1 and γH2AX foci were analysed at various time-points post-irradiation. The focus was on identifying whether OGG1 and γH2AX were responsive to CDD induced by α-IR, particularly at later time-points post-IR where CDD persists.

Figure 3.5A shows OGG1 and γH2AX foci kinetics following γ-IR in UMSCC74A cells. OGG1 foci numbers increased rapidly reaching 59 (±3) foci/cell at 30 min, followed by a gradual decrease. By 24 h, OGG1 foci numbers returned to control levels. γH2AX followed a similar pattern, with a peak of 64 (±3) foci/cell at 30 min, decreasing to control levels by 24 h. From the peak to the 24 h time-point (minus the controls), there was a 110% loss of OGG1 and 94% for γH2AX foci, indicating that most IR-induced lesions were repaired. The kinetics observed here are very similar to those observed with HeLa cells, see **Appendix B**.

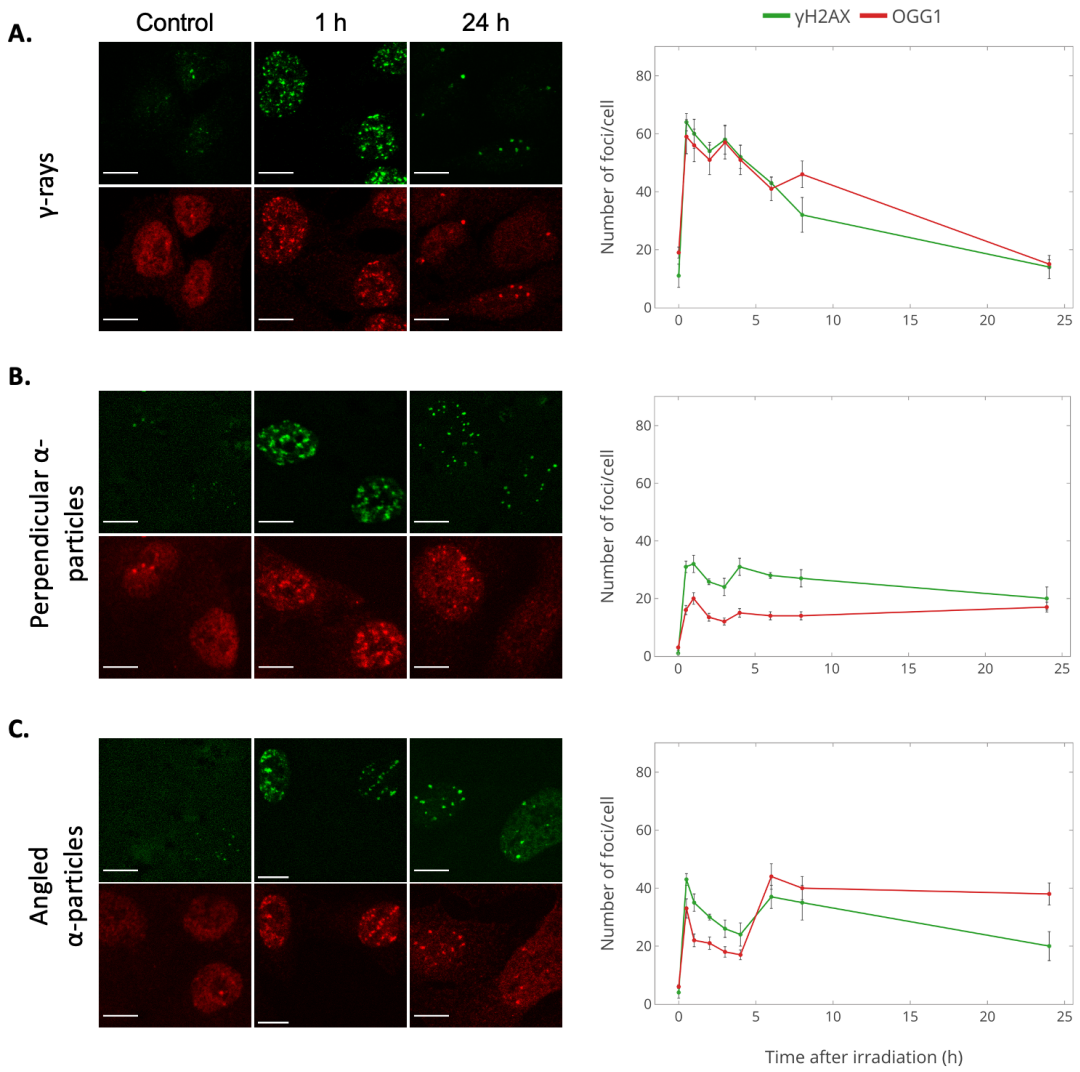

Figure 3.5: γH2AX and OGG1 foci kinetics following low- or high-LET IR in UMSCC74A cells - OGG10-StarRed and γH2AX-AlexaFluor488 foci kinetics in unirradiated (control, 0) and 4 Gy irradiated cells with **A.** γ-IR, **B.** perpendicular α-IR and **C.** angled α-IR, imaged using confocal microscopy. Images from key time-points are presented. Error bars represent standard deviation (SD) among three independent replicates. Scale bars, 10 μm.

Next, OGG1 and γH2AX foci kinetics following perpendicular α-IR were investigated. As seen in **Figure 3.5B**, OGG1 foci yield peaked at 20 (±3) foci/cell 1 h after α-IR, followed by a small decrease in numbers by 24 h. Similarly, γH2AX foci peaked at 32 (±3) 1 h post-IR, decreasing until 24 h. From the peak to the 24 h time-point (minus the controls), there was an 18% loss of OGG1 and 39% for γH2AX foci. A larger proportion of residual foci was observed at 24 h following α-IR, compared with γ-IR.

To complement standard perpendicular α-particle irradiations, cells were also exposed at a shallow angle (70° to the normal) of cell monolayers to maximise the resolution of individual foci along the x-y axis (see **Methods 2.2.14.3** for details). **Figure 3.5C** shows OGG1 and γH2AX kinetics after angled α-IR. OGG1 foci peaked at 33 (±4) foci/cell 30 min post-IR, decreasing until 4 h, followed by a sharp 159% increase at 6 h, and decreasing 14% until 24 h. Interestingly, the large increase at 6 h was not observed with γ-IR nor perpendicular α-IR. Similarly, γH2AX foci peaked at 43 (±2) 30 min post-IR, decreasing until 4 h, increasing 53% at 4 h, decreasing 46% until 24 h.

The increase in OGG1 foci from the 30 min time-point is counterintuitive and requires further investigation. A potential explanation is that the dose used was too high, leading to significant foci overlap at early time-points and thus a reduction in foci that are resolvable. Another explanation is that closely spaced foci, which appeared as single foci, moved apart and became resolvable over time. Alternatively, as cells spread and attached to the bottom of the dish (mylar-based), more foci became resolvable. From the peak to the 24 h time-point (minus the controls), there was a 59% loss of γH2AX but a 19% increase of OGG1 foci.

OGG1 and γH2AX foci kinetics clearly differed with increasing LET. This was distinctly

observed on **Figure 3.6**, where the number of OGG1 (top) and γH2AX (bottom) foci/cell relative to values at 30 min after irradiation were plotted. The trends of OGG1 and γH2AX after γ-IR were similar. For high-LET irradiated cells, both OGG1 and γH2AX foci numbers quickly decreased after the peak at early time-points, particularly after perpendicular α-IR. At later time-points, the normalised numbers of OGG1 foci were significantly higher for high-LET compared to low-LET, particularly at 24 h post-IR. This was also observed with γH2AX, although not as distinct. This shows that these α-IR-induced foci remained for longer than those induced by γ-IR, possibly reflecting the increased complex nature of damage formed by α-IR. The quick fall in foci at early time-points following high-LET IR was unexpected and requires further investigation.

Overall, unlike low-LET induced damage, most CDD inflicted by high-LET IR was more difficult to repair or likely irreparable. This may be due to either the generation of more complex CDD (i.e. greater number of lesions within each cluster) or the production of multiple sites of CDD within close proximity along the α-particle track. Consequently, the structure and spatial distribution of foci after low- and high-LET IR were evaluated next.

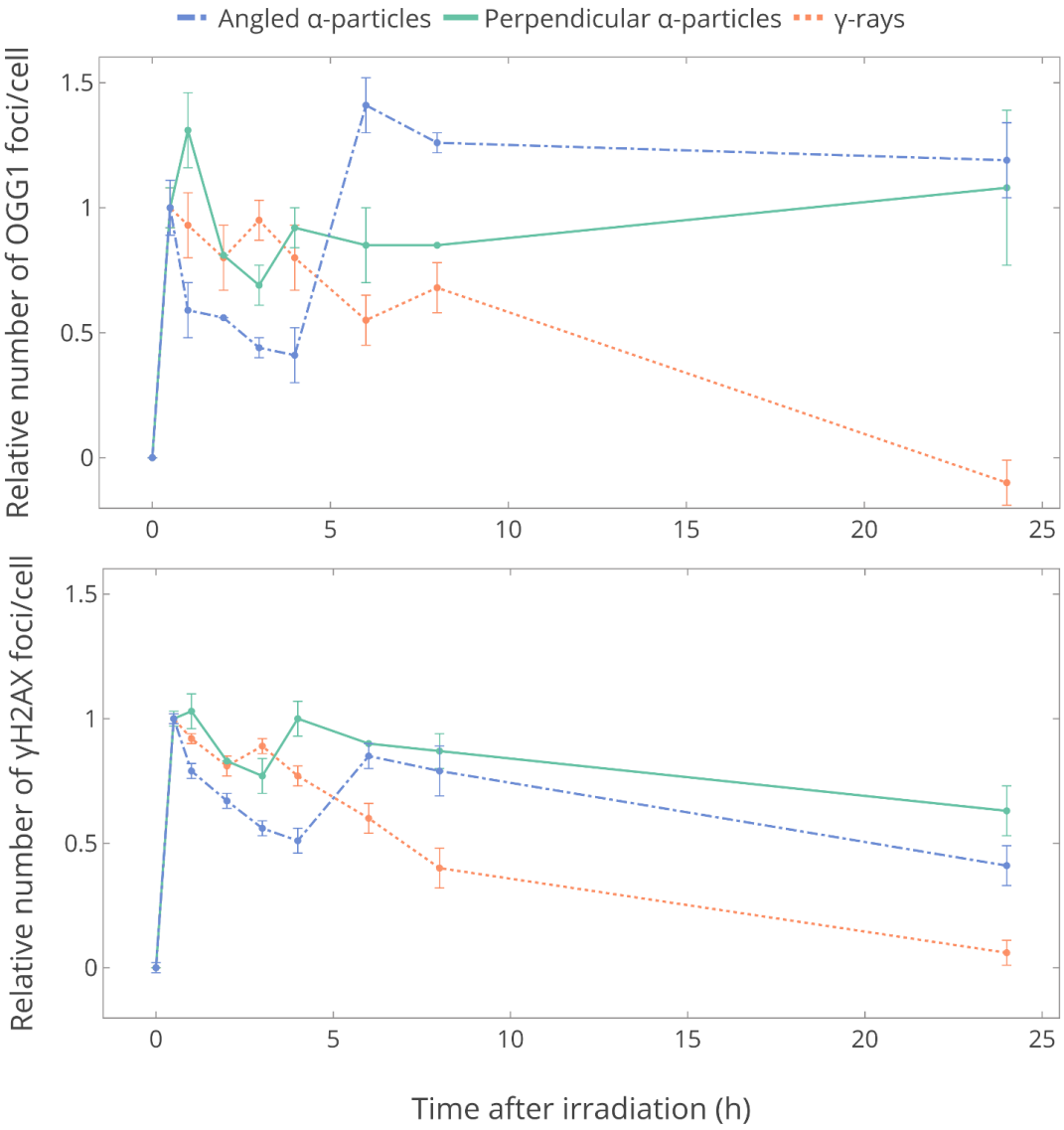

Figure 3.6: Normalised γH2AX and OGG1 foci kinetics following low- or high-LET IR in UMSCC74A cells - Number of OGG1 (top) and γH2AX (bottom) foci/cell relative to values at 30 min after irradiation minus control samples (0 h) with low-LET γ-rays, high-LET perpendicular or high-LET angled α-particles in UMSCC74A cells. Error bars represent SD among three independent replicates.

3.2.5 Evaluation of Foci Structure as a Function of Radiation Quality

The OGG1/γH2AX foci induced by low- and high-LET IR differed in morphology, particularly their sizes. **Figure 3.7** shows the mean foci area of OGG1 and γH2AX foci over time before and after γ-IR and α-IR in HeLa (**7A**) and UMSCC74A cells (**7B**). The mean foci area ($\sim$0.3 μm^2) of OGG1 and γH2AX in the unirradiated controls (0 h) were very similar in both HeLa and UMSCC74A cells. As seen in **Figure 3.7A**, the mean area of OGG1 foci induced by all irradiation types increased at 1 h post-IR (13% after γ-IR, 131% after perpendicular α-IR and 53% after angled α-IR), with the largest rise seen after α-IR. A larger increase was observed for γH2AX, with a 19% surge in mean foci size after γ-IR, 131% after perpendicular α-IR and 133% after angled α-IR.

The smaller size of OGG1 foci observed after angled α-IR could be due to the close arrangement of the foci in z for perpendicular α-IR tracks. The images used to calculate the foci area were a compression of 3D image stacks, creating a 2D image. Thus, the information in the z axis, along the path of the perpendicular α-particle track, contains multiple foci compressed into a single focus. If individual OGG1 foci were more spread out than γH2AX foci, particularly in the z, upon compression of the 3D stack, the foci would appear larger. Instead, after angled α-IR, the true (smaller) size may have been revealed. Overall, the mean area of OGG1 and γH2AX foci induced by high-LET α-particles were larger than those induced by low-LET γ-rays.

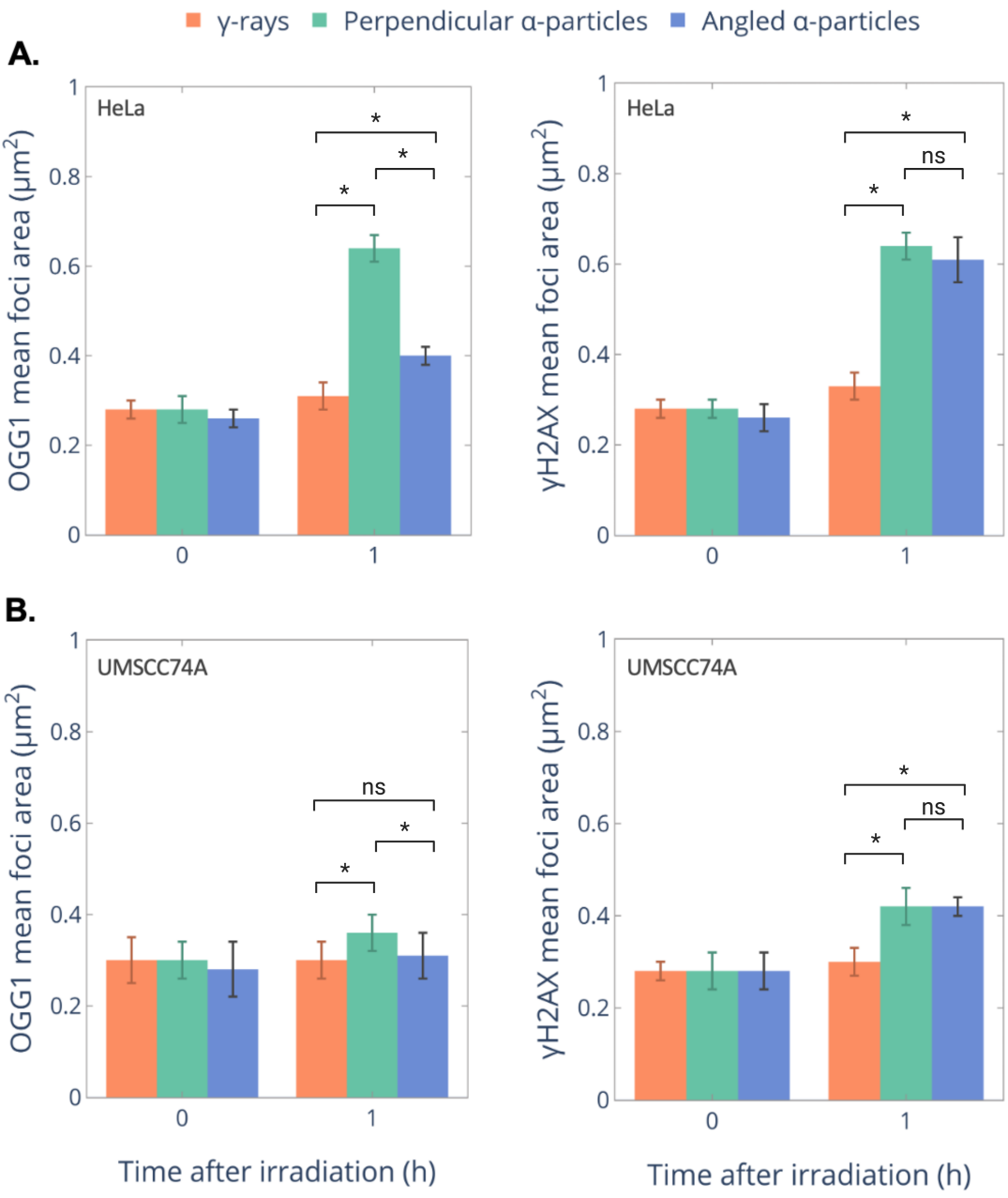

Figure 3.7: γH2AX and OGG1 foci area after low- and high-LET IR in HeLa and UMSCC74A cells - Mean foci area of γH2AX and OGG1 foci in unirradiated (0) and 4 Gy irradiated **A.** HeLa cells and **B.** UMSCC74A cells 1 h post-IR and imaged with confocal microscopy. Error bars represent SD among three independent replicates. $*p<0.05$ and 'ns' not significant as analysed by a two-sample t-test. ∼1,500 cells from each cell line were analysed.

In UMSCC74A cells, there was a 24% increase in OGG1 foci size after perpendicular α-IR and 13% after angled α-IR at 1 h post IR. In contrast, a small increase was observed in the γH2AX mean foci area 1 h after γ-IR (6%) and a large increase after α-IR (50% for both perpendicular and angled IR). While γH2AX and OGG1 foci sizes increase after high-LET IR, the rises were smaller compared to HeLa cells, potentially indicating a lesser or different response to IR. For example, differences in OGG1 levels or in the kinases which trigger γH2AX formation. In the case of perpendicular α-IR, the variation could be due to differences within the thickness of the nucleus.

To further evaluate the relationship between foci morphology and radiation quality, the spatial changes in 3D using individual consecutive confocal slices were analysed. **Figure 3.8** shows OGG1 (**8A**) and γH2AX (**8B**) foci 1 h after γ-IR and perpendicular α-IR in HeLa cells. On the left, 2D maximum intensity images comprise twelve confocal slices obtained with a z-step size of 0.66 μm, while on the right, four individual consecutive confocal slices are shown. Both OGG1 and γH2AX foci induced by γ-IR were only present in a few slices, as these clearly appear and disappear between one or maximum two slices. In contrast, several foci induced by perpendicular α-IR were present in at least four slices, equivalent to 2.64 μm. Additionally, most foci are clearly large and some appear to be composed of several smaller, closely spaced foci (referred to as foci clusters), showing the importance of correlations along the α-particle track.

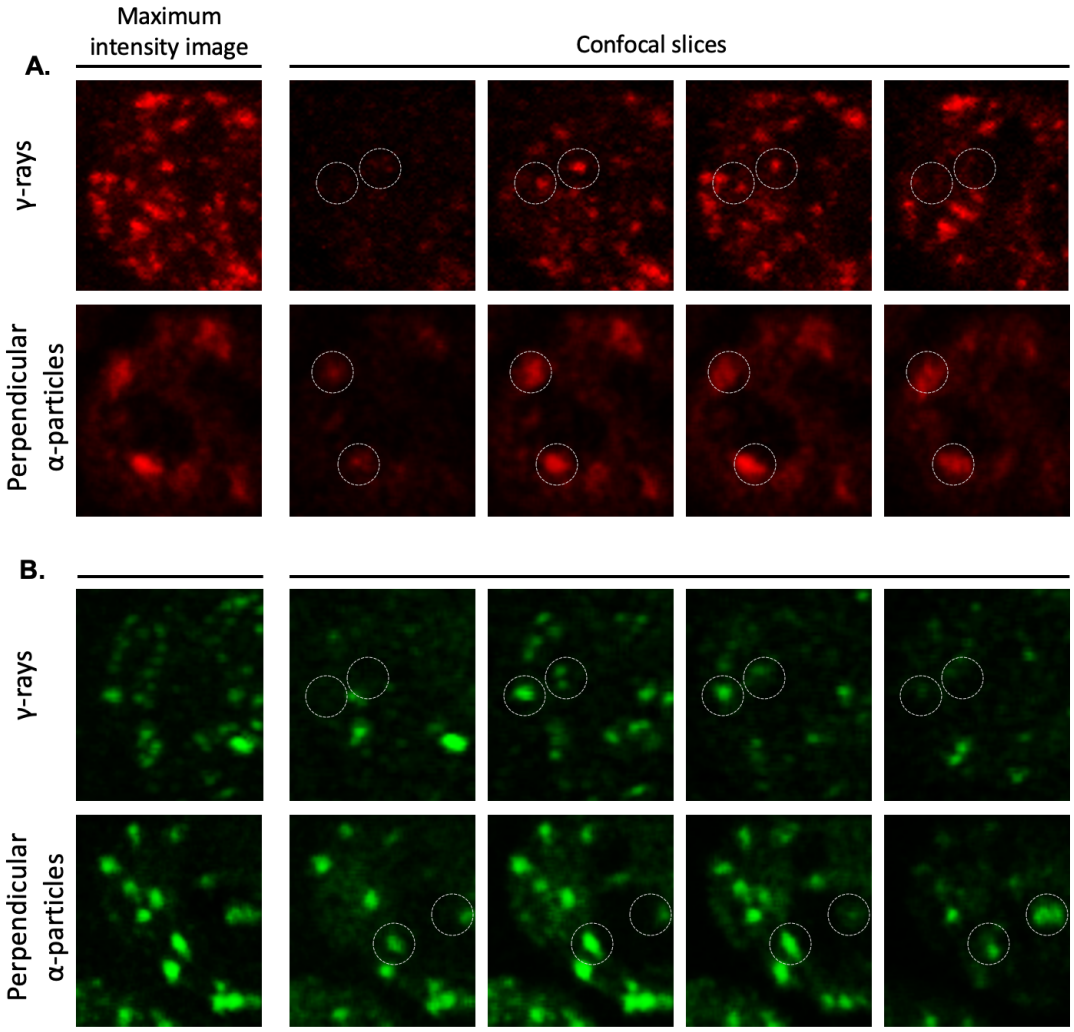

Figure 3.8: OGG1 and γH2AX foci persist spatially for longer after high-LET IR compared with low-LET in HeLa cells - Comparison of **A) OGG1-StarRed** and **B) γH2AX-AlexaFluor488** foci. 2D maximum intensity images, shown on the left, comprise twelve confocal slices obtained with a z-step of 0.66 μm. On the right, four individual consecutive slices show the spatial persistence of foci in the z direction. Cells were irradiated with 4 Gy low-LET γ-IR or high-LET perpendicular α-IR and left to repair for 1 h. Representative images from at least three independent repeats.

To investigate the foci clusters observed in high-LET irradiated cells, fluorescence intensity profiles along the paths of several foci were analysed and compared with those induced by low-LET IR on the same images presented in **Figure 3.8**. The line profiles on **Figure 3.9A** show that OGG1 foci induced by low-LET γ-IR reveal one fluorescence maxima, corresponding to one morphologically regular and spatially separated foci, thus no cluster is present. In contrast, after high-LET α-IR, the three peaks within the one foci cluster indicate it is comprised of three individual OGG1 foci. The same was observed in **Figure 3.9B** with γH2AX foci. This was expected as DNA damage sites produced by γ-IR are likely to be randomly distributed over the nucleus and unlikely to be correlated.

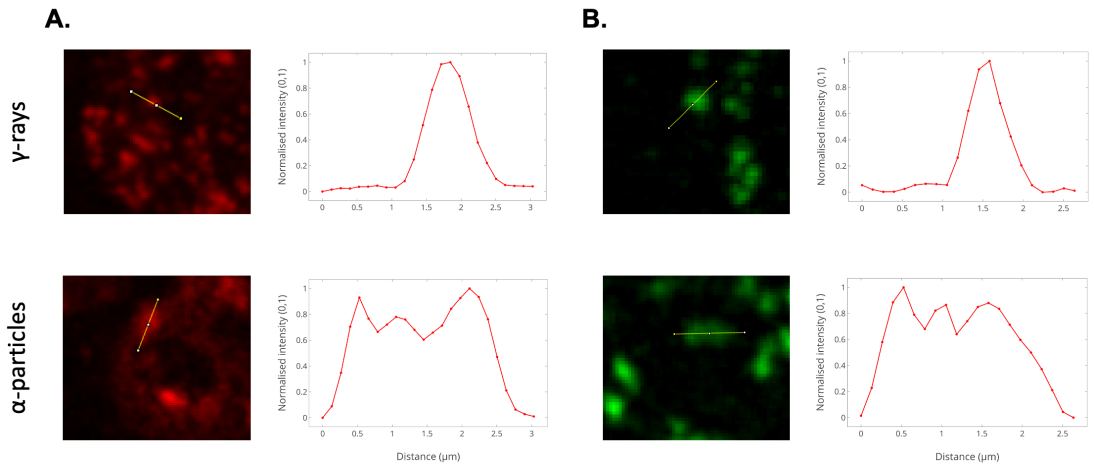

Figure 3.9: Identification of individual OGG1 and γH2AX foci within clusters induced by low- and high-LET IR - Comparison of **A) OGG1-StarRed** and **B) γH2AX-AlexaFluor488** foci. 2D maximum intensity image and fluorescence intensity profiles along the path of one large foci are shown. Cells were irradiated with 4 Gy low-LET γ-IR or high-LET perpendicular α-IR and left to repair for 1 h. Representative images from three independent repeats.

Overall, a significantly greater proportion of OGG1 and γH2AX foci were present in more slices and as clusters in cells exposed to high-LET α-particles compared to those exposed to low-LET γ-rays.

3.2.6 OGG1-γH2AX Colocalisation

Next, the overlap between OGG1 and γH2AX at different time-points following low- and high-LET IR in HeLa and UMSCC74A cells was assed. To statistically quantify their colocalisation, Pearson's correlation coefficient (r) was used, where +1 indicates high correlation between two molecules, 0 suggests no correlation and -1 indicates an inverse correlation. As shown in **Figure 3.10A**, a higher degree of foci colocalisation was observed after high-LET IR at all time-points in HeLa cells, compared with low-LET. For example, at 1 h post-IR, the r value after γ-IR was 0.59 while 0.78 for perpendicular α-IR, indicating moderate colocalisation after γ-IR and strong colocalisation following α-IR. Colocalisation decreased over time for all radiation qualities. Very similar colocalisation was observed between angled and perpendicular α-IR. Stronger colocalisation was observed at 30 min following perpendicular α-IR (0.87 for perpendicular, 0.77 for angled α-particles and 0.61 for γ-rays). Unirradiated samples show similar colocalisation values between all radiation qualities (0.28 for γ-rays, 0.23 for perpendicular and 0.32 for angled α-particles).

A similar trend was observed in UMSCC74A cells, shown in **Figure 3.10B**, where foci colocalisation was stronger after high-LET compared with low-LET IR. Colocalisation also decreased over time following all radiation qualities. Unlike HeLa cells, there was a small increase in colocalisation 24 h after high-LET IR (2% for angled and 9% after perpendicular α-IR). This was unlike low-LET, where colocalisation decreased 53%.

Overall, these results reveal a difference in OGG1 and γH2AX foci colocalisation induced by high- and low-LET IR, reflecting the increased complex nature of the damage produced by α-IR.

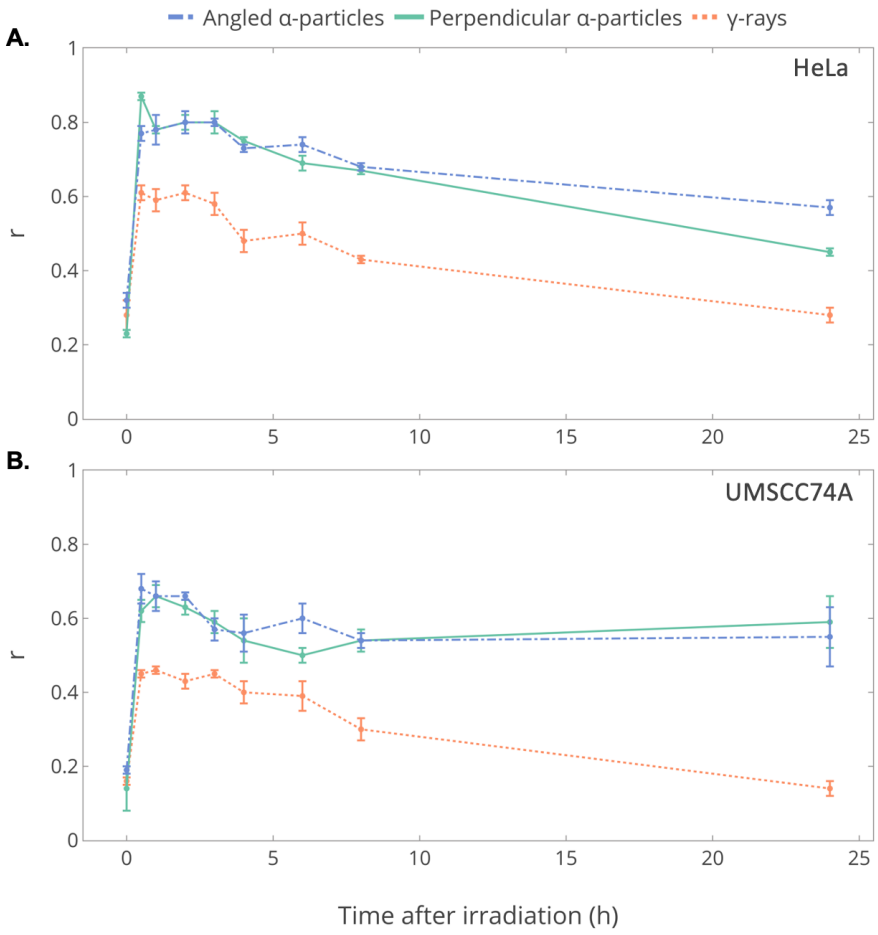

Figure 3.10: γH2AX and OGG1 foci colocalisation following low- or high-LET IR in HeLa and UMSCC74A cells - Colocalisation (r, Pearson's correlation coefficient) of OGG1 and γH2AX foci at various time-points following irradiation with 4 Gy low-LET γ-rays, high-LET perpendicular or high-LET angled α-particles in **A.** HeLa and **B.** UMSCC74A cells. Representative data from three independent experiments.

3.2.7 Expected Number of α-particle Tracks Using Fluence and Dose Measurements

The nominal exposure dose quoted for the α-IR refers to a dose averaged across the whole area of the irradiated dish and is expected that the actual dose rate at the centre of the dish will be higher than average. A more accurate determination of the fluence and therefore dose was made by irradiating novel fluorescence nuclear track detectors (FNTDs) in the identical geometry to the cell irradiations in advance of performing the α-particle irradiations to define the dose delivery. These were used to image individual α-particle tracks for a standard perpendicular irradiation with a corresponding dose of 1 Gy (**Figure 3.11A**), as well as an angled irradiation (**Figure 3.11B**). The average number of tracks on **Figure 3.11A** was 147 ($\pm$21) in an area of 2621 μm, giving a fluence of 0.0561 particles μm^{-2}. This corresponds to a dose of 1.086 Gy (equation 1, **Methods 2.2.14.3**) and an average of 7.29 tracks Gy^{-1} (equation 2, **Methods 2.2.14.3**) for a mean cell nuclear area of 130 μm^2. Thus, for a 4 Gy perpendicular α-IR, an average of $\sim$29 tracks/nucleus, and thus foci, were expected. The yields of γH2AX foci observed in **Figure 3.5B** closely correspond to the expected number of tracks. Next, this was repeated for the angled irradiation in **Figure 3.11B**. The average number of tracks was 44 ($\pm$6) in an area of 3162 μm, giving a fluence of 0.0139 particles μm^{-2}. This corresponds to an incident dose of 0.274 Gy and an average of 1.8 tracks Gy^{-1}. Thus, for a 4 Gy angled α-IR, an average of $\sim$7 tracks/nucleus were expected. Due to the high 4 Gy dose used in these studies, it was not possible to count the individual number of tracks observed in **Figure 3.5C** as they were no longer well defined. Thus, a smaller dose should be used for an accurate comparison between the expected and actual number of tracks.

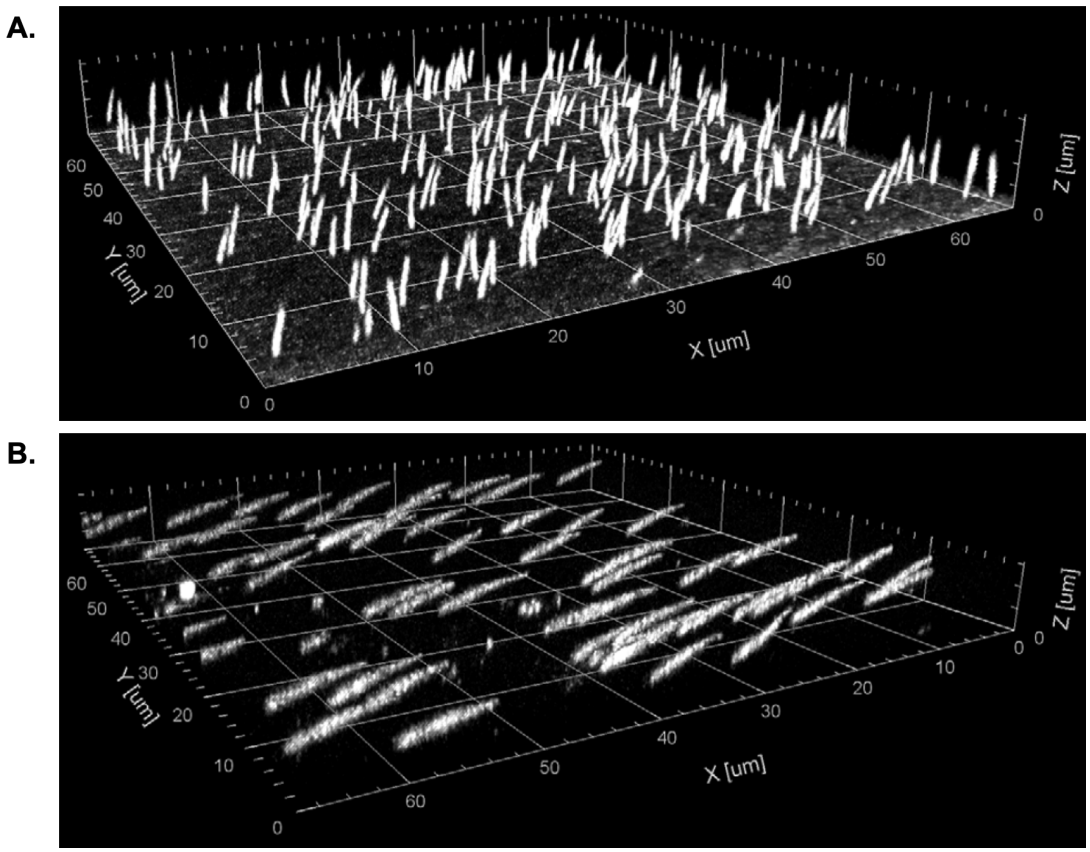

Figure 3.11: α-particle tracks visualised in 3D using FNTDs - A. Standard 1 Gy perpendicular irradiation. **B.** Angled irradiation after 50 traversals of the slit. Images were taken on a confocal microscope. Representative data from two independent experiments.

3.2.8 OGG1 and γH2AX Foci Formation Following Exposure to Olaparib

It has previously been shown that PARP inhibitors radiosensitise HeLa and UM-SCC74A cells (Dok *et al.*, 2020; Kötter *et al.*, 2014; Nickson *et al.*, 2017). Thus, the effect of PARP inhibitor Olaparib in combination with 4 Gy low- and high-LET IR on the yields of OGG1 and γH2AX foci was investigated.

Figure 3.12A shows OGG1 and γH2AX foci kinetics following a 16 h incubation with 100 nM Olaparib and γ-IR. 100 nM was chosen to enable comparison with ongoing studies by collaborators (Nickson *et al.*, 2017). PARP inhibition led to increased γH2AX foci yields, particularly at early time-points. A higher proportion of OGG1 foci remained by 24 h post-IR. The increase in OGG1 foci yields at ∼6 h requires further investigation. The repair efficiency of OGG1 was 64% compared to 110% in samples without Olaparib (shown as dashed lines), indicating OGG1 foci persistence and thus increased base damage in the presence of Olaparib. In comparison, the 98% loss of γH2AX foci after 24 h was very similar to that observed in samples without Olaparib (94%, shown as dashed lines), suggesting most DSBs were repaired over time. This was also observed in HeLa cells (see **Appendix C**).

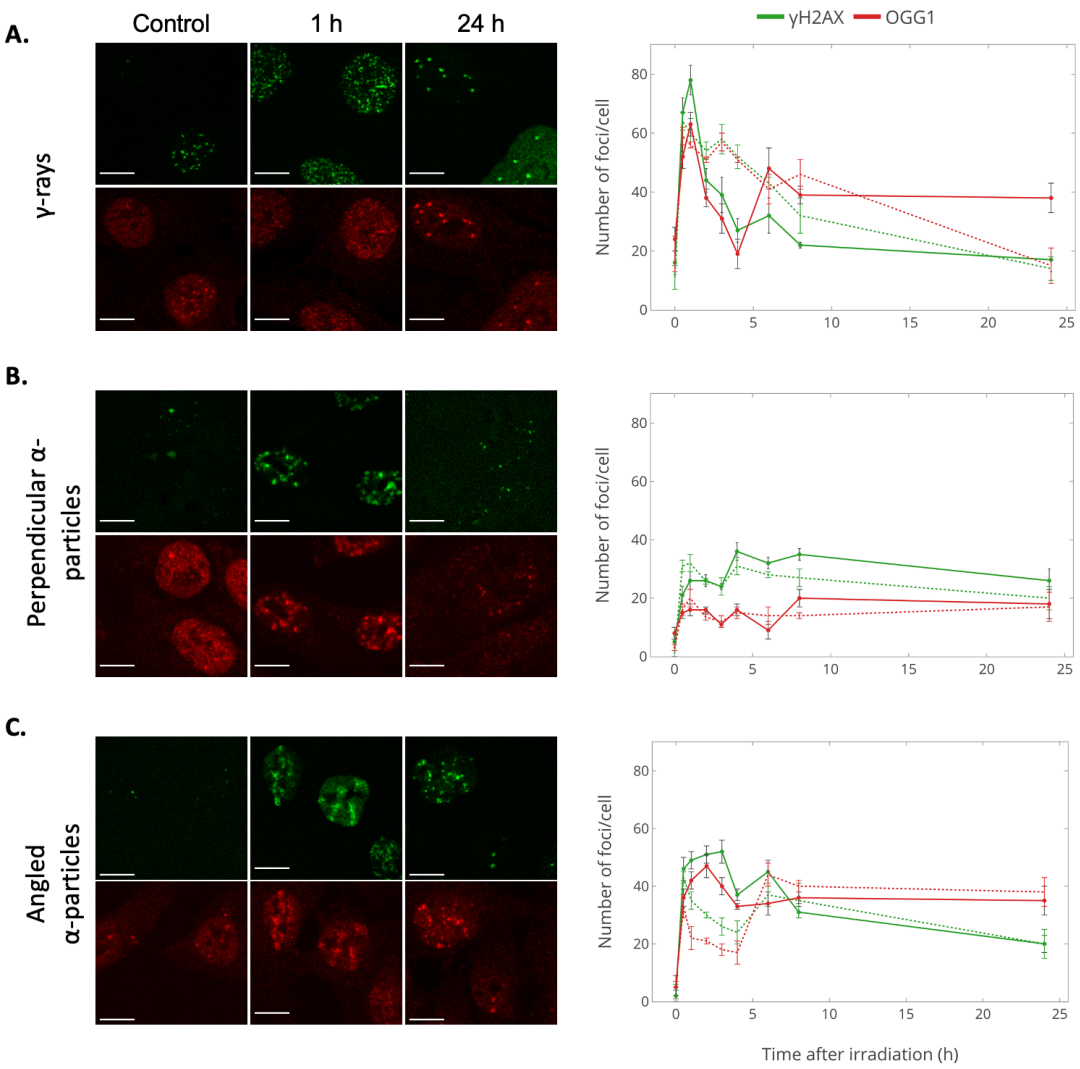

Figure 3.12: γH2AX and OGG1 foci kinetics following exposure to Olaparib and low- or high-LET IR in UMSCC74A cells - OGG1-StarRed and γH2AX-AlexaFluor488 foci kinetics in unirradiated (control, 0) and 4 Gy irradiated cells with **A.** γ-IR, **B.** perpendicular α-IR and **C.** angled α-IR, imaged using confocal microscopy. Dotted lines represent kinetics without Olaparib. Images from key time-points are presented. Error bars represent SD among two independent replicates. Scale bars, 10 μm.

Subsequently, OGG1 and γH2AX foci kinetics following Olaparib incubation and perpendicular (**Figure 3.12B**) and angled (**Figure 3.12C**) α-IR were investigated. As seen in **Figure 3.12B**, PARP inhibition resulted in lower γH2AX and OGG1 foci yields at early time-points and higher yields at later time-points compared to samples without Olaparib (dashed lines). This was also observed in HeLa cells (**Appendix C**). Foci persistence observed from 6 to 24 h indicated little to no repair. From the peak to the 24 h time-point (minus the controls), there was a 25% increase in OGG1 and a 1% decrease in γH2AX foci. Compared with low-LET, a larger proportion of residual foci were observed at late time-points following α-IR (also observed in HeLa cells).

Figure 3.12C shows OGG1 and γH2AX kinetics after Olaparib incubation and angled α-IR. PARP inhibition resulted in higher OGG1 and γH2AX foci yields at early time-points and similar numbers at later time-points. γH2AX and OGG1 peaked at later time-points compared with low-LET irradiated samples. From the peak to the 24 h time-point (minus the controls), a 64% loss of γH2AX and 29% loss of OGG1 foci were observed. This was due to the high foci yields in the earlier time-points. While the yields are higher after angled α-IR, the trend was very similar to perpendicular α-IR. For both perpendicular and angled α-IR, the persistence of OGG1 foci at late time-points, indicated that very little repair occurred. This was also observed in HeLa cells. Overall, the combination of 100 nM Olaparib incubation and perpendicular α-IR led to an increase in DSB and base damage yields and persistence, suggesting inaccurate repair or decreased repairability. Additionally, as also observed in HeLa cells, PARP inhibition disrupted DSB repair after high-LET IR, but not after low-LET IR.

Due to COVID-19, this experiment was repeated only twice. At least two more repeats will allow further validation of data.

3.2.9 OGG1 and γH2AX Foci Kinetics Following Low and High Energy Protons, Proof of Principle

Proton beam irradiation can generate CDD with the proportion dependent on energy and associated LET, particularly at and around the Bragg peak. To investigate this, UMSCC74A cells were irradiated with 4 Gy high-energy (59 MeV, ∼1 keV/μm) or low-energy (11 MeV, ∼12 keV/μm) protons. The yields of OGG1 and γH2AX foci were analysed at various time-points post-IR. These conditions have been utilised previously and demonstrated differences in the levels of CDD generated (Carter *et al.*, 2018). **Figure 3.13A** shows OGG1 and γH2AX kinetics before and after high energy proton IR in UMSCC74A cells. OGG1 foci yields peaked at 24 (±5) foci/cell 1 h post-IR, followed by a decrease beyond control levels by 24 h. γH2AX followed a similar trend, with a peak at 40 (±5) foci/cell 1 h post-IR, also decreasing to beyond control levels by 24 h. The 142% repair efficiency for γH2AX and 162% for OGG1 indicate that all IR-induced DSB and non-DSB lesions were repaired and that the control levels were high. This was a similar trend to that previously observed after low-LET γ-IR (**Figure 3.5A**).

In comparison, **Figure 3.13B** shows OGG1 and γH2AX foci kinetics following low energy protons. OGG1 and γH2AX foci yields peaked at 28 (±4) and 53 (±5) foci/cell respectively, 2 h following IR and decreased until 24 h. Compared with high energy proton IR, there were more OGG1 and γH2AX foci observed at 4 h, indicating DSB and base damage persistence. OGG1 persistence at 8 and 24 h was not apparent. The repair kinetics of foci for both proton energies are closer to those observed for γ-rays, rather than α-particles. Although the LET for low energy protons is raised, it is still significantly lower than the 120 keV/μm for α-particles. Similar to high energy

protons, the 121% repair efficiency for γH2AX and 153% for OGG1 indicate high repair efficiency. It is important to note that the control levels were high.

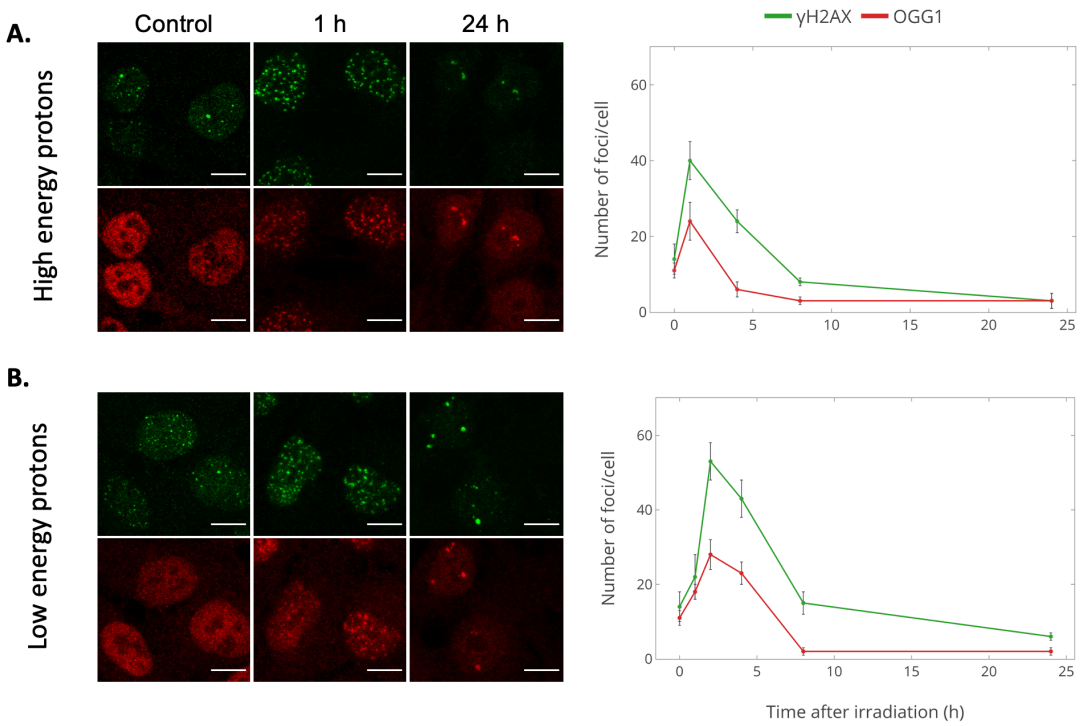

Figure 3.13: γH2AX and OGG1 foci kinetics following low or high energy protons in UMSCC74A cells - OGG1-StarRed and γH2AX-AlexaFluor488 foci kinetics in unirradiated (0) and 4 Gy irradiated cells with **A.** high energy and **B.** low energy protons, imaged using confocal microscopy. Images from key time-points are presented. Error bars represent SD between samples from one experiment. Scale bars, 10 μm.

3.2.10 OGG1 and γH2AX Foci Formation Following Exposure to Olaparib and Protons

As shown in **Figure 3.12**, Olaparib exposure led to disrupted DNA repair UMSCC74A cells. Thus, the effect of PARP inhibitor Olaparib in combination with low and high energy protons was investigated next. **Figure 3.14A** shows OGG1 and γH2AX foci kinetics following a 16 h incubation with 100 nM Olaparib and high energy protons. PARP inhibition increased γH2AX foci yields at late time-points (4, 8 and 24 h) while those in the control and 1 h post-IR samples remained unaffected. Compared to samples without Olaparib (dashed lines), OGG1 foci yields were lower in the control and 1 h samples, but higher at late time-points post-IR, particularly at 24 h where the number of foci was two times higher. The repair efficiency for γH2AX was 93% and 63% for OGG1, compared to 142% and 162% in samples without Olaparib. Overall, this indicates DSB and non-DSB persistence in the presence of Olaparib after high energy protons.

Figure 3.14B shows OGG1 and γH2AX foci kinetics after Olaparib incubation and low energy proton irradiation. PARP inhibition resulted in higher γH2AX foci yields at all time-points post-IR as well as foci persistence after 24 h. Olaparib had mostly no effect on OGG1 foci yields, except for the 24 h time-point, where the number of foci was six times higher than without Olaparib. The repair efficiency for γH2AX was 107% and 89% for OGG1, compared to 121% and 153% in samples without Olaparib.

Overall, the combination of 100 nM Olaparib incubation and low energy proton irradiation led to increased DSB and base damage yields as well as persistence, suggesting inaccurate repair or decreased repairability.

Due to COVID-19, this experiment was only able to be repeated once. Other experiments were performed but closure of the lab prevented this data from being analysed. At least two more repeats will allow further validation of the results.

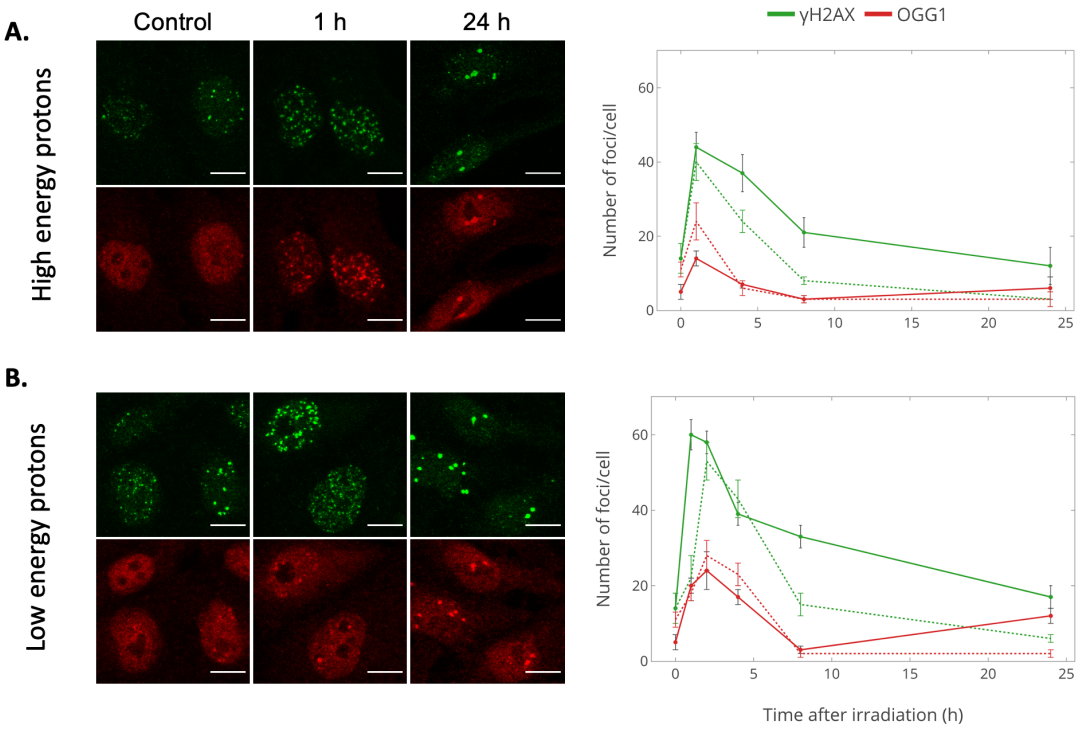

Figure 3.14: γH2AX and OGG1 foci kinetics following exposure to Olaparib and low or high energy protons in UMSCC74A cells - OGG1-StarRed and γH2AX-AlexaFluor488 foci kinetics in unirradiated (0) and 4 Gy irradiated cells with **A.** high energy and **B.** low energy protons, imaged using confocal microscopy. Dotted lines represent kinetics without Olaparib. Images from key timepoints are presented. Error bars represent SD between samples from one experiment. Scale bars, 10 μm.

3.3 Discussion

Kinetics studies reveal OGG1 involvement in CDD processing

Several proteins were tested to investigate their involvement in the cellular response to CDD induced by high-LET IR to understand which pathways are involved in their processing. PARP1, $H2B_{ub}$ and RNF20 antibodies were unsuitable for IF staining. Recent studies have shown that RNF20 and $H2B_{ub}$ are involved in the repair of CDD induced by high-LET IR using the same antibodies for comet assays (Carter *et al.*, 2018), suggesting the antibodies used here were incompatible with IF. Other PARP1 antibodies have been used previously for IF (Amé *et al.*, 2009; Meder *et al.*, 2005; Thorslund *et al.*, 2005). Thus, future work is needed to optimise PARP1, RNF20 and $H2B_{ub}$ foci visualisation in cells to investigate these evidently important factors.

To accurately measure the biological effects of radiation, this study monitored different types of DNA damage, namely DSBs and non-DSBs (primarily base damage) using γH2AX and OGG1 foci as surrogate markers, respectively. Immunofluorescence has been extensively used for the measurement of simple damage and detection of one type of lesion. However, the simultaneous detection of two or more types of lesions (e.g. DSB and non-DSB as demonstrated here) has only been described in a few studies (Asaithamby *et al.*, 2011a; Nikitaki *et al.*, 2016a,b; Zhang *et al.*, 2016). This could be due to challenges such as low signal-to-noise caused by high background from non-DSB repair proteins (unlike DSB markers such as γH2AX which become present upon DSB formation).

In agreement with other studies that evaluated γH2AX foci (Höglund *et al.*, 2001; Leatherbarrow *et al.*, 2006; Staaf *et al.*, 2012), γH2AX and OGG1 foci persisted for

longer after high-LET compared with low-LET in UMSCC74A and HeLa cells. The reduced repair efficiency of DSBs and non-DSBs, as well as greater foci yields at 24 h, reflected the increased complex nature of the damage formed by α-IR (Goodhead, 2006; Pinto *et al.*, 2005). The fluctuations observed at early time-points are likely to be natural experimental point-to-point variation. Alternatively, these could be potentially be explained by non-DSB damage being converted into DSBs during their processing (Gulston *et al.*, 2004). However, these would vary from cell to cell and also through cell cycle stages, so further investigations are needed to confirm this. The differences in kinetics and foci yields between perpendicular and angled α-IR were likely due to lesion clustering along the α-particle track and underestimation of the true foci number under one focus in the z direction (Antonelli *et al.*, 2015; Nikitaki *et al.*, 2016a). Due to the increased resolution power achieved with angled α-IR, foci that would be otherwise omitted in the z are resolved in the x-y axis. It is unlikely that different types of damage are being produced as cells were irradiated with the same source and dose. It would be interesting to explore the spatial distribution of the foci along these angled α-particle tracks using SR microscopy techniques described in **Chapter 5**.

In UMSCC74A cells, a fast and slow component of repair was detected following IR. The observed two-phase pattern in kinetics of IR-induced foci (IRIF), with a fast and slow component, has been previously observed with γH2AX (Hamada *et al.*, 2006; Staaf *et al.*, 2012; Suzuki *et al.*, 2006). Following IR, the fast repair rate is linked to the repair of simple DSBs, and slower repair for complex damage. As LET rises, the complexity of damage increases, so the slower rate dominates. Overall, OGG1 appears to process clustered DNA damage after high-LET IR, particularly at late time-points post-IR.

The number of γH2AX foci was consistently higher than OGG1 at the peak (1 h) fol-

lowing IR. The ratio of γH2AX:OGG1 foci was higher following high-LET IR compared to low-LET IR. This was expected as general complexity will be greater with increasing LET and a much higher percentage of DNA lesions will have a DSB as part of the cluster. In general, a range of 4-16 foci/Gy/cell depending on the cell line and radiation quality were measured. This is in agreement with previous studies with γH2AX foci after different LETs (Leatherbarrow *et al.*, 2006; Löbrich *et al.*, 2010; Nikitaki *et al.*, 2016a; Rübe *et al.*, 2008). The kinetics of IRIF disappearance in cells exposed to α-particles in both HeLa and UMSCC74A cells were somewhat slower than that recorded by some studies (Costes *et al.*, 2006; Leatherbarrow *et al.*, 2006; Riballo *et al.*, 2004; Schmid *et al.*, 2010; Staaf *et al.*, 2012). Variation in the kinetics of IRIF foci are common across the literature due to differences in staining procedures, image capture and analysis, cell lines and antibodies used. Additionally, the cells used in this study were not synchronised, thus the standard deviations and high number of foci in unirradiated cells could have been influenced by the cells being in different cell cycle phases. With more time available, the cell cycle phase could be taken into account by synchronising the cells, analysing their DNA content by flow cytometry analysis such as fluorescence-activated cell sorting (FACS) or using a cell cycle marker to indicate the phase of cells being scored. This would also help explain certain observations, such as the decrease in foci yields 24 h post-IR beyond control levels, which requires further investigation. One likely explanation is the enhanced presence of background foci within the nucleus of control cells during S-phase of the cell cycle (Costes *et al.*, 2006; Marková *et al.*, 2007). Future studies are needed to determine if there was a significant shift in the distribution of cells through the cell cycle (at later times compared to controls).

Information on the yields and properties of OGG1 foci is rather scarce. OGG1 re-

cruitment to sites of laser-induced damage (Lan *et al.*, 2004), iron-particle tracks (Asaithamby *et al.*, 2011a,b) and UVA (Campalans *et al.*, 2007) have been previously investigated. The colocalisation of OGG1 with 53BP1 and XRCC1 after iron and silicon ions irradiation has also been previously explored (Asaithamby *et al.*, 2011b; Nikitaki *et al.*, 2016a). These studies showed OGG1 localised to sites of clustered damage caused by high-LET IR. The work presented in this dissertation is the first comprehensive study to quantify and compare OGG1 foci kinetics over time after low- and high-LET IR in UMSCC74A and HeLa cells.

Due to the orthogonal configuration of the irradiation setup, each γH2AX foci in cells irradiated with perpendicular α-IR was expected to represent one particle traversal. As noted in **Figure 3.11**, the γH2AX foci yield observed after perpendicular α-IR was in agreement with the theoretical number of α-particle tracks (as calculated based on fluence from the FNTD measurements), particularly when the background number of foci were taken into account. Since the mean cell thickness of $\sim$5-6 μm is considerably less than the $\sim$20 μm range for the α-particles, comparatively little of the particle's energy was likely lost while traversing a cell. However, this will vary depending on cell thickness. These results demonstrated the usefulness of the novel FNTDs at detecting both perpendicular and angled α-particle tracks. While conventional dosimeters (such as CR-39) are excellent at detecting low fluence α-particles on their surface, high resolution FNTDs allow the detection of higher fluence over a wide range of angles (Akselrod *et al.*, 2006, 2011).

Low and high energy protons were also used to generate CDD in varying frequency and complexity. Preliminary data showed a higher OGG1 and γH2AX foci yield after low energy protons. However, due to unexpected laboratory shut down from COVID-19,

this proton experiment was only able to be repeated once and further experiments were also halted. At least two more repeats will allow further validation of the results and better interpretation of what they mean. Due to the LET of protons at both energies being significantly lower than that from α-particles, more protons traversed the nucleus to deliver the same dose and there was a lower probability of multiple correlated foci per track. Thus, the foci distribution observed across the nucleus was more similar to the random distribution observed by γ-rays. Previous studies have shown differences in the mechanism of repair of CDD after low and high energy protons in UMSCC74A cells (Britten *et al.*, 2013; Carter *et al.*, 2018; Chaudhary *et al.*, 2014). Further repeats will reveal more insights into the differences in response to radiation of varying LET.

OGG1 is the main protein involved in the detection and excision of oxidised bases and abasic sites (Aburatani *et al.*, 1997). Thus, it has been extensively used as a marker of non-DSB DNA lesions for many decades (Nikitaki *et al.*, 2016b). The use of γH2AX foci as a DSB marker is a well-established and sensitive method. However, it is important to consider the possibility of underestimating DSBs, particularly when comparing to other techniques such as gel electrophoresis which tend to detect increased numbers of DSBs compared to the γH2AX method (Kinner *et al.*, 2008; Singh *et al.*, 2013). For example, previous data using cold lysis PFGE protocols (to minimise conversion of heat-labile sites to DSBs) identified a peak of $\sim$25 DSBs/Gy/cell after low-LET IR (Stenerlöw *et al.*, 2003), while γH2AX foci studies tend to detect 14-16 foci/Gy/cell (Leatherbarrow *et al.*, 2006; Nikitaki *et al.*, 2016a). There are ongoing discussions about whether a single γH2AX focus reflects one DSB or if it depends on the cell, radiation quality and dose (Du *et al.*, 2011; Falk *et al.*, 2010; Hausmann *et al.*, 2018; Natale *et al.*, 2017; Scherthan *et al.*, 2008). Each γH2AX foci is unlikely to represent a single DNA

lesion because of the optical limitations of the microscope. Super-resolution microscopy methods could significantly contribute to these investigations. This topic is explored in **Chapter 5**. Combining modelling and biochemical assays with cellular approaches will allow more precise analysis of the lesions induced by high-LET α-IR.

Depending on the cell type used, foci yield has been shown to change linearly with radiation dose delivered to a cell in the low dose range (Asaithamby *et al.*, 2009; Costes *et al.*, 2010). Some studies have shown saturation and loss of foci detection at doses above 2-4 Gy (Avondoglio *et al.*, 2009; Barbieri *et al.*, 2019; Corre *et al.*, 2010; Kinner *et al.*, 2008; Mahrhofer *et al.*, 2006; Nikitaki *et al.*, 2016a). Thus, the 4 Gy used in this study could have resulted in some foci overlapping and saturation. Future studies are warranted to measure OGG1 kinetics at different doses to investigate the effects of foci overlapping, as well as with super-resolution microscopy to address the limited resolution of confocal microscopes.

An important aspect of these experiments is the limitation of antibody labelling. Antibody aggregates and non-specific staining (as shown at the beginning of this chapter with RNF20, PARP1 and $H2B_{ub}$) may have resulted in false positive signals. To minimise these effects, staining conditions were carefully optimised and visual checks were performed to distinguish staining artefacts. This study is limited by the use of only two cell lines. Further studies are warranted to investigate OGG1 and γH2AX kinetics in more detail using 3D cell spheroids and *in vivo* models. Additionally, the use of mutant cell lines with defects in DSB and non-DSB repair will allow more extensive insights. Combining biochemical assays with the cellular results shown here will also allow further validation of the kinetics observed.

Spatial distribution and foci morphology studies

Morphological and spatial distribution data revealed an increase in OGG1 and γH2AX foci size, and also persistence in the z-axis after high-LET IR. Additionally, groups of individual foci within one cluster were observed only after high-LET IR, reflecting the complexity induced by increasing LET. The greater complexity of DSBs may lead to bigger foci in part due to extended lifetime, but also importantly due to the correlation of breaks along the track, these individual foci are less likely to be resolved and result in what is observed as a larger focus. This data is in close agreement with previous studies that observed larger IRIF and persistence in the z-axis after exposure to high-LET compared with low-LET radiation (Bracalente *et al.*, 2010; Costes *et al.*, 2006; Jezkova *et al.*, 2018; Leatherbarrow *et al.*, 2006; Staaf *et al.*, 2012; Timm *et al.*, 2018). Thus, foci size could potentially be used as a marker for the effects of varying radiation qualities, as well as the intrinsic radiosensitivity of cells. This highlights the importance of using morphological analyses to further understand the response to low- and high-LET induced damage. To date, knowledge in these areas remains incomplete due to technical challenges in microscopy approaches, particularly super-resolution techniques; this topic is explored in **Chapter 5**.

Foci size following γ-rays were similar in size to control foci, but α-particle induced foci were larger due to correlation of breaks along the track. Bigger foci were detected in HeLa compared with UMSCC74A cells. This could be due to differences in the cell thickness. If HeLa cells were thicker, then this would lead to larger foci, particularly following perpendicular α-IR. If foci deviated from the perpendicular, those at the top of the track may be offset from those at the bottom but still overlap. Additionally, thicker cells are often accompanied by a smaller nuclear area, which would make it

more likely to increase foci overlap at different heights. With more time available, it would be interesting to track foci area over time and with dose, as well as in other cell lines.

Colocalisation studies

Colocalisation data between DSB (γH2AX) and non-DSB (OGG1) foci showed weaker colocalisation after low-LET, with increased correlation following high-LET IR (**Figure 3.10**). This suggests an increase in damage complexity with LET in both UMSCC74A and HeLa cells, in agreement with previous studies that have also observed increased colocalisation of DSB and non-DSB markers after high-LET IR (Nikitaki *et al.*, 2016a,b; Zhang *et al.*, 2016). The increased colocalisation may appear to be partly related to bigger foci. However, foci size did not correlate with colocalisation. For example, in HeLa cells, OGG1 and γH2AX sizes were very similar after γ-IR and perpendicular α-IR (**Figure 3.7**). In contrast, their sizes were significantly different after angled α-IR. Meanwhile, OGG1 and γH2AX colocalisation after perpendicular and angled IR was very similar, while colocalisation was different after γ-IR. Thus, it is unlikely that the colocalisation increase after α-IR was due only to foci size.

This colocalisation study was performed using 2D maximum intensity projections of the 3D confocal stacks, essentially losing the information in the z. Future work is needed to repeat this analysis in 3D using recently developed methods (Lavancier *et al.*, 2019), as it may reveal interesting information about the spatial arrangement of these proteins. Colocalisation was measured using the Pearson's correlation coefficient (PCC). This common and simple approach has been criticised for its dependence on intensity values (Costes *et al.*, 2004). PCC values can be depressed if measured over an image with

heterogenous expression, for example from cell-cell variability in protein expression. This can lead to under-representation of the high degree of correlation between two probes. This issue is particularly pervasive in studies using transient GFP expression, where protein expression varies widely (Dunn *et al.*, 2011). While this was not the case for the samples presented here (as antibody labelling provides a more constant level of expression), some variation was observed as cells were not synchronised in the same cell cycle phase. PCC values can also be wrongly biased from low-intensity background pixels (Dunn *et al.*, 2011). One solution is to exclude irrelevant pixels by thresholding the image, restricting analysis to those above a certain intensity. The Costes method for estimating thresholds is a robust and reproducible method to support accurate measurement of PCC (Costes *et al.*, 2004; Wu *et al.*, 2012). It is a widely established technique proven to eliminate bias and improve PCC results due to being independent of signal levels and background (Dunn *et al.*, 2011; Kumari *et al.*, 2019; Quanz *et al.*, 2012; Wu *et al.*, 2012). Thus, by using Costes automatic thresholding and PCC throughout this study, a more accurate measure of colocalisation was obtained. Other groups have recently developed approaches specifically for detecting foci colocalisation that claim to be more accurate as they are based on focus topology (Mavragani *et al.*, 2017; Nikitaki *et al.*, 2016a,b). With more time available, I would incorporate these methods and compare with the results presented here.

PARP inhibition with Olaparib

PARP inhibition is an increasingly common strategy for cancer therapy and has been shown to enhance radiotherapy sensitization in HeLa and OPSCC (oropharyngeal squamous cell carcinoma) cell lines (including radioresistant UMSCC74A cells) in several

studies (Dok *et al.*, 2020; Javle *et al.*, 2011; Kohn *et al.*, 2017; Kötter *et al.*, 2014; Murai *et al.*, 2012; Nickson *et al.*, 2017; Scott *et al.*, 2015). Additionally, several clinical studies are currently recruiting patients for combination therapy with PARP inhibitors and radiotherapy (Dok *et al.*, 2020). Despite this, the mechanism of action behind the enhanced sensitivity remains unclear. A recent report on HPV-negative OPSCC cells showed the effectiveness of PARP inhibitors is based on more than just HR ability (Nickson *et al.*, 2017). While most studies focus on the importance of dose (Bridges *et al.*, 2014; Verhagen *et al.*, 2015), the data presented here focused on the differences in response to low- and high-LET IR. In this study, Olaparib incubation and high-LET α-particle irradiation increased OGG1 and γH2AX yields and foci persistence in HeLa and UMSCC74A cells. This was not observed after low-LET IR, suggesting high-LET radiation may induce more DNA damage and thus be more effective as treatment of radioresistant cells. This was also partly observed after low energy protons. However, due to COVID-19, experiments involving Olaparib were not repeated enough times. Further repeats are required to validate and interpret these results.

Interestingly, several other studies have also shown inaccurate repair following high-LET IR exposure, as well as in combination with Olaparib (Baldeyron *et al.*, 2002; Bentley *et al.*, 2004; Hirai *et al.*, 2012; Kötter *et al.*, 2014). One particular study suggested this was due to a switch to an inaccurate alternative end-joining (Alt-Ej) repair pathway which is dependent on PARP1, thus consequent inhibition of PARP1 with Olaparib led to impaired DSB repair and enhanced sensitisation to IR (Kötter *et al.*, 2014). To confirm this hypothesis, future work could include testing HeLa and UMSCC74A cells for markers indicating their switch to Alt-Ej.

A recent study showed that the binding ability between Ku70 and Ku80, as well as

between Ku and DNA is crucial in determining whether repair will occur via NHEJ or Alt-Ej (Mansour *et al.*, 2013). Additionally, several groups have identified that these protein interactions are impaired more frequently in tumours compared to normal tissues (Costantini *et al.*, 2007; Parrella *et al.*, 2006; Pucci *et al.*, 2001). Consequently, in the next chapter of this dissertation, **Chapter 4**, the interactions between Ku70 and Ku80 are explored.

3.4 Conclusion

In conclusion, BER protein OGG1 processes clustered DNA damage generated from high-LET IR. Additionally, the synergistic ability of PARP inhibitor Olaparib in combination with high-LET IR to increase both DSB and base damage persistence and decreased repairability was also partly shown in preliminary studies. This new discovery could contribute to improving high-LET radiotherapy. Additionally, it contributes to our understanding of molecular mechanisms that eventually lead to the observed biological consequences from DNA damage clustering.

Chapter 4

The Power of Two: Ku70-80 Dimerisation in Living Cells

4.1 Brief Introduction

As described in the **Introduction**, recent studies have shown the binding ability of DNA repair proteins Ku70 and Ku80, as well as between Ku and DNA, has a crucial role in determining the pathway of choice for DSB repair (Mansour *et al.*, 2013). Additionally, this protein-protein interaction is impaired more frequently in tumours compared to normal tissues (Cohen *et al.*, 2004; Costantini *et al.*, 2007; Parrella *et al.*, 2006; Pucci *et al.*, 2001). So far, Ku70-80 binding has been studied using *in vitro* techniques, which lack information about their spatiotemporal dynamics (Frit *et al.*, 2019). Despite current knowledge of Ku function as a major effector in genome integrity and proper cellular development, live cell studies are lacking. As well as its role in NHEJ and DNA damage repair, Ku has been shown to be involved in V(D)J recombination, telomere maintenance, gene silencing, apoptosis and aging (Boulton *et al.*, 1998; Gu *et al.*, 1997; Li *et al.*, 2007; Taccioli *et al.*, 1994). This chapter seeks to develop the understanding of Ku interaction and regulation in relation to DNA repair in living cells.

The working hypothesis is the following:

- Key repair proteins Ku70 and Ku80 act as monomers in healthy, living cells. Upon DNA damage, these proteins form heterodimers which bind to the broken DNA ends and recruit other proteins to facilitate DSB processing. Tagging fluorophores on different ends of the proteins will not affect their localisation nor their function within the context of living cells.

Methods

Ku70 and Ku80 were tagged with fluorescent proteins EGFP and mCherry (**Methods 2.2.8**). HEK293 cells were transiently transfected with Ku70 and Ku80 constructs, and their interaction was evaluated using live cell microscopy techniques FRET-FLIM (Förster Resonance Energy Transfer-Fluorescence Lifetime Imaging Microscopy) and BiFC (Bimolecular Fluorescence Complementation). Different N- and C-terminal tagging combinations were tested. Laser micro-irradiations were employed to induce DNA damage.

4.2 Results

4.2.1 Visualising mCherry- and EGFP-tagged Ku70/Ku80 in HEK293 Cells

To investigate the interaction between Ku70 and Ku80, both proteins were tagged on their amino- or carboxyl-termini (N- or C-, respectively) with EGFP or mCherry fluorescent proteins. For example, the corresponding notation for Ku70 tagged to EGFP was Ku70-EGFP (C') and EGFP-Ku70 (N') (as shown in **Figure 4.1A**).

The subcellular localisation of EGFP- and mCherry-tagged Ku proteins was investigated to validate the constructs. HEK293 cells were transiently transfected and imaged using confocal microscopy 48 h post-transfection at 37°C. As shown in **Figure 4.1**, all four EGFP-tagged constructs, Ku70-EGFP (C'), Ku80-EGFP (C'), EGFP-Ku70 (N'), EGFP-Ku80 (N'), localised to the nucleus, as evident by the presence of fluorescence intensity. Similarly, **Figure 4.2** shows all mCherry-tagged constructs, Ku70-mCherry (C'), Ku80-mCherry (C'), mCherry-Ku70 (N') and mCherry-Ku80 (N'), also localised to the nucleus. Thus, the position of the fluorescent tag did not appear to alter the nuclear localisation of Ku70/80.

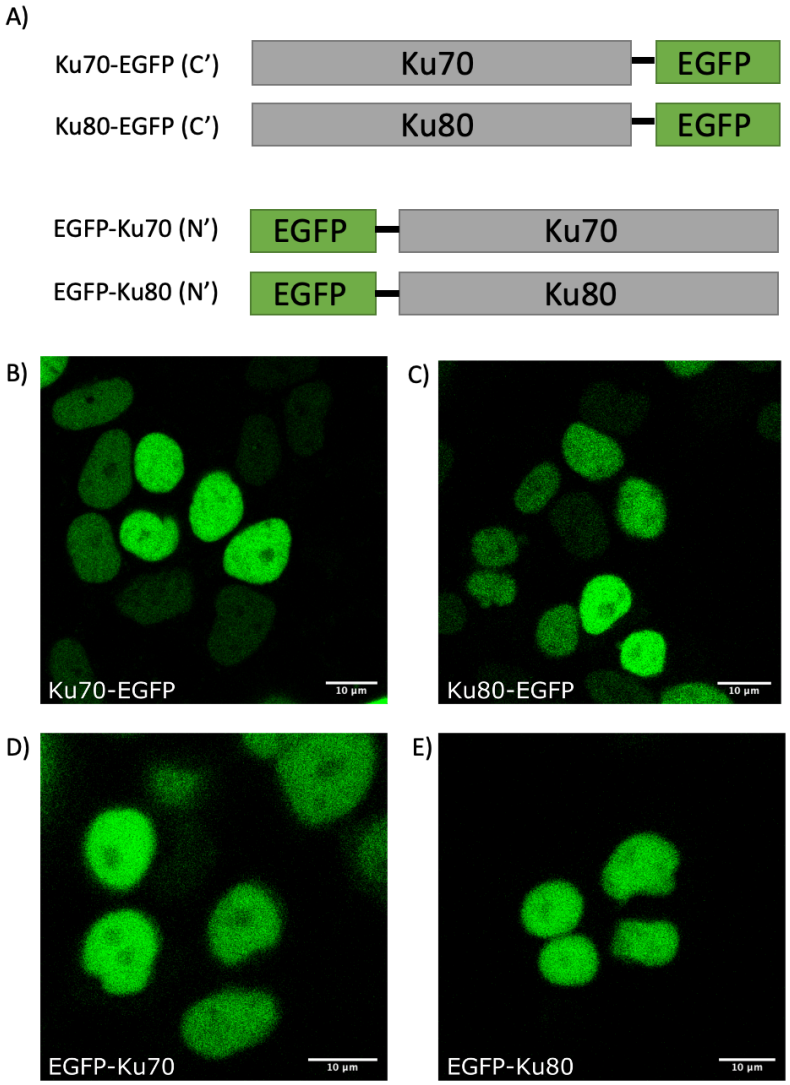

Figure 4.1: Localisation of N- and C-terminally tagged Ku70 and Ku80 with EGFP in HEK293 cells - **A)** Schematic diagrams of EGFP-tagged Ku70 and Ku80 constructs, at their C- or N-termini. Confocal images of **B)** Ku70-EGFP (C'), **C)** Ku80-EGFP (C'), **D)** EGFP-Ku70 (N') and **E)** EGFP-Ku80 (N') in live HEK293 cells. Cells were imaged at 37°C, 48 h post-transfection. Representative data from at least three independent experiments. Scale bars, 10 μm.

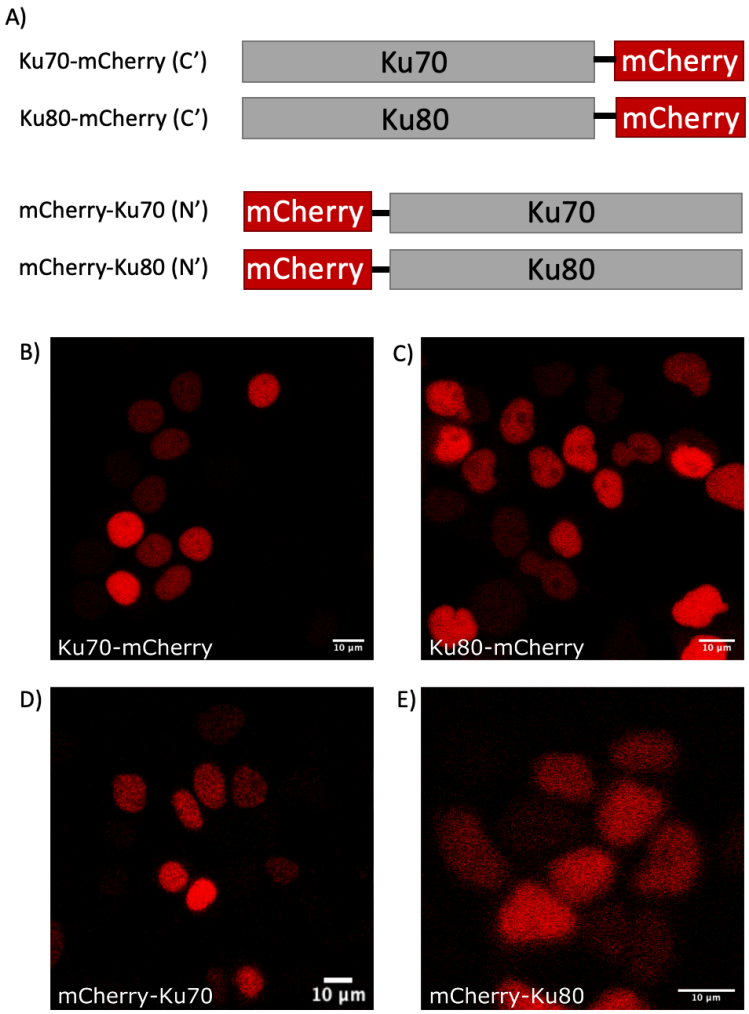

Figure 4.2: Localisation of N- and C-terminally tagged Ku70 and Ku80 with mCherry in HEK293 cells - **A)** Schematic diagrams of mCherry-tagged Ku70 and Ku80 constructs, at their C- or N-termini. Confocal images of **B)** Ku70-mCherry (C'), **C)** Ku80-mCherry (C'), **D)** mCherry-Ku70 (N') and **E)** mCherry-Ku80 (N') in live HEK293 cells. Samples were imaged at 37°C 48 h post-transfection. Representative data from at least three independent experiments. Scale bars, 10 μm.

The localisation of Ku70-EGFP (C') was compared in two other cell lines (HeLa and CHO) by confocal microscopy, shown **Figure 4.3**. Ku70 localisation was very similar to that observed in HEK293 cells. Transfection efficiency appeared lower in both cell lines, possibly due to the transfection reagent not working as well in CHO and HeLa cells compared to HEK293 cells.

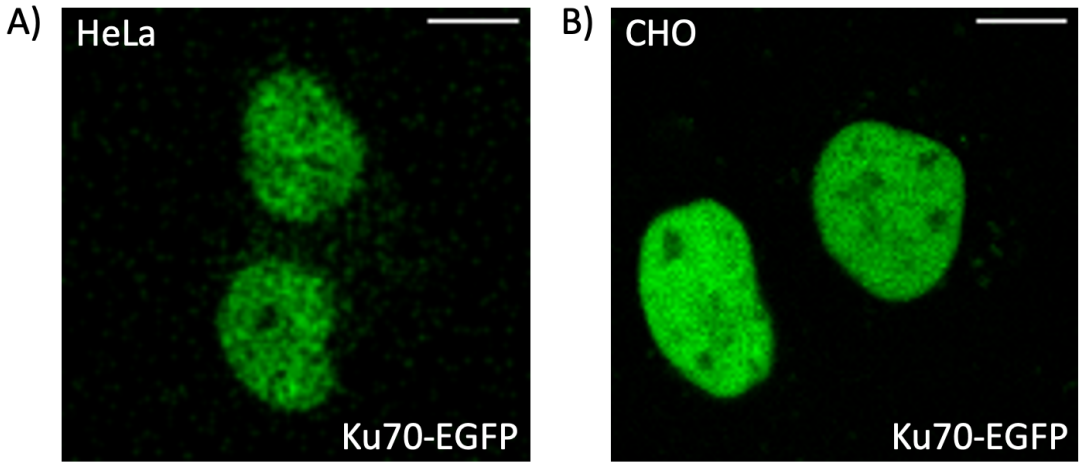

Figure 4.3: Localisation of Ku70-EGFP in HeLa and CHO cells - Confocal images of Ku70-EGFP (C') expression in live **A)** HeLa and **B)** CHO cells. Samples were imaged 48 h post-transfection at 37°C. Representative data from two independent experiments. Scale bars, 10 μm.

4.2.2 DNA Damage Induction to Check Ku70/Ku80 Function

After verifying the expression of the Ku70 and Ku80 constructs, their function was assessed by inducing DNA damage and checking for recruitment to the damage site. HEK293 cells were transiently transfected with the respective constructs, and imaged before and immediately after irradiation with a 405 nm laser (1 mW) to generate a 10 sec traversal through the nucleus of a single cell (**Methods 2.2.17.1**). These exposure conditions were selected as previous studies have shown they generate enough damage to recruit Ku70 and Ku80, while inducing minimal disruption to cells (Reynolds, 2009).

Figure 4.4 shows EGFP-tagged Ku70/80 (Ku70-EGFP (C'), Ku80-EGFP (C'), EGFP-Ku70 (N'), EGFP-Ku80 (N')) expression before and after irradiation. A line of recruitment was observed where the damage had been induced, as evident by the increase in fluorescence intensity at the irradiated areas. This indicated movement and recruitment of Ku to the sites of damage and suggested proteins were functional. The same recruitment was observed for all mCherry-tagged constructs (Ku70-mCherry (C'), Ku80-mCherry (C'), mCherry-Ku70 (N') and mCherry-Ku80 (N')) in **Figure 4.5**. Thus, protein tagging with EGFP and mCherry did not affect Ku70/80 function. The differences in the thickness of the lines observed were likely due to variation in the focal plane of the cells as they were irradiated and imaged.

Taken together, the data showed fluorescently tagged Ku70 and Ku80 were successfully expressed and functional in HEK293 cells.

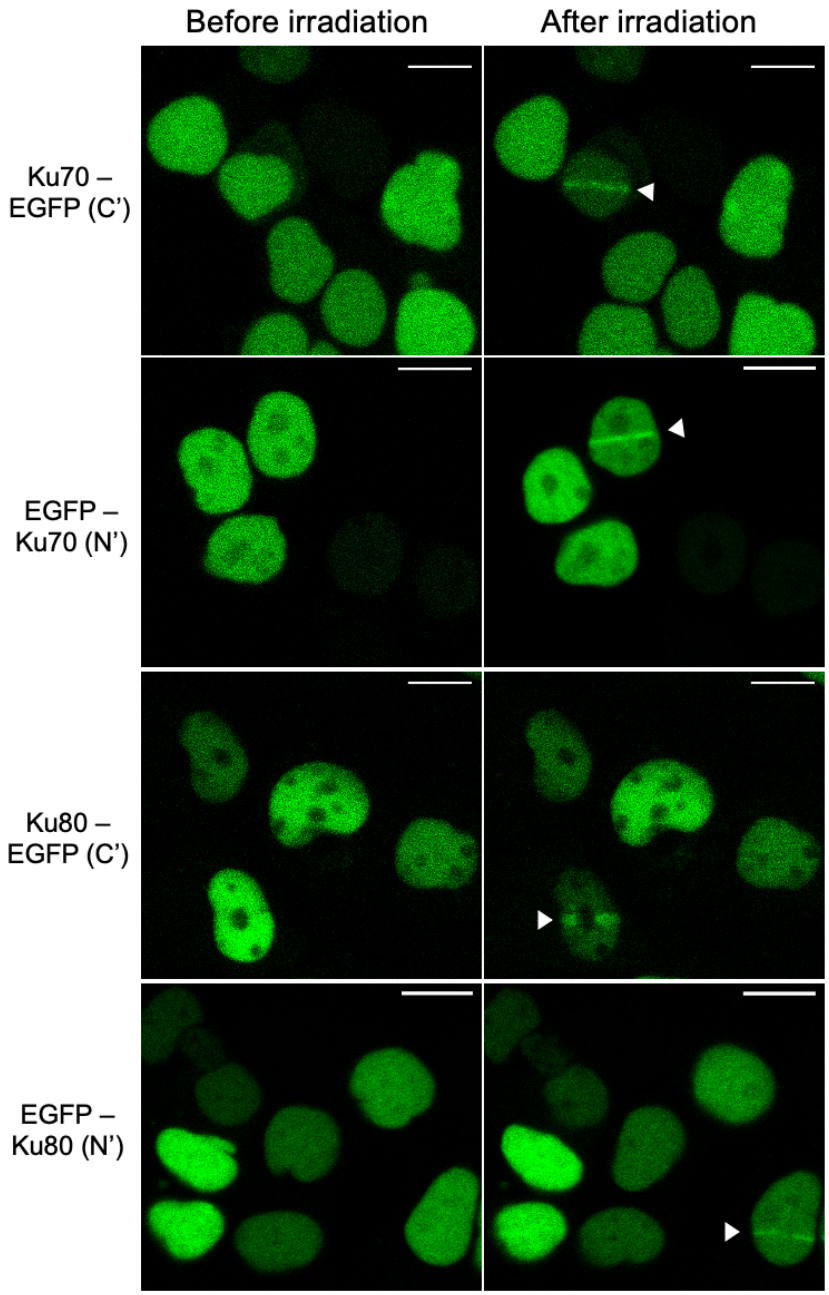

Figure 4.4: EGFP-tagged Ku70 and Ku80 recruitment to laser-induced damage in HEK293 cells - Confocal images of HEK293 cells expressing Ku70-EGFP (C'), EGFP-Ku70 (N'), Ku80-EGFP (C') and EGFP-Ku80 (N') before and immediately after single-cell line irradiation with a 405 nm laser (1 mW) for 10 sec. Cells were imaged 48 h post-transfection at 37°C. Representative data from at least three independent experiments. Scale bars, 10 μm.

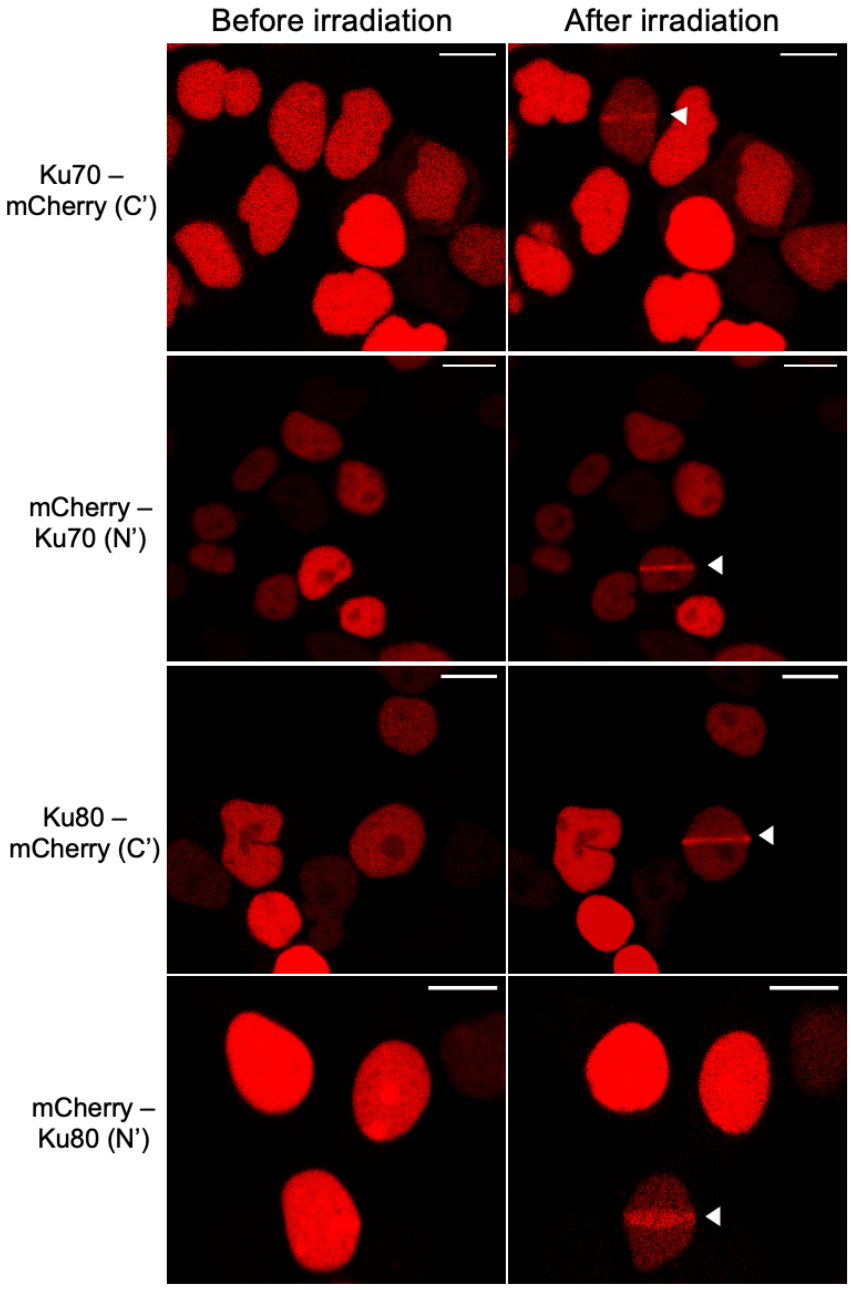

Figure 4.5: mCherry-tagged Ku70 and Ku80 recruitment to laser-induced damage in HEK293 cells - Confocal images of HEK293 cells expressing Ku70-mCherry (C'), mCherry-Ku70 (N'), Ku80-mCherry (C') and mCherry-Ku80 (N') before and immediately after single-cell line irradiation with a 405 nm laser (1 mW) for 10 sec. Cells were imaged 48 h post-transfection at 37°C. Representative data from at least three independent experiments. Scale bars, 10 μm.

4.2.3 Characterisation of the FRET-FLIM System

4.2.3.1 mCherry Suitability as an EGFP Acceptor for FRET-FLIM

Prior to performing the FRET-FLIM measurements, the suitability of mCherry as an acceptor for EGFP was investigated. HEK293 cells were transiently transfected with free mCherry and imaged 48 h post-transfection at 37°C. mCherry was excited using multiphoton 910 nm (the same wavelength used to excite EGFP) and the fluorescence lifetime was recorded. As seen in **Figure 4.6**, there were no emitted photon counts collected, evident by the lack of signal in the lifetime map and distribution. This showed mCherry was a suitable acceptor for EGFP. If emission had been collected, it would have indicated mCherry excitation at 910 nm and thus emission that overlapped with the measured EGFP emission. This would have resulted in a skewed lifetime measurement towards shorter values when co-expressed with EGFP (as observed with other red fluorescent proteins, see **Discussion**). Thus, it was critical to check that no emission was observed from mCherry prior to co-expression experiments with EGFP.

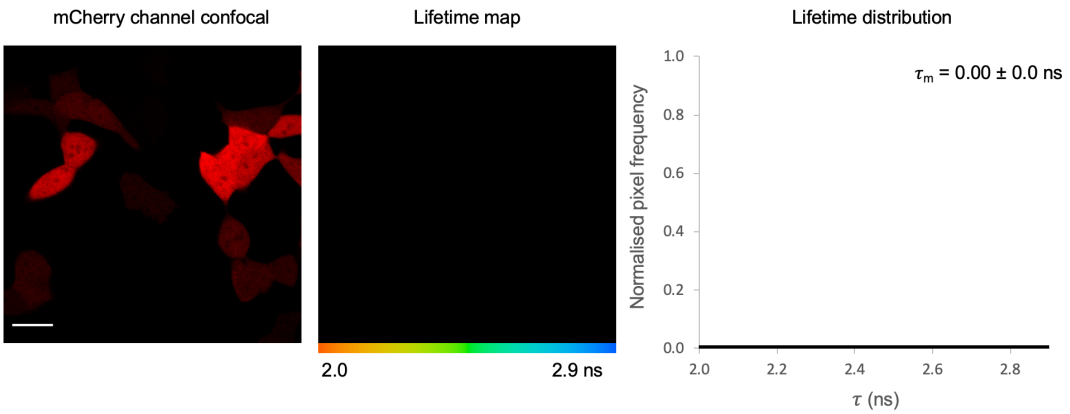

Figure 4.6: Lack of signal shows mCherry is a suitable acceptor for EGFP during multiphoton FRET-FLIM - Confocal image of free mCherry expressed in HEK293 cells (left). The mean fluorescence lifetime (τ) at each pixel is shown using a pseudocolour scale representing lifetime values ranging from 2.0 to 2.9 ns (middle). Corresponding lifetime distribution (histogram) across the image (right). The average mode across all analysed images for each sample is shown (τ_{m}). Error represents standard deviation (SD) from three independent experiments. Scale bar, 10 μm.

4.2.3.2 Assessing the Specificity of FLIM to Detect FRET

Having confirmed mCherry as a suitable acceptor for EGFP, the sensitivity and specificity of FLIM to detect FRET was examined in HEK293 cells. Close proximity (<10 nm) between the donor (EGFP) and the acceptor (mCherry) is a pre-requisite for achieving measurable FRET. As a negative control, the lifetime of free EGFP when co-expressed with free mCherry (**Figure 4.7B**) was measured. As a positive control, EGFP-mCherry fused via an 8-AA (amino acid) linker (**Figure 4.7C**) was tested under the same conditions. The linker was ∼2.8 nm in distance; this is significantly below the maximum 10 nm distance required for the detection of FRET, making it a suitable positive control.

As seen in **Figure 4.7A**, the lifetime of free EGFP was 2.61 ± 0.03 ns. When co-expressed with free mCherry (**Figure 4.7B**), the lifetime was 2.63 ± 0.02 ns. The similarity in mean lifetimes between the two samples indicated a lack of FRET in the negative control. In comparison, shown in **Figure 4.7C**, a reduced EGFP lifetime of 2.28 ± 0.05 ns in cells expressing the fused EGFP-mCherry linker protein was observed. In accordance with previous studies (Ahmed *et al.*, 2019; Kriechbaumer *et al.*, 2015; Stubbs *et al.*, 2005), a reduction of at least ∼200 ps in the natural lifetime of EGFP is considered to be a direct protein-protein interaction. Thus, the 330 ps lifetime reduction observed in the positive control indicated FRET. The close proximity of the EGFP and mCherry fluorophores held together by the very short linker peptide led to FRET, while in **Figure 4.7B**, the free EGFP and mCherry were colocalised but did not interact. These results confirmed that the combination of FRET with FLIM could be used as a nanoscopic ruler for determining direct physical interactions within the magnitude of several nanometres, validating the FRET-FLIM system.

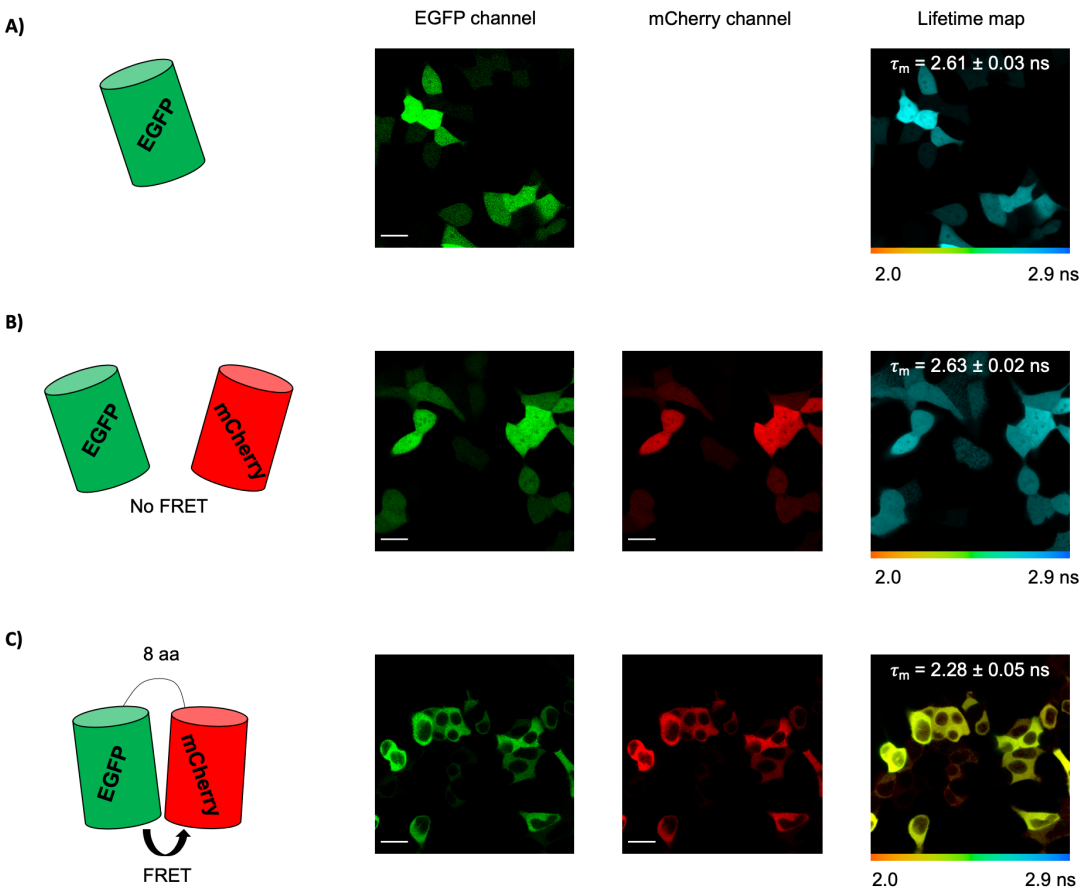

Figure 4.7: Assessing the specificity and sensitivity of the FRET-FLIM assay to detect protein-protein interactions - HEK293 cells **A)** expressing free EGFP, **B)** co-expressing free EGFP and mCherry and **C)** expressing EGFP-mCherry tandem fused via an 8-AA linker were imaged using multiphoton microscopy 48 h post-transfection at 37°C. The mean fluorescence lifetime (τ) at each pixel is shown using a pseudocolour scale representing lifetime values ranging from 2.0 to 2.9 ns. The average mode (τ_m) across all analysed images is shown. Error represents SD from three independent experiments. Scale bars, 10 μm.

4.2.4 Ku70-80 Interactions in Living Cells Revealed by FRET-FLIM

Following the validation of the FRET-FLIM system, transiently transfected HEK293 cells were analysed to measure Ku70 and Ku80 interactions. Since the orientations of the donor (EGFP) and acceptor (mCherry) could potentially influence FRET efficiency, all possible combinations of N- and C-terminal tagging were tested. For each combination, the lifetime of the donor-only and donor plus acceptor were compared. To visualise the fluorescence lifetime (τ) of the donor at each pixel, a 'lifetime map' is presented for each sample using a pseudocolour scale ranging from 2.0 to 2.9 ns. The corresponding lifetime distribution across the image is shown with a histogram ('lifetime distribution'), where dashed lines indicate the mode. The average mode across all analysed images for each sample is shown on each curve as τ_{m}.

To begin with, the interaction between Ku70 (C'-tagged) as donor and Ku80 as acceptor (C'- and N'-tagged) was investigated. As shown in **Figure 4.8A**, the lifetime of Ku70-EGFP (C') was 2.63 ± 0.03 ns. Upon co-expression with Ku80-mCherry (C') (**Figure 4.8B**), the Ku70-EGFP (C') lifetime was quenched to 2.32 ± 0.01 ns. This 310 ps change in donor lifetime was considered to be significant and indicative of FRET. When co-expressed with mCherry-Ku80 (N') (**Figure 4.8C**), the lifetime of Ku70-EGFP (C') was also quenched (from 2.63 ± 0.03 ns to 2.31 ± 0.02 ns), showing a 320 ps change. These results indicated a direct interaction between Ku70 and Ku80 in living cells. Most importantly, this showed the interaction was independent of DNA damage. The relative lifetime changes are directly dependent on the physical distance or separation of Ku70 and Ku80. Thus, the large lifetime changes observed here suggested the C-terminus of Ku70 was in close proximity to the C- and N-termini of Ku80.

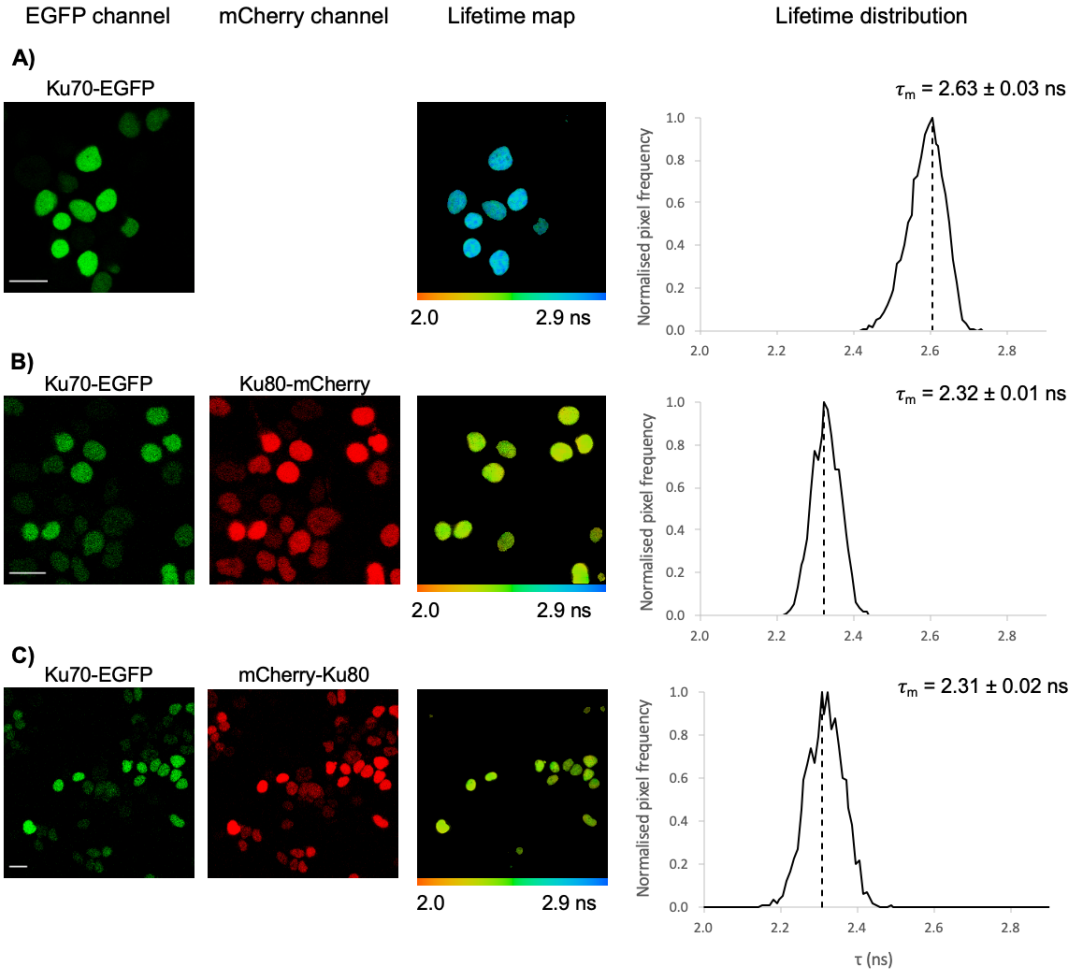

Figure 4.8: FRET-FLIM measurements of Ku70-EGFP (C'), Ku80-mCherry (C') and mCherry-Ku80 (N') - HEK293 cells **A)** expressing Ku70-EGFP (C'), **B)** co-expressing Ku70-EGFP (C') + Ku80-mCherry (C') and **C)** co-expressing Ku70-EGFP (C') + mCherry-Ku80 (N') were imaged using multi-photon microscopy 48 h post-transfection at 37°C. The lifetime map, distribution and average mode (τ_{m}) of the donor (Ku70-EGFP) are shown. Error represents SD from three independent experiments. Scale bars, 10 μm.

Next, the interaction between Ku70 (N'-tagged) as a donor and Ku80 as an acceptor (C'- and N'-tagged) was measured. **Figure 4.9A** shows the natural lifetime of EGFP-Ku70 (N') was 2.54 ± 0.03 ns. Upon co-expression with Ku80-mCherry (C') (**Figure 4.9B**), no interaction was observed, as evident by the lack of significant change in the EGFP-Ku70 (N') lifetime (2.49 ± 0.01 ns). This suggested the N-terminus of Ku70 and the C-terminus of Ku80 were not in close proximity or were in an unfavourable position for FRET to occur. This finding also showed the position of the fluorescent tag was critical for examining Ku70-Ku80 interactions.

Figure 4.9C shows the co-expression of EGFP-Ku70 (N') and mCherry-Ku80 (N') and revealed there were two leading lifetime populations in the sample; one of ∼2.5 ns (close to the natural lifetime of EGFP-Ku70 (N')) and another of 2.42 ± 0.04 ns. This suggests that only some molecules may be interacting. From this data, it is not possible to conclude if there was an interaction, as the 120 ps lifetime change fell outside the 200 ps confidence for a direct interaction. This could be indicative of an unfavourable dipole orientation of the EGFP and mCherry which was suboptimal for FRET.

Similarly, **Figure 4.10** shows the interaction between Ku80 (N'-tagged) as a donor and Ku70 as an acceptor (C'- and N'-tagged). Upon co-expression of EGFP-Ku80 (N') and mCherry-Ku70 (N') (**Figure 4.10B**), two populations of lifetimes were revealed. One population of cells had a lifetime of ∼2.5 ns (close to the lifetime of EGFP-Ku80 (N'), 2.52 ± 0.01 ns), while another had a lifetime of 2.38 ± 0.01 ns. This 140 ps quench was not a significant reduction, again suggesting a suboptimal orientation for FRET to occur. The same phenomenon is seen in **Figure 4.10C** with the co-expression of EGFP-Ku80 (N') and Ku70-mCherry (C'). While one population of cells had a lifetime of ∼2.5 ns, a second population with a lifetime of 2.39 ± 0.03 ns was measured.

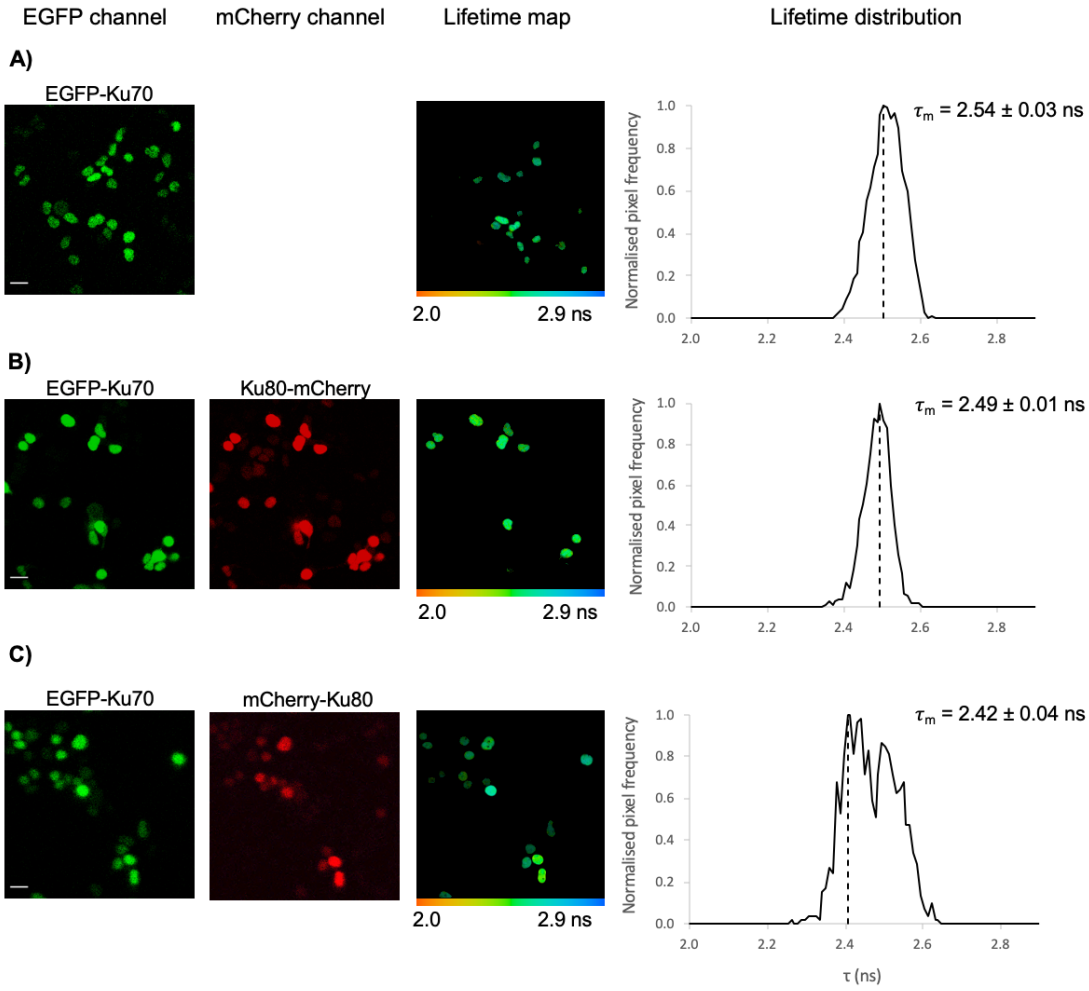

Figure 4.9: FRET-FLIM measurements of EGFP-Ku70 (N'), Ku80-mCherry (C') and mCherry-Ku80 (N') - HEK293 cells **A)** expressing EGFP-Ku70 (N'), **B)** co-expressing EGFP-Ku70 (N') + Ku80-mCherry (C') or **C)** co-expressing EGFP-Ku70 (N') + mCherry-Ku80 (N') were imaged using multiphoton microscopy 48 h post-transfection at 37°C. The lifetime map, distribution and average mode (τ_m) of the donor (EGFP-Ku70) are shown. Error represents SD from three independent experiments. Scale bars, 10 μm.

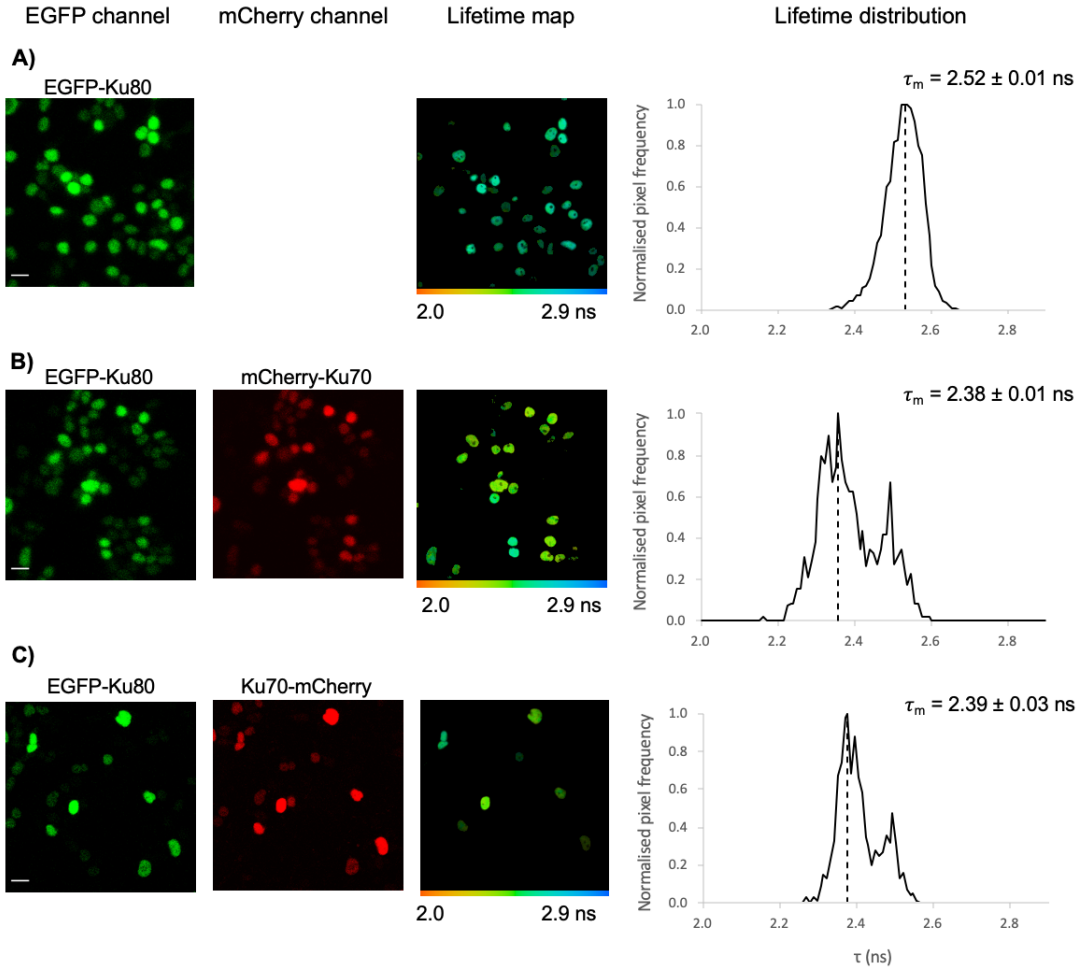

Figure 4.10: FRET-FLIM measurements of EGFP-Ku80 (N'), mCherry-Ku70 (N') and Ku70-mCherry (C') - HEK293 cells **A)** expressing EGFP-Ku80 (N'), **B)** co-expressing EGFP-Ku80 (N') + mCherry-Ku70 (N') and **C)** co-expressing EGFP-Ku80 (N') + Ku70-mCherry (C') were imaged using multiphoton microscopy 48 h post-transfection at 37°C. The lifetime map, distribution and average mode (τ_m) of the donor (EGFP-Ku80) are shown. Error represents SD from three independent experiments. Scale bars, 10 μm.

Finally, the interaction between Ku80 (C'-tagged) as a donor and Ku70 as an acceptor (C'- and N'-tagged) was tested. **Figure 4.11A** shows the natural lifetime of Ku80-EGFP (C') was 2.61 ± 0.03 ns. Upon co-expression with mCherry-Ku70 (N'), there was no change in lifetime (2.58 ± 0.02 ns). Similarly, in cells co-expressing Ku80-EGFP (C') and Ku70-mCherry (C') (**Figure 4.11C**), the lifetime was 2.59 ± 0.02 ns. This indicated these proteins were not in a favourable position for FRET. Taken together with the results shown in **Figure 4.9**, the data suggested the C-terminus of Ku80 and the N-terminus of Ku70 were not in close proximity.

A summary of the FRET-FLIM results is shown in **Figure 4.12**. As indicated by the large changes in lifetime seen in **Figure 4.12 (A-D)**, the C-terminus of Ku70 was likely to be in close proximity to the C'- and N'-termini of Ku80, while the N-terminals of both proteins were far apart. This is clearly shown in the 3D rendered model of the heterodimer in **Figure 4.12E.** This model was based on the relative lifetime changes observed with FRET-FLIM, as these were directly dependent on the physical distance or separation of Ku70 and Ku80. The images shown in **Figure 4.12E.** represent the structure of Ku70 and Ku80 with their termini labelled, and aim to highlight the proximity of different termini to each other.

Overall, the FRET-FLIM data revealed Ku70 and Ku80 interact in live HEK293 cells in the absence of DNA damage. The position of the fluorescent tag was critical for examining these interactions.

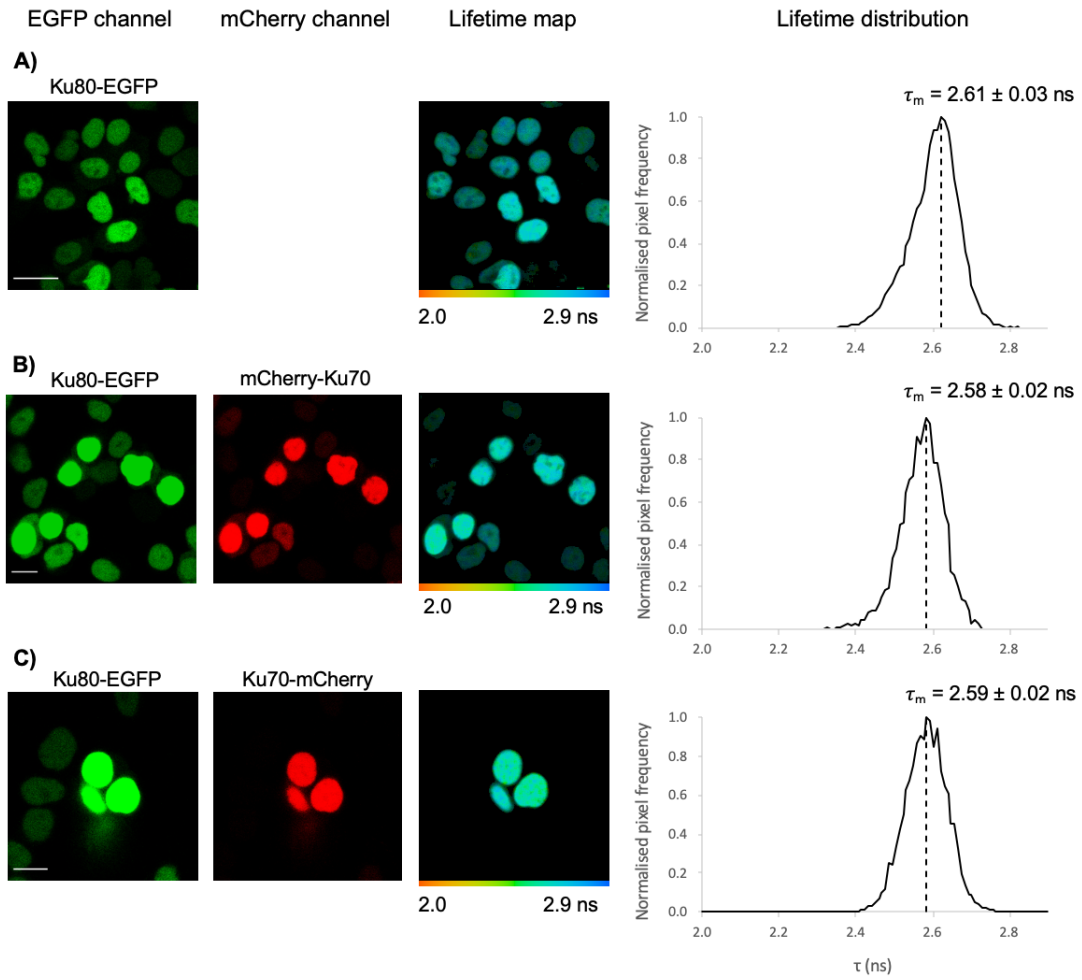

Figure 4.11: FRET-FLIM measurements of Ku80-EGFP (C'), mCherry-Ku70 (N') and Ku70-mCherry (C') - HEK293 cells **A)** expressing Ku80-EGFP (C'), **B)** co-expressing Ku80-EGFP (C') + mCherry-Ku70 (N') and **C)** co-expressing Ku80-EGFP (C') + Ku70-mCherry (C') were imaged using multiphoton microscopy 48 h post-transfection at 37°C. The lifetime map, distribution and average mode (τ_m) of the donor (Ku80-EGFP) are shown. Error represents SD from three independent experiments. Scale bars, 10 μm.

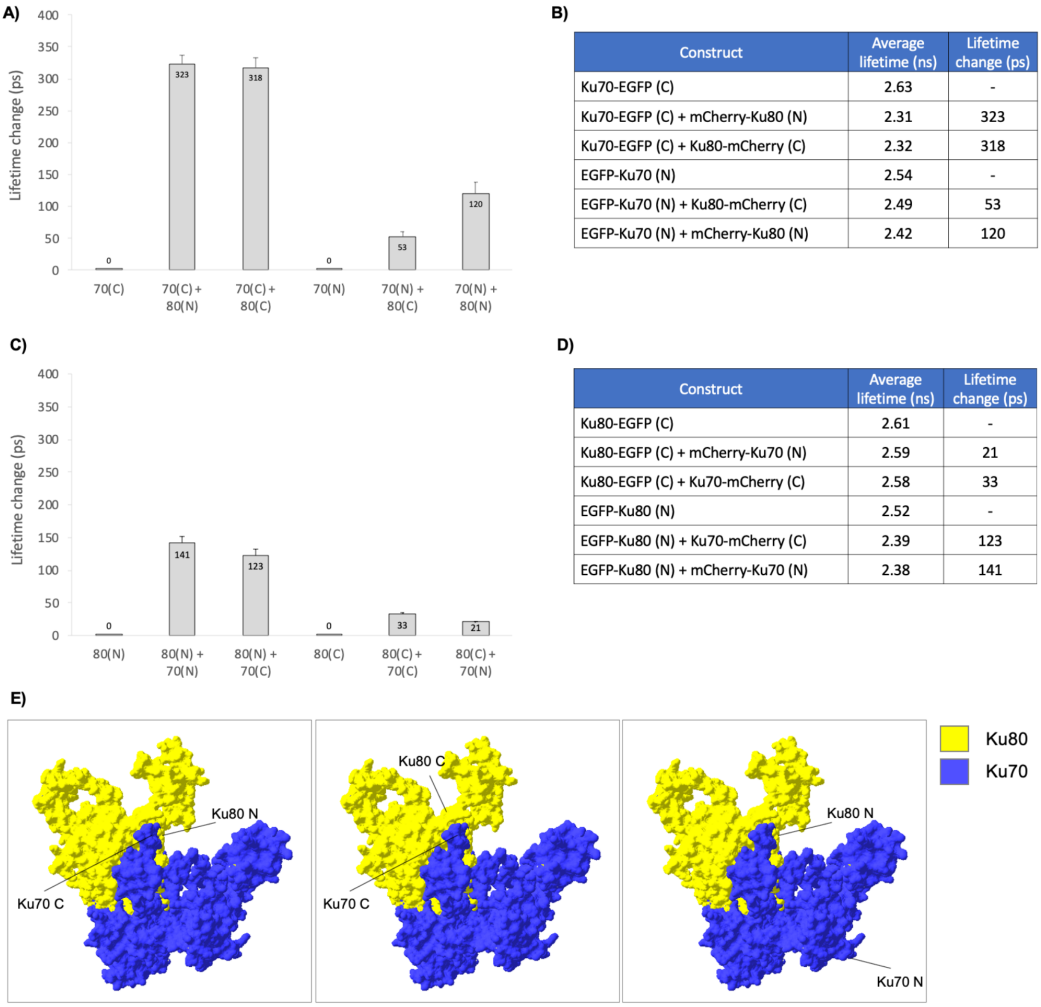

Construct	Average lifetime (ns)	Lifetime change (ps)
Ku70-EGFP (C)	2.63	-
Ku70-EGFP (C) + mCherry-Ku80 (N)	2.31	323
Ku70-EGFP (C) + Ku80-mCherry (C)	2.32	318
EGFP-Ku70 (N)	2.54	-
EGFP-Ku70 (N) + Ku80-mCherry (C)	2.49	53
EGFP-Ku70 (N) + mCherry-Ku80 (N)	2.42	120

Construct	Average lifetime (ns)	Lifetime change (ps)
Ku80-EGFP (C)	2.61	-
Ku80-EGFP (C) + mCherry-Ku70 (N)	2.59	21
Ku80-EGFP (C) + Ku70-mCherry (C)	2.58	33
EGFP-Ku80 (N)	2.52	-
EGFP-Ku80 (N) + Ku70-mCherry (C)	2.39	123
EGFP-Ku80 (N) + mCherry-Ku70 (N)	2.38	141

Figure 4.12: Summary of Ku70-Ku80 interactions and new 3D rendered model based on FRET-FLIM data - Bar graph of lifetime changes in each sample, comparing the different N- and C-terminal tagging combinations of Ku70 (**A**&**B**) and Ku80 (**C**&**D**) to EGFP. Error represents SD from three independent experiments. **E)** New Ku70-Ku80 binding model based on the lifetime changes observed with FRET-FLIM. Ku70 and Ku80 termini are outlined to show their proximity. Model made in SwissPDBViewer (version 4.10).

4.2.5 EGFP and mCherry Unsuitability for 405 nm Laser Irradiation Followed by FRET-FLIM

Once the Ku70-Ku80 dimerisation was detected, laser irradiation was used to study this interaction at DNA damage sites. The working hypothesis was that there would be a change in the interaction upon DNA damage induction, as Ku bound to the broken DNA ends.

Firstly, to test that EGFP and mCherry were suitable for laser irradiation followed by FRET-FLIM analysis, HEK293 cells were transiently transfected with free EGFP (excited with 910 nm) or free mCherry (excited with 561 nm), and imaged before and immediately after irradiation. A 10 sec irradiation through a single cell was performed with a 405 nm laser (1 mW) (**Methods 2.2.17.1**). As observed in **Figure 4.13A**, the lifetime of EGFP unexpectedly decreased from 2.58 ns to 2.44 ns following irradiation. This 140 ps reduction in lifetime was only observed in the irradiated cell (indicated by the white arrow), while the un-irradiated cells in the same field of view remained unaffected. This experiment was repeated with cells expressing free mCherry, shown in **Figure 4.13B**, and an increase in lifetime from 1.60 ns to 1.75 ns was observed. This 150 ps increase in lifetime was only observed in the nucleus of the cell that was irradiated, as indicated by the white arrow, while the surrounding cells remained unaffected.

These results suggested EGFP and mCherry underwent a structural modification (i.e. chromophore ionisation) and/or the environment around the fluorescent molecules had been altered. Both of these scenarios would lead to the lifetime changes observed here. Overall, these findings showed EGFP and mCherry were unsuitable fluorophores for FRET-FLIM studies following 405 nm laser irradiation. Thus, the interaction of Ku70 and Ku80 at laser-induced DNA damage sites was not possible to be investigated.

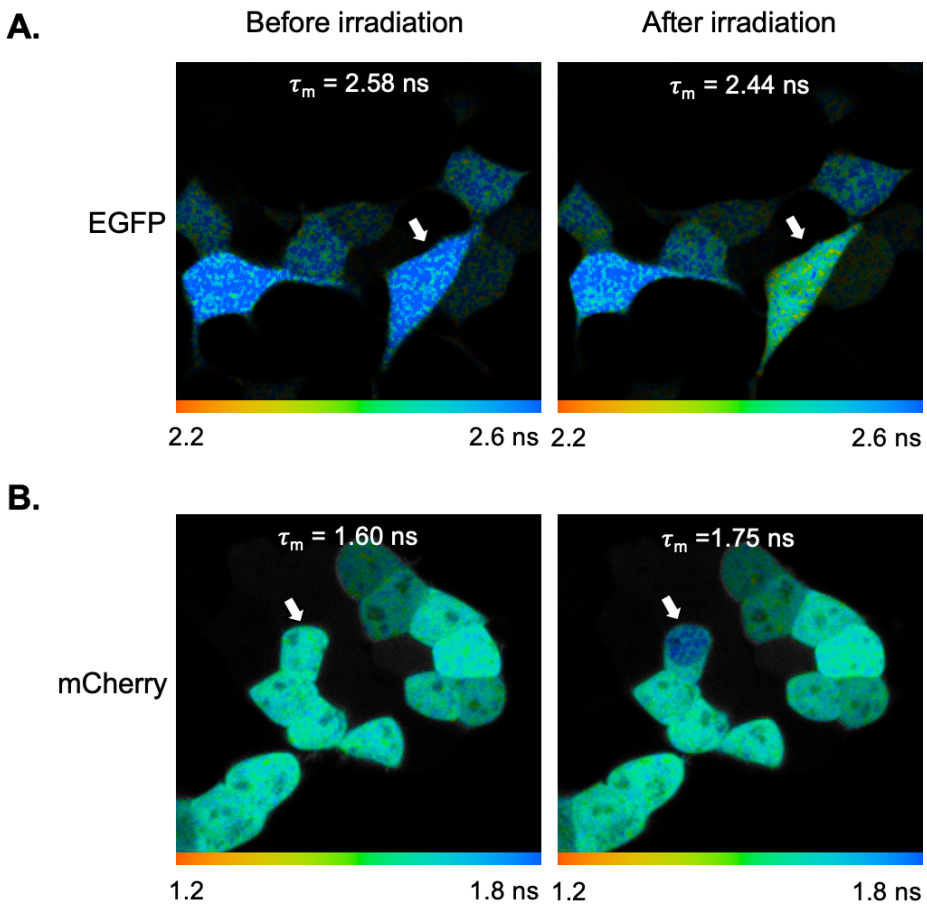

Figure 4.13: EGFP and mCherry are unsuitable for 405 nm laser irradiation followed by analysis with FRET-FLIM - Individual HEK293 cells expressing **A)** EGFP or **B)** mCherry were irradiated with a 405 nm laser for 10 sec (indicated by the white arrow). Cells were imaged 48 h post-transfection at 37°C before and immediately after irradiation. The lifetime map and average mode (τ_m) are shown. Representative data from three independent experiments.

4.2.6 Using BiFC to Validate the FRET-FLIM Results

To verify the results obtained with FRET-FLIM, a BiFC assay was employed (**Figure 4.14A**). Venus fluorescent protein (a yellow fluorescent protein variant) was split into two non-fluorescent fragments, namely VN155 and VC155 (VN and VC, respectively). Ku70 was fused to VN and Ku80 to VC (**Methods 2.2.9**). The working hypothesis was that upon dimerisation of Ku70 and Ku80, the reconstitution of the Venus fluorescent protein, and thus the presence of fluorescence, would indicate Ku70 and Ku80 interact in living cells.

4.2.6.1 Positive Control - bFos and bJun Interaction

As a positive control, bJun-VN and bFos-VC plasmids were used. These proteins have been previously shown to interact using BiFC (Shyu *et al.*, 2006). The DNA transfection concentration was optimised (500 ng/plasmid) to achieve low toxicity and high fluorescence intensity. HEK293 cells were transiently transfected with bJun-VN (**Figure 4.14B**), bFos-VC (**Figure 4.14C**) and co-transfected with both constructs (**Figure 4.14D**). Cells were imaged 24 h post-transfection at 37°C. Confocal imaging revealed the presence of fluorescence signal only upon co-expression, indicating bFos-VC and bJun-VN had formed a complex. This became detectable when the Venus fluorophore was re-constituted from the two complementary moieties brought into contact by the interacting bFos and bJun. Lack of fluorescence intensity when bJun-VN and bFos-VC were expressed separately (**Figure 4.14B-C**) showed there was no self-assembly from each individual fragment.

Fluorescence intensity from the confocal data from each sample was quantified and

plotted, **Figure 4.14E**. Box plots clearly showed very low fluorescence intensities were detected from bJun-VN (median=2) and bFos-VN only samples (median=3), likely generated from background signal. In contrast, high fluorescence intensities were measured upon co-expression (median=1622, Q1=1058, Q3=2763, minimum=748 and maximum=3249). Overall, these results indicated that increases in fluorescence intensity reflected specific protein-protein interactions, validating the BiFC system.

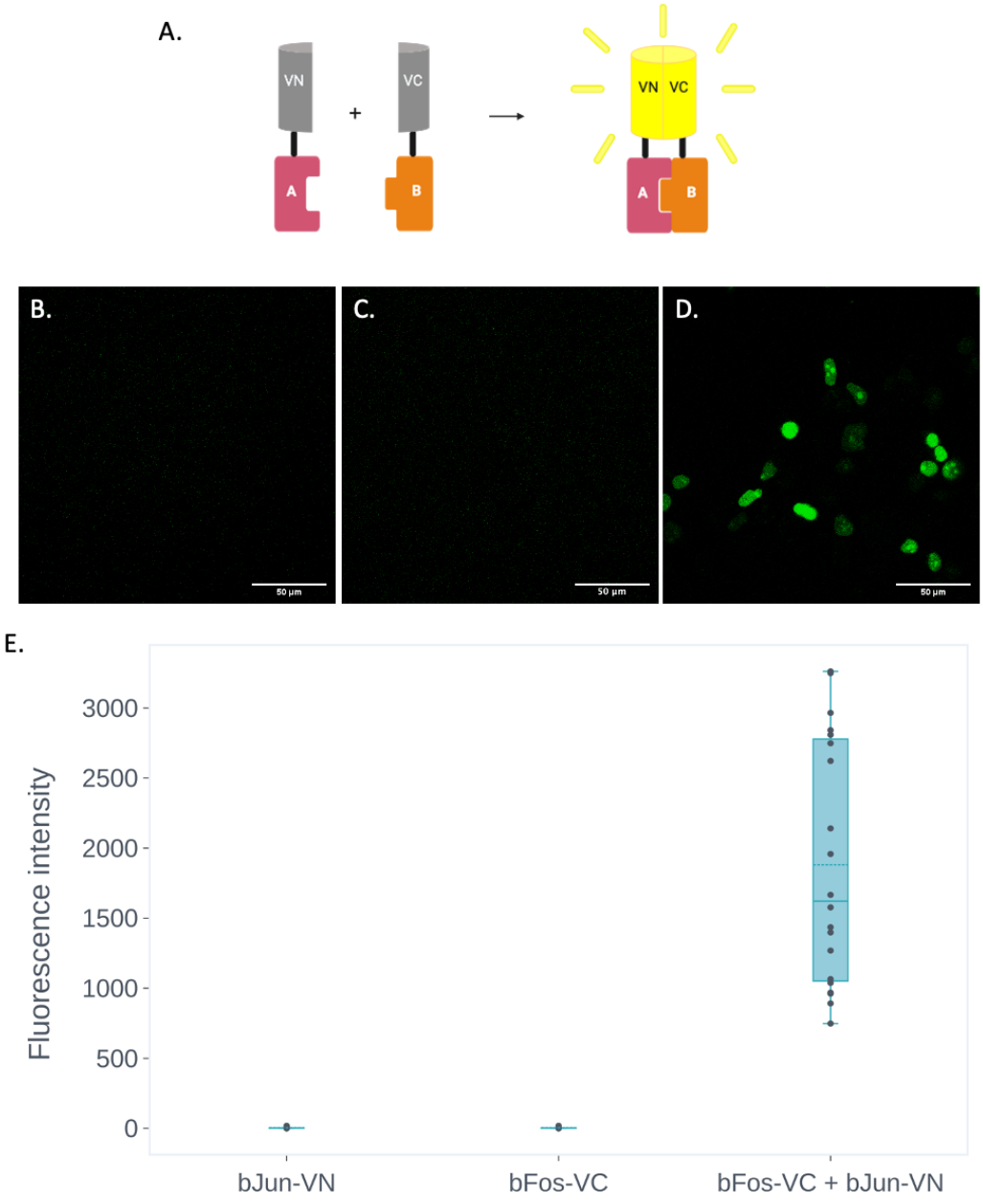

Figure 4.14: BiFC positive control in HEK293 cells - A. Schematic of BiFC principle. Confocal images of HEK293 cells expressing **B.** bJun-VN, **C.** bFos-VC and **D.** bJun-VN and bFos-VC. Cells were imaged 24 h post-transfection at 37°C. **E.** Box plot showing the fluorescence intensities of each sample. Representative data from three independent experiments. Scale bars, 50 μm.

4.2.6.2 Ku70-Ku80 Interactions Validated by BiFC

Following validation of the BiFC system, HEK293 cells expressing Ku70-VN (C') and Ku80-VC (C') were imaged using confocal microscopy. Cells were imaged 24 h post-transfection at 37°C. As shown in **Figure 4.15**, bright fluorescence was detected only upon co-expression of both fragments, indicating a protein-protein interaction. In contrast, no fluorescence was detected upon expression of individual constructs **Figure 4.15A-B.** These results were supported by quantification of the confocal images, shown in **Figure 4.15G.** Box plots revealed very weak fluorescence intensities in samples expressing either Ku70-VN (median=2) or Ku80-VC alone (median=1), while high fluorescence intensities were measured upon co-expression (median= 1699, Q1=1083, Q3=2104, minimum=784 and maximum=3261). These results revealed Ku70 and Ku80 interact in live HEK293 cells.

To validate the results, a negative control was made using a Ku70 mutant attached to the VN fragment (*Ku70-L385R-VN*). The mutation was done on amino acid 385 (L385R), as it is known to disrupt the Ku80 binding domain, while localisation and expression remain unaffected (Koike *et al.*, 2001). As observed in **Figure 4.15E**, upon co-transfection of *Ku70-L385R-VN* and wild-type Ku80-VC, the heterodimer formation was abrogated, as evident by the lack of fluorescence signal in both the confocal image and box plot (**Figure 4.15G**, median=2). The point mutation L385R on Ku70 targeted its C-terminus. The lack of interaction observed with the mutant further supports the FRET-FLIM data, which indicated the C-terminus of Ku70 interacted with Ku80.

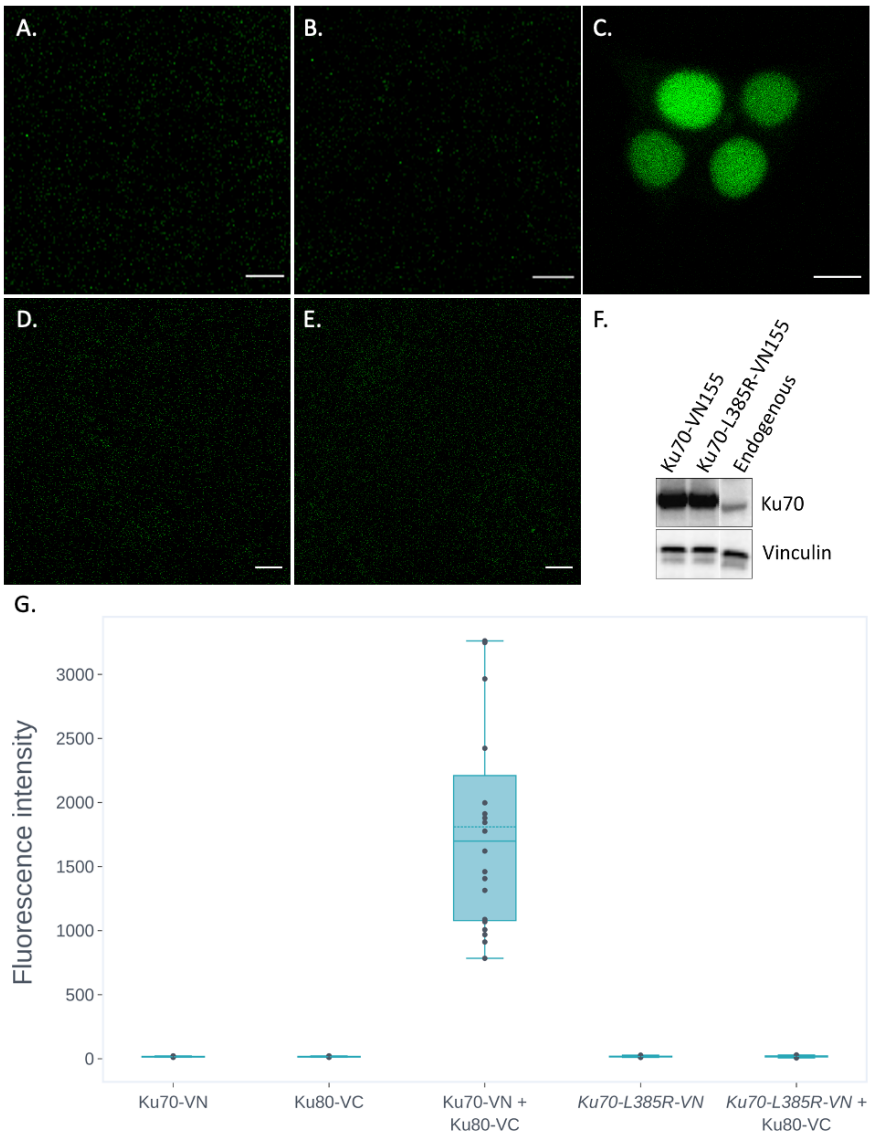

Figure 4.15: BiFC validates Ku70-Ku80 interactions in HEK293 cells - Confocal images of HEK293 cells expressing **A.** Ku70-VN, **B.** Ku80-VC, **C.** Ku70-VN + Ku80-VC, **D.** *Ku70-L385R-VN* and **E.** *Ku70-L385R-VN* + Ku80-VC. Cells were imaged 24 h post-transfection at 37°C. **F.** Box plot showing the fluorescence intensities from each sample. **G.** Western blot showing Ku70 labelling of wild-type Ku70-VN and mutant *Ku70-L385R-VN* in transfected and un-transfected cells. Blots were probed with vinculin as a loading control. Representative data from three independent experiments. Scale bars, 5 μm.

Expression of *Ku70-L385R-VN* alone also showed no fluorescence, indicating lack of self-assembly from the mutant fragment (**Figure 4.15D** and **4.15G**, median=1). Western blot analysis was used to ascertain that lack of fluorescence from the *Ku70-L385R-VN* samples was not due to low plasmid expression. As shown in **Figure 4.15F**, the expression of mutant *Ku70-L385R-VN* was comparable to wild-type Ku70-VN protein levels, and higher than endogenous. This showed gene expression remained unaffected by the mutation and validated that lack of fluorescence was due to the disruption of Ku70-Ku80 binding rendering the VC-VN fragments unable to emit fluorescence.

As shown by the confocal data in **Figure 4.15**, the Venus moieties did not interfere with normal nuclear localisation of Ku70/80. To check protein functionality had not been affected, recruitment of Ku70-VN and Ku80-VC to laser-generated sites of DNA damage was measured. Irradiations were conducted with a 405 nm laser to generate a 10 sec traversal through a single cell nucleus (**Methods 2.2.17.1**). HEK293 cells co-expressing Ku70-VN and Ku80-VC were imaged before **Figure 4.16A** and immediately after laser irradiation **Figure 4.16B**. A clear line of recruitment where the damage was induced can be seen, as evident by the increase in fluorescence intensity at the irradiated areas. The movement and recruitment of Ku to the sites of damage indicated the Ku70-VN and Ku80-VC were functional and thus unaffected by VN/VC tagging.

Taken together, BiFC results showed Ku70 and Ku80 form heterodimers in living cells without the induction of DNA lesions, providing further evidence to support the Ku70-Ku80 interaction is independent of DNA damage.

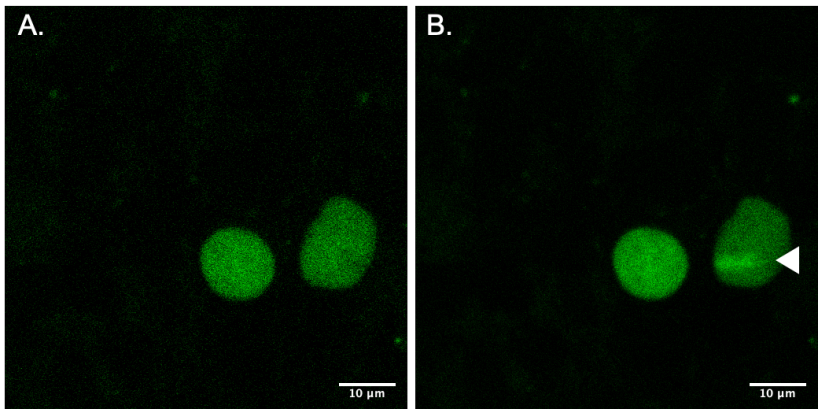

Figure 4.16: Ku70-VN and Ku80-VC recruitment to laser-induced damage in HEK293 cells - HEK293 cells co-expressing Ku70-VN and Ku80-VC were imaged before (**A.**) and immediately after (**B.**) single-cell irradiation in the form of a line with a 405 nm laser (1 mW) for 10 sec. Cells were imaged 24 h post-transfection at 37°C. Representative data from three independent experiments.

4.3 Discussion

FRET-FLIM and BiFC revealed Ku70 and Ku80 interact in living cells

The study presented here is the first to demonstrate Ku70 and Ku80 interact in living cells. This finding reports that the Ku heterodimer exists as pre-formed and stable in the absence of DNA damage. This is in accordance with previous studies carried out using Ku-deficient cell lines (Gu *et al.*, 1997), affinity chromatography (Ramsden *et al.*, 1998), dysfunctional mutants (Fujimoto *et al.*, 2018; Jin *et al.*, 1997; Koike *et al.*, 2001) and structural studies (Cary *et al.*, 1997; Walker *et al.*, 2001). Others have also shown Ku70-80 interactions using yeast two-hybrid systems (Cary *et al.*, 1998; Tamura *et al.*, 2002) and immunoprecipitation (Jin *et al.*, 2020). From the FRET-FLIM data, a new 3D model of Ku70-Ku80 binding was created based on the relative lifetime changes, as these were directly dependent on the physical distance or separation between Ku70 and Ku80. This model is consistent with those derived from single-particle EM structural (Rivera-Calzada *et al.*, 2007), as well as cryo-EM (Rivera-Calzada *et al.*, 2005; Spagnolo *et al.*, 2006) and X-ray crystallography (Walker *et al.*, 2001) data, which showed the C terminus of Ku70 was in close proximity to both the N and C termini of Ku80, as observed here.

Unlike the studies mentioned above, the experiments presented in this chapter were conducted in living cells, which enabled the investigation of interactions in real time. Live-cell studies are less susceptible to experimental artefacts as cellular integrity is preserved (Huber *et al.*, 2003; Schnell *et al.*, 2012). Neither FRET-FLIM nor BiFC require any special treatment of cells, including fixation or lysis, allowing minimal perturbation of the normal cellular environment. In contrast, cell fixation has been shown

to cause disruptions to the natural lifetime of EGFP (Ahmed *et al.*, 2019; Neuhaus *et al.*, 1998; Schnell *et al.*, 2012), which would directly affect the FRET-FLIM results.

Contrary to intensity-based methods (Fujimoto *et al.*, 2018; Koike *et al.*, 2001), FRET-FLIM is less influenced by artifacts such as probe concentration, photobleaching, scattered light, and non-uniform illumination, as it relies on the chromophore's fluorescence lifetime (Becker, 2014). While BiFC depends on intensity-based quantification, the background signal is minimal as fluorescence emission only occurs upon protein interaction (Kerppola, 2008). Additionally, unlike FRET-FLIM, the interacting proteins are not required to be in close proximity (<10 nm apart), making BiFC a more sensitive technique (Kerppola, 2009).

Despite having many benefits, BiFC and FRET-FLIM present some drawbacks. For example, BiFC requires fragmented fluorescent proteins, and only a small number of these proteins are available for mammalian systems (Miller *et al.*, 2015). As with any fluorescent tag, protein functionality may be affected, thus it is important to check for function. To avoid false positives, it is essential to have an appropriate negative control, such as a non-interacting point mutant, which may not be possible if this information is unknown (Kodama *et al.*, 2012). Unlike FRET-FLIM, it is not possible to monitor dynamic protein interactions using BiFC, as complex formation may be irreversible (Shyu *et al.*, 2008), although several studies suggest otherwise (Cole *et al.*, 2007; Guo *et al.*, 2005; Kang *et al.*, 2010; Sung *et al.*, 2007). One key limitation of FRET-FLIM is the influence of external factors in the microenvironment surrounding the donor fluorophore, including local viscosity, pH, polarity and temperature (Suhling *et al.*, 2015). Thus, it is critical to perform suitable controls to avoid false-negatives and false-positives.

FRET-FLIM controls and optimisation

The sensitivity and specificity of FLIM to detect FRET was examined using an EGFP-mCherry construct fused by an 8-AA linker (referred to as 'tandem'). Unexpectedly and unlike all other constructs, the localisation of the tandem was cytoplasmic. As this construct does not have a nuclear localisation signal sequence and is ∼55 kDa in size, it may have been unable to diffuse through the nuclear membrane, thus was excluded from the nucleus (Görlich *et al.*, 1999; Weis, 2003). Another explanation could be that the cytoplasmic localisation was caused by the linker. Future experiments are needed to investigate this by changing the AA sequence and assessing the localisation.

The choice of acceptor for FRET-FLIM experiments was critical in avoiding false conclusions. For example, red fluorescent proteins such as DsRed have been shown to produce green emission upon 910 excitation. This results in an average lifetime which is shorter than with EGFP alone, erroneously indicating a protein interaction (Ahmed, 2018; Ahmed *et al.*, 2019). In the work presented here, mCherry was found to be a suitable EGFP acceptor, in agreement with previous reports (Ahmed, 2018; Ahmed *et al.*, 2019; Kim *et al.*, 2012).

Gene overexpression provides a useful tool for imaging proteins that would otherwise remain undetected using other methods. However, the abnormally high concentrations of overexpressed proteins may lead to abnormal cell behaviour (Prelich, 2012), including the forcing of non-interacting proteins together (Taipale, 2018). Additionally, the choice of fluorescent protein and the terminus to which it is tagged to are essential for protein expression and function (Costantini *et al.*, 2015; Fritz *et al.*, 2008; Huang *et al.*, 2014; Shemiakina *et al.*, 2012). In the study presented here, EGFP and mCherry

tagging did not appear to disrupt Ku70/80 localisation or function, however, the position of the tag affected the FRET-FLIM results. This highlights the importance of tagging proteins at both the N- and C-termini and performing interaction studies with all eight combinations. Lack of optimisation can lead to false negatives and thus misinterpretation of data, as previously observed in FLIM experiments with alpha-synuclein molecules (Klucken *et al.*, 2006). In future studies, applying the same approach to BiFC would be advantageous, as due to time constraints, only C-terminal tagged constructs were made and examined. Future work entailing the use of CRISPR/Cas9 technology to tag endogenous Ku70 and Ku80 with GFP, or stable cell lines, could be used instead of the current overexpression system. In addition, improvements to the FRET-FLIM methodology could be made by using more stable and brighter fluorophores, such as the recently developed mScarlet (Bindels *et al.*, 2016).

Localisation and recruitment studies

EGFP- and mCherry-tagged Ku70 and Ku80 showed nuclear localisation in HEK293, HeLa and CHO cells. These results were consistent with their functions, as they play key roles in multiple nuclear processes, in agreement with many previous studies performed in human, CHO, mouse and canine cell lines (Koike, 2002; Koike *et al.*, 1998, 2001, 2015, 2017a,b). Occasionally, Ku was found to localise to cell nucleoli. This was likely due to the focal plane during imaging, or the cell cycle stage. Ku localisation has been shown to be dependent on the cell cycle phase, as well as on the cell line used (Britton *et al.*, 2013; Higashiura *et al.*, 1992; Li *et al.*, 1992). While not observed here, Ku has also been detected in other cell compartments including the cytoplasm (Hada *et al.*, 2016) during specific phases. As localisation is affected by the cell cycle, further

work could involve investigating Ku70-Ku80 interactions in synchronised cells.

Ku70/80 function was checked by measuring protein recruitment to sites of DNA damage induced by a 405 nm laser. Rapid localisation of Ku70 and Ku80 to the site of damage was in accordance with many other studies (Bekker-Jensen *et al.*, 2006; Kim *et al.*, 2005; Koike *et al.*, 2015; Mari *et al.*, 2006; Reynolds *et al.*, 2012). Laser irradiation allows the generation of highly localised areas of damage, while the surrounding remains intact (Holton *et al.*, 2017). Additionally, in contrast to most radiation systems, laser set-ups can generate damage with cells kept at 37°C, providing a more accurate method for measuring protein kinetics. However, laser irradiations produce a wide spectrum of DNA lesions (including cross-links, SSBs and DSBs) which are highly dependent on laser power and wavelength applied (Aleksandrov *et al.*, 2018; Holton *et al.*, 2017; Mortusewicz *et al.*, 2007). In addition, there have been several attempts to relate this type of damage to dose with little success (Holton *et al.*, 2017; Reynolds, 2009). This makes the DNA lesions difficult to characterise and results challenging to interpret.

While laser irradiations worked well for measuring Ku70/80 recruitment using confocal imaging, it was unsuitable for determining interactions with FRET-FLIM. The lifetime of EGFP decreased upon irradiation, potentially from a modification to the environment around the fluorophore, such as a change in pH. A recent study performed with EGFP in plants found the pH of the sample decreased from 8.0 to 5.0 upon 405 nm laser irradiation (Sattarzadeh *et al.*, 2015). This supports the premise that the changes in EGFP lifetime observed here were driven by variations in pH. To overcome this problem, a more stable variant of EGFP could be used. Two likely candidates are the recently developed pH-tdGFP (Roberts *et al.*, 2016) and monomeric ultra-stable

GFP (muGFP) (Scott *et al.*, 2018), which benefit from high fluorescence stability and maintaining their fluorescent properties in acidic conditions. Future studies to test their suitability as donor molecules using FRET-FLIM are required.

This finding meant it was not possible to study Ku70-80 interactions upon DNA damage. Due to time constraints, it was unfeasible to examine the effect of IR on Ku interactions. Additionally, the X-ray source available was not physically close to the FRET-FLIM set-up, and thus would have been difficult to accurately measure protein interactions in living cells without introducing flaws. The comparison after low- and high-LET IR (such as X-rays and alpha-particles), where the frequency and complexity of DNA damage will be different, was also not explored and requires further investigation.

Further work with FRET-FLIM

While the observation of Ku70-Ku80 interactions was significant, it would have been advantageous to find inhibitors to disrupt and further validate the interactions observed. To date, only one small molecule inhibitor ('Compound L') of the heterodimer has been identified (Weterings *et al.*, 2016). This compound has been shown to diminish Ku70-Ku80 binding (using an electrophoretic mobility shift assay) and sensitise two human cancer cell lines to IR. This initial work demonstrated the potential of this inhibitor as an anti-cancer drug, but only provided a small snapshot of its capabilities. Testing this inhibitor using FRET-FLIM would provide information on the mechanism of this drug. Identifying where and how Ku (and other NHEJ) inhibitors function within cancer cells and tissues is crucial in understanding their mechanism and effectiveness on a sub-cellular level and optimising their effect (Ahmed, 2018; Ahmed *et al.*, 2019;

Rutkowska *et al.*, 2016; Stumpf, 2005).

This study is limited by the use of only one cell line. Further studies are warranted to investigate Ku70-80 interactions in more detail using other cell lines, particularly mutant cells with defects in NHEJ, which will allow more extensive analyses of this repair pathway. Additionally, Ku70-80 binding has been shown to be impaired more frequently in tumours compared to normal tissues using biochemical methods (Costantini *et al.*, 2007; Parrella *et al.*, 2006; Pucci *et al.*, 2001). Thus, further work is needed to investigate the differences in Ku70-80 interactions between normal and malignant cells using live imaging.

Determining multiple protein interactions simultaneously is key to defining exact DNA signalling and repair mechanisms. The application of three-colour FRET-FLIM (Grant *et al.*, 2008; Laviv *et al.*, 2016; Sun *et al.*, 2010) and three-colour BiFC (Lee *et al.*, 2008) could be used to detect novel interactions between multiple proteins in living cells. For example, interactions between Ku70, Ku80 and DNA-PKcs (known to drive pancreatic cancer progression and metastasis) (Goodwin *et al.*, 2014, 2015), RECQ1 (overexpressed and amplified in many cancers) (Parvathaneni *et al.*, 2013; Sharma, 2014) and TRF2 (upregulation in this interaction is linked to gastric cancer progression) (Hu *et al.*, 2010; Ribes-Zamora *et al.*, 2013; Song *et al.*, 2000) could be investigated to deepen our understanding of the many functions of Ku70/80 and their role in disease. Additionally, the interaction between NHEJ (Ku70/80) and HR markers (such as BRCA1) could reveal insight into what pathway drives DSB repair in cancer cells and how it relates to patient outcome (Alshareeda *et al.*, 2013).

4.4 Conclusion

In conclusion, this is the first study to show Ku70 and Ku80 interact in living cells, with the Ku heterodimer pre-formed and stable even in the absence of DNA damage. From a technical point of view, FRET-FLIM and BiFC were demonstrated to be well suited for measuring protein-protein interactions in living cells. The position of the fluorescent tag on Ku70 and Ku80 termini resulted in varying FRET-FLIM results, showing that lack of optimisation can lead to false negatives and thus misinterpretation of FRET-FLIM data. While Ku70/80 recruited to sites of laser-induced damage, it was not possible to determine whether they acted as monomers or heterodimers at the DNA damage site. This was because the natural EGFP lifetime was altered following irradiation. It is hoped this work will be used to gain a better understanding of Ku70-80 interactions in disease and as a predictor of patient outcome.

Chapter 5

Super-resolution Imaging Applied to DNA Double-strand Breaks

5.1 Brief Introduction

As outlined in the **Introduction**, DNA double-strand breaks (DSBs) are key lesions produced by ionising radiation (IR) in determining the ultimate response of the cell. DSB formation triggers the cellular DNA damage response, including phosphorylation of histone variant H2AX, producing gamma-H2AX (γH2AX), which is paramount in recruiting multiple key DNA repair proteins. One of these is 53BP1, which localises rapidly to sites of damage and plays a crucial role in determining the repair pathway of choice between HR or NHEJ. The induction and repair of DSBs can be monitored by visualising γH2AX and 53BP1 foci formation. While their induction has been shown to correlate with dose (Rothkamm *et al.*, 2003), there is some discrepancy in the yield and kinetics of foci formation and repair. These kinetics also differ from other detection methods, most notably Pulse-field Gel Electrophoresis (PFGE) which typically shows a repair half-time of $\sim$20 min for low-LET induced DSBs (Kinner *et al.*, 2008), while

the peak for γH2AX foci is typically observed at ∼30 min. Much progress has been made in uncovering the basic IR-induced responses and mechanisms. However, due to limitations in the resolution of standard microscopes, less is known about foci at the nanometre scale. Emerging evidence suggests γH2AX and 53BP1 foci may be sub-divided in functional or structural domains.

The working hypothesis of this chapter is the following:

- Super-resolution (SR) microscopy techniques can be employed to gain further insights into the fine structure, formation and spatial distribution of γH2AX and 53BP1 foci following low-LET IR. Confocal imaging may underestimate the number of foci per cell.

Methods

HeLa cells were irradiated with 2 Gy low-LET X-rays, labelled with γH2AX-AlexaFluor488 and 53BP1-SiR and imaged using advanced microscopy (**Methods 2.2.17**). SR microscopy techniques with varying resolution (Airyscan, Hyvolution, STED, SIM and GSDIM) were used to compare foci yields, localisation and structure with conventional confocal or widefield microscopy. 2D images were analysed using an automated foci-counting macro (**Methods 2.2.18**). Visual checks were performed on all images after processing for quality assurance. Out-of-focus cells, incomplete nuclei and foci outside of the nucleus were not scored.

Publications for this chapter:

D'Abrantes, S. *et al.* (2017). Super-Resolution Nanoscopy Imaging Applied to DNA Double-Strand Breaks. *Radiation Research*, **189**, 19-31.

5.2 Results

5.2.1 γH2AX and 53BP1 Foci Kinetics Following X-ray IR

Initially, the formation of γH2AX and 53BP1 foci following IR exposure was investigated. The focus was on finding the peak of foci yield after IR and detecting any possible foci saturation. HeLa cells were irradiated with 2 Gy X-rays, fixed at various time-points post-IR and imaged using confocal microscopy. **Figure 5.1** shows 53BP1 and γH2AX foci kinetics, where γH2AX and 53BP1 numbers increased gradually reaching a maximum of 34 (±3) and 34 (±2) foci/cell at 30 min post-IR, followed by a decrease towards control levels by 24 h. As the 30 min time-point represented peak DSB repair, subsequent experiments were performed on cells fixed at this time post-IR. No saturation (i.e. reaching a maximum level of detectable foci due to foci overlapping) was observed over time.

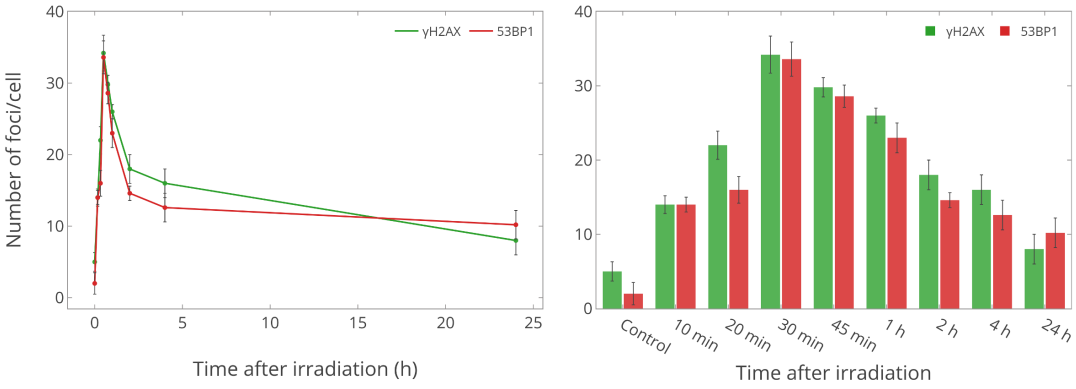

Figure 5.1: γH2AX and 53BP1 foci kinetics following X-ray exposure in HeLa cells - Line and bar graph showing the mean number of γH2AX and 53BP1 foci/cell before and after exposure to 2 Gy X-rays, imaged using confocal microscopy. Foci were counted using an automated script. Standard deviation (SD) among three independent replicates. 120 cells were scored per experiment.

5.2.2 Airyscan and Hyvolution Microscopy of γH2AX and 53BP1 Foci Following X-ray IR

To address the effect of improved optical resolution, γH2AX and 53BP1 foci structure was compared using conventional confocal and pseudo-SR Airyscan microscopy. **Figure 5.2** shows Airyscan yielded highly resolved γH2AX foci that are missing from the confocal images. A single focus identified by confocal microscopy (**Figure 5.2A**) was further resolved by Airyscan into substructures, referred to as nano-foci (**Figure 5.2B**). Fluorescence intensity profiles taken along the paths of several foci between the yellow arrows were analysed and compared. The normalised line profile in **Figure 5.2A** revealed one fluorescence maxima with a diameter (as indicated by the full-width at half maximum, FWHM, of the peak) of 1040 nm, corresponding to one morphologically regular and spatially separated γH2AX foci. In contrast, upon Airyscan microscopy (**Figure 5.2B**), the three peaks within the same area indicated the presence of three individual nano-foci with diameters of 140, 200 and 160 nm. As evident by the images, Airyscan resulted in not only improved contrast but also signal. This was observed consistently across the imaged cell population within all samples.

Next, 53BP1 foci were visualised. One 53BP1 focus in the confocal image (**Figure 5.2C**) resolved into two or potentially three individual nano-foci in the Airyscan image (**Figure 5.2D**). While there was an improvement in the signal-to-noise ratio (SNR) after Airyscan, 53BP1 nano-foci were not as well defined as γH2AX, as better γH2AX resolution and foci separation was observed. This may be explained by the Rayleigh Criterion which describes that shorter wavelengths lead to better resolution. A longer wavelength, 640 nm, was employed to image 53BP1-SiR, compared with the shorter 488 nm to visualise γH2AX-A488.

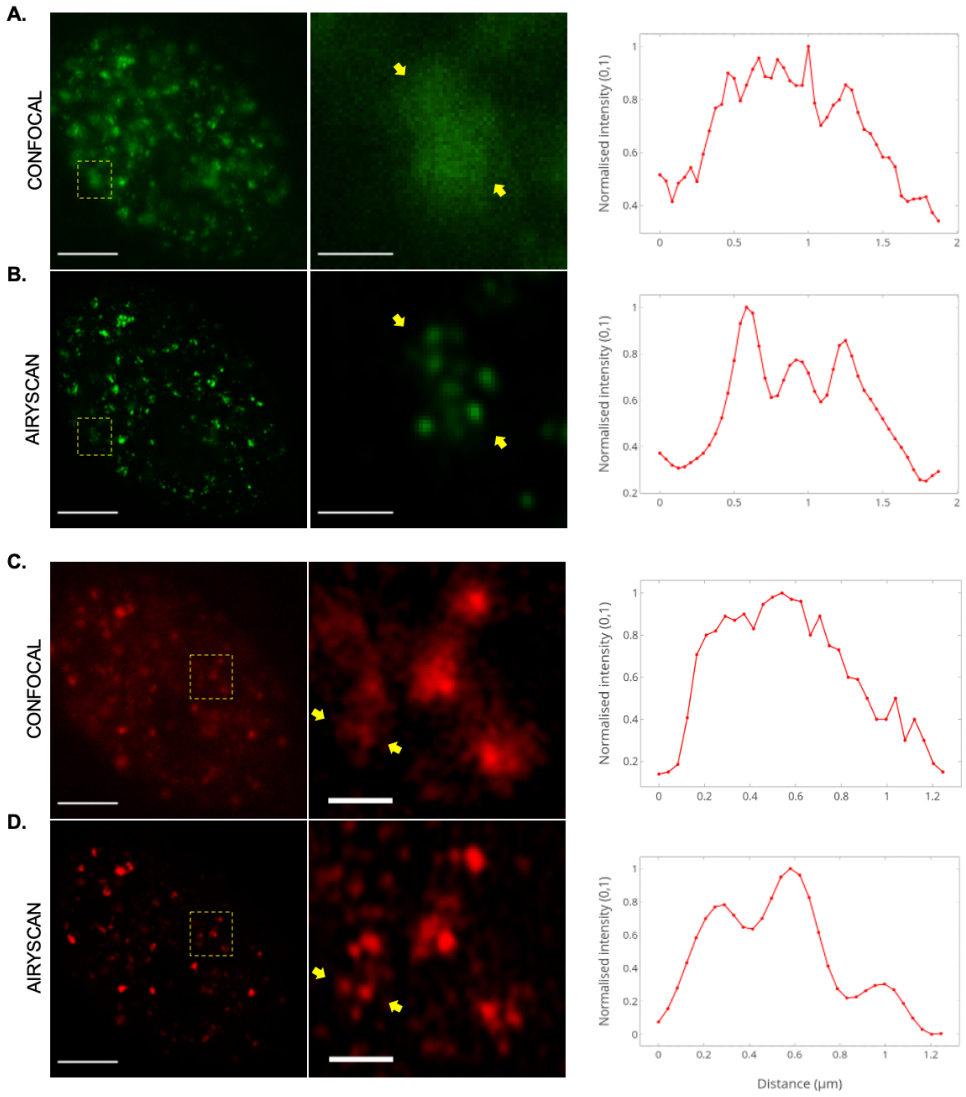

Figure 5.2: γH2AX and 53BP1 foci comparison between Airyscan and confocal microscopy - γH2AX-AlexaFluor488 foci following 2 Gy X-rays in a typical HeLa cell 30 min post-IR, imaged with **A.** confocal and **B.** Airyscan (scale bars, 5 μm). Expanded views of the yellow-boxed region (scale bar, 1 μm). Normalised line profiles taken from regions between the yellow arrows. FWHM of the confocal peak was 1040 nm, while the three Airyscan peaks were 140, 200 and 160 nm. 53BP1-SiR foci under the same conditions, imaged with **C.** confocal and **D.** Airyscan. Representative data from at least three independent experiments.

The best resolution achieved with Airyscan was ∼120 nm, 20 nm below the 140 nm resolution suggested by the manufacturer. This could be due to the 'point-like' nature of foci, as the localisation precision during the Airyscan image processing is more effective than one of an irregular shape. Airyscan is one of many techniques which uses pixel reassignment to improve resolution. Another technique is Hyvolution, explored next.

HeLa cells were irradiated with 2 Gy X-rays, labelled with γH2AX and imaged using confocal (**Figure 5.3A**) and Hyvolution (**Figure 5.3B**). Improvements in SNR and contrast of images upon Hyvolution imaging were clearly observed across all cells imaged. Individual foci were further resolved into nano-foci, as evident by the expanded view in **Figure 5.3B**. Shown in the line profiles, Hyvolution yielded foci diameters of 149 and 140 nm, while the same foci imaged with confocal resulted in diameters of 216 and 190 nm, demonstrating the improved resolution obtained. Resolution and SNR improvements were also observed with 53BP1 foci. Hyvolution images (**Figure 5.3D**) revealed several nano-foci of 180 and 270 nm, while confocal showed one large 710 nm focus (**Figure 5.3C**). As with Airyscan, 53BP1 foci were not as defined as γH2AX.

The best resolution achieved with Hyvolution was ∼140 nm (matching the manufacturer's suggested optimal resolution), similar to that obtained with Airyscan. Airyscan and Hyvolution are considered 'pseudo-SR' techniques because they provide a modest resolution improvement. As Hyvolution relies primarily on deconvolution, it is predisposed to artefacts such as striping, ringing or patterning. Therefore, critically assessing the data by using other techniques to validate the results is key, particularly when quantifying foci. Another way of identifying flaws in the deconvolved images is by visual inspection of optical aberrations, such as non-homogeneous illumination between the centre and edges of the sample.

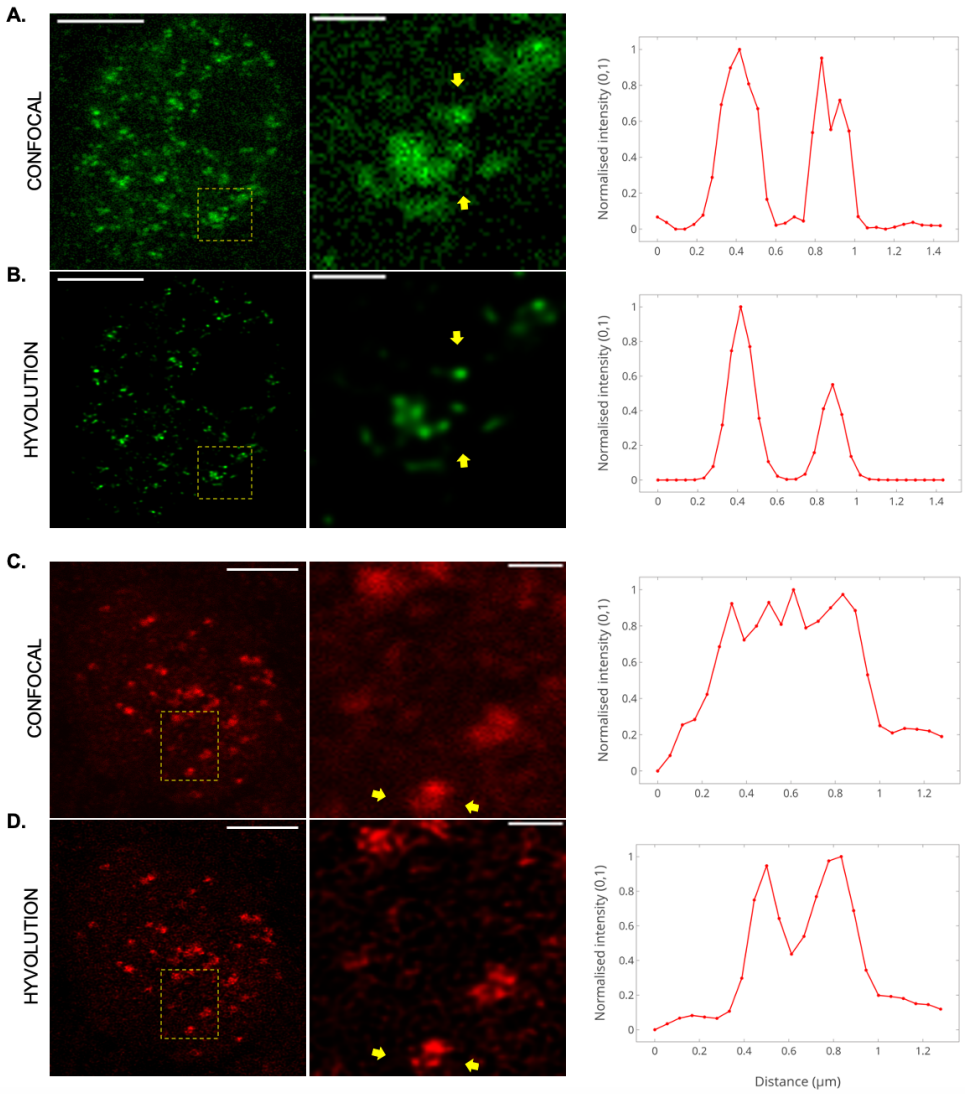

Figure 5.3: γH2AX and 53BP1 foci comparison with Hyvolution and confocal microscopy - γH2AX-AlexaFluor488 foci after 2 Gy X-rays in a typical HeLa cell 30 min post-IR, imaged with **A.** confocal and **B.** Hyvolution (scale bars, 5 μm). Confocal FWHM: 216 and 190 nm; Hyvolution FWHM: 149 and 140 nm. Expanded views of the yellow-boxed region (scale bar, 1 μm). Normalised line profiles taken from regions between the yellow arrows. 53BP1-SiR foci under the same conditions, imaged with **C.** confocal and **D.** Hyvolution. Confocal FWHM: 710 nm; Hyvolution FWHM: 180 and 270 nm. Representative data from three independent experiments.

5.2.3 STED Microscopy of γH2AX and 53BP1 Foci After X-ray IR

Airyscan and Hyvolution microscopy provided a modest improvement in resolution, but not enough to investigate the fine structure of γH2AX and 53BP1 foci. To gauge the actual morphological foci characteristics, STED microscopy was employed next.

HeLa cells were irradiated with 2 Gy X-rays, fixed 30 min post-IR, labelled with γH2AX and imaged using confocal (**Figure 5.4A**) and STED microscopy (**Figure 5.4B**). **Figures 5.4A-B** show γH2AX foci further resolved into an average of three to four nano-foci, with as many as seven in some cases. Some simply looked smaller and did not resolve into additional nano-foci. As shown by the line profiles, one γH2AX focus with a 260 nm diameter using confocal resolved into two nano-foci of 80 and 70 nm diameters with STED. Interestingly, the increase in optical resolution by a factor of two to three with STED led to the detection of more than six nano-foci within each focus in many instances.

Next, 53BP1 foci were evaluated. Due to the lesser resolution obtained with SiR, 53BP1 was analysed with AlexaFluor488 rather than SiR. As shown in **Figures 5.4C-D**, most 53BP1 foci resolved to smaller punctuates rather than multiple foci. This suggests that the use of SR (instead of confocal) to quantify foci may be more useful when visualising γH2AX rather than 53BP1, as 53BP1 foci numbers would be less affected by underscoring. Compared with γH2AX, 53BP1-labelled nuclei had less background signal. The line profiles show one 53BP1 focus with a 295 nm diameter with confocal imaging resolved into two nano-foci of 61 and 62 nm diameters with STED.

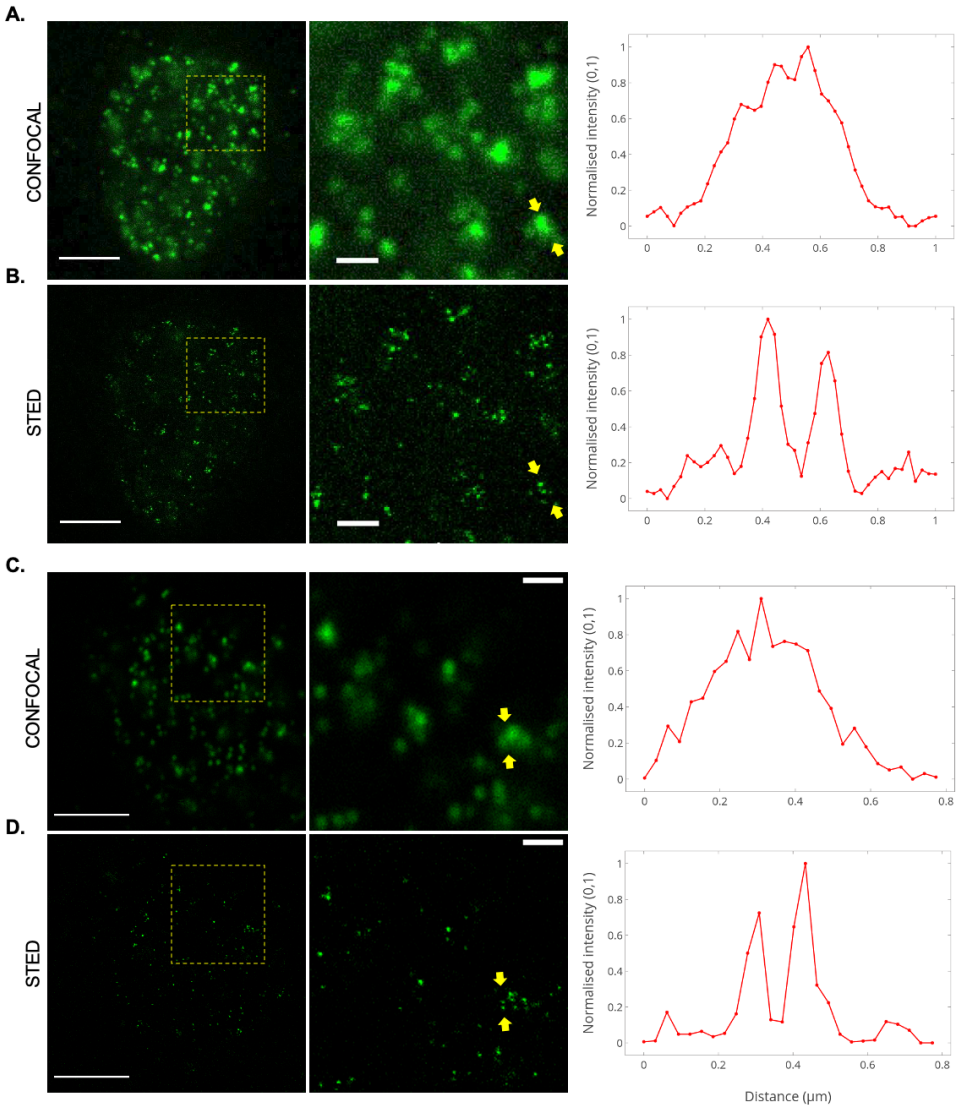

Figure 5.4: γH2AX and 53BP1 foci comparison with STED and confocal microscopy - γH2AX-AlexaFluor488 foci after 2 Gy X-rays in a typical HeLa cell 30 min post-IR, imaged with **A.** confocal and **B.** STED (scale bars, 5 μm). Confocal FWHM: 260; STED FWHM: 80 and 70 nm. Expanded views of the yellow-boxed region (scale bar, 1 μm). Normalised line profiles taken from regions between the yellow arrows. 53BP1-AlexaFluor488 foci under the same conditions, imaged with **C.** confocal and **D.** STED. Confocal FWHM: 295 nm; STED FWHM: 61 and 62 nm. Representative data from three independent experiments.

5.2.4 γH2AX and 53BP1 Foci Quantification Comparison Among Confocal, Airyscan and STED Microscopy

Next, γH2AX and 53BP1 foci were quantified at 30 min and 5 h post-IR and compared among different microscopy techniques to identify whether the improved resolution led to the detection of more foci per cell. Foci were counted using an automated ImageJ script (**Methods 2.2.18**). **Figure 5.5A** shows γH2AX kinetics in unirradiated and 2 Gy X-ray irradiated HeLa cells. A small number of foci/cell were detected in unirradiated samples with all microscopy types (3 (±2) after confocal, 4 (±3) after Airyscan and 15 (±9) after STED). Foci yields increased quickly 30 min after irradiation reaching 47 (±11) foci/cell with confocal, 57 (±10) after Airyscan and 221 (±33) following STED imaging. Thus, for every γH2AX focus detected with confocal, 1.2 nano-foci were detected with Airyscan and 4.7 nano-foci with STED. This can be visualised on **Figure 5.5B**, where upon imaging the same field of view of the sample, foci were clearly resolved into smaller nano-foci after STED imaging. These same ratios were also observed for the control samples, where the foci observed were likely due to replication processes. As shown in **Figure 5.5A**, γH2AX foci numbers decreased 5h post-IR to 13 (±5) with confocal, 16 (±4) with Airyscan and 55 (±8) with STED. All three samples showed a ∼70% reduction from the 30 min time-point.

Similar results were also observed with 53BP1 foci. As observed in **Figure 5.5C**, few foci were detected in the unirradiated control samples, namely 2 (±1) after confocal, 3 (±2) after Airyscan and 8 (±8) after STED. An increase in foci was observed 30 min post-IR to 48 (±8) with confocal, 55 (±15) with Airyscan and 209 (±61) with STED. For every 53BP1 focus identified with confocal, 1.2 nano-foci were detected with Airyscan and 4.4 nano-foci with STED. This can be clearly visualised in **Figure 5.5D**,

where several nano-foci identified with STED were missing on the confocal image. At 5h post-IR, a ∼70% decrease in 53BP1 foci was measured with confocal and Airyscan, while an 85% reduction was detected using STED (14 (±5) with confocal, 16 (±7) with Airyscan and 31 (±11) with STED). In contrast to γH2AX, the confocal:STED foci ratio observed at 30 min (4.4) was higher than at 5 h post-IR (2.2), indicating that 53BP1 foci did not resolve as well at later time-points. This could be due to the diminished fluorescence intensity or foci size not being sufficient enough to allow acceptable SR. As this was not seen with γH2AX foci, it is possible that the secondary antibody also influenced this observation. Alternatively, this could also be explained by differences in the rates of removal of 53BP1 and γH2AX.

Higher standard deviations were obtained from 53BP1-labelled samples. This was caused by higher background, as well as the non-uniform distribution and morphology of 53BP1 (visualised in **Figure 5.5D**). Unlike γH2AX, 53BP1 foci appeared more elongated and less well defined, presenting challenges when measuring foci yields.

Overall, confocal and Airyscan imaging underestimate the number of foci/cell by a factor of four to five when compared with STED.

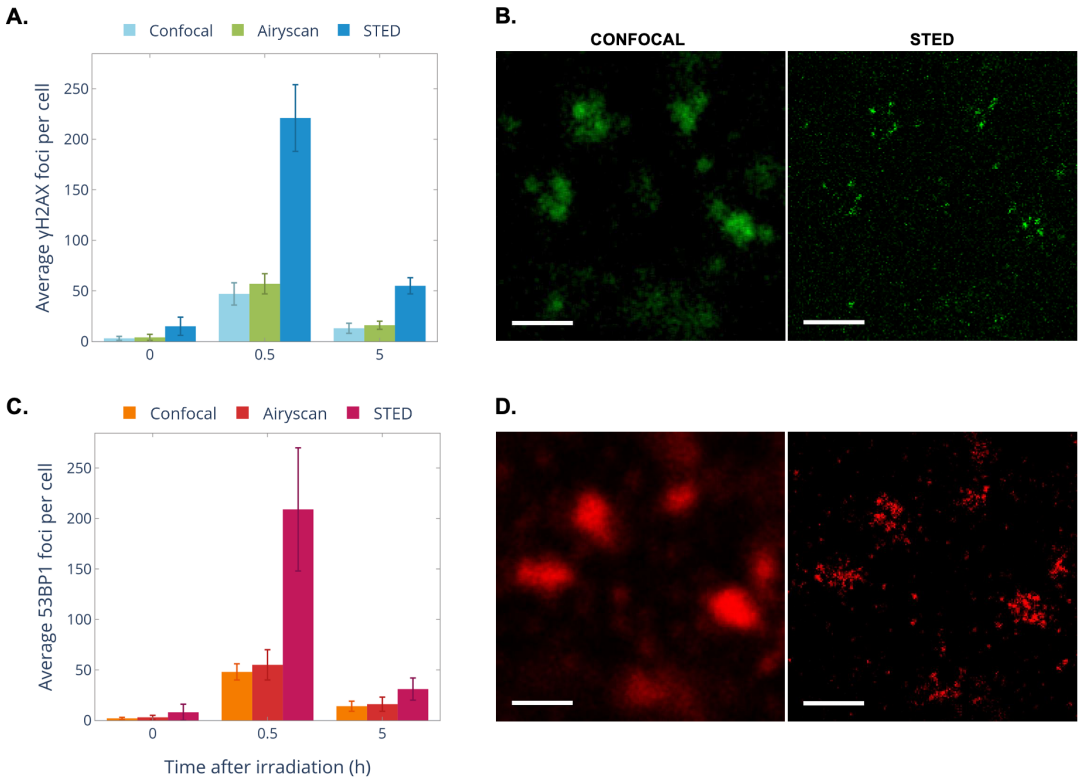

Figure 5.5: γH2AX and 53BP1 foci quantification following X-ray IR compared using confocal, Airyscan and STED microscopy - **A.** Bar chart showing the average number of γH2AX foci/cell before (0) and after (30 min and 5h) 2 Gy X-ray IR. **B.** γH2AX-AlexaFluor488 foci in a typical HeLa cell imaged with confocal and STED (scale bars, 1 μm). **C.** Bar chart showing the average number of 53BP1 foci/cell before and after IR. **D.** 53BP1-SiR foci in a typical cell imaged with confocal and STED (scale bars, 1 μm). SD among three independent replicates. >34 images were collected from each time-point.

5.2.5 γH2AX and 53BP1 Colocalisation Comparison Between Confocal and STED Microscopy

Differences in foci quantification after confocal and STED imaging sparked questions about whether their colocalisation would also be influenced by resolution. Consequently, the overlap between γH2AX and 53BP1 at 30 min post-IR was assessed in HeLa cells and compared between confocal and STED microscopy. Confocal data in **Figure 5.6A** shows colocalisation between γH2AX and 53BP1 as evident by the overlay of green and red fluorescence that appear yellow. In contrast, lack of yellow areas in the STED image in **Figure 5.6B** reveal that the foci were spatially separated.

To statistically quantify the differences in colocalisation between the two imaging techniques, both Pearson's and Mander's coefficients were measured, assessing both correlation and co-occurrence (Adler *et al.*, 2010). Mander's overlap coefficients M1 and M2 analyse how much signal from the green channel overlaps with signal from the red channel. High co-occurrence is indicated by M1 and M2 having a similar value, both higher than 0.5. Low co-occurrence is reflected by a high (>0.5) M1 and a low (<0.5) M2 value, or vice versa. Meanwhile, Pearson's correlation coefficient (PCC) measures the linear correlation within pixels containing both red and green signal, where a +1 value indicates high correlation between two molecules, 0 suggests no correlation and -1 indicates an inverse correlation. As shown in **Figure 5.6Ai**, PCC measurements using confocal microscopy revealed a median of 0.33, IQR (interquartile range) of 0.23 (Q3=0.52 and Q1=0.30) and average of 0.42. The median and average indicated a moderately strong correlation, while the IQR and maximum value (0.675) revealed many areas of strong correlation. M1 and M2 median values (0.58 and 0.78, respectively) were both higher than 0.5, indicating strong co-occurrence. In contrast, **Figure 5.6Bi**

shows that STED imaging resulted in a PCC median of -0.01, IQR of 0.18 (Q3=0.12 and Q1=-0.06) and average of 0.02. All PCC measures indicate very weak or no correlation. A high M1 and low M2 median value (0.07 and 0.86, respectively) indicate poor co-occurrence. Overall, some γH2AX and 53BP1 foci colocalise when imaged using confocal, while they show weak or no colocalisation when imaged with SR STED.

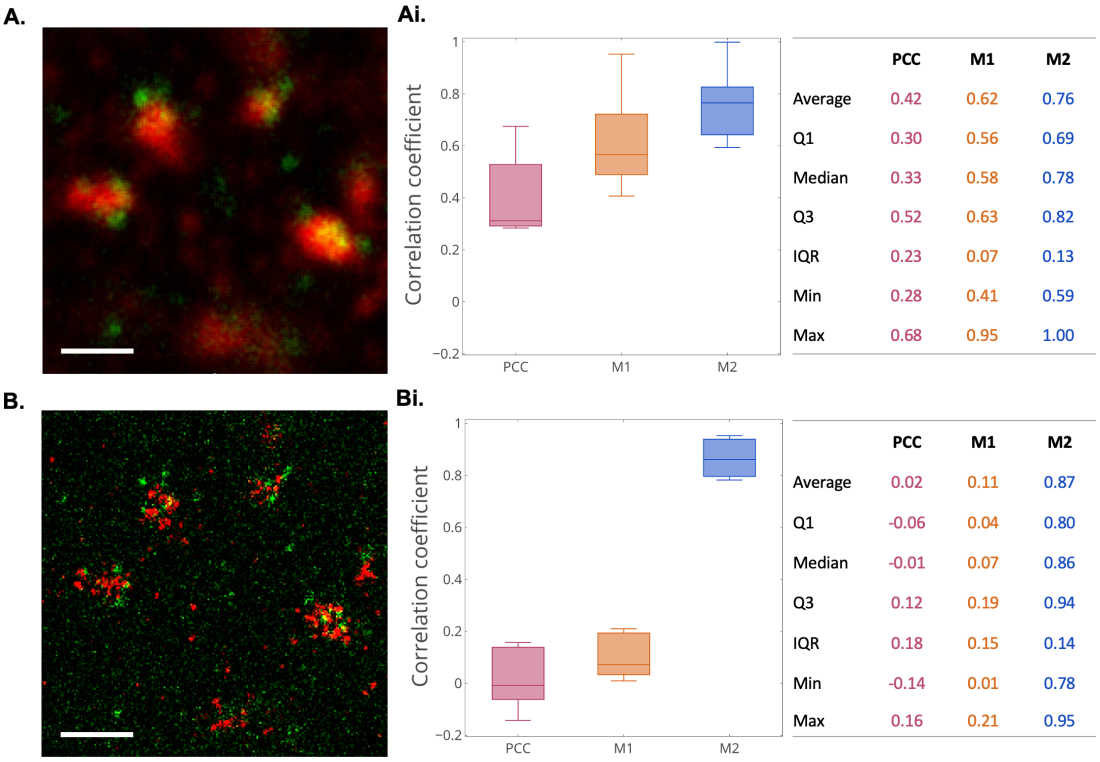

	PCC	M1	M2
Average	0.42	0.62	0.76
Q1	0.30	0.56	0.69
Median	0.33	0.58	0.78
Q3	0.52	0.63	0.82
IQR	0.23	0.07	0.13
Min	0.28	0.41	0.59
Max	0.68	0.95	1.00

	PCC	M1	M2
Average	0.02	0.11	0.87
Q1	-0.06	0.04	0.80
Median	-0.01	0.07	0.86
Q3	0.12	0.19	0.94
IQR	0.18	0.15	0.14
Min	-0.14	0.01	0.78
Max	0.16	0.21	0.95

Figure 5.6: γH2AX and 53BP1 colocalisation following X-rays compared using confocal and STED microscopy - 53BP1-SiR and γH2AX-AlexaFluor488 colocalisation in 2 Gy X-ray irradiated HeLa cells, fixed 30 min post-IR and imaged with **A.** confocal and **B.** STED (scales bar, 1 μm). **Ai**/**Bi**. Box plots showing the quantified colocalisation of γH2AX and 53BP1 foci by PCC, M1 and M2 after confocal (**Ai**) and STED (**Bi**) microscopy. Individual statistics for the average, Q1, median, Q3, IQR, Min and Max shown. Data from 30 images from three independent experiments.

5.2.6 SIM of γH2AX and 53BP1 Foci Following X-ray IR

To address the effect of improved optical resolution using SIM, γH2AX and 53BP1 foci structure was compared to widefield microscopy. Unlike Airyscan and STED, which are confocal-based, SIM relies on a widefield set-up (see **Introduction section 1.5**). HeLa cells were irradiated with 2 Gy X-rays, fixed 30 min post-IR and imaged using widefield and SIM microscopy. **Figures 5.7A-B** shows SIM yielded highly resolved γH2AX nano-foci that are missing from the widefield image. The line profile in **Figure 5.7A** reveals one fluorescence maxima with a diameter of 290 nm, corresponding to one large γH2AX foci. In contrast, upon SIM (**Figure 5.7B**), a smaller peak within the same area indicates an improvement in resolution down to 112 nm. As expected, the best resolution achieved with SIM was a ∼2-fold improvement from widefield.

Next, 53BP1 foci were analysed. **Figures 5.7C-D** shows 53BP1 foci in the widefield image were resolved into smaller nano-foci in the SIM images. In line with Airyscan and Hyvolution, 53BP1 nano-foci were not as well defined as γH2AX. Line profiles revealed one large focus with widefield (**Figure 5.7C**) of diameter 560 nm resolved into three smaller nano-foci of 215 and 185 nm with SIM (**Figure 5.7D**).

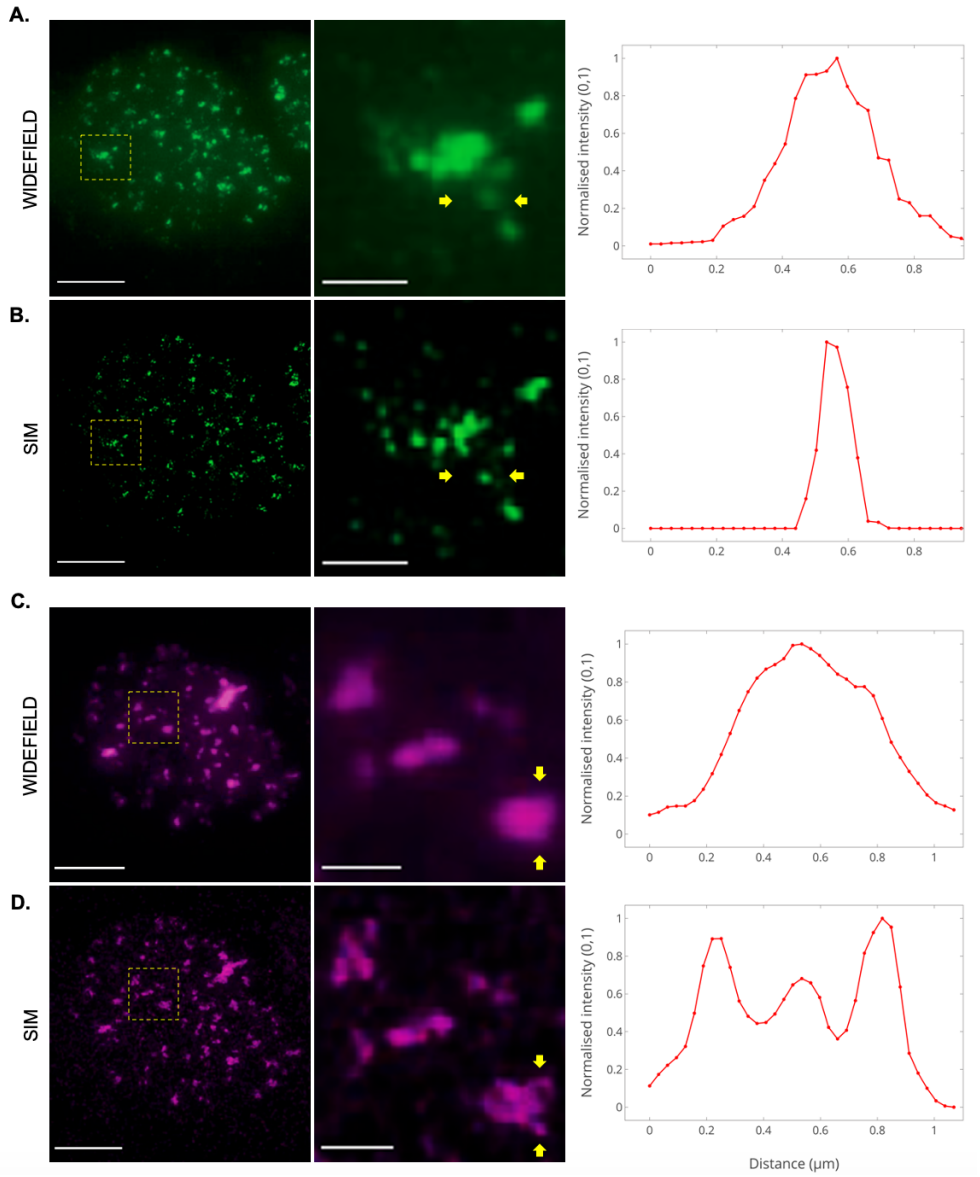

Figure 5.7: γH2AX and 53BP1 foci comparison with SIM and widefield microscopy - γH2AX-AlexaFluor488 foci after 2 Gy X-rays in a typical HeLa cell 30 min post-IR, imaged with **A.** widefield and **B.** SIM (scale bars, 5 μm). Widefield FWHM: 290 nm; SIM FWHM: 112 nm. Expanded views of the yellow-boxed region (scale bar, 1 μm). Normalised line profiles taken from regions between the yellow arrows. 53BP1-SiR foci under the same conditions, imaged with **C.** widefield and **D.** SIM. Widefield FWHM: 560 nm; SIM FWHM: 215 and 185 nm. Representative data from two independent experiments.

5.2.7 GSDIM of γH2AX and 53BP1 Foci Following X-ray IR

Lastly, to address the effect of using single-molecule localisation imaging with the best lateral resolution among optical methods, γH2AX and 53BP1 foci structure were investigated using GSDIM and compared to widefield microscopy. Like SIM, GSDIM relies on a widefield set-up. HeLa cells were irradiated with 2 Gy X-rays, fixed 30 min post-IR and imaged using widefield and GSDIM microscopy. **Figures 5.8A-B** show GSDIM yielded the best γH2AX foci resolution, with a FWHM of 49 and 44 nm, while the widefield image of the same area showed one large foci of 302 nm diameter.

At the time of this investigation, GSDIM was only available with a single channel, thus γH2AX and 53BP1 were both labelled with secondary antibody AlexaFluor488 and imaged separately. **Figures 5.8C-D** show 53BP1 foci in the widefield image resolved into several smaller nano-foci in the GSDIM images. Line profiles revealed two large foci in the widefield image of 183 nm and 302 nm diameter (**Figure 5.8C**). These resolved into three significantly smaller nano-foci of 35 nm, 34 nm and 40 nm diameter with GSDIM (**Figure 5.8D**). A very small area was selected for the close-up images, resulting in pixelated widefield images.

The best resolution achieved with GSDIM, and overall in this study, was ∼35 nm. Interestingly, this was achieved with 53BP1 foci. Unlike Airyscan, STED and SIM (which show larger diameters for SiR-tagged 53BP1 foci), AlexaFluor488-tagged 53BP1 yielded better resolutions than γH2AX with GSDIM. This highlights the importance of using secondary antibodies with shorter excitation and emission wavelengths (such as blue AlexaFluor405 or green AlexaFluor488) for SR imaging.

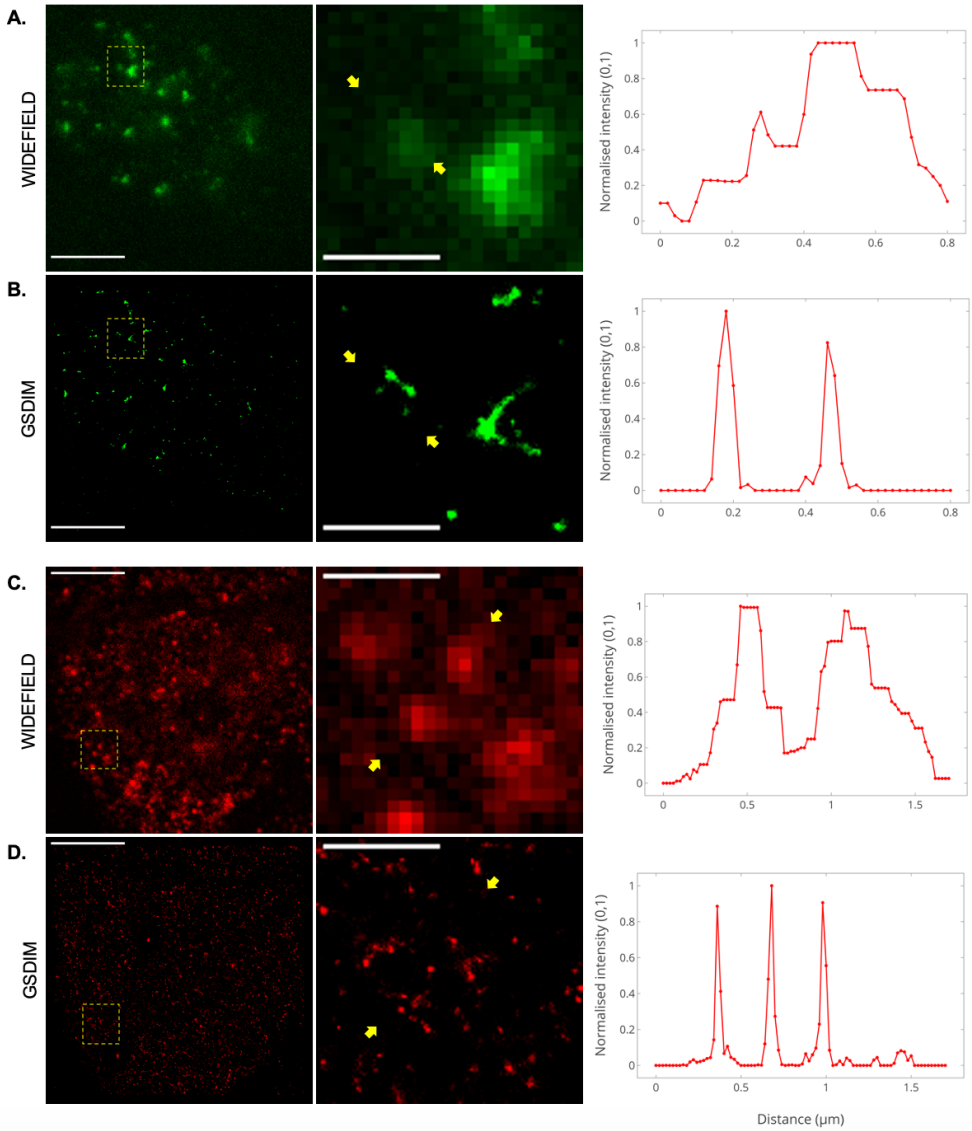

Figure 5.8: γH2AX and 53BP1 foci comparison between GSDIM and widefield microscopy - γH2AX-AlexaFluor488 foci after 2 Gy X-rays in a typical HeLa cell 30 min post-IR, imaged with **A.** widefield and **B.** GSDIM (scale bars, 5 μm). Widefield FWHM: 302 nm; GSDIM FWHM: 49 and 44 nm. Expanded views of the yellow-boxed region (scale bar, 1 μm). Normalised line profiles taken from regions between the yellow arrows. 53BP1-SiR foci under the same conditions, imaged with **C.** widefield and **D.** GSDIM. Widefield FWHM: 183 and 302 nm; GSDIM FWHM: 35, 34 and 40 nm. Representative data from one independent experiment.

5.3 Discussion

Super-resolution microscopy reveals insight into foci substructure

This is the first study to use a variety of SR methods to enable the identification of the elementary structural units of two key DSB signalling and repair proteins, γH2AX and 53BP1, following IR exposure. Confocal microscopy did not provide enough resolution to investigate their structure. While GSDIM yielded the best resolution ($\sim$35 nm, a $\sim$10-fold improvement compared to widefield), this complex SR technique comes with many challenges. For example, very high laser powers are required (leading to phototoxicity, making it generally incompatible with live-cell imaging), specialised fluorophores and buffers are needed, image acquisition takes many hours, the algorithmic processing can lead to artefacts and the interpretation of the often-surprising results can be difficult (Van De Linde *et al.*, 2011a,b). These peculiarities mean it is not widely employed and only available in specialist imaging facilities. A small number of groups have recently used other single molecule localisation microscopy (SMLM) techniques to investigate DNA repair proteins, offering key insights into the deep structure of foci and how this relates to chromatin conformational changes on the nanoscale (Hausmann *et al.*, 2018; Varga *et al.*, 2019). These studies are in agreement with the data presented here whereby a repair focus is made up of nano-foci and SMLM is well-suited for investigating foci structure.

STED microscopy yielded a large $\sim$4-fold resolution improvement (down to $\sim$60 nm), without most of the major drawbacks of GSDIM. However, STED suffers from reliability issues as the equipment is hard to maintain and laser alignment is susceptible to temperature fluctuations. SIM has the advantages of being live-cell compatible and

working with any fluorophore. However, it requires specialised optical components (making the equipment expensive and specialist) and is artefact prone, while able to only double resolution. Additionally, SIM needs the acquisition of 3-9 images to reconstruct a SR image, making it slow and thus suboptimal for some live cell experiments. In comparison, Airyscan yielded a similar resolution to SIM (∼140 nm) while being more user friendly, widely accessible and costing significantly less.

Due to the many challenges associated with GSDIM (outlined above), only 5 cells were imaged, and the experiment was not repeated. Thus, further quantitative evaluation of foci, such as number of foci/cell, colocalisation and spatial density variation, was not possible. With more time available, these measurements would improve the current data. Additionally, due to limited availability of the equipment, SIM experiments were performed only twice. Thus, SIM and GSDIM experiments would benefit from more repeats.

The nano-foci observed with high- and super-resolution microscopy could be additional foci undetected by (resolution-limited) widefield or confocal, or it could reveal the substructure of one focus. The number of foci observed with STED (∼221) far exceeded the expected number of DSBs (60-80 DSBs/2 Gy X-rays). Additionally, the nano-foci were observed in highly clustered areas where the confocal foci were observed, rather than being randomly distributed throughout the nucleus. This suggests that the nano-foci are likely part of the substructure of foci. In future studies, this could be further investigated by assessing how foci quantification varies with dose. If the nano-foci were substructure, reducing the dose should not have much effect. However, if the nano-foci were due to resolution, then the number of nano-foci would be expected to fall.

In agreement with previous studies, STED revealed that γH2AX and 53BP1 nano-foci have different morphologies (Ochs *et al.*, 2019; Reindl *et al.*, 2015, 2017). The γH2AX nano-foci sizes and features observed with GSDIM were in line with other SR investigations (Perez *et al.*, 2016), and were in the order of nucleosomes. It is possible that these nano-foci represent the local chromatin structure at DSB sites. The chromosome-territory-interchromatin-compartment model, CT-IC, (Cremer *et al.*, 2001) suggests that higher-order chromatin structures are built from small loops with interchromatin space in between (Visser *et al.*, 2000). This model could explain the gaps observed between individual nano-foci. Additionally, this would support the accumulating evidence demonstrating that each γH2AX nano-focus represents a chromatin loop (Bewersdorf *et al.*, 2006; Natale *et al.*, 2017; Perez *et al.*, 2016; Varga *et al.*, 2019), also supported by modelling studies (Tommasino *et al.*, 2015).

γH2AX foci quantification allows the investigation of radiation-induced DSBs in the low dose range down to mGy (Rothkamm *et al.*, 2009), as well as up to doses of several Gy (Costes *et al.*, 2006, 2010). Foci yield has been shown to change linearly with radiation dose delivered to a cell in the low dose range (Costes *et al.*, 2010), but is highly dependent on the cell type used (Asaithamby *et al.*, 2009). Some studies have shown a loss of detection with increasing dose due to foci overlapping above 1 Gy (Costes *et al.*, 2006, 2010). In contrast, others have shown linearity in γH2AX foci with dose up to 2 Gy (Barbieri *et al.*, 2019), 4 Gy (Avondoglio *et al.*, 2009; Corre *et al.*, 2010; Mahrhofer *et al.*, 2006) and even 20 Gy (Tommasino *et al.*, 2015). Thus, the 2 Gy used in this study could have resulted in some foci overlapping and saturation, however this was not visually observed in any of the analysed images. The use of SR techniques should result in extending the linearity to higher doses. Future studies are

warranted to investigate this with a dose response involving high doses and quantifying foci with SR.

The foci frequency reached a maximum of ∼30 foci/nucleus/Gy approximately ∼30 min after exposure to X-rays, in agreement with previous studies in several human cell lines for both γH2AX (Costes *et al.*, 2007; Leatherbarrow *et al.*, 2006; Wilson *et al.*, 2010) and 53BP1 foci (Costes *et al.*, 2007; Schultz *et al.*, 2000). The exact delay is known to be dependent on cell type and experimental protocols (Rothkamm *et al.*, 2009). Similar delays have also been observed with other techniques such as flow cytometry (Macphail *et al.*, 2003). In contrast, these delays are not observed with PFGE, as 25-35 DSB/Gy are detected immediately following IR (Stenerlöw *et al.*, 2003; Wang *et al.*, 2001). PFGE studies suggest a repair half-time of ∼20 min (Iliakis *et al.*, 2004). Consequently, some DSBs may have already been repaired before the foci yield was measured at 30 min. One explanation for the differences between PFGE and foci formation kinetics could be the inability of microscope techniques to detect small foci with low signal at early time-points.

There is some evidence that γH2AX is an indicator of other lesions other than DSBs, as seen from spontaneous foci found in non-irradiated normal cells (Cleaver *et al.*, 2011; Costes *et al.*, 2010; De Feraudy *et al.*, 2010; McManus *et al.*, 2005; Pankotai *et al.*, 2009; Pospelova *et al.*, 2009). This is why in addition to γH2AX, 53BP1 was also analysed as part of this study to visualise DSBs. Other techniques such as neutral filter elution or PFGE require high doses to detect significant effects (Löbrich *et al.*, 1996). Methods such as flow cytometry do not allow the direct investigation of DSBs/cell, but rather a sum of signal from all cells analysed (Kataoka *et al.*, 2006).

Another important aspect of these experiments is the temperature during irradiation. The samples were placed on ice during the irradiations to halt repair. However, the temperature may have been high enough to allow some repair during the irradiation as well as during sample transport back to the laboratory for processing. These may have altered the foci yields, particularly as the samples were fixed soon after IR (30 min).

It is crucial to exclude staining artefacts from immunofluorescence. All antibodies used were monoclonal IgG antibodies of the same size and varying antigen binding sites, with an average diameter of ∼16 nm (Harris *et al.*, 1997). The localisation precision of GSDIM is ∼12 nm (Sisario *et al.*, 2018), thus it was possible to conclude that the ∼40 nm size of the nano-foci was not due to the artefacts. False-positives may have occurred due to antibody aggregates and non-specific staining (Barnard *et al.*, 2013). However, careful optimisation of staining conditions and visual checks were performed to distinguish staining artefacts based on their morphology. In future studies, artefacts could be identified using software, such as the recently developed NanoJ-SQUIRREL, which generates a quality score and quantitative map of SR defects (Culley *et al.*, 2018).

Confocal imaging significantly underestimates the number of foci per cell

The SR findings in this work challenge the idea that one γH2AX focus represents one DSB. This is likely to have consequences for the interpretation of radiation biology data, as γH2AX immunofluorescence assays have become the standard method for DSB detection given its sensitivity to low radiation doses (Deniz *et al.*, 2016; Fernandez-Capetillo *et al.*, 2004; Kroeber *et al.*, 2015; Lobachevsky *et al.*, 2016; Sisario *et al.*, 2018). For example, γH2AX foci quantification has been used to aid dose measurements during radiotherapy (Sak *et al.*, 2007; Shah *et al.*, 2016; Zahnreich *et al.*, 2015) and

for radiation accidents as a way of triaging people (Barnard *et al.*, 2015; Garty *et al.*, 2011; Redon *et al.*, 2010), as well as for the risk of IR exposure during clinical scans (Beels *et al.*, 1903; Kuefner *et al.*, 2009, 2010; Löbrich *et al.*, 2005; Redon *et al.*, 2011). As summarised in **Table 2** below, experiments have shown that standard widefield or confocal microscopy significantly underestimated the number of foci by a factor of 2-5, thus also underestimating the underlying DNA damage induced. Consequently, the given radiation dose against foci formed may be incorrectly scored. This is particularly important in the case of high-LET radiation where complex lesions result in bigger foci within particle tracks (Costes *et al.*, 2006). Further investigations are required to evaluate the relationship between dose and foci quantification using SR following low- and high-LET radiation.

	Time (h)	**Confocal - ∼250 nm**	**Airyscan - ∼120 nm**	**STED - ∼60 nm**
γH2AX	0	3 ±2	4 ±3	15 ±9
	0.5	47 ±11	57 ±10	221 ±33
	5	13 ±5	16 ±4	55 ±8
53BP1	0	2 ±1	3 ±2	8 ±8
	0.5	48 ±8	55 ±15	209 ±61
	5	14 ±5	16 ±7	31 ±11

Table 2: Comparison table of foci yields for different imaging techniques.

The quantification of IR-induced foci requires large samples for statistical robustness. Thus, the automation of systems to count foci is critical for these types of experiments. The use of an automated methods provides not only time savings but also a robust and objective measure (Schneider *et al.*, 2019). Manual counting has been shown to be prone to inaccuracies and biases, yield low throughput and vary between different operators

(Böcker *et al.*, 2006; Feng *et al.*, 2017; Lapytsko *et al.*, 2015). On the other hand, the number foci identified by automated scripts is dependent on the scoring criteria and may result in differences in foci yields. The ImageJ script developed to quantify foci for this study relied on specific criteria that determined what was considered a focus. The script was calibrated by comparing the results with foci yields scored by eye. While scoring by eye may be subjective, it was done to minimise errors in the recognition and counting of foci related to the script. The robustness of the criteria is affected by sample labelling and image acquisition, thus it was crucial to keep all sample and imaging parameters the same (Ronneberger *et al.*, 2008). While the absolute number of foci may vary with scoring criteria, as the same criteria was used across all samples, the general trends remained the same. One way to improve the consistency of foci analysis across different data-sets may be the training of supervised machine learning algorithms (Herbert *et al.*, 2014; Sommer *et al.*, 2013).

This study aimed to show the differences in foci yield between techniques of varying resolution in 2D. The use of 2D imaging may have underestimated foci yields as only a portion of the damage was in focus during image acquisition, and thus did not reflect the 3D nature of the samples (Bolte *et al.*, 2006). Direct visualisation of the 3D distribution of foci within the cell nucleus could provide novel insights into the spatial organisation and function of γH2AX and 53BP1 (Desai *et al.*, 2005; Hernández *et al.*, 2013). Most techniques discussed here provided high lateral (x-y) resolution. However, all techniques were limited by poor axial (z) resolution, thus investigations in 3D were not possible. Recent advances in 3D STED (Velasco *et al.*, 2019; Zdańkowski *et al.*, 2020) show promise for conducting future studies. The data presented is also limited by the use of one cell line and fixed samples. Further studies are warranted to investigate foci

structure and colocalisation with SR in living cells, as well as in more detail using normal cell lines and 3D cell spheroids. Techniques such as the recently developed lightsheet localisation microscopy enable imaging of large 3D samples with ∼75 nm lateral resolution (Lu *et al.*, 2019), offering promise for SR studies.

The results shown for the overall number of foci are averages from cell samples that were not synchronised to a specific cell cycle phase. Endogenous signals observed in the control samples in **Figure 5.5** can be attributed to DSBs produced at stalled and collapsed replication forks commonly observed in cancer cell lines (Halazonetis *et al.*, 2008; Tsantoulis *et al.*, 2008). The remaining foci observed 5 h post-IR, also in **Figure 5.5**, could be replication-induced due to the enhanced presence of background foci during S-phase of the cell cycle (Costes *et al.*, 2006; Marková *et al.*, 2007). Another possible explanation is the processing of non-DSB lesions into DSBs (Gulston *et al.*, 2004). This study primarily focused on investigating the relative differences in foci quantification among microscopy techniques of varying lateral resolution. Others have shown the importance of the cell cycle when detecting foci (Bauerschmidt *et al.*, 2009; Rothkamm *et al.*, 2003), due to differences in DNA content (Wardman *et al.*, 2007). Thus, future studies are needed to take the cell cycle into account by performing FACS analysis or using synchronised cells.

Confocal imaging overestimates the colocalisation of γH2AX and 53BP1

Colocalisation data between γH2AX and 53BP1 showed that foci mostly colocalise when imaged using confocal, while they show weak colocalisation when imaged with SR microscopy. Previous studies using confocal microscopy have also shown colocalisation of these two proteins in CHO cells, human fibroblasts and lymphocytes (Croco *et al.*,

2017; De Feraudy *et al.*, 2010; Holcomb *et al.*, 2008; Horn *et al.*, 2011; Manders *et al.*, 1992). Since this study, others have proposed a lack of γH2AX-53BP1 foci colocalisation at the nanoscale using STED (Reindl *et al.*, 2017) and SMLM (Depes *et al.*, 2018). One proposed explanation and model is that γH2AX labels dense chromatin territories while instead 53BP1 is situated within the perichromatin region and interchromatin compartment around the DSB (Reindl *et al.*, 2017). This is in agreement with the CT-IC model previously described.

It has previously been shown that the repair of multiple DSBs does not occur at the damage site, but rather get relocated to 'repair centres', represented as one large γH2AX focus (Neumaier *et al.*, 2012). If 53BP1 labelled part but not all of this repair centre, it could explain why 53BP1 and γH2AX colocalised with confocal but not SR. Consequently, the spatial distribution of foci relative to each other may be better understood using SR and raises questions about performing localisation studies with confocal microscopy alone. This is likely to be important when attempting to resolve foci following high-LET radiation, where the foci are clustered together along the narrow path of these particles. Colocalisation data between DSB (γH2AX) and non-DSB (OGG1) foci presented in **Chapter 3** showed increased colocalisation after high-LET IR. Additionally, recent SR studies have shown IR-induced foci had different morphological characteristics with varying LET (Oike *et al.*, 2016; Reindl *et al.*, 2017). Thus, further work is needed to compare the differences in foci structure and colocalisation with SR techniques after high-LET IR.

This colocalisation study was performed using the same approach as described in **Chapter 3**, thus the limitations and future improvements outlined in that chapter apply here too. For example, colocalisation measurements were performed on fixed cells. An im-

proved approach would involve using single-molecule FRET (Selvin *et al.*, 2008; Weiss, 2000), where the physical interaction of individually labelled proteins (rather than their colocalisation) can be evaluated in living cells with ∼10 nm resolution (Murakoshi *et al.*, 2004; Sakon *et al.*, 2010). Reporting of FRET combined with FLIM (see **Chapter 4**) would provide an even more robust readout. This is because unlike intensity-based methods, FRET-FLIM analysis reports specifically on the changes in donor lifetime pixel-by-pixel, independent from noise and background contributions. Single-molecule FRET has been recently used to investigate the interactions of nuclear proteins with chromatin (Basu *et al.*, 2018), as well as the dynamic interactions between two nucleosomes (Lee *et al.*, 2011).

5.4 Conclusion

In conclusion, confocal imaging alone may significantly underestimate the number of foci by a factor of 2-5, as each focus was further resolved into smaller nano-foci when using SR. Colocalisation studies revealed that the spatial distribution of foci may be best understood using SR techniques, as γH2AX and 53BP1 foci did not colocalise at the SR level of <100 nm (while they do show colocalisation at the confocal level ∼300 nm). While standard techniques enable the study of relative variations in foci yields following IR, SR offers greater precision for foci quantification and the interpretation of associated radiation biology. From a technical point of view, SR was demonstrated to be well suited for measuring the fine structure and localisation of chromatin-associated proteins in great detail, with a resolution well below 100 nm. Revealing deeper insights into the organisation and structure of DNA repair proteins following IR contributes to our understanding of cancer radiotherapy.

Chapter 6

Overall Discussion

This body of research has focused on three main areas, including (1) assessing if previously identified proteins can be observed as foci at sites of DNA damage following IR exposure, (2) determining if Ku70 and Ku80 interact in living cells in the presence and absence of DNA damage, and (3) evaluating if super-resolution microscopy is better suited for measuring the yield and localisation of IR-induced foci compared to standard confocal microscopy. The overall aim was to contribute to the understanding of the underlying mechanisms of DNA repair following radiation, and in particular, how this varies with radiation quality, using microscopy methods that would retain the physiological environment of mammalian cells.

Clustered DNA damage, CDD, is a key product of IR exposure with the complexity of clustered damage sites increasing with the ionisation density and LET of radiation (Goodhead, 1994; Nikjoo *et al.*, 1998; Ottolenghi *et al.*, 1997). CDD may be comprised of non-DSB clustered sites (containing SSBs, base lesions or AP sites (Goodhead, 1994; Ward, 1994)), as well as complex DSBs which have other types of DNA lesions in close proximity (Nikjoo *et al.*, 1998). CDD lesions are more difficult to repair than dispersed

lesions, as well as more mutagenic (Nickoloff *et al.*, 2020; Sage *et al.*, 2011; Singleton *et al.*, 2002). Mutations may arise directly at the clusters during inaccurate processing and repair, as well as indirectly as persistent non-DSB clusters may get converted into DSBs during replication, leading to repair-resistant DSBs (Allen *et al.*, 2011a; Harper *et al.*, 2010; Sage *et al.*, 2011). Thus, it is crucial to evaluate CDD induction and processing in mammalian cells. DSBs are among the most deleterious DNA lesions, as they are repaired with less fidelity, in particular DSB clusters which are more mutagenic and cytotoxic than isolated DSBs (Nickoloff *et al.*, 2020). DSB induction triggers the formation of γH2AX, and subsequent recruitment of repair protein 53BP1, which localises rapidly to DSB sites. The induction and repair of DSBs can be monitored by visualising γH2AX and 53BP1 foci formation.

While the induction of γH2AX foci has been shown to correlate with dose (Rothkamm *et al.*, 2003), there is some discrepancy in the yield, structure and kinetics of foci formation and disappearance. These kinetics also differ from those observed by other detection methods, most notably Pulse-Field Gel Electrophoresis (PFGE), which typically shows a repair half-time of $\sim$20 min for low-LET induced DSBs (Kinner *et al.*, 2008), while the peak for γH2AX foci is typically observed at $\sim$30 min. Much progress has been made in uncovering the basic IR-induced responses and mechanisms. However, due to limitations in the spatial resolution of standard microscopes, less is known about the localised IR effects at the nanometre spatial scale. This is where IR is expected to be most efficient at producing correlated damage due to spatial pattern of energy deposition, especially along the tracks of high-LET particles.

Super-resolution (SR) microscopy was employed to gain further insights into the fine structure, formation and spatial distribution of γH2AX and 53BP1 foci following low-

LET IR. Samples were visualised and quantified using several SR techniques with varying resolution (Airyscan, Hyvolution, STED, SIM and GSDIM) and compared to conventional widefield or confocal microscopy. Conventional microscopy did not provide enough resolution to investigate the structure of γH2AX and 53BP1 foci in mammalian cells (e.g. **Figure 5.4**), as additional nano-foci were observed with all SR techniques. These nano-foci were likely part of the focus substructure, in agreement with other SMLM (Hausmann *et al.*, 2018; Varga *et al.*, 2019), STED (Reindl *et al.*, 2015; Schwarz *et al.*, 2019) and SIM (Hagiwara *et al.*, 2017; Perez *et al.*, 2016) SR studies. Several experimental (Bewersdorf *et al.*, 2006; Iacovoni *et al.*, 2010; Natale *et al.*, 2017; Perez *et al.*, 2016; Varga *et al.*, 2019) and modelling (Tommasino *et al.*, 2015) studies have proposed that each γH2AX nano-focus represents a chromatin loop. Each of these loops involve ∼2 Mbp of DNA (Yokota *et al.*, 1995). γH2AX has been proposed to spread over several Mbps from the original lesion site in a non-uniform and asymmetrical manner, as assessed by chromatin immunoprecipitation (ChIP) studies (Meier *et al.*, 2007). This suggests γH2AX may also be found reasonably far from the actual DSB. Indeed, pan-nuclear phosphorylation of H2AX mediated by ATM and DNA-PKcs has been observed at CDD sites induced by heavy ion IR (Meyer *et al.*, 2013). It is then apparent not all γH2AX foci represent a DSB. Recent work comparing γH2AX foci with SIM and confocal estimated the DNA content of foci. They found γH2AX foci observed with confocal covered several Mbp while those visualised with SR spanned 40-160 kb. Using a combination of ChIP and SR techniques, they concluded γH2AX nano-foci observed with SR correspond to single chromatin loops, while foci observed with confocal reflect multiple loops (Natale *et al.*, 2017). This not only supports the findings presented across **Chapter 5**, but also validates that the results observed were not false-positives caused by antibody-induced artefacts.

The colocalisation of γH2AX and 53BP1 has been investigated by other groups using confocal microscopy (Croco *et al.*, 2017; De Feraudy *et al.*, 2010; Holcomb *et al.*, 2008; Horn *et al.*, 2011; Manders *et al.*, 1992). While this is in agreement with the data observed here with confocal, weak colocalisation was observed when imaged with SR microscopy (**Figure 5.6**). This may indicate that while γH2AX and 53BP1 are located within the same repair compartment at the micrometer scale, they have a different localisation within the compartment at the nanometre scale. Since this study was published in 2017, others have also observed a lack of γH2AX-53BP1 foci colocalisation at the nanoscale using STED (Reindl *et al.*, 2017) and SMLM (Depes *et al.*, 2018). An earlier study on 53BP1 and RAD51 foci has similarly demonstrated anti-correlation when using STED (Reindl *et al.*, 2015). This is unlikely to be due to the non-uniform expansion of γH2AX (explained above) as experiments using ChIP show γH2AX and 53BP1 spread to the same extent (∼450 kb) in mammalian cells (Meier *et al.*, 2007). One proposed explanation and model is that γH2AX labels dense chromatin domains while instead 53BP1 is situated within the perichromatin region and interchromatin compartment around the DSB (Reindl *et al.*, 2017). The arrangement of 53BP1 at the periphery has been linked to the known function of 53BP1 in antagonising the resection of DSB during repair (Panier *et al.*, 2014). These findings raise questions about using standard confocal microscopy for evaluating the localisation, morphology and function of proteins in mammalian cells.

Confocal and widefield microscopy underestimated the number of γH2AX and 53BP1 foci by a factor of 2-5, as each focus was further resolved into smaller foci when using SR (**Figures 5.5**). While these foci are likely to be part of the focus sub-structure, it will be key to investigate how the SR quantification varies with dose in future experiments, as

confocal may be underestimating the underlying DNA damage induced. Additionally, γH2AX immunofluorescence assays are routinely used for detecting DSBs due to their sensitivity to low radiation doses (Deniz *et al.*, 2016; Fernandez-Capetillo *et al.*, 2004; Kroeber *et al.*, 2015; Lobachevsky *et al.*, 2016; Sisario *et al.*, 2018), such as to aid dose measurements during radiotherapy (Sak *et al.*, 2007; Shah *et al.*, 2016; Zahnreich *et al.*, 2015) and for triaging people after radiation accidents (Barnard *et al.*, 2015; Garty *et al.*, 2011; Redon *et al.*, 2010). Thus, it is important to optimise the γH2AX assay. This information, coupled with improvements to accessibility and widespread use of SR techniques, could be exploited for the optimisation and interpretation of future radiobiology experiments.

The data in **Figure 5.5** aimed to show the differences in foci yield between techniques of varying resolution in 2D. This may have have resulted in an underestimation of foci yields, as only a portion of the damage was in focus during image acquisition. Direct visualisation of the 3D distribution of foci within the cell nucleus could provide novel insights into the spatial organisation and function of γH2AX and 53BP1, as well as other chromatin-bound proteins (Desai *et al.*, 2005; Hernández *et al.*, 2013). However, SR imaging in 3D remains challenging due to fast photobleaching of fluorescent probes, high level of background noise and long acquisition times. Recent advances in 3D STED (Velasco *et al.*, 2019; Zdańkowski *et al.*, 2020) show promise for future investigations.

Studies have shown the delay in processing and repair of CDD by persistence in DNA repair protein foci (Sage *et al.*, 2017; Vitti *et al.*, 2019). High-LET radiation (such as α-particles and carbon ions) has an elevated propensity to form CDD in comparison with low-LET γ-rays or X-rays (Georgakilas *et al.*, 2013). Cluster complexity (number of lesions within one cluster) also rises with increasing LET (Georgakilas *et al.*, 2013;

Hada *et al.*, 2006). This is one of the reasons why high-LET radiotherapy is expected to have greater therapeutic effectiveness and represents a promising alternative for radioresistant tumours. Despite this, the differences in signalling and repair mechanisms involved in the recognition and processing of CDD, particularly those produced by α-particles and protons (at and around the Bragg peak), are currently unclear. The data presented in **Chapter 3** focuses on the often overlooked non-DSB clustered damage, while **Chapters 4** and **5** concentrate on DSB induction and repair. Recent studies have identified OGG1, a base excision repair protein, as an essential component of CDD repair (Nikitaki *et al.*, 2016a). To investigate its recruitment to sites of CDD, OGG1 and γH2AX foci were evaluated following low- and high-LET IR in UMSCC74A and HeLa cells using confocal microscopy.

Kinetics, structural and colocalisation studies revealed the involvement of OGG1 in CDD processing generated from high-LET IR, particularly at late time-points post-IR. Kinetics data revealed OGG1 and γH2AX foci persisted for longer after α-IR compared with γ-IR (**Figures 3.5** and **3.6**). This has been observed by other groups with γH2AX foci (Höglund *et al.*, 2001; Leatherbarrow *et al.*, 2006; Staaf *et al.*, 2012). The reduced repair efficiency of DSBs (γH2AX) and non-DSBs (OGG1) likely reflected the increased complex nature of the damage formed by α-IR (Goodhead, 2006; Pinto *et al.*, 2005). (Asaithamby *et al.*, 2011c) have proposed that persistent lesions observed here (those irreparable by 24 h) are due to the exceedingly complex DNA damage, rather than the previously suggested idea that long-lasting damage is inaccessible to repair proteins due to chromatin organisation (Goodarzi *et al.*, 2010). Foci yield fluctuations observed at early time-points were likely natural experimental point-to-point variation. Angled α-IR was expected to yield more foci compared with perpendicular α-IR, as foci that

would be otherwise omitted in the z should be resolved in the x-y axis. At peak expression, γ-IR resulted in 15 OGG1 and 16 γH2AX foci/Gy/cell, while perpendicular α-IR yielded 5 OGG1 and 8 γH2AX foci/Gy/cell, and angled α-IR led to 8 OGG1 and 11 γH2AX foci/Gy/cell. This demonstrated angled α-IR provided an improved way of visualising foci that would otherwise be obscured in the z-axis, as well as investigating their spatial distribution along individual tracks. The lack of resolution improvement at other time-points requires further investigation, in particular with a lower dose to avoid foci saturation. Narrow, densely-ionising tracks can produce correlated DSB across higher orders of DNA packing, such as nucleosomes, chromatin fibre and fibre loops; these would not be observed as separate events by conventional imaging techniques. Thus, future studies could address the use of angled α-IR combined with SR microscopy techniques from **Chapter 5**, to gain better lateral resolution and thus further resolve foci structure along the α-particle track.

The γH2AX foci yields observed were in agreement with previous studies (Leatherbarrow *et al.*, 2006; Löbrich *et al.*, 2010; Nikitaki *et al.*, 2016a; Rübe *et al.*, 2008). For example, (Leatherbarrow *et al.*, 2006) detected an average of 14 γH2AX foci/Gy/cell after γ-ray IR, while (Nikitaki *et al.*, 2016a) measured 16 γH2AX foci/Gy/cell. Foci disappearance in cells exposed to α-IR was somewhat slower than recorded by some investigations (Costes *et al.*, 2006; Leatherbarrow *et al.*, 2006; Riballo *et al.*, 2004; Schmid *et al.*, 2010; Staaf *et al.*, 2012). For example, (Leatherbarrow *et al.*, 2006) found 80% of γH2AX foci were repaired at 6 h following perpendicular α-IR (incident LET 120 keV/μm), while only $\sim$40% was observed here (**Figure 3.6**). Variation in IR-induced foci (IRIF) kinetics are common across the literature due to differences in cell types and antibodies used, time-points, staining procedures, image capture and analysis. Compa-

rable OGG1 kinetics investigations are lacking in the current literature, and thus it is difficult to compare foci yields. A couple of groups (Asaithamby *et al.*, 2011b; Nikitaki *et al.*, 2016a) have visualised OGG1 localisation to DNA damage sites induced by iron and silicon ion IR. Both of these studies reported OGG1 localisation to sites of clustered damage caused by high-LET IR, in agreement with the α-particle data presented here. The work presented in **Chapter 3** is the first comprehensive study to quantify and compare OGG1 foci kinetics over time after low- and high-LET IR in UMSCC74A and HeLa cells.

Low and high energy proton irradiation was also used to generate CDD in varying frequency and complexity. Preliminary data (**Figure 3.13**) showed a higher OGG1 and γH2AX foci yield in UMSCC74A cells after low energy protons, supporting previous studies with the same cell line (Britten *et al.*, 2013; Carter *et al.*, 2018; Chaudhary *et al.*, 2014). In comparison to α-particles, protons are likely to cause a mixture of both non-DSB and DSB CDD (Friedland *et al.*, 2017; Girdhani *et al.*, 2013; Vitti *et al.*, 2019). Additionally, the LET of α-IR was significantly higher than that of protons. Thus, further work on the effects of protons on OGG1 and γH2AX foci is needed to understand the differences between high-LET α-particles and protons. Due to unexpected laboratory shut down from COVID-19, this proton experiment was only repeated once. At least two more repeats will allow further validation and a better interpretation of the results.

Investigations into the structure and spatial distribution of OGG1 and γH2AX revealed an increase in foci size (**Figure 3.7**), as well as persistence in the z-axis after high-LET IR (**Figure 3.8**). Additionally, groups of individual foci within one cluster were observed only after high-LET IR, reflecting the complexity induced by increasing LET

(**Figure 3.9**). The greater complexity of DSBs may lead to bigger foci in part due to extended lifetime, but also importantly due to the correlation of breaks along the track, these individual foci are less likely to be resolved and result in what is observed as a larger foci. This data is in close agreement with previous studies that observed a difference in IRIF size and persistence in the z-axis in cells exposed to high-LET compared with low-LET radiation (Bracalente *et al.*, 2010; Costes *et al.*, 2006; Jezkova *et al.*, 2018; Leatherbarrow *et al.*, 2006; Neumaier *et al.*, 2012; Nikitaki *et al.*, 2016a; Staaf *et al.*, 2012; Timm *et al.*, 2018). For example, γH2AX foci size was $\sim$0.3 μm^2 after γ-rays (LET 0.3 keV/μm) and $\sim$0.6 μm^2 after perpendicular α-particles (LET 121 keV/μm). Similarly, (Nikitaki *et al.*, 2016a) detected $\sim$0.4 μm^2 after low-LET X-rays (LET 0.3 keV/μm) and $\sim$0.7 μm^2 after high-LET argon ion exposure (LET 270 keV/μm). Thus, foci size could potentially be used as a marker for the effects of varying radiation qualities. This emphasised the importance of investigating the morphological characteristics of repair foci (rather than just the yields) to further understand variations in the response to different radiation qualities. To date, knowledge in this area remains lacking due to technical challenges in microscopy, particularly SR approaches. This was addressed in **Chapter 5**, which confirmed that confocal imaging did not provide enough resolution to investigate the sub-structure of foci. Thus, future studies are warranted to measure foci area and investigate foci structure after low- and high-LET IR using SR. Additional experiments are also needed to track foci area with dose.

One important aspect of this study was the use of an automated script to quantify foci in **Chapters 3** and **5**, which was calibrated and optimised by eye. While scoring by eye may be subjective, it was done to minimise errors in the recognition and counting of

foci related to the script. Automated foci quantification provided not only time savings but also a reproducible and objective measure (Schneider *et al.*, 2019). However, the number foci is dependent on the scoring criteria, and the robustness of the criteria is strongly affected by sample labelling and image acquisition. This is why it was crucial to keep all parameters the same while preparing and imaging samples (Ronneberger *et al.*, 2008). While the absolute number of foci may vary with scoring criteria, as the same criteria was used across all samples the general trends remained the same. In future studies, the use of supervised machine learning algorithms is likely to improve the robustness of analysis across different image data-sets (Herbert *et al.*, 2014; Sommer *et al.*, 2013).

Another key facet of the work presented in **Chapters 3** and **5** was the dose used. Depending on the cell type used, foci yield has been shown to change linearly with radiation dose delivered (Asaithamby *et al.*, 2009; Costes *et al.*, 2010). Some studies have shown a loss of detection with increasing dose due to overlapping of foci above 1 Gy (Costes *et al.*, 2006, 2010). In contrast, others have shown linearity in γH2AX foci with dose up to 2-4 Gy (Avondoglio *et al.*, 2009; Barbieri *et al.*, 2019; Corre *et al.*, 2010; Kinner *et al.*, 2008; Mahrhofer *et al.*, 2006; Nikitaki *et al.*, 2016a). Consequently, the 2 Gy used in **Chapters 5** may have resulted in some foci overlapping. However, the use of SR techniques should result in extending of the linearity to higher doses, so any overlap would have likely been minimal. The 4 Gy used in **Chapters 3** was chosen to enable comparison with ongoing studies by collaborators (Carter *et al.*, 2018). This may have led to foci overlapping and saturation. Future studies are required to measure foci kinetics at varying doses following different radiation qualities, as well as with SR microscopy to investigate foci overlapping and address the limited resolution

of the confocal microscope. This will be particularly important for angled α-particle irradiations where it was not always possible to identify individual tracks. The use of lower doses will also be useful to separate independent foci events from correlated nano-foci forming part of a larger focus.

Colocalisation data between DSB (γH2AX) and non-DSB (OGG1) foci (**Figure 3.10**) showed weak colocalisation after low-LET γ-IR which increased with rising LET, suggesting an increase in damage complexity with LET, as well as an increase in correlation of these events along individual tracks. This is in agreement with others that have also observed increased colocalisation of DSB and non-DSB markers after high-LET IR (Nikitaki *et al.*, 2016a,b; Zhang *et al.*, 2016). For example, (Nikitaki *et al.*, 2016a) detected low level colocalisation for 53BP1/γH2AX and OGG1/APE1 foci after X-ray irradiation and higher colocalisation following α-IR. Colocalisation studies in **Chapter 5** revealed the spatial distribution of foci was best understood using SR techniques rather than confocal. Therefore, γH2AX-OGG1 colocalisation could be performed with SR microscopy to improve this study.

Colocalisation studies in **Chapters 3** and **5** were performed using 2D maximum intensity projections of 3D confocal stacks, essentially losing the information in the z. Future work is needed to repeat this analysis in 3D using recently developed methods (Lavancier *et al.*, 2019), as it may reveal interesting information about the spatial arrangement of these proteins. Some groups have formulated approaches specifically for detecting foci colocalisation based on focus topology (Mavragani *et al.*, 2017; Nikitaki *et al.*, 2016a,b). With more time available, I would incorporate these methods and compare with the results presented here.

The use of PARP inhibitors is an increasingly common strategy for cancer therapy and has been shown to induce radiosensitisation in several human cell lines, including HeLa and UMSCC74A (Dok *et al.*, 2020; Kötter *et al.*, 2014; Nickson *et al.*, 2017). Despite this, the mechanism of action behind the enhanced sensitivity remains unclear. The synergistic ability of PARP inhibitor Olaparib in combination with high-LET IR increased not only DSB but also base damage yields as well as decreased repairability (**Figure 3.12**). This was not observed after low-LET IR, suggesting high-LET radiation may be more effective for treatment of radioresistant cells. This was also partly observed after low energy protons (**Figure 3.14**). However, due to COVID-19, experiments involving Olaparib were not repeated enough times, thus more repeats are required to confirm these observations. This data supports the accumulating evidence demonstrating the synergistic ability of PARP inhibitors in combination with radiotherapy for treatment of radioresistant cells, particularly those in head and neck squamous cell carcinoma (Dok *et al.*, 2020; Nickson *et al.*, 2017; Weaver *et al.*, 2015; Wurster *et al.*, 2016). While most studies focus on the importance of dose (Bridges *et al.*, 2014; Verhagen *et al.*, 2015), the data presented here focused on the differences in response to low- and high-LET IR.

Other studies have also shown a link between inaccurate repair and high-LET IR exposure, as well as in combination with Olaparib (Baldeyron *et al.*, 2002; Bentley *et al.*, 2004; Hirai *et al.*, 2012; Kötter *et al.*, 2014). It has been suggested that this could be due to switching to the error-prone Alt-Ej repair pathway, fuelled by lack of binding ability between Ku70 and Ku80 (Kötter *et al.*, 2014). Consequently, Ku70 and Ku80 binding was investigated in **Chapter 4**.

The data presented in **Chapter 4** was the first to show Ku70-80 interaction in liv-

ing cells with the Ku heterodimer pre-formed and stable even in the absence of DNA damage (**Figure 4.12**). This was done by tagging Ku70 and Ku80 to fluorescent proteins mCherry and EGFP and validated using two independent microscopy techniques, FRET-FLIM and BiFC. To determine if the FRET-FLIM results were influenced by the choice and position of the fluorescent proteins, Ku70 and Ku80 were each tagged on different termini. While EGFP and mCherry tagging did not disrupt Ku70/80 localisation or function (**Figures 4.4-5**), the position of the tag did affect the FRET-FLIM results (**Figure 4.12**). This highlights the importance of performing comprehensive controls when investigating protein-protein interactions, as lack of optimisation may lead to false-negatives and thus data misinterpretation, as previously observed (Klucken *et al.*, 2006).

Following confirmation of the Ku70-80 interaction, the next step was to investigate Ku70-80 binding upon DNA damage. The most feasible way to induce damage was via 405 nm laser micro-irradiation, which has been used extensively to recruit Ku70 and Ku80 to sites of damage (Bekker-Jensen *et al.*, 2006; Kim *et al.*, 2005; Koike *et al.*, 2015; Mari *et al.*, 2006; Reynolds *et al.*, 2012). Laser micro-irradiations provide an easy and quick method to generate thin and highly localised geometric lines of damage, while allowing cells to be kept in optimal growth conditions. However, the damage produced is difficult to quantify and may be different from the photochemical damaged caused by IR (Holton *et al.*, 2017; Kong *et al.*, 2009). UV-A photons are weakly absorbed by DNA, so the damage caused by 405 nm lasers is expected to be indirect, in particular from temperature rises and production of free radicals and reactive oxygen species (Holton *et al.*, 2017; Kong *et al.*, 2009). Prior to testing Ku70-80 interactions, free EGFP and mCherry were measured to make sure their lifetimes remained the same before and after

laser micro-irradiation. Unexpectedly, the natural lifetimes of EGFP and mCherry were both found to be sensitive to 405 nm irradiation. Thus, it was not possible to measure the effect of DNA damage on Ku70-80 interactions. Future investigations are needed to apply the knowledge gained from this study and address Ku70-80 binding at DNA damage sites, particularly after low- and high-LET IR, and in combination with Olaparib. Ku70-80 binding has been shown to be impaired more frequently in tumours compared to normal tissues using biochemical methods (Costantini *et al.*, 2007; Parrella *et al.*, 2006; Pucci *et al.*, 2001). Investigating the differences in Ku70-80 interactions between normal and malignant cells is crucial to understanding what drives DSB repair in cancer cells and how it can be targeted in a clinical capacity.

An important aspect to consider is that all experiments were conducted using asynchronous cells. While cell cycle was not the main focus of this study, others have shown the importance of the cell cycle when detecting foci (Bauerschmidt *et al.*, 2009; Costes *et al.*, 2006; Marková *et al.*, 2007; Rothkamm *et al.*, 2003; Wardman *et al.*, 2007) and identifying the localisation of Ku (Britton *et al.*, 2013; Higashiura *et al.*, 1992; Li *et al.*, 1992). Laboratory shut down due to COVID-19 prevented the scheduled FACS analysis to determine the predominant cell cycle stage for samples in **Chapter 3**. In future studies, the phase could be taken into account by either synchronising the cells, analysing their DNA content by FACS or using a cell cycle marker.

The experiments performed in all chapters could be improved by expanding the work to other cell lines. Further studies are warranted to compare the results obtained using both normal and mutant cell lines, as well as 3D cell spheroids. Additionally, combining modelling and biochemical assays with cellular approaches will allow better analysis of the results obtained.

While experiments in **Chapters 3** and **5** were conducted using cell fixation, it was important that the Ku70-80 interaction in **Chapter 4** was investigated in living cells. This was so that spatiotemporal dynamics could be detected and because protein-protein interactions may be affected by fixation and immunoprecipitation (Ahmed *et al.*, 2019; Neuhaus *et al.*, 1998; Schnell *et al.*, 2012; Wu *et al.*, 2007). One of the reasons for using cell fixation in **Chapters 3** and **5** was that post-translational histone modifications are very difficult to visualise in living cells but can be conveniently detected using antibodies. Additionally, the dishes used to irradiate cells with α-particles presented many issues regarding microscope focus drift and autofluorescence, thus challenging with long time-course live-cell experiments. Lastly, most of the SR techniques used in **Chapter 5** were incompatible with live-cell imaging due to the high laser powers and extensive image acquisition and processing times required, which have been shown to result in phototoxicity and photodamage even at low laser intensities (Wäldchen *et al.*, 2015). Antibody aggregates and non-specific binding are the main disadvantages of using immunofluorescence labelling, as these may result in false-positives or false-negatives (Barnard *et al.*, 2013). Additionally, fixing cells limits the tracking of the dynamic behaviour of repair events. This antibody work provided the foundation to identify the general dynamics of the cellular response to low- and high-LET IR. Consequently, in the future it would be useful to use fluorophore-labelled proteins in living cells to identify any differences in the kinetics studies using living cells. While most DSBs are produced at the time of irradiation, non-DSB lesions can lead to the induction of new DSBs at later times. Live-cell imaging would allow the delayed production of foci to be identified. This would also permit following the relative movement of individual foci. Although subject to extensive study, large-scale mobility of DSBs remains poorly understood, particularly after the induction of highly localised damage

(Marnef *et al.*, 2017). The use of live-cell time-lapse microscopy has been identified as a key method to gain insights into how DSB mobility impacts genome integrity (Marnef *et al.*, 2017).

IR is an effective and significant cancer therapy due to the induction of cell death. While most patients who are treated with external beam radiotherapy receive X-rays (Murshed, 2019), high-LET radiation shows great promise for the treatment of challenging, radioresistant cancers such as head and neck squamous cell carcinoma (Allen *et al.*, 2011b). High-LET IR results in higher cell death induction and in the activation of different DNA repair mechanisms compared to low-LET IR, potentially leading to different manifestations and development of normal tissue damage (Niemantsverdriet *et al.*, 2012). Therefore, to optimally exploit the benefits of radiotherapy with high-LET IR, it is important to understand the underlying mechanisms of DNA repair and associated signalling with different radiation qualities so they can be taken taken into account during treatment planning. In addition, targeting proteins that are involved in CDD repair with drugs such as Olaparib could be used to increase the efficacy of radiotherapy. Understanding how clustered damage is repaired can aid the design of future therapies which can be used in combination with radiotherapy to enhance the radiosensitisation effect.

In conclusion, the key and novel findings of this work are the following:

- Confocal imaging alone may significantly underestimate the number of foci by a factor of 2-5, as each X-ray induced γH2AX and 53BP1 focus was further resolved into smaller nano-foci when using SR.
- The spatial distribution of foci may be best understood using SR techniques, as

γH2AX-53BP1 colocalisation was significantly overestimated at the confocal level ($\sim$300 nm) when compared to SR ($<$100 nm).

- Slower repair kinetics, increased size and higher complexity of OGG1 foci at sites of CDD were observed for high-LET α-particles compared to low-LET γ-rays. PARP inhibitor Olaparib in combination with IR resulted in raised foci persistence at CDD sites.

- Angled α-particle irradiation provided an improved method for distinguishing and visualising individual foci along the particle track, when compared to perpendicular α-IR.

- Ku70 and Ku80 interact in living cells, with the Ku heterodimer pre-formed and stable, even in the absence of DNA damage. Fluorescent proteins EGFP and mCherry are unsuitable for 405 nm laser irradiation followed by FRET-FLIM analysis.

Bibliography

Abbe, E. (1873). Contributions to the Theory of the Microscope and Microscopic Detection (Translated from German). *Archiv für Mikroskopische Anatomie*, **13**, 191–219.

Abbotts, R. *et al.* (2017). Coordination of DNA Single Strand Break Repair. *Free Radical Biology and Medicine*, **107**, 228–244.

Aburatani, H. *et al.* (1997). Cloning and Characterization of Mammalian 8-hydroxyguanine-specific DNA Glycosylase/apurinic, Apyrimidinic Lyase, a Functional MutM Homologue. *Cancer Research*, **57**, 2151–2156.

Adams, K.E. *et al.* (2006). Recruitment of ATR to Sites of Ionising Radiation-Induced DNA Damage Requires ATM and Components of the MRN Protein Complex. *Oncogene*, **25**, 3894–3904.

Adler, J. *et al.* (2010). Quantifying Colocalization by Correlation: The Pearson Correlation Coefficient Is Superior to the Mander's Overlap Coefficient. *Cytometry Part A*, **77**, 733–742.

Ahmed, A.R. (2018). *Determining S6k1 Localisation and Interactions with Mtorc1 in Live Cells Using Fluorescence Lifetime Imaging Microscopy*. Ph.D. thesis, Oxford Brookes University.

Ahmed, A.R. *et al.* (2019). Direct Imaging of the Recruitment and Phosphorylation of S6K1 in the mTORC1 Pathway in Living Cells. *Scientific Reports*, **9**, 3408.

Akselrod, G.M. *et al.* (2006). A Novel Al2O3 Fluorescent Nuclear Track Detector for Heavy Charged Particles and Neutrons. *Nuclear Instruments and Methods in Physics Research, Section B: Beam Interactions with Materials and Atoms*, **247**, 295–306.

Akselrod, M.S. *et al.* (2011). Fluorescent Nuclear Track Detector Technology - a New Way to Do Passive Solid State Dosimetry. *Radiation Measurements*, **46**, 1671–1679.

Aleksandrov, R. *et al.* (2018). Protein Dynamics in Complex DNA Lesions. *Molecular Cell*, **69**, 1046–1061.

Allen, C. *et al.* (2011a). More Forks on the Road to Replication Stress Recovery. *Journal of Molecular Cell Biology*, **3**, 4–12.

Allen, C. *et al.* (2011b). Heavy Charged Particle Radiobiology: Using Enhanced Biological Effectiveness and Improved Beam Focusing to Advance Cancer Therapy. *Mutation Research/Fundamental and Molecular Mechanisms of Mutagenesis*, **711**, 150–157.

BIBLIOGRAPHY

Alshareeda, A.T. *et al.* (2013). Clinicopathological Significance of KU70/KU80, a Key DNA Damage Repair Protein in Breast Cancer. *Breast Cancer Research and Treatment*, **139**, 301–310.

Amé, J.C. *et al.* (2009). Detection of the Nuclear Poly(ADP-ribose)-Metabolizing Enzymes and Activities in Response to DNA Damage. *Methods in Molecular Biology*, **464**, 267–283.

Antonelli, F. *et al.* (2015). Induction and Repair of DNA DSB as Revealed by H2AX Phosphorylation Foci in Human Fibroblasts Exposed to Low- and High-LET Radiation: Relationship with Early and Delayed Reproductive Cell Death. *Radiation Research*, **183**, 417–431.

Asaithamby, A. *et al.* (2009). Cellular Responses to DNA Double-Strand Breaks After Low-Dose γ-Irradiation. *Nucleic Acids Research*, **37**, 3912–3923.

Asaithamby, A. *et al.* (2011a). Mechanism of Cluster DNA Damage Repair in Response to High-atomic Number and Energy Particles Radiation. *Mutation Research/Fundamental and Molecular Mechanisms of Mutagenesis*, **711**, 87–99.

Asaithamby, A. *et al.* (2008). Repair of HZE-Particle-Induced DNA Double-Strand Breaks in Normal Human Fibroblasts. *Radiation Research*, **169**, 437–446.

Asaithamby, A. *et al.* (2011b). Unrepaired Clustered DNA Lesions Induce Chromosome Breakage in Human Cells. *Proceedings of the National Academy of Sciences of the United States of America*, **108**, 8293–8298.

Asaithamby, A. *et al.* (2011c). Irreparable Complex DNA Double-strand Breaks Induce Chromosome Breakage in Organotypic Three-dimensional Human Lung Epithelial Cell Culture. *Nucleic Acids Research*, **39**, 5474–5488.

Audebert, M. *et al.* (2004). Involvement of Poly(ADP-ribose) Polymerase-1 and XRCC1/DNA Ligase III in an Alternative Route for DNA Double-Strand Breaks Rejoining. *Journal of Biological Chemistry*, **279**, 55117–55126.

Avondoglio, D. *et al.* (2009). High Throughput Evaluation of γ-H2AX. *Radiation Oncology*, **4**, 31.

Bakkenist, C.J. *et al.* (2003). DNA Damage Activates ATM Through Intermolecular Autophosphorylation and Dimer Dissociation. *Nature*, **421**, 499–506.

Baldeyron, C. *et al.* (2002). A Single Mutated BRCA1 Allele Leads to Impaired Fidelity of Double Strand Break End-joining. *Oncogene*, **21**, 1401–10.

Banin, S. *et al.* (1998). Enhanced Phosphorylation of p53 by ATM in Response to DNA Damage. *Science*, **281**, 1674–1677.

Barbieri, S. *et al.* (2019). Predicting DNA Damage Foci and Their Experimental Readout With 2D Microscopy: A Unified Approach Applied to Photon and Neutron Exposures. *Scientific Reports*, **9**, 14019.

Barendsen, G.W. *et al.* (1963). Effects of Different Ionizing Radiations on Human Cells in Tissue Culture: III. Experiments with Cyclotron-Accelerated α-Particles and Deuterons. *Radiation Research*, **18**, 106–119.

Barnard, S. *et al.* (2013). The Shape of the Radiation Dose Response for DNA Double-Strand Break Induction and Repair. *Genome Integrity*, **4**, 1.

Barnard, S. *et al.* (2015). The First γ-H2AX Biodosimetry Intercomparison Exercise of the Developing European Biodosimetry Network RENEB. *Radiation Protection Dosimetry*, **164**, 265–270.

Basu, S. *et al.* (2018). FRET-enhanced Photostability Allows Improved Single-Molecule Tracking of Proteins and Protein Complexes in Live Mammalian Cells. *Nature Communications*, **9**, 2520.

Bauerschmidt, C. *et al.* (2009). Cohesin Promotes the Repair of Ionizing Radiation-Induced DNA Double-Strand Breaks in Replicated Chromatin. *Nucleic Acids Research*, **38**, 477–487.

Becker, W. (2014). *Becker & Hickl TCSPC Handbook*. 6th edn.

Beels, L. *et al.* (1903). γ-H2AX Foci as a Biomarker for Patient X-ray Exposure in Pediatric Cardiac Catheterization: Are We Underestimating Radiation Risks? *Circulation*, **120**, 1903–1909.

Bekker-Jensen, S. *et al.* (2006). Spatial Organization of the Mammalian Genome Surveillance Machinery in Response to DNA Strand Breaks. *Journal of Cell Biology*, **173**, 195–206.

Bennardo, N. *et al.* (2008). Alternative-NHEJ Is a Mechanistically Distinct Pathway of Mammalian Chromosome Break Repair. *PLoS Genetics*, **4**, e1000110.

Bentley, J. *et al.* (2004). DNA Double Strand Break Repair in Human Bladder Cancer Is Error Prone and Involves Microhomology-associated End-joining. *Nucleic Acids Research*, **32**, 5249–5259.

Betzig, E. *et al.* (2006). Imaging Intracellular Fluorescent Proteins at Nanometer Resolution. *Science*, **313**, 1643–1645.

Bewersdorf, J. *et al.* (2006). H2AX Chromatin Structures and Their Response to DNA Damage Revealed by 4Pi Microscopy. *Proceedings of the National Academy of Sciences of the United States of America*, **103**, 18137–18142.

Bindels, D.S. *et al.* (2016). mScarlet: A Bright Monomeric Red Fluorescent Protein for Cellular Imaging. *Nature Methods*, **14**, 53–56.

Bird, L.E. (2011). High Throughput Construction and Small Scale Expression Screening of Multi-tag Vectors in Escherichia Coli. *Methods*, **55**, 29–37.

Bird, L.E. *et al.* (2015). Green Fluorescent Protein-based Expression Screening of Membrane Proteins in Escherichia coli. *Journal of Visualized Experiments*, **95**, e52357.

Bird, R.P. *et al.* (1975). Survival of Synchronized Chinese Hamster Cells Exposed to Radiation of Different Linear-Energy Transfer. *International Journal of Radiation Biology and Related Studies in Physics, Chemistry and Medicine*, **27**, 105–120.

Blöcher, D. (1988). DNA Double-Strand Break Repair Determines the RBE of α-Particles. *International Journal of Radiation Biology*, **54**, 761–771.

BIBLIOGRAPHY

Böcker, W. *et al.* (2006). Computational Methods for Analysis of Foci: Validation for Radiation-Induced γ-H2AX Foci in Human Cells. *Radiation Research*, **165**, 113–124.

Bolte, S. *et al.* (2006). A Guided Tour into Subcellular Colocalization Analysis in Light Microscopy. *Journal of Microscopy*, **224**, 213–232.

Bonassi, S. *et al.* (2008). Chromosomal Aberration Frequency in Lymphocytes Predicts the Risk of Cancer: Results From a Pooled Cohort Study of 22 358 Subjects in 11 Countries. *Carcinogenesis*, **29**, 1178–1183.

Borlinghaus, R.T. *et al.* (2016). HyVolution – the Smart Path to Confocal Super-Resolution. *Nature Methods*, **13**, i–iii.

Bottanelli, F. *et al.* (2016). Two-colour Live-Cell Nanoscale Imaging of Intracellular Targets. *Nature Communications*, **7**, 10778.

Boulton, S.J. *et al.* (1998). Components of the Ku-dependent Non-homologous End-joining Pathway are Involved in Telomeric Length Maintenance and Telomeric Silencing. *EMBO Journal*, **17**, 1819–1828.

Bracalente, C. *et al.* (2010). Assessment of γH2AX Nuclear Foci Number and Size in Normal and Repair-deficient Cells Irradiated with Low and High Linear Energy Transfer Radiation. *International Journal of Low Radiation*, **7**, 393–408.

Brenner, D.J. *et al.* (1992). Constraints on Energy Deposition and Target Size of Multiply Damaged Sites Associated With DNA Double-Strand Breaks. *International Journal of Radiation Biology*, **61**, 737–748.

Bridges, K.A. *et al.* (2014). Niraparib (MK-4827), a Novel Poly(ADP-ribose) Polymerase Inhibitor, Radiosensitizes Human Lung and Breast Cancer Cells. *Oncotarget*, **5**, 5076–5086.

Britten, R.A. *et al.* (2013). Variations in the RBE for Cell Killing Along the Depth-Dose Profile of a Modulated Proton Therapy Beam. *Radiation Research*, **179**, 21–28.

Britton, S. *et al.* (2013). A New Method for High-resolution Imaging of Ku Foci to Decipher Mechanisms of Dna Double-strand Break Repair. *Journal of Cell Biology*, **202**, 579–595.

Buermeyer, A.B. *et al.* (1999). Mammalian DNA Mismatch Repair. *Annual Review of Genetics*, **33**, 533–564.

Burma, S. *et al.* (2001). ATM Phosphorylates Histone H2AX in Response to DNA Double-strand Breaks. *Journal of Biological Chemistry*, **276**, 42462–42467.

Burrows, C.J. *et al.* (1998). Oxidative Nucleobase Modifications Leading to Strand Scission. *Chemical Reviews*, **98**, 1109–1152.

Caldecott, K.W. *et al.* (1995). Characterization of the XRCC1-DNA Ligase III Complex in Vitro and Its Absence From Mutant Hamster Cells. *Nucleic Acids Research*, **23**, 4836–4843.

Campalans, A. *et al.* (2007). UVA Irradiation Induces Relocalisation of the DNA Repair Protein hOGG1 to Nuclear Speckles. *Journal of Cell Science*, **120**, 23–32.

Carson, C.T. *et al.* (2003). The Mre11 Complex Is Required for ATM Activation and the G2/M Checkpoint. *EMBO Journal*, **22**, 6610–6620.

Carter, R.J. *et al.* (2018). Complex DNA Damage Induced by High Linear Energy Transfer Alpha-Particles and Protons Triggers a Specific Cellular DNA Damage Response. *International Journal of Radiation Oncology Biology Physics*, **100**, 776–784.

Carter, R.J. *et al.* (2019). Characterisation of Deubiquitylating Enzymes in the Cellular Response to High-LET Ionizing Radiation and Complex DNA Damage. *International Journal of Radiation Oncology Biology · Physics*, **104**, 656–665.

Cary, R.B. *et al.* (1997). DNA Looping by Ku and the DNA-dependent Protein Kinase. *Proceedings of the National Academy of Sciences of the United States of America*, **94**, 4267–4272.

Cary, R.B. *et al.* (1998). A Central Region of Ku80 Mediates Interaction With Ku70 in Vivo. *Nucleic Acids Research*, **26**, 974–979.

Chaudhary, P. *et al.* (2014). Relative Biological Effectiveness Variation along Monoenergetic and Modulated Bragg Peaks of a 62-MeV Therapeutic Proton Beam: A Preclinical Assessment. *International Journal of Radiation Oncology Biology Physics*, **90**, 27–35.

Chaudhry, M.A. (2007). Base Excision Repair of Ionizing Radiation-Induced DNA Damage in G1 and G2 Cell Cycle Phases. *Cancer Cell International*, **7**, 15–26.

Chen, Z. *et al.* (2008). Mechanism of Homologous Recombination From the RecA-ssDNA/dsDNA Structures. *Nature*, **453**, 489–494.

Cleaver, J.E. *et al.* (2011). Phosphorylated H2Ax Is Not an Unambiguous Marker for DNA Double-Strand Breaks. *Cell Cycle*, **10**, 3223–3224.

Cohen, H.Y. *et al.* (2004). Acetylation of the c terminus of ku70 by cbp and pcaf controls bax-mediated apoptosis. *Molecular cell*, **13**, 627–638.

Cole, K.C. *et al.* (2007). Use of Bimolecular Fluorescence Complementation to Study in Vivo Interactions Between Cdc42p and Rdi1p of Saccharomyces Cerevisiae. *Eukaryotic Cell*, **6**, 378–387.

Corre, I. *et al.* (2010). Plasma Membrane Signaling Induced by Ionizing Radiation. *Mutation Research/Reviews in Mutation Research*, **704**, 61–67.

Costantini, L.M. *et al.* (2015). A Palette of Fluorescent Proteins Optimized for Diverse Cellular Environments. *Nature Communications*, **6**, 7670.

Costantini, S. *et al.* (2007). Interaction of the Ku Heterodimer With the DNA Ligase IV/Xrcc4 Complex and Its Regulation by DNA-PK. *DNA Repair*, **6**, 712–722.

Costes, S.V. *et al.* (2004). Automatic and Quantitative Measurement of Protein-protein Colocalization in Live Cells. *Biophysical Journal*, **86**, 3993–4003.

Costes, S.V. *et al.* (2006). Imaging Features that Discriminate between Foci Induced by High- and Low-LET Radiation in Human Fibroblasts. *Radiation Research*, **165**, 505–515.

Costes, S.V. *et al.* (2007). Image-based Modeling Reveals Dynamic Redistribution of DNA Damage Into Nuclear Sub-Domains. *PLoS Computational Biology*, **3**, e155.

BIBLIOGRAPHY

Costes, S.V. *et al.* (2010). Spatiotemporal Characterization of Ionizing Radiation Induced DNA Damage Foci and Their Relation to Chromatin Organization. *Mutation Research*, **704**, 78–87.

Cox, R. *et al.* (1979). Mutation and Inactivation of Cultured Mammalian Cells Exposed to Beams of Accelerated Heavy Ions. III. Human Diploid Fibroblasts. *International Journal of Radiation Biology and Related Studies in Physics, Chemistry and Medicine*, **36**, 149–160.

Cremer, T. *et al.* (2001). Chromosome Territories, Nuclear Architecture and Gene Regulation in Mammalian Cells. *Nature Reviews Genetics*, **2**, 292–301.

Croco, E. *et al.* (2017). DNA Damage Detection by 53BP1: Relationship to Species Longevity. *Journals of Gerontology - Series A Biological Sciences and Medical Sciences*, **72**, 763–770.

Culley, S. *et al.* (2018). Quantitative Mapping and Minimization of Super-Resolution Optical Imaging Artifacts. *Nature Methods*, **15**, 263–266.

Czornak, K. *et al.* (2008). Mystery of DNA Repair: The Role of the MRN Complex and ATM Kinase in DNA Damage Repair. *Journal of Applied Genetics*, **49**, 383–396.

D'Abrantes, S. *et al.* (2017). Super-Resolution Nanoscopy Imaging Applied to DNA Double-Strand Breaks. *Radiation Research*, **189**, 19–31.

De Feraudy, S. *et al.* (2010). A Minority of Foci or Pan-nuclear Apoptotic Staining of γH2AX in the S Phase after UV Damage Contain DNA Double-strand Breaks. *Proceedings of the National Academy of Sciences of the United States of America*, **107**, 6870 – 6875.

Demmerle, J. *et al.* (2017). Strategic and Practical Guidelines for Successful Structured Illumination Microscopy. *Nature Protocols*, **12**, 988–1010.

Demple, B. *et al.* (1991). Cloning and Expression of APE, the cDNA Encoding the Major Human Apurinic Endonuclease: Definition of a Family of DNA Repair Enzymes. *Proceedings of the National Academy of Sciences of the United States of America*, **88**, 11450–11454.

Deniz, M. *et al.* (2016). In Vitro Model for DNA Double-Strand Break Repair Analysis in Breast Cancer Reveals Cell Type-Specific Associations With Age and Prognosis. *FASEB Journal*, **30**, 3786–3799.

Depes, D. *et al.* (2018). Single-molecule Localization Microscopy as a Promising Tool for γH2AX/53BP1 Foci Exploration. *European Physical Journal D*, **72**, 1–11.

Desai, N. *et al.* (2005). Immunofluorescence Detection of Clustered γ-H2AX Foci Induced by HZE-particle Radiation. *Radiation Research*, **164**, 518–522.

Dickson, R.M. *et al.* (1997). On/off Blinking and Switching Behaviour of Single Molecules of Green Fluorescent Protein. *Nature*, **388**, 355–358.

Dobbs, T.A. *et al.* (2008). Interplay of Two Major Repair Pathways in the Processing of Complex Double-Strand DNA Breaks. *DNA repair*, **7**, 1372–1383.

Dok, R. *et al.* (2020). Radiosensitization Approaches for HPV-positive and HPV-negative Head and Neck Squamous Carcinomas. *International Journal of Cancer*, **146**, 1075–1085.

Du, G. *et al.* (2011). Spatial Dynamics of DNA Damage Response Protein Foci along the Ion Trajectory of High-LET Particles. *Radiation Research*, **176**, 706–715.

Dunn, K.W. *et al.* (2011). A Practical Guide to Evaluating Colocalization in Biological Microscopy. *American Journal of Physiology - Cell Physiology*, **300**, 723–742.

Durante, M. *et al.* (2010). Charged Particles in Radiation Oncology. *Nature Reviews Clinical Oncology*, **7**, 37–43.

Durante, M. *et al.* (2013). From DNA Damage to Chromosome Aberrations: Joining the Break. *Mutation Research - Genetic Toxicology and Environmental Mutagenesis*, **756**, 5–13.

Eggeling, C. *et al.* (2015). Lens-based Fluorescence Nanoscopy. *Quarterly Reviews of Biophysics*, **48**, 178–243.

Escribano-Díaz, C. *et al.* (2013). A Cell Cycle-Dependent Regulatory Circuit Composed of 53BP1-RIF1 and BRCA1-CtIP Controls DNA Repair Pathway Choice. *Molecular Cell*, **49**, 872–883.

Falk, M. *et al.* (2010). Higher-order Chromatin Structure in DSB Induction, Repair and Misrepair. *Mutation Research - Reviews in Mutation Research*, **704**, 88–100.

Feng, J. *et al.* (2017). A Novel Automatic Quantification Method for High-Content Screening Analysis of DNA Double Strand-Break Response. *Scientific Reports*, **7**, 9581.

Ferguson, D.O. *et al.* (1996). Recombinational Repair of Gaps in DNA Is Asymmetric in Ustilago Maydis and Can Be Explained by a Migrating D-loop Model. *Proceedings of the National Academy of Sciences of the United States of America*, **93**, 5419–5424.

Fernandez-Capetillo, O. *et al.* (2004). H2AX: The Histone Guardian of the Genome. *DNA Repair*, **3**, 959–967.

Fielden, E.M. *et al.* (1992). Early Processes in Radiation-Induced DNA Damage. *The British Journal of Radiology Supplement*, **24**, 18–22.

Friedland, W. *et al.* (2017). Comprehensive Track-Structure Based Evaluation of DNA Damage by Light Ions From Radiotherapy-Relevant Energies Down to Stopping. *Scientific Reports*, **7**, 45161.

Frit, P. *et al.* (2019). Plugged Into the Ku-DNA Hub: The NHEJ Network. *Progress in Biophysics and Molecular Biology*, **147**, 62–76.

Fritz, J.V. *et al.* (2008). Direct Vpr-Vpr Interaction in Cells Monitored by Two Photon Fluorescence Correlation Spectroscopy and Fluorescence Lifetime Imaging. *Retrovirology*, **5**, 87.

Fromme, J.C. *et al.* (2004). DNA Glycosylase Recognition and Catalysis. *Current Opinion in Structural Biology*, **14**, 43–49.

Fujimoto, H. *et al.* (2018). Acetylation of Nuclear Localization Signal Controls Importin-mediated Nuclear Transport of Ku70. *bioRxiv*.

Furusawa, Y. *et al.* (2000). Inactivation of Aerobic and Hypoxic Cells From Three Different Cell Lines by Accelerated (3)He-, (12)C- And (20)Ne-ion Beams. *Radiation research*, **154**, 485–496.

Garty, G. *et al.* (2011). Infrastructure to Support Ultra High Throughput Biodosimetry Screening After a Radiological Event. *International Journal of Radiation Biology*, **87**, 754–765.

Gell, D. *et al.* (1999). Mapping of Protein-Protein Interactions Within the DNA-dependent Protein Kinase Complex. *Nucleic Acids Research*, **27**, 3494–3502.

Georgakilas, A.G. *et al.* (2013). Induction and Repair of Clustered DNA Lesions: What Do We Know So Far? *Radiation Research*, **180**, 100–109.

Gerritsen, H.C. *et al.* (2002). Fluorescence Lifetime Imaging in Scanning Microscopes: Acquisition Speed, Photon Economy and Lifetime Resolution. *Journal of Microscopy*, **206**, 218–224.

Girdhani, S. *et al.* (2013). Biological Effects of Proton Radiation: What We Know and Don't Know. *Radiation Research*, **179**, 257–272.

Goodarzi, A.A. *et al.* (2010). The Influence of Heterochromatin on DNA Double-strand Break Repair: Getting the Strong, Silent Type to Relax. *DNA Repair*, **9**, 1273–1282.

Goodhead, D.T. (1994). Initial Events in the Cellular Effects of Ionizing Radiations: Clustered Damage in DNA. *International Journal of Radiation Biology*, **65**, 7–17.

Goodhead, D.T. (2006). Energy Deposition Stochastics and Track Structure: What about the Target? *Radiation Protection Dosimetry*, **122**, 3–15.

Goodhead, D.T. *et al.* (1993). Effects of Radiations of Different Qualities on Cells: Molecular Mechanisms of Damage and Repair. *International Journal of Radiation Biology*, **63**, 543–556.

Goodwin, J.F. *et al.* (2014). Beyond DNA Repair: DNA-PK Function in Cancer. *Cancer Discovery*, **4**, 1126–1139.

Goodwin, J.F. *et al.* (2015). DNA-PKcs-Mediated Transcriptional Regulation Drives Prostate Cancer Progression and Metastasis. *Cancer Cell*, **28**, 97–113.

Görlich, D. *et al.* (1999). Transport Between the Cell Nucleus and the Cytoplasm. *Annual Review of Cell and Developmental Biology*, **15**, 607–660.

Göttfert, F. *et al.* (2013). Coaligned Dual-Channel STED Nanoscopy and Molecular Diffusion Analysis at 20 Nm Resolution. *Biophysical Journal*, **105**, L01–L03.

Grant, D.M. *et al.* (2008). Multiplexed FRET to Image Multiple Signaling Events in Live Cells. *Biophysical Journal*, **95**, L69–71.

Grawunder, U. *et al.* (1997). Activity of DNA Ligase IV Stimulated by Complex Formation With XRCC4 Protein in Mammalian Cells. *Nature*, **388**, 492–495.

Gu, Y. *et al.* (1997). Ku70-deficient Embryonic Stem Cells Have Increased Ionizing Radiosensitivity, Defective DNA End-Binding Activity, and Inability to Support V(D)J Recombination. *Proceedings of the National Academy of Sciences of the United States of America*, **94**, 8076–8081.

Gulston, M. *et al.* (2002). Clustered DNA Damage Induced by Gamma Radiation in Human Fibroblasts (HF19), Hamster (V79-4) Cells and Plasmid DNA Is Revealed as Fpg and Nth Sensitive Sites. *Nucleic Acids Research*, **30**, 3464–3472.

Gulston, M. *et al.* (2004). Processing of Clustered DNA Damage Generates Additional Double-strand Breaks in Mammalian Cells Post-irradiation. *Nucleic Acids Research*, **32**, 1602–1609.

Guo, Y. *et al.* (2005). Phospholipase Cβ2 Binds to and Inhibits Phospholipase Cδ1. *Journal of Biological Chemistry*, **280**, 1438–1447.

Gustafsson, M.G. (2000). Surpassing the Lateral Resolution Limit by a Factor of Two Using Structured Illumination Microscopy. *Journal of Microscopy*, **198**, 82–87.

Hada, M. *et al.* (2006). Spectrum of Complex DNA Damages Depends on the Incident Radiation. *Radiation Research*, **165**, 223–230.

Hada, M. *et al.* (2016). Cytosolic Ku70 Regulates Bax-mediated Cell Death. *Tumor Biology*, **37**, 13903–13914.

Hagiwara, Y. *et al.* (2017). 3D-structured Illumination Microscopy Reveals Clustered DNA Double-strand Break Formation in Widespread γH2AX Foci After High LET Heavy-ion Particle Radiation. *Oncotarget*, **8**, 109370.

Halazonetis, T.D. *et al.* (2008). An Oncogene-Induced DNA Damage Model for Cancer Development. *Science*, **319**, 1352–1355.

Hall, E.J. *et al.* (2012). *Radiobiology for the Radiologist*. Lippincott Williams & Wilkins, 7th edn.

Hamada, N. *et al.* (2006). Histone H2AX Phosphorylation in Normal Human Cells Irradiated with Focused Ultrasoft X Rays: Evidence for Chromatin Movement during Repair. *Radiation Research*, **166**, 31–38.

Harper, J.V. *et al.* (2010). Radiation Induced DNA DSBs: Contribution From Stalled Replication Forks? *DNA repair*, **9**, 907–913.

Harris, L.J. *et al.* (1997). Refined Structure of an Intact IgG2a Monoclonal Antibody. *Biochemistry*, **36**, 1581–1597.

Hartwell, L.H. *et al.* (1989). Checkpoints: Controls That Ensure the Order of Cell Cycle Events. *Science*, **246**, 629–34.

Hausmann, M. *et al.* (2018). Super-resolution Localization Microscopy of Radiation-induced Histone H2AX-phosphorylation in Relation to H3K9-trimethylation in HeLa Cells. *Nanoscale*, **10**, 4320–4331.

Hell, S.W. *et al.* (1994). Breaking the Diffraction Resolution Limit by Stimulated Emission: Stimulated-Emission-Depletion Fluorescence Microscopy. *Optics Letters*, **19**, 780–782.

Herbert, A.D. *et al.* (2014). FindFoci: A Focus Detection Algorithm With Automated Parameter Training That Closely Matches Human Assignments, Reduces Human Inconsistencies and Increases Speed of Analysis. *PLoS ONE*, **9**, e114749.

BIBLIOGRAPHY

Hernández, L. *et al.* (2013). Highly Sensitive Automated Method for DNA Damage Assessment: γ-H2AX Foci Counting and Cell Cycle Sorting. *International Journal of Molecular Sciences*, **14**, 15810–15826.

Higashiura, M. *et al.* (1992). Immunolocalization of Ku-proteins (p80/p70): Localization of p70 to Nucleoli and Periphery of Both Interphase Nuclei and Metaphase Chromosomes. *Experimental Cell Research*, **201**, 444–451.

Hill, M.A. (2020). Radiation Track Structure: How the Spatial Distribution of Energy Deposition Drives Biological Response. *Clinical Oncology*, **32**, 75–83.

Hirai, T. *et al.* (2012). Radiosensitization Effect of Poly(ADP-ribose) Polymerase Inhibition in Cells Exposed to Low and High Liner Energy Transfer Radiation. *Cancer Science*, **103**, 1045–1050.

Höckel, M. *et al.* (1996). Hypoxia and Radiation Response in Human Tumors. In *Seminars in Radiation Oncology*, vol. 6, 3–9, Elsevier.

Höglund, E. *et al.* (2001). Induction and Rejoining of DNA Double-Strand Breaks in Normal Human Skin Fibroblasts after Exposure to Radiation of Different Linear Energy Transfer: Possible Roles of Track Structure and Chromatin Organization. *Radiation Research*, **155**, 818–825.

Holcomb, V.B. *et al.* (2008). Ku80 Deletion Suppresses Spontaneous Tumors and Induces a p53-mediated DNA Damage Response. *Cancer Research*, **68**, 9497–9502.

Holton, N.W. *et al.* (2017). Application of Laser Micro-irradiation for Examination of Single and Double Strand Break Repair in Mammalian Cells. *Journal of Visualized Experiments*, **127**, e56265.

Horn, S. *et al.* (2011). γ-H2AX-based Dose Estimation for Whole and Partial Body Radiation Exposure. *PLoS ONE*, **6**, e25113.

Hu, C.D. *et al.* (2002). Visualization of Interactions Among bZIP and Rel Family Proteins in Living Cells Using Bimolecular Fluorescence Complementation. *Molecular Cell*, **9**, 789–798.

Hu, H. *et al.* (2010). Expression of TRF1, TRF2, TIN2, TERT, KU70, and BRCA1 Proteins Is Associated With Telomere Shortening and May Contribute to Multistage Carcinogenesis of Gastric Cancer. *Journal of Cancer Research and Clinical Oncology*, **136**, 1407–1414.

Huang, L. *et al.* (2014). Potential Pitfalls and Solutions for Use of Fluorescent Fusion Proteins to Study the Lysosome. *PLoS ONE*, **9**, e88893.

Huang, L.K. *et al.* (1995). Image Segmentation by Histogram Thresholding Using Fuzzy Sets. *Pattern Recognition*, **11**, 1457–1465.

Huber, L.A. *et al.* (2003). Organelle Proteomics: Implications for Subcellular Fractionation in Proteomics. *Circulation Research*, **92**, 962–968.

Huff, J. (2015). The Airyscan Detector from ZEISS: Confocal Imaging with Improved Signal-to-noise Ratio and Super-resolution. *Nature Methods*, **12**, i–ii.

Hutchinson, F. (1966). The Molecular Basis for Radiation Effects on Cells. *Cancer Research*, **9**, 2045–2052.

Iacovoni, J.S. *et al.* (2010). High-resolution Profiling of γH2AX around DNA Double Strand Breaks in the Mammalian Genome. *The EMBO journal*, **29**, 1446–1457.

ICRP (1998). Genetic Susceptibility to Cancer: ICRP Publication 79. Tech. Rep. 1-2, Annals of the ICRP.

ICRP (2005). Low-dose Extrapolation of Radiation-related Cancer Risk: ICRP Publication 99. Tech. Rep. 4, Annals of the ICRP.

ICRU (1970). ICRU Report 16: Linear Energy Transfer. Tech. Rep. 1, Journal of the International Commission on Radiation Units and Measurements.

Iliakis, G. *et al.* (2004). Mechanisms of DNA Double Strand Break Repair and Chromosome Aberration Formation. *Cytogenetic and Genome Research*, **104**, 14–20.

Ira, G. *et al.* (2004). DNA End Resection, Homologous Recombination and DNA Damage Checkpoint Activation Require CDK1. *Nature*, **431**, 1011–1017.

Iyer, R. *et al.* (2000). Effects of Ionizing Radiation in Targeted and Nontargeted Cells. *Archives of Biochemistry and Biophysics*, **376**, 14–25.

Javle, M. *et al.* (2011). The Role of PARP in DNA Repair and Its Therapeutic Exploitation. *British Journal of Cancer*, **105**, 1114–1122.

Jenner, T.J. *et al.* (1993). Induction and Rejoining of DNA Double-Strand Breaks in V79-4 Mammalian Cells Following γ- And α-Irradiation. *International Journal of Radiation Biology*, **64**, 265–273.

Jezkova, L. *et al.* (2018). Particles with Similar LET Values Generate DNA Breaks of Different Complexity and Reparability: A High-resolution Microscopy Analysis of γH2AX/53BP1 Foci. *Nanoscale*, **10**, 1162–1179.

Jin, H. *et al.* (2020). FOXL2 Directs DNA Double-Strand Break Repair Pathways by Differentially Interacting With Ku. *Nature Communications*, **11**, 1–17.

Jin, S. *et al.* (1997). Double-strand Break Repair by Ku70 Requires Heterodimerization With Ku80 and DNA Binding Functions. *The EMBO Journal*, **16**, 6874–6885.

Kacperek, A. (2009). Protontherapy of eye tumours in the UK: a review of treatment at Clatterbridge. *Applied Radiation and Isotopes*, **67**, 378–386.

Kadhim, M. *et al.* (2013). Non-targeted Effects of Ionising Radiation—implications for Low Dose Risk. *Mutation Research/Reviews in Mutation Research*, **752**, 84–98.

Kang, P.J. *et al.* (2010). The Rsr1/Bud1 GTPase Interacts With Itself and the Cdc42 GTPase During Bud-Site Selection and Polarity Establishment in Budding Yeast. *Molecular Biology of the Cell*, **21**, 3007–3016.

Kanno, S.i. *et al.* (2007). A Novel Human AP Endonuclease With Conserved Zinc-Finger-Like Motifs Involved in DNA Strand Break Responses. *EMBO Journal*, **26**, 2094–2103.

Kass, E.M. *et al.* (2010). Collaboration and Competition Between DNA Double-Strand Break Repair Pathways. *FEBS Letters*, **584**, 3703–3708.

BIBLIOGRAPHY

Kastan, M.B. *et al.* (2004). Cell-cycle Checkpoints and Cancer. *Nature*, **432**, 316–323.

Kataoka, Y. *et al.* (2006). Flow Cytometric Analysis of Phosphorylated Histone H2AX Following Exposure to Ionizing Radiation in Human Microvascular Endothelial Cells. *Journal of Radiation Research*, **47**, 245–257.

Kerppola, T.K. (2008). Bimolecular Fluorescence Complementation (BiFC) Analysis as a Probe of Protein Interactions in Living Cells. *Annual Review of Biophysics*, **37**, 465–487.

Kerppola, T.K. (2009). Visualization of Molecular Interactions Using Bimolecular Fluorescence Complementation Analysis: Characteristics of Protein Fragment Complementation. *Chemical Society Reviews*, **38**, 2876–2886.

Kim, J. *et al.* (2012). Quantification of Protein Interaction in Living Cells by Two-Photon Spectral Imaging With Fluorescent Protein Fluorescence Resonance Energy Transfer Pair Devoid of Acceptor Bleed-Through. *Cytometry Part A*, **81**, 112–119.

Kim, J.S. *et al.* (2005). Independent and Sequential Recruitment of NHEJ and HR Factors to DNA Damage Sites in Mammalian Cells. *Journal of Cell Biology*, **170**, 341–347.

Kinner, A. *et al.* (2008). γ-H2AX in Recognition and Signaling of DNA Double-Strand Breaks in the Context of Chromatin. *Nucleic acids research*, **36**, 5678–5694.

Klucken, J. *et al.* (2006). Detection of Novel Intracellular α-Synuclein Oligomeric Species by Fluorescence Lifetime Imaging. *The FASEB Journal*, **20**, 2050–2057.

Kodama, Y. *et al.* (2010). An Improved Bimolecular Fluorescence Complementation Assay With a High Signal-To-Noise Ratio. *BioTechniques*, **49**, 793–805.

Kodama, Y. *et al.* (2012). Bimolecular Fluorescence Complementation (BiFC): A 5-year Update and Future Perspectives. *BioTechniques*, **53**, 285–298.

Kohn, E.C. *et al.* (2017). The HRD Decision — which PARP Inhibitor to Use for Whom and When. *Clinical Cancer Research*, **23**, 7155–7157.

Koike, M. (2002). Dimerization, Translocation and Localization of Ku70 and Ku80 Proteins. *Journal of Radiation Research*, **43**, 223–236.

Koike, M. *et al.* (1998). Subcellular Localization and Protein-Protein Interaction Regions of Ku Proteins. *Biochemical and Biophysical Research Communications*, **252**, 679–685.

Koike, M. *et al.* (2001). Dimerization and Nuclear Localization of Ku Proteins. *Journal of Biological Chemistry*, **276**, 11167–11173.

Koike, M. *et al.* (2015). Nuclear Localization of Mouse Ku70 in Interphase Cells and Focus Formation of Mouse Ku70 at DNA Damage Sites Immediately After Irradiation. *Journal of Veterinary Medical Science*, **77**, 1137–1142.

Koike, M. *et al.* (2017a). Cloning, Localization and Focus Formation at DNA Damage Sites of Canine Ku70. *Journal of Veterinary Medical Science*, **79**, 554–561.

Koike, M. *et al.* (2017b). Cloning of Canine Ku80 and Its Localization and Accumulation at DNA Damage Sites. *FEBS Open Bio*, **7**, 1854–1863.

Kong, X. *et al.* (2009). Comparative Analysis of Different Laser Systems to Study Cellular Responses to DNA Damage in Mammalian Cells. *Nucleic Acids Research*, **37**, e68.

Kötter, A. *et al.* (2014). Inhibition of PARP1-dependent End-joining Contributes to Olaparib-mediated Radiosensitization in Tumor Cells. *Molecular Oncology*, **8**, 1616–1625.

Kraemer, M. *et al.* (2003). The Increased Biological Effectiveness of Heavy Charged Particles: From Radiobiology to Treatment Planning. *Technology in Cancer Research and Treatment*, **2**, 427–436.

Kriechbaumer, V. *et al.* (2015). Reticulomics: Protein-Protein Interaction Studies With Two Plasmodesmata-Localized Reticulon Family Proteins Identify Binding Partners Enriched at Plasmodesmata, Endoplasmic Reticulum, and the Plasma Membrane. *Plant Physiology*, **169**, 1933–1945.

Kroeber, J. *et al.* (2015). Distinct Increased Outliers Among 136 Rectal Cancer Patients Assessed by γH2AX. *Radiation Oncology*, **10**, 36.

Krokan, H.E. *et al.* (1997). DNA Glycosylases in the Base Excision Repair of DNA. *Biochemical Journal*, **325**, 1–16.

Kuefner, M.A. *et al.* (2009). DNA Double-Strand Breaks and Their Repair in Blood Lymphocytes of Patients Undergoing Angiographic Procedures. *Investigative Radiology*, **44**, 440–446.

Kuefner, M.A. *et al.* (2010). Effect of CT Scan Protocols on X-Ray-Induced DNA Double-Strand Breaks in Blood Lymphocytes of Patients Undergoing Coronary CT Angiography. *European Radiology*, **20**, 2917–2924.

Kumari, N. *et al.* (2019). G-quadruplex Structures Contribute to Differential Radiosensitivity of the Human Genome. *iScience*, **21**, 288–307.

Lan, L. *et al.* (2004). In Situ Analysis of Repair Processes for Oxidative DNA Damage in Mammalian Cells. *Proceedings of the National Academy of Sciences of the United States of America*, **101**, 13738–13743.

Lapytsko, A. *et al.* (2015). FoCo: A Simple and Robust Quantification Algorithm of Nuclear Foci. *BMC Bioinformatics*, **16**, 392.

Lavancier, F. *et al.* (2019). Testing Independence Between Two Random Sets for the Analysis of Colocalization in Bio-imaging. *Biometrics*, **76**.

Laviv, T. *et al.* (2016). Simultaneous Dual-Color Fluorescence Lifetime Imaging With Novel Red-Shifted Fluorescent Proteins. *Nature Methods*, **13**, 989–992.

Lea, D.E. (1946). *Actions of Radiation on Living Cells*, vol. 158. Cambridge University Press.

Leatherbarrow, E.L. *et al.* (2006). Induction and Quantification of γ-H2AX Foci Following Low and High LET-irradiation. *International Journal of Radiation Biology*, **82**, 111–118.

Lee, J.Y. *et al.* (2011). Effects of Histone Acetylation by Piccolo NuA4 on the Structure of a Nucleosome and the Interactions Between Two Nucleosomes. *Journal of Biological Chemistry*, **286**, 11099–11109.

Lee, L.Y. *et al.* (2008). Vectors for Multi-Color Bimolecular Fluorescence Complementation to Investigate Protein-Protein Interactions in Living Plant Cells. *Plant Methods*, **4**, 24.

Lehnert, S. (2008). *Biomolecular Action of Ionizing Radiation*. Medical Physics and Biomedical Engineering Series, Taylor & Francis Group, Boca Raton, FL.

Li, H. *et al.* (2007). Deletion of ku70, ku80, or both causes early aging without substantially increased cancer. *Molecular and Cellular Biology*, **27**, 8205–8214.

Li, L.L. *et al.* (1992). Cell Cycle-Dependent Migration of the DNA-binding Protein Ku80 Into Nucleoli. *Experimental Cell Research*, **199**, 262–268.

Lilley, D.M. (2000). Structures of Helical Junctions in Nucleic Acids. *Quarterly Reviews of Biophysics*, **33**, 109–159.

Lin, F.L. *et al.* (1984). Model for Homologous Recombination During Transfer of DNA Into Mouse L Cells: Role for DNA Ends in the Recombination Process. *Molecular and Cellular Biology*, **4**, 1020–1034.

Lindahl, T. *et al.* (2000). Repair of Endogenous DNA Damage. *Cold Spring Harbor Symposia on Quantitative Biology*, 127–133.

Lobachevsky, P. *et al.* (2016). Compromized DNA Repair as a Basis for Identification of Cancer Radiotherapy Patients With Extreme Radiosensitivity. *Cancer Letters*, **383**, 212–219.

Löbrich, M. *et al.* (1996). Non-random Distribution of DNA Double-Strand Breaks Induced by Particle Irradiation. *International Journal of Radiation Biology*, **70**, 493–503.

Löbrich, M. *et al.* (2005). In Vivo Formation and Repair of DNA Double-Strand Breaks After Computed Tomography Examinations. *Proceedings of the National Academy of Sciences of the United States of America*, **102**, 8984–8989.

Löbrich, M. *et al.* (2010). γH2AX Foci Analysis for Monitoring DNA Double-strand Break Repair: Strengths, Limitations and Optimization. *Cell Cycle*, **9**, 662–669.

Lu, C.H. *et al.* (2019). Lightsheet Localization Microscopy Enables Fast, Large-Scale, and Three-Dimensional Super-Resolution Imaging. *Communications Biology*, **2**, 177.

Lyer, R.R. *et al.* (2006). DNA Mismatch Repair: Functions and Mechanisms. *Chemical Reviews*, **106**, 302–323.

Ma, Y. *et al.* (2002). Hairpin Opening and Overhang Processing by an Artemis/DNA-dependent Protein Kinase Complex in Nonhomologous End Joining and V(D)J Recombination. *Cell*, **108**, 781–794.

Macphail, S.H. *et al.* (2003). Expression of Phosphorylated Histone H2AX in Cultured Cell Lines Following Exposure to X-rays. *International Journal of Radiation Biology*, **79**, 351–358.

Mahrhofer, H. *et al.* (2006). Radiation Induced DNA Damage and Damage Repair in Human Tumor and Fibroblast Cell Lines Assessed by Histone H2AX Phosphorylation. *International Journal of Radiation Oncology Biology Physics*, **64**, 573–580.

MALYARCHUK, S. *et al.* (2009). Apex1 Can Cleave Complex Clustered DNA Lesions in Cells. *DNA Repair*, **8**, 1343–1354.

MANDERS, E.M.M. *et al.* (1992). Dynamics of Three-Dimensional Replication Patterns During the S-phase, Analysed by Double Labelling of DNA and Confocal Microscopy. *Journal of Cell Science*, **103**, 857–862.

MANSOUR, W.Y. *et al.* (2010). The Alternative End-Joining Pathway for Repair of DNA Double-Strand Breaks Requires PARP1 but Is Not Dependent Upon Microhomologies. *Nucleic Acids Research*, **38**, 6065–6077.

MANSOUR, W.Y. *et al.* (2013). The Absence of Ku but Not Defects in Classical Non-homologous End-joining Is Required to Trigger PARP1-dependent End-joining. *DNA Repair*, **12**, 1134–1142.

MARI, P.O. *et al.* (2006). Dynamic Assembly of End-Joining Complexes Requires Interaction Between Ku70/80 and XRCC4. *Proceedings of the National Academy of Sciences of the United States of America*, **103**, 18597–18602.

MARKOVÁ, E. *et al.* (2007). Kinetics and Dose-response of Residual 53BP1/γ-H2AX Foci: Co-localization, Relationship with DSB Repair and Clonogenic Survival. *International Journal of Radiation Biology*, **85**, 319–329.

MARNEF, A. *et al.* (2017). Organizing DNA Repair in The Nucleus: DSBs Hit The Road. *Current Opinion in Cell Biology*, **46**, 1–8.

MAVRAGANI, I.V. *et al.* (2017). Complex DNA Damage: A Route to Radiation-induced Genomic Instability and Carcinogenesis. *Cancers*, **9**, 91.

MCFADDEN, C.H. *et al.* (2016). Time-lapse monitoring of dna damage colocalized with particle tracks in single living cells. *International Journal of Radiation Oncology Biology Physics*, **96**, 221–227.

MCMANUS, K.J. *et al.* (2005). ATM-dependent DNA Damage-Independent Mitotic Phosphorylation of H2AX in Normally Growing Mammalian Cells. *Molecular Biology of the Cell*, **16**, 5013–5025.

MEDER, V.S. *et al.* (2005). PARP-1 and PARP-2 Interact with Nucleophosmin/B23 and Accumulate in Transcriptionally Active Nucleoli. *Journal of Cell Science*, **118**, 211–222.

MEIER, A. *et al.* (2007). Spreading of Mammalian DNA-damage Response Factors Studied by ChIP-chip at Damaged Telomeres. *The EMBO journal*, **26**, 2707–2718.

MEYER, B. *et al.* (2013). Clustered DNA Damage Induces Pan-nuclear H2AX Phosphorylation Mediated by ATM and DNA-PK. *Nucleic Acids Research*, **41**, 6109–6118.

MILLER, K.E. *et al.* (2015). Bimolecular Fluorescence Complementation (BiFC) Analysis: Advances and Recent Applications for Genome-Wide Interaction Studies. *Journal of Molecular Biology*, **427**, 2039–2055.

MILLER, R.C. *et al.* (1995). The Biological Effectiveness of Radon-Progeny α Particles. II. Oncogenic Transformation as a Function of Linear Energy Transfer. *Radiation Research*, **142**, 54–60.

BIBLIOGRAPHY

Mimitou, E.P. *et al.* (2008). Sae2, Exo1 and Sgs1 Collaborate in DNA Double-Strand Break Processing. *Nature*, **455**, 770–774.

Moore, J.K. *et al.* (1996). Cell Cycle and Genetic Requirements of Two Pathways of Nonhomologous End-joining Repair of Double-strand Breaks in Saccharomyces Cerevisiae. *Molecular and Cellular Biology*, **16**, 2164–2173.

Mortusewicz, O. *et al.* (2007). XRCC1 and PCNA Are Loading Platforms With Distinct Kinetic Properties and Different Capacities to Respond to Multiple DNA Lesions. *BioMed Central Molecular Biology*, **8**, 81–89.

Murai, J. *et al.* (2012). Trapping of PARP1 and PARP2 by Clinical PARP Inhibitors. *Cancer Research*, **72**, 5588–5599.

Murakoshi, H. *et al.* (2004). Single-molecule Imaging Analysis of Ras Activation in Living Cells. *Proceedings of the National Academy of Sciences of the United States of America*, **101**, 7317–7322.

Murshed, H. (2019). *Fundamentals of Radiation Oncology: Physical, Biological, and Clinical Aspects*. Academic Press.

Myers, J.S. *et al.* (2006). Rapid Activation of ATR by Ionizing Radiation Requires ATM and Mre11. *Journal of Biological Chemistry*, **281**, 9346–9350.

Nakamura, K. *et al.* (2011). Regulation of Homologous Recombination by RNF20-Dependent H2B Ubiquitination. *Molecular Cell*, **41**, 515–528.

Natale, F. *et al.* (2017). Identification of the Elementary Structural Units of the DNA Damage Response. *Nature Communications*, **8**, 15760.

National Research Council USA (2006). Health Risks from Exposure to Low Levels of Ionizing Radiation. BEIR VII Phase 2. *National Academies Press*.

Neuhaus, E.M. *et al.* (1998). Ethane-freezing/methanol-fixation of Cell Monolayers: A Procedure for Improved Preservation of Structure and Antigenicity for Light and Electron Microscopies. *Journal of Structural Biology*, **121**, 326–342.

Neumaier, T. *et al.* (2012). Evidence for Formation of DNA Repair Centers and Dose-Response Nonlinearity in Human Cells. *Proceedings of the National Academy of Sciences of the United States of America*, **109**, 443–448.

Nick McElhinny, S.A. *et al.* (2000). Ku Recruits the XRCC4-ligase IV Complex to DNA Ends. *Molecular and Cellular Biology*, **20**, 2996–3003.

Nick McElhinny, S.A. *et al.* (2005). A Gradient of Template Dependence Defines Distinct Biological Roles for Family X Polymerases in Nonhomologous End Joining. *Molecular Cell*, **19**, 357–366.

Nickoloff, J.A. *et al.* (2020). Clustered DNA Double-Strand Breaks: Biological Effects and Relevance to Cancer Radiotherapy. *Genes*, **11**, 99.

Nickson, C.M. *et al.* (2017). Misregulation of DNA Damage Repair Pathways in HPV-positive Head and Neck Squamous Cell Carcinoma Contributes to Cellular Radiosensitivity. *Oncotarget*, **8**, 29963 – 29975.

Niemantsverdriet, M. *et al.* (2012). High and Low LET Radiation Differentially Induce Normal Tissue Damage Signals. *International Journal of Radiation Oncology Biology Physics*, **83**, 1291–1297.

Nikitaki, Z. *et al.* (2016a). Measurement of Complex DNA Damage Induction and Repair in Human Cellular Systems after Exposure to Ionizing Radiations of Varying Linear Energy Transfer (LET). *Free Radical Research*, **50**, S64–S78.

Nikitaki, Z. *et al.* (2016b). Non-dSB Clustered DNA Lesions. Does Theory Colocalize with the Experiment? *Radiation Physics and Chemistry*, **128**, 26–35.

Nikjoo, H. *et al.* (1998). Track Structure in Radiation Biology: Theory and Applications. *International Journal of Radiation Biology*, **73**, 355–364.

Nikjoo, H. *et al.* (2001). Computational Approach for Determining the Spectrum of DNA Damage Induced by Ionizing Radiation. *Radiation Research*, **156**, 577–583.

Ochs, F. *et al.* (2019). Stabilization of Chromatin Topology Safeguards Genome Integrity. *Nature*, **574**, 571–574.

Oike, T. *et al.* (2016). Visualization of Complex DNA Double-Strand Breaks in a Tumor Treated With Carbon Ion Radiotherapy. *Scientific Reports*, **6**, 22275.

Ottolenghi, A. *et al.* (1997). DNA Complex Lesions Induced by Protons and α-Particles: Track Structure Characteristics Determining Linear Energy Transfer and Particle Type Dependence. *Radiation and Environmental Biophysics*, **36**, 97–103.

Panier, S. *et al.* (2014). Double-strand Break Repair: 53BP1 Comes Into Focus. *Nature Reviews Molecular cell biology*, **15**, 7–18.

Pankotai, T. *et al.* (2009). DNA Damage Response in the Absence of DNA Lesions Continued. *Cell Cycle*, **8**, 4025–4026.

Parrella, P. *et al.* (2006). Expression and Heterodimer-binding Activity of Ku70 and Ku80 in Human Non-melanoma Skin Cancer. *Journal of Clinical Pathology*, **59**, 1181–1185.

Parvathaneni, S. *et al.* (2013). Human RECQ1 Interacts with Ku70/80 and Modulates DNA End-Joining of Double-Strand Breaks. *PLoS ONE*, **8**, e62481.

Paull, T.T. *et al.* (2000). A Critical Role for Histone H2AX in Recruitment of Repair Factors to Nuclear Foci After DNA Damage. *Current Biology*, **10**, 886–895.

Pawlik, T.M. *et al.* (2004). Role of Cell Cycle in Mediating Sensitivity to Radiotherapy. *International Journal of Radiation Oncology Biology Physics*, **59**, 928–942.

Perez, R.L. *et al.* (2016). Superresolution Light Microscopy Shows Nanostructure of Carbon Ion Radiation-Induced DNA Double-Strand Break Repair Foci. *FASEB Journal*, **30**, 2767–2776.

Peterson, S.R. *et al.* (1995). Loss of the Catalytic Subunit of the DNA-dependent Protein Kinase in DNA Double-Strand-Break-Repair Mutant Mammalian Cells. *Proceedings of the National Academy of Sciences of the United States of America*, **8**, 3171–3174.

BIBLIOGRAPHY

Petrini, J.H.J. *et al.* (2003). The Cellular Response to DNA Double-Strand Breaks: Defining the Sensors and Mediators. *Trends in Cell Biology*, **13**, 458–462.

Pinto, M. *et al.* (2005). Evidence for Complexity at the Nanometer Scale of Radiation-Induced DNA DSBs as a Determinant of Rejoining Kinetics. *Radiation Research*, **164**, 73–85.

Plotly Technologies Inc. (2015). Collaborative Data Science.

Pospelova, T.V. *et al.* (2009). Pseudo-DNA Damage Response in Senescent Cells. *Cell Cycle*, **8**, 4112–4118.

Povirk, L.F. *et al.* (2007). Processing of 3'-phosphoglycolate-terminated DNA Double Strand Breaks by Artemis Nuclease. *Journal of Biological Chemistry*, **282**, 3547–3558.

Prasad, R. *et al.* (1996). Specific Interaction of DNA Polymerase-Beta and DNA Ligase I in a Multiprotein Base Excision Repair Complex From Bovine Testis. *Journal of Biological Chemistry*, **271**, 16000–16007.

Prelich, G. (2012). Gene Overexpression: Uses, Mechanisms, and Interpretation. *Genetics*, **190**, 841–854.

Prise, K.M. *et al.* (1998). A Review of DSB Induction Data for Varying Quality Radiations. *International Journal of Radiation Biology*, **74**, 173–184.

Pucci, S. *et al.* (2001). Tumor Specific Modulation of KU70/80 DNA Binding Activity in Breast and Bladder Human Tumor Biopsies. *Oncogene*, **20**, 739–747.

Quanz, M. *et al.* (2012). Heat Shock Protein 90α (Hsp90α) Is Phosphorylated in Response to DNA Damage and Accumulates in Repair Foci. *Journal of Biological Chemistry*, **287**, 8803–8815.

Ramadan, K. *et al.* (2004). De Novo DNA Synthesis by Human DNA Polymerase-Lambda, DNA Polymerase-Mu and Terminal Deoxyribonucleotidyl Transferase. *Journal of Molecular Biology*, **339**, 395–404.

Ramsden, D.A. *et al.* (1998). Ku Protein Stimulates DNA End Joining by Mammalian DNA Ligases: A Direct Role for Ku in Repair of DNA Double-Strand Breaks. *EMBO Journal*, **17**, 609–614.

Rasmussen, R.E. *et al.* (1964). Evidence for Repair of Ultra-Violet Damaged Deoxyribonucleic Acid in Cultured Mammalian Cells. *Nature*, **203**, 1360–1362.

Redon, C.E. *et al.* (2010). The Use of γ-H2AX as a Biodosimeter for Total-Body Radiation Exposure in Non-Human Primates. *PLoS ONE*, **5**, e15544.

Redon, C.E. *et al.* (2011). Qγ-H2AX, an Analysis Method for Partial-body Radiation Exposure Using γ-H2AX in Non-human Primate Lymphocytes. *Radiation Measurements*, **46**, 877–881.

Reindl, J. *et al.* (2015). Nanoscopic Exclusion Between Rad51 and 53BP1 After Ion Irradiation in Human HeLa Cells. *Physical Biology*, **12**, 066005.

Reindl, J. *et al.* (2017). Chromatin Organization Revealed by Nanostructure of Irradiation Induced γH2AX, 53BP1 and Rad51 Foci. *Scientific Reports*, **7**, 40616.

Reynolds, P. (2009). *Investigation of Cellular DNA Damage Induced by Multiphoton Laser Light Absorption of Near Infrared Femtosecond Laser Pulses*. Ph.D. thesis, University of Reading.

Reynolds, P. *et al.* (2012). The Dynamics of Ku70/80 and DNA-PKcs at DSBs Induced by Ionizing Radiation Is Dependent on the Complexity of Damage. *Nucleic Acids Research*, **40**, 10821–10831.

Riballo, E. *et al.* (2004). A Pathway of Double-strand Break Rejoining Dependent upon ATM, Artemis, and Proteins Locating to γ-H2AX Foci. *Molecular Cell*, **16**, 715–724.

Ribes-Zamora, A. *et al.* (2013). TRF2 Interaction with Ku Heterotetramerization Interface Gives Insight into c-NHEJ Prevention at Human Telomeres. *Cell Reports*, **5**, 194–206.

Rivera-Calzada, A. *et al.* (2005). Three-dimensional Structure and Regulation of the DNA-dependent Protein Kinase Catalytic Subunit (DNA-PKcs). *Structure*, **13**, 243–255.

Rivera-Calzada, A. *et al.* (2007). Structural Model of Full-Length Human Ku70-Ku80 Heterodimer and Its Recognition of DNA and DNA-PKcs. *EMBO Reports*, **8**, 56–62.

Roberts, T.M. *et al.* (2016). Identification and Characterisation of a pH-stable GFP. *Scientific Reports*, **6**, 28166.

Rodriguez-Berriguete, G. *et al.* (2018). Nucleoporin 54 Contributes to Homologous Recombination Repair and Post-replicative DNA Integrity. *Nucleic Acids Research*, **46**, 7731–7746.

Ronneberger, O. *et al.* (2008). Spatial Quantitative Analysis of Fluorescently Labeled Nuclear Structures: Problems, Methods, Pitfalls. *Chromosome Research*, **16**, 523–562.

Roos, W.P. *et al.* (2006). DNA Damage-Induced Cell Death by Apoptosis. *Trends in Molecular Medicine*, **12**, 440–450.

Rothkamm, K. *et al.* (2009). γ-H2AX as Protein Biomarker for Radiation Exposure. *Annali dell'Istituto Superiore di Sanita*, **45**, 265–271.

Rothkamm, K. *et al.* (2003). Evidence for a Lack of DNA Double-Strand Break Repair in Human Cells Exposed to Very Low X-Ray Doses. *Proceedings of the National Academy of Sciences of the United States of America*, **100**, 5057–5062.

Rübe, C.E. *et al.* (2008). DNA Double-Strand Break Rejoining in Complex Normal Tissues. *International Journal of Radiation Oncology Biology Physics*, **72**, 1180–1187.

Rust, M.K. *et al.* (2006). Sub-diffraction-limit Imaging by Stochastic Optical Reconstruction Microscopy (STORM). *Nature Methods*, **3**, 793–795.

Rüther, U. (1980). Construction and Properties of a New Cloning Vehicle, Allowing Direct Screening for Recombinant Plasmids. *Molecular & General Genetics*, **178**, 475–477.

Rutkowska, A. *et al.* (2016). A Modular Probe Strategy for Drug Localization, Target Identification and Target Occupancy Measurement on Single Cell Level. *ACS Chemical Biology*, **11**, 2541–2550.

Sage, E. *et al.* (2011). Clustered DNA Lesion Repair in Eukaryotes: Relevance to Mutagenesis and Cell Survival. *Mutation Research/Fundamental and Molecular Mechanisms of Mutagenesis*, **711**, 123–133.

Sage, E. *et al.* (2017). Radiation-induced Clustered DNA Lesions: Repair and Mutagenesis. *Free Radical Biology and Medicine*, **107**, 125–135.

Sak, A. *et al.* (2007). γ-H2AX Foci Formation in Peripheral Blood Lymphocytes of Tumor Patients after Local Radiotherapy to Different Sites of the Body: Dependence on the Dose-distribution, Irradiated Site and Time from Start of Treatment. *International Journal of Radiation Biology*, **83**, 639–652.

Sakon, J.J. *et al.* (2010). Detecting the Conformation of Individual Proteins in Live Cells. *Nature Methods*, **7**, 203–205.

Sarasin, A. *et al.* (1997). Human Cancer and DNA Repair-Deficient Diseases. *Cancer Detection and Prevention*, **21**, 406–411.

Sattarzadeh, A. *et al.* (2015). Green to Red Photoconversion of GFP for Protein Tracking in Vivo. *Scientific Reports*, **5**, 11771.

Scherthan, H. *et al.* (2008). Accumulation of DSBs in γ-H2AX Domains Fuel Chromosomal Aberrations. *Biochemical and Biophysical Research Communications*, **371**, 694–697.

Schindelin, J. *et al.* (2012). Fiji: An open-source platform for biological-image analysis. *Nature Methods*, **9**, 676–682.

Schmid, T.E. *et al.* (2010). Differences in the Kinetics of γ-H2AX Fluorescence Decay after Exposure to Low and High LET Radiation. *International Journal of Radiation Biology*, **86**, 682–691.

Schneider, J. *et al.* (2019). Open Source Bioimage Informatics Tools for the Analysis of Dna Damage and Associated Biomarkers. *Journal of Laboratory and Precision Medicine*, **4**.

Schnell, U. *et al.* (2012). Immunolabeling Artifacts and the Need for Live-Cell Imaging. *Nature Methods*, **9**, 152–158.

Schultz, L.B. *et al.* (2000). p53 Binding Protein 1 (53BP1) Is an Early Participant in the Cellular Response to DNA Double-Strand Breaks. *Journal of Cell Biology*, **151**, 1381–1390.

Schwarz, B. *et al.* (2019). Nanoscopic Analysis of 53BP1, BRCA1 and Rad51 Reveals New Insights in Temporal Progression of DNA-repair and Pathway Choice. *Mutation Research/Fundamental and Molecular Mechanisms of Mutagenesis*, **816**, 111675.

Scott, C.L. *et al.* (2015). Poly (ADP-ribose) Polymerase Inhibitors: Recent Advances and Future Development. *Journal of Clinical Oncology*, **33**, 1397–1406.

Scott, D.J. *et al.* (2018). A Novel Ultra-Stable, Monomeric Green Fluorescent Protein for Direct Volumetric Imaging of Whole Organs Using CLARITY. *Scientific Reports*, **8**, 667.

Selvin, P.R. (2000). The Renaissance of Fluorescence Resonance Energy Transfer. *Nature Structural Biology*, **7**, 730–734.

Selvin, P.R. *et al.* (2008). *Single-molecule Techniques: A Laboratory Manual*. CSHL Press.

Setlow, R.B. *et al.* (1964). The Disappearance of Thymine Dimers From DNA: An Error-Correcting Mechanism. *Proceedings of the National Academy of Sciences of the United States of America*, **51**, 226–231.

Shah, K. *et al.* (2016). γH2AX Expression in Cytological Specimens as a Biomarker of Response to Radiotherapy in Solid Malignancies. *Diagnostic Cytopathology*, **44**, 141–146.

Shah, S.N. *et al.* (2010). Defective Mismatch Repair, Microsatellite Mutation Bias, and Variability in Clinical Cancer Phenotypes. *Cancer Research*, **70**, 431–435.

Shaltiel, I.A. *et al.* (2015). The Same, Only Different - DNA Damage Checkpoints and Their Reversal Throughout the Cell Cycle. *Journal of Cell Science*, **128**, 607–620.

Shaner, N.C. *et al.* (2008). Improving the Photostability of Bright Monomeric Orange and Red Fluorescent Proteins. *Nature Methods*, **5**, 545–551.

Shao, L. *et al.* (2011). Super-resolution 3D Microscopy of Live Whole Cells Using Structured Illumination. *Nature Methods*, **8**, 1044–1046.

Sharma, S. (2014). An Appraisal of RECQ1 Expression in Cancer Progression. *Frontiers in Genetics*, **5**, 426.

Shemiakina, I.I. *et al.* (2012). A Monomeric Red Fluorescent Protein with Low Cytotoxicity. *Nature communications*, **3**, 1204.

Sheppard, C.J.R. *et al.* (1977). Image Formation in the Scanning Microscope. *Optica Acta: International Journal of Optics*, **24**, 1051–1073.

Shyu, Y.J. *et al.* (2008). Fluorescence Complementation: An Emerging Tool for Biological Research. *Trends in Biotechnology*, **26**, 622–630.

Shyu, Y.J. *et al.* (2006). Identification of New Fluorescent Protein Fragments for Bimolecular Fluorescence Complementation Analysis Under Physiological Conditions. *BioTechniques*, **40**, 61–66.

Singh, S.K. *et al.* (2013). Reduced Contribution of Thermally Labile Sugar Lesions to DNA Double Strand Break Formation after Exposure to Heavy Ions. *Radiation Oncology*, **8**, 77.

Singhal, R.K. *et al.* (1995). DNA Polymerase-Beta Conducts the Gap-Filling Step in Uracil-Initiated Base Excision Repair in a Bovine Testis Nuclear Extract. *Journal of Biological Chemistry*, **270**, 949–957.

Singleton, B.K. *et al.* (2002). Clustered DNA Damage Leads to Complex Genetic Changes in Irradiated Human Cells. *Cancer Research*, **62**, 6263–6269.

Sisario, D. *et al.* (2018). Nanostructure of DNA Repair Foci Revealed by Superresolution Microscopy. *FASEB Journal*, fj201701435.

Sobol, R.W. *et al.* (1996). Requirement of Mammalian DNA Polymerase-Beta in Base-Excision Repair. *Nature*, **379**, 183–186.

Sommer, C. *et al.* (2013). Machine Learning in Cell Biology - Teaching Computers to Recognize Phenotypes. *Journal of Cell Science*, **126**, 5529–5539.

Song, K. *et al.* (2000). Interaction of Human Ku70 With TRF2. *FEBS Letters*, **481**, 81–85.

Spagnolo, L. *et al.* (2006). Three-dimensional Structure of the Human DNA-PKcs/Ku70/Ku80 Complex Assembled on DNA and Its Implications for DNA DSB Repair. *Molecular Cell*, **22**, 511–519.

Staaf, E. *et al.* (2012). γ-H2AX Foci in Cells Exposed to a Mixed Beam of X-rays and α Particles. *Genome Integrity*, **3**, 8.

Stenerlöw, B. *et al.* (2003). Measurement of Prompt DNA Double-Strand Breaks in Mammalian Cells without Including Heat-Labile Sites: Results for Cells Deficient in Nonhomologous End Joining. *Radiation Research*, **159**, 502–510.

Stiff, T. *et al.* (2004). ATM and DNA-PK Function Redundantly to Phosphorylate H2AX after Exposure to Ionizing Radiation. *Cancer Research*, **64**, 2390–2396.

Stubbs, C.D. *et al.* (2005). The Use of Time-Resolved Fluorescence Imaging in the Study of Protein Kinase C Localisation in Cells. *BMC Cell Biology*, **6**, 22.

Stucki, M. *et al.* (2005). MDC1 Directly Binds Phosphorylated Histone H2AX to Regulate Cellular Responses to DNA Double-Strand Breaks. *Cell*, **123**, 1213–1226.

Stumpf, W.E. (2005). Drug Localization and Targeting With Receptor Microscopic Autoradiography. *Journal of Pharmacological and Toxicological Methods*, **51**, 25–40.

Suhling, K. *et al.* (2015). Fluorescence Lifetime Imaging (FLIM): Basic Concepts and Some Recent Developments. *Medical Photonics*, **27**, 3–40.

Sun, Y. *et al.* (2010). Three-color Spectral FRET Microscopy Localizes Three Interacting Proteins in Living Cells. *Biophysical Journal*, **99**, 1274–1283.

Sung, M.K. *et al.* (2007). Bimolecular Fluorescence Complementation Analysis System for in Vivo Detection of Protein-protein Interaction in Saccharomyces Cerevisiae. *Yeast*, **24**, 767–775.

Sung, P. (1994). Catalysis of ATP-dependent Homologous DNA Pairing and Strand Exchange by Yeast RAD51 Protein. *Science*, **265**, 1241–1243.

Sung, P. *et al.* (2006). Mechanism of Homologous Recombination: Mediators and Helicases Take on Regulatory Functions. *Nature Reviews Molecular Cell Biology*, **7**, 739–750.

Suzuki, M. *et al.* (2006). Phosphorylated Histone H2AX Foci Persist on Rejoined Mitotic Chromosomes in Normal Human Diploid Cells Exposed to Ionizing Radiation. *Radiation Research*, **164**, 269–276.

Symington, L.S. *et al.* (2011). Double-Strand Break End Resection and Repair Pathway Choice. *Annual Review of Genetics*, **45**, 247–271.

Taccioli, G. *et al.* (1994). Ku80: Product of the XRCC5 Gene and Its Role in DNA Repair and V(D)J Recombination. *Science*, **265**, 1442–1445.

Taipale, M. (2018). Two Protein/Protein Interaction Assays in One Go. *Molecular Systems Biology*, **14**, e8485.

Tamura, K. *et al.* (2002). Identification of Ku70 and Ku80 Homologues in Arabidopsis Thaliana: Evidence for a Role in the Repair of DNA Double-Strand Breaks. *Plant Journal*, **29**, 771–781.

Thacker, J. *et al.* (1979). Mutation and Inactivation of Cultured Mammalian Cells Exposed to Beams of Accelerated Heavy Ions. II. Chinese Hamster V79 Cells. *International Journal of Radiation Biology and Related Studies in Physics, Chemistry and Medicine*, **36**, 137–148.

Thompson, J.M. *et al.* (2019). Tracking down α-particles: The Design, Characterisation and Testing of a Shallow-angled α-particle Irradiator. *Radiation Protection Dosimetry*, **183**, 264–269.

Thorslund, T. *et al.* (2005). Cooperation of the Cockayne Syndrome Group B Protein and Poly(ADP-Ribose) Polymerase 1 in the Response to Oxidative Stress. *Molecular and Cellular Biology*, **25**, 7625–7636.

Timm, S. *et al.* (2018). Clustered DNA Damage Concentrated in Particle Trajectories Causes Persistent Large-scale Rearrangements in Chromatin Architecture. *Radiotherapy and Oncology*, **129**, 600–610.

Tomkinson, A.E. *et al.* (2001). Completion of Base Excision Repair by Mammalian DNA Ligases. *Progress in Nucleic Acid Research and Molecular Biology*, **68**, 151–164.

Tommasino, F. *et al.* (2015). Induction and Processing of the Radiation-Induced γ-H2AX Signal and Its Link to the Underlying Pattern of DSB: A Combined Experimental and Modelling Study. *PLoS ONE*, **10**, e0129416.

Tracy, B.L. *et al.* (2015). Variation in RBE for Survival of V79-4 Cells as a Function of α-Particle (Helium Ion) Energy. *Radiation Research*, **184**, 33–45.

Truong, L.N. *et al.* (2013). Microhomology-mediated End Joining and Homologous Recombination Share the Initial End Resection Step to Repair DNA Double-Strand Breaks in Mammalian Cells. *Proceedings of the National Academy of Sciences of the United States of America*, **110**, 7720–7725.

Tsantoulis, P.K. *et al.* (2008). Oncogene-induced Replication Stress Preferentially Targets Common Fragile Sites in Preneoplastic Lesions. A Genome-Wide Study. *Oncogene*, **27**, 3256–3264.

Uematsu, N. *et al.* (2007). Autophosphorylation of DNA-PKCS Regulates Its Dynamics at DNA Double-Strand Breaks. *Journal of Cell Biology*, **177**, 219–229.

UNSCEAR (1993). Sources and Effects of Ionizing Radiation, 1993 Report. Tech. rep., United Nations Scientific Committee on the Effects of Atomic Radiation, New York.

Ustione, A. *et al.* (2011). A Simple Introduction to Multiphoton Microscopy. *Journal of microscopy*, **243**, 221–226.

Van De Linde, S. *et al.* (2011a). Photoinduced Formation of Reversible Dye Radicals and Their Impact on Super-resolution Imaging. *Photochemical and Photobiological Sciences*, **10**, 499–506.

Van De Linde, S. *et al.* (2011b). Direct Stochastic Optical Reconstruction Microscopy with Standard Fluorescent Probes. *Nature Protocols*, **6**, 991–1009.

Varga, D. *et al.* (2019). Quantification of DNA Damage Induced Repair Focus Formation via Super-Resolution dSTORM Localization Microscopy. *Nanoscale*, **11**, 14226–14236.

Velasco, M.G.M. *et al.* (2019). 3D Super-resolution Deep-tissue Imaging in Living Mice. *bioRxiv*.

Verhagen, C.V. *et al.* (2015). Extent of Radiosensitization by the PARP Inhibitor Olaparib Depends on Its Dose, the Radiation Dose and the Integrity of the Homologous Recombination Pathway of Tumor Cells. *Radiotherapy and Oncology*, **116**, 358–365.

Visser, A. *et al.* (2000). High Resolution Analysis of Interphase Chromosome Domains. *Journal of Cell Science*, **113**, 2585–2593.

Vitti, E.T. *et al.* (2019). The Radiobiological Effects of Proton Beam Therapy: Impact on DNA Damage and Repair. *Cancers*, **11**, 946.

Wäldchen, S. *et al.* (2015). Light-induced Cell Damage in Live-cell Super-resolution Microscopy. *Scientific Reports*, **5**, 15348.

Walker, J.R. *et al.* (2001). Structure of the Ku Heterodimer Bound to DNA and Its Implications for Double-Strand Break Repair. *Nature*, **412**, 607–614.

Wang, H. *et al.* (2001). Efficient Rejoining of Radiation-Induced DNA Double-Strand Breaks in Vertebrate Cells Deficient in Genes of the RAD52 Epistasis Group. *Oncogene*, **20**, 2212–2224.

Wang, H. *et al.* (2005). DNA Ligase III as a Candidate Component of Backup Pathways of Nonhomologous End Joining. *Cancer Research*, **65**, 4020–4030.

Ward, I.M. *et al.* (2001). Histone H2AX Is Phosphorylated in an ATR-dependent Manner in Response to Replicational Stress. *Journal of Biological Chemistry*, **51**, 47759–62.

Ward, I.M. *et al.* (2003). Accumulation of Checkpoint Protein 53BP1 at DNA Breaks Involves Its Binding to Phosphorylated Histone H2AX. *Journal of Biological Chemistry*, **278**, 19579–19582.

Ward, J. (1999). New Paradigms for Low-Dose Radiation Response in Proceedings of the American Statistical Association Conference on Radiation and Health. San Diego, California, USA. June 14-17, 1998. *Radiation Research*, **151**, 92–117.

Ward, J.F. (1988). DNA Damage Produced by Ionizing Radiation in Mammalian Cells: Identities, Mechanisms of Formation, and Reparability. *Progress in Nucleic Acid Research and Molecular Biology*, **35**, 95–125.

Ward, J.F. (1994). The Complexity of DNA Damage: Relevance to Biological Consequences. *International Journal of Radiation Biology*, **66**, 427–432.

Wardman, P. *et al.* (2007). Radiosensitization by Nitric Oxide at Low Radiation Doses. *Radiation Research*, **167**, 475–484.

Weaver, A.N. *et al.* (2015). DNA Double Strand Break Repair Defect and Sensitivity to Poly ADP-ribose Polymerase (PARP) Inhibition in Human Papillomavirus 16-positive Head and Neck Squamous Cell Carcinoma. *Oncotarget*, **6**, 26995–27007.

Weis, K. (2003). Regulating Access to the Genome: Nucleocytoplasmic Transport Throughout the Cell Cycle. *Cell*, **112**, 441–451.

Weiss, S. (2000). Measuring Conformational Dynamics of Biomolecules by Single Molecule Fluorescence Spectroscopy. *Nature Structural Biology*, **7**, 724–729.

Weterings, E. *et al.* (2016). A Novel Small Molecule Inhibitor of the DNA Repair Protein Ku70/80. *DNA Repair*, **43**, 98–106.

Wilson, P.F. *et al.* (2010). Inter-individual Variation in DNA Double-Strand Break Repair in Human Fibroblasts Before and After Exposure to Low Doses of Ionizing Radiation. *Mutation Research/Fundamental and Molecular Mechanisms of Mutagenesis*, **683**, 91–97.

Wilson, T. *et al.* (1984). *Theory and Practice of Scanning Optical Microscopy*, vol. 180. Academic Press London.

Wolff, S. (1998). The Adaptive Response in Radiobiology: Evolving Insights and Implications. *Environmental Health Perspectives*, **106**, 277–283.

Wright, E.G. (1998). Radiation-induced Genomic Instability in Haemopoietic Cells. *International Journal of Radiation Biology*, **74**, 681–687.

Wu, Y. *et al.* (2007). Detecting Protein-Protein Interactions by Far Western Blotting. *Nature Protocols*, **2**, 3278–3284.

Wu, Y. *et al.* (2012). Critical Evaluation of Quantitative Colocalization Analysis in Confocal Fluorescence Microscopy. *Interdisciplinary Sciences: Computational Life Sciences*, **4**, 27–37.

Wurster, S. *et al.* (2016). PARP1 Inhibition Radiosensitizes HNSCC Cells Deficient in Homologous Recombination by Disabling the DNA Replication Fork Elongation Response. *Oncotarget*, **7**, 9732–9741.

Yadav, R.B. *et al.* (2013). mTOR Direct Interactions with Rheb-GTPase and Raptor: Subcellular Localization Using Fluorescence Lifetime Imaging. *BioMed Central Cell Biology*, **14**.

Yang, L. *et al.* (2012). Secretory Vesicles Are Preferentially Targeted to Areas of Low Molecular SNARE Density. *PLoS ONE*, **7**, e49514.

Yano, K.I. *et al.* (2008). Ku Recruits XLF to DNA Double-Strand Breaks. *EMBO Reports*, **9**, 91–96.

Yokota, H. *et al.* (1995). Evidence for the Organization of Chromatin in Megabase Pair-Sized Loops Arranged Along a Random Walk Path in the Human G0/G1 Interphase Nucleus. *The Journal of Cell Biology*, **130**, 1239–1249.

Zahnreich, S. *et al.* (2015). Biodosimetry Based on γ-H2AX Quantification and Cytogenetics after Partial- and Total-Body Irradiation during Fractionated Radiotherapy. *Radiation Research*, **183**, 432–446.

BIBLIOGRAPHY

Zdańkowski, P. *et al.* (2020). Numerically Enhanced Stimulated Emission Depletion Microscopy with Adaptive Optics for Deep-Tissue Super-Resolved Imaging. *ACS Nano*, **14**, 394–405.

Zhang, X. *et al.* (2005). The Mre11/Rad50/Xrs2 Complex and Non-Homologous End-Joining of Incompatible Ends in S. Cerevisiae. *DNA Repair*, **4**, 1281–1294.

Zhang, X. *et al.* (2016). Both Complexity and Location of DNA Damage Contribute to Cellular Senescence Induced by Ionizing Radiation. *PLoS ONE*, **11**, e0155725.

Zhou, B.B. *et al.* (2000). The DNA Damage Response: Putting Checkpoints in Perspective. *Nature*, **408**, 433–439.

Zhu, Z. *et al.* (2008). Sgs1 Helicase and Two Nucleases Dna2 and Exo1 Resect DNA Double-Strand Break Ends. *Cell*, **134**, 981–994.

Appendices

Section A

A1. Labelling Reagents

5% milk powder	Sigma-Aldrich
AlexaFluor488, R37114	Thermofisher Scientific
Anti-53BP1 antibody, A300-272A	Bethyl Laboratories
Anti-H2Bub antibody, MM-0029-P	Medimabs
Anti-Ku70 antibody, ab83501	Abcam
Anti-OGG1 antibody, NB100-106	Novus biologicals
Anti-PARP-1 antibody, sc-53643	Santacruz Biotechnology
Anti-phospho-H2A.X (Ser139) antibody, JBW301	Millipore
Anti-rabbit IgG, HRP-linked Antibody, 7074	Cell-Signalling Technology
Anti-RNF20 antibody, A300-714A	Bethyl Laboratories
Bovine serum albumin (BSA)	Sigma-Aldrich
Cellytic M lysis buffer	Sigma-Aldrich
iBlot 1 Gel Transfer Device	Thermofisher Scientific
Novex Sharp Pre-stained Protein Standard	Thermofisher Scientific
NuPAGE 4-12% Bis-Tris Protein Gel	Thermofisher Scientific
NuPAGE LDS Sample Buffer (1X)	Thermofisher Scientific
NuPAGE MES SDS Running Buffer (10X)	Thermofisher Scientific

Olaparib (S1060-SEL)	Stratech Scientific
Paraformaldehyde, 4%	Sigma-Aldrich
Pierce^{TM} ECL Western Blotting Substrate	Thermofisher Scientific
Polyvinylidene difluoride (PVDF) membranes	Thermofisher Scientific
ProLong Gold Antifade Mountant with DAPI	Thermofisher Scientific
Silicon rhodamine, SC003	Spirochrome
STAR635P, ST635P-1002	Aberrior
Triton-X-100	Sigma-Aldrich
Tween-20	Sigma-Aldrich
Unconjugated goat anti-rabbit antibody, 31210	Thermofisher Scientific
X Cell SureLock Mini-Cell Electrophoresis System	Thermofisher Scientific

A2. Cloning Reagents

TBE (1X)	Sigma-Aldrich
Agar plate	Thermofisher Scientific
Agarose	Sigma-Aldrich
Carbenicillin (CB), 50 mg/ml	Sigma-Aldrich
DNA Gel Loading Dye (6X)	Thermofisher Scientific
HyperLadder 1 kb	Bioline
Kanamycin (Kan), 35 mg/ml	Sigma-Aldrich
AMicrocentrifuge tubes	Eppendorf
NanoDrop 8000 Spectrophotometer	Thermofisher Scientific
NucleoSpin Gel and PCR Clean-up kit	Macherey-Nagel
Phusion Flash High-Fidelity PCR Master Mix (2X)	Thermofisher Scientific
PowerPac Basic Power Supply	BioRad
Quick-Fusion Cloning Kit	Biotool
S.O.C medium	Invitrogen
Scalpel	Swann-Morton

Spreader	VWR
SYBRSafe stain	Thermofisher Scientific
Veriti 96-Well Thermal Cycler	Thermofisher Scientific

A3. Kit Reagents

NucleoSpin Gel and PCR Clean-up Kit

Binding buffer NTI

Wash buffer NT3

Elution buffer NE (5 mM Tris/HCl)

NucleoSpin Gel and PCR clean-up columns

2 mL collection tubes

Quick-Fusion Cloning Kit

Fusion enzyme

5X Fusion buffer

Linearized control vector (2.7 kb)

Control DNA fragment (500 bp)

QIAprep Spin Miniprep Kit

QIAprep spin columns

Buffers P1, P2, N3, PB, PE and EB

LyseBlue

Loading dye

RNase A

A4. LB Preparation

LB

LB was prepared as follows: 25 g LB (Melford) was added to 1 L deionised water and autoclaved (∼8 cycles, 15 min per cycle at 121°C).

LB Agar

To prepare LB agar, 25 g of LB plus 20 g of bactoagar were mixed in 1 L of deionised water and autoclaved as described above.

A5. TBS and TBST Preparation

TBS

10X TBS was prepared using 200 mM Tris and 1500 mM NaCl per litre of deionised water and stirred with a magnetic stirrer for 15 min before adjusting the solution to a pH of 7.4 with 12 N HCl.

TBST

1X TBST buffer contained 10% 10X TBS in deionised water and stirred with a magnetic stirrer for 15 min before addition of 0.1% Tween-20 and further 15 min of stirring.

Section B

OGG1 and γH2AX Foci Kinetics After Low- and High-LET IR in HeLa Cells

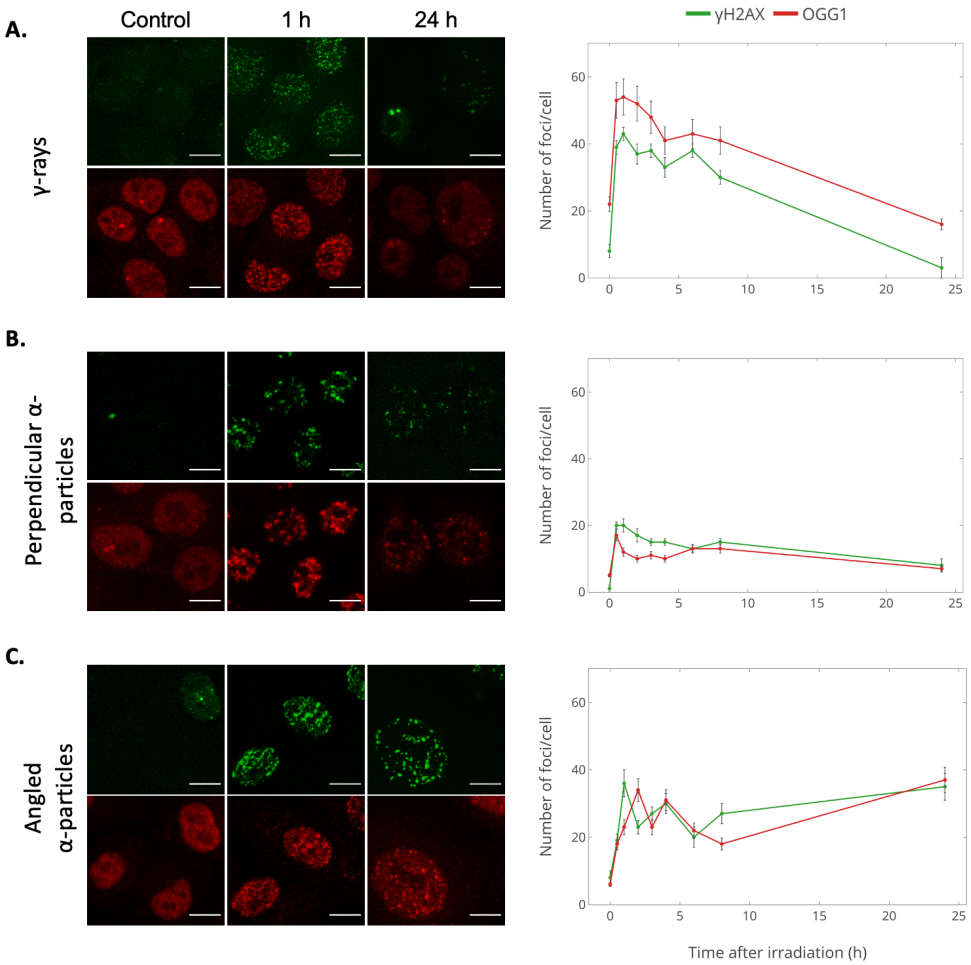

γH2AX and OGG1 foci kinetics following low- or high-LET IR in HeLa cells. OGG1-red and γH2AX-green foci kinetics in unirradiated (control, 0) and 4 Gy irradiated cells with **A.** γ-IR, **B.** perpendicular α-IR and **C.** angled α-IR, imaged using confocal microscopy. Images from key time-points are presented. Error bars represent standard deviation (SD) among three independent replicates. Scale bars, 10 μm.

Section C

OGG1 and γH2AX Foci Kinetics in HeLa Cells After Low- and High-LET IR and Olaparib Exposure

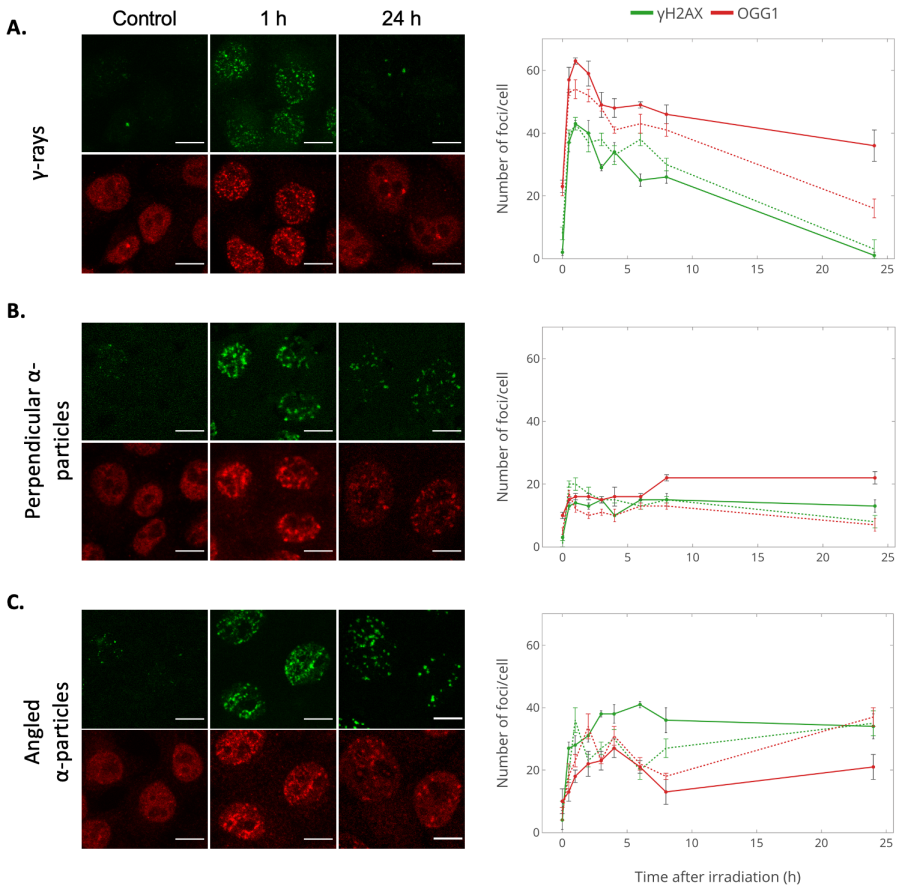

γH2AX and OGG1 foci kinetics following incubation with Olaparib and exposure to low- or high-LET IR in HeLa cells. OGG1-red and γH2AX-green foci kinetics in unirradiated (0) and 4 Gy irradiated cells with **A.** γ-IR, **B.** perpendicular α-IR and **C.** angled α-IR, imaged using confocal microscopy. Dotted lines represent kinetics without Olaparib. Images from key time-points are presented. Error bars represent standard deviation among two independent replicates. Scale bars, 10 μm.

Section D

Copies of Published Papers

RADIATION RESEARCH **189**, 19–31 (2018)
0033-7587/18 $15.00

DOI: 10.1667/RR14594.1

This article has been removed from this version of the thesis due to copyright restrictions

Radiation Protection Dosimetry (2019), pp. 1–6 doi:10.1093/rpd/ncy300

TRACKING DOWN ALPHA-PARTICLES: THE DESIGN, CHARACTERISATION AND TESTING OF A SHALLOW-ANGLED ALPHA-PARTICLE IRRADIATOR

James M. Thompson[1], Amy Elliott[1], Sofia D'Abrantes[1], Gabriel O. Sawakuchi[2] and Mark A. Hill[1,*]
[1]CRUK/MRC Oxford Institute for Radiation Oncology, University of Oxford, Gray Laboratories, ORCRB Roosevelt Drive, Oxford OX3 7DQ, UK
[2]Department of Radiation Physics, The University of Texas MD Anderson Cancer Center, 1400 Pressler St., Unit 1420, Houston, TX 77030, USA

*Corresponding author: mark.hill@oncology.ox.ac.uk

Human exposure to α-particles from radon and other radionuclides is associated with carcinogenesis, but if well controlled and targeted to cancer cells, α-particles may be used in radiotherapy. Thus, it is important to understand the biological effects of α-particles to predict cancer risk and optimise radiotherapy. To enable studies of α-particles in cells, we developed and characterised an α-particle automated irradiation rig that allows exposures at a shallow angle (70° to the normal) of cell monolayers in a 30 mm diameter dish to complement standard perpendicular irradiations. The measured incident energy of the α-particles was 3.3 ± 0.5 MeV (LET in water = 120 keV μm^{-1}), with a maximum incident dose rate of 1.28 ± 0.02 Gy min^{-1}, which for a 5 μm cell monolayer corresponds to a mean dose rate of 1.57 ± 0.02 Gy min^{-1} and a mean LET in water of 154 keV μm^{-1}. The feasibility of resolving radiation-induced DNA double-strand breaks (DSB) foci along the track of α-particles was demonstrated using immunofluorescent labelling with γH2AX and 53BP1 in normal MRC-5 human lung cells.

INTRODUCTION

Alpha-particles from radon and its progeny contribute approximately to 50% of the annual effective dose to the UK population, but the concentration of radon can vary by many orders of magnitude depending on location. Additionally, there is increasing interest in the clinical use of α-particle radionuclides to treat a variety of cancers, including radionuclides conjugated with monoclonal antibodies developed to directly target tumour cells[1]. Thus, it is important to understand the mechanism of α-particles interaction with biological systems to accurately predict cancer risk and optimise radiotherapy.

These α-particles have high ionisation densities and the energy transferred per unit distance [or linear energy transfer (LET)] is high compared to low-LET radiation such as X-rays and γ-rays. α-particles are typically emitted with energies ranging from 5 to 8 MeV, corresponding to ranges in tissue from 37–77 μm. As an α-particle slows down, its LET increases from ~70 to 90 keV μm^{-1} at the start of the track to a peak of ~237 keV μm^{-1} towards the end of the track before falling again at the very end of its range. In comparison to low-LET radiation, α-particles have a higher relative biological effectiveness (RBE) at inducing a range of biological end-points[2], including cell inactivation[3–5], mutation induction[6, 7] and transformation[8]. The RBE increases with increasing LET up to a peak around 100 keV μm^{-1} and then decreases at higher LET values[3, 5]. For example, for 3.2 MeV α-particles incident on V79-4 cells (average LET of 131 keV μm^{-1} across the cell) a maximum low-dose RBE (RBE_M) of 10.2 ± 0.2 was reported[5]. The high RBE of α-particles is due to its densely ionising track structure[9, 10], which induces clustered DNA damage (two or more lesions within one or two helical turns of DNA). This includes DNA double-strand breaks (DSB) and complex DSB (consisting of simple DSB with additional strand breaks and/or base damage within the cluster). Monte Carlo modelling shows that the yield of DSB which are complex is ~90%, for α-particles, compared to ~30–50% for low-LET radiation (e.g. X-rays and γ-rays)[11, 12]. These complex DSB result in decreased DSB repair rate and increased residual DSB yield[13].

In addition to the high efficiency at inducing complex DSB, α-particles also produce spatially and temporally correlated DSB along the narrow track of the particle (maximum range of δ-electrons typically <0.1 μm, with ~90% of energy deposition within 10 nm)[14]. This occurs in individual chromosomes within the nucleus (e.g. in DNA around nucleosomes and chromatin fibre/loops) and between separate chromosomes occupying adjacent territories[15, 16]. The close proximity of these breaks increases the probability of illegitimate re-joining producing chromosomal rearrangements. As a result, the passage of a single α-particle is efficient at producing complex chromosome aberrations (requiring three or more breaks in two or more

chromosomes), in contrast to mainly simple aberrations (maximum of two breaks in two chromosomes) observed for low doses of low-LET X-rays[16, 17].

Biological effects of α-particles have been studied with conventional irradiation of a cell monolayer with a perpendicular beam (relative to the dish) of α-particles[5, 18, 19]. However, it is difficult to resolve surrogates for DNA lesions, such as foci, because of the diffraction-limited resolution of conventional microscopes—where spatial resolution is even poorer in the z-axis. This low-resolution in the z-axis limits the study of DNA repair kinetics. To allow using the higher spatial resolution in the focal plane ($x - y$) of conventional microscopes, we modified the existing Oxford α-particle irradiator to enable shallow angle irradiations of cell monolayers. We further validated our setup with initial immunofluorescence studies demonstrating the improved spatial resolution of foci along α-particle tracks.

METHODS

Shallow-angled α-particle irradiator rig

The shallow-angled irradiation rig enables irradiation of cell monolayers at a 70° angle to the normal by scanning custom made irradiation dishes across a collimated α-particle beam (~4 mm × 30 mm) at the required angle. These glass-walled irradiation dishes (30 mm internal diameter) incorporate a 0.9 µm PET (polyethylene terephthalate; DuPont Teijin films, Dumfries, UK) base to minimise energy loss of traversing α-particles. The design of the rig is illustrated in Figure 1 and was built to attach to the top of the existing Oxford α-particle irradiator[18], with the source raised so that the emitted α-particles traverse 10 mm in helium prior to exiting the 2.5 µm PET window and a subsequent 54 mm in helium to the 0.9 µm PET base of the irradiation dish at the centre of the 4 mm wide final (second) collimating slit (i.e. a source to cell distance of 64 mm). The plane of this slit is at a 20° angle to the normal of the 1 GBq ^{238}Pu source and parallel to the dish base. Both the original irradiator chamber and the inside of the angled-irradiator rig were continuously flushed with helium at atmospheric pressure. The irradiation dish is scanned across the angled slit using a stepper motor, with the limit switches used to define the range of motion. An in-house built controller was used to set the total number of traversals, with each traversal (from one limit switch to the other) taking 5.6 s. An O-ring seal ensures that the helium environment is maintained under the dish as it is scanned, along with a PTFE gasket between the moving plate holding the dish and the static plate holding the slit. The response following shallow-angle exposures was compared to the response of cells irradiated perpendicular to the base with 3.26 MeV (LET in water of 121 keV µm^{-1}) α-particle using the standard Oxford irradiator[5, 18].

Fluence, energy and dose measurements

The total fluence of α-particles and therefore the dose delivered to the dish was ultimately determined by the number of traversals of the dish across the slit. However, the fluence per traversal could also be varied by selecting the aperture directly above the ^{238}Pu source (25, 4.5. 1.4 or 0.5 mm diameter; the 25 mm aperture is larger than the source with a diameter of ~20 mm) and the width of first collimating slit (currently either 1 mm or 7.5 mm wide; 30 mm long).

The fluence of α-particles across the scanned dish was determined using 25 mm diameter fluorescence nuclear track detector (FNTD) discs (Landauer Inc., Stillwater, OK, USA)[20] placed directly on the PET base at the centre of the irradiation dish. The FNTDs were subsequently exposed by traversing the dish over the slit five times for the 7.5 mm wide first collimating slit and 50 times for the 1 mm wide first collimating slit. Following irradiation, the resulting tracks were imaged with a Zeiss LSM 710 confocal microscope using a 63×/1.4 oil objective and a 5 mW HeNe laser (excitation 633 nm, collection 634 nm–755 nm). The 1024 × 1024 pixel (135 × 135 µm^2) images were averaged over eight collections per slice with a dwell time of 3.15 µs pixel^{-1} per collection.

Energy measurements were performed using an A300-17AM Passivated Implanted Planar Silicon (PIPS) surface barrier detector (Canberra Industries Inc., Meriden, CT, USA) coupled to an alpha spectrometer comprised of a Model *2003BT* charge sensitive FET input pre-amplifier and a DSA-1000 multichannel analyser (Canberra Industries Inc., Meriden, CT, USA). The detector and spectrometer were calibrated using a three peak (^{239}Pu, ^{241}Am and ^{244}Cm) calibration source (Isotrak QCRB2508, AEA technology QSA, Didcot, UK) in a vacuum chamber. The three dominate peaks produced with the detector at the same angle as the dish correspond to α-particle energies of 5.156 MeV, 5.486 MeV and 5.805 MeV with respective full width half maximum (FWHM) values of 18 keV, 14 keV and 13 keV. Measurements were performed with the surface barrier detector directly behind the PET base of a sample irradiation dish, flushed with helium.

As the α-particles traverse the cell and lose energy, there is a corresponding increase in LET. Therefore, the mean dose to the cell is different to the incident dose to the cell at the PET-cell interface and is dependent on distribution of cell thicknesses. The average dose to the cell monolayer at a given depth for α-particles incident on the cell at an angle θ to the normal of the dish base can be calculated using:

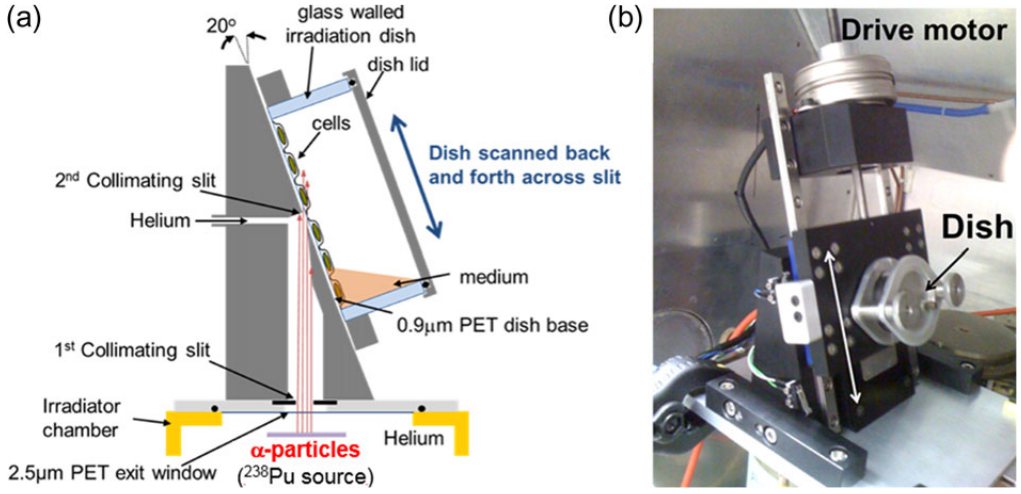

Figure 1. Shallow-angled α-particle rig positioned above the exit window of the Oxford α-particle irradiator: (**a**) schematic (not to scale) and (**b**) photograph with double-headed arrow showing direction of motion.

$$D = \Phi L/(\rho \cos\theta) \quad (1)$$

where ρ is the density, Φ is the particle fluence and L is the LET in water [this corresponds to D (Gy) = 0.16 × Φ (particles μm^{-2}) × L (keV μm^{-1})/cos θ, assuming a cell density of 1 g cm^{-3}]. For a given incident energy, E_i, the variation in energy and LET along the remaining path of the α-particle as it slows down can be determined using SRIM stopping power data for helium ions in water[21, 22]. Equation (1) can then be used to calculate the relative variation in dose per incident particle of energy E_i as a function depth in a cell monolayer of thickness, t. An estimate of the average dose to the cell monolayer was calculated from the measured total fluence, Φ, and numerically integrated across the measured incident energy spectrum, for a 5 μm cell monolayer thickness[5].

Cell culture

MRC-5 human foetal lung fibroblast cells were cultured in minimum essential medium (MEM) supplemented with 10% FBS (foetal bovine serum), 1% NEAA (non-essential amino acids), 100 units ml^{-1} penicillin (Sigma-Aldrich), 100 μg ml^{-1} streptomycin (Sigma-Aldrich) and 2 mM L-Glutamine (Sigma-Aldrich). Cells were incubated at 37°C with 5% CO_2 humidified air. Approximately 1 day prior to irradiation, 3×10^5 cells in 2 ml were plated in irradiation dishes to produce an attached cell monolayer on the PET dish base.

Immunofluroescent labelling of DSB

Following irradiations, cells were incubated for 30 min then washed with phosphate-buffered saline (PBS) (Thermo Fisher Scientific), fixed in 1 ml 4% paraformaldehyde solution (Sigma-Aldrich) for 30 min at 4°C, then washed three times in PBS prior to storing at 4°C. Each dish was subsequently treated with 1 mL permeabilising buffer (0.25% Triton X-100 (Sigma-Aldrich) in PBS) for 5 min at room temperature, washed three times with PBS prior to incubating in 1 mL blocking buffer (1% BSA, bovine serum albumin (Sigma-Aldrich), in PBS) for 15 min at room temperature. The cells were then incubated in the primary antibody solution for 45 min at room temperature. The primary antibody solution consisted of 1 μg mouse anti-γH2AX antibody (Merck Millipore) and 1 μg rabbit anti-53BP1 (Bethyl Laboratories) made up to 500 μl in blocking buffer. Samples were then washed three times with PBS, before incubating in secondary antibody solution for 30 min in the dark at room temperature. The secondary antibody solution consisted of 1 μg AlexaFluor 488 donkey anti-mouse (Thermo Fisher Scientific) and 1 μg AlexaFluor 633 anti-rabbit (Thermo Fisher Scientific) made up to 500 μL in blocking buffer. Samples were finally washed three times with PBS in the dark prior to adding Vectashield Mounting Medium containing DAPI (Vector Laboratories Ltd.) and covering with a 22 mm diameter glass coverslip. The samples were stored in the dark at 4°C. Imaging was performed using a Zeiss LSM 800 confocal scanner with a 63x oil objective.

RESULTS

Fluence, energy and dose measurements

FNTDs were used to image individual α-particle tracks for a standard perpendicular irradiation and shallow-angled irradiations (Figure 2). For the shallow-angled irradiations, the measured α-particle

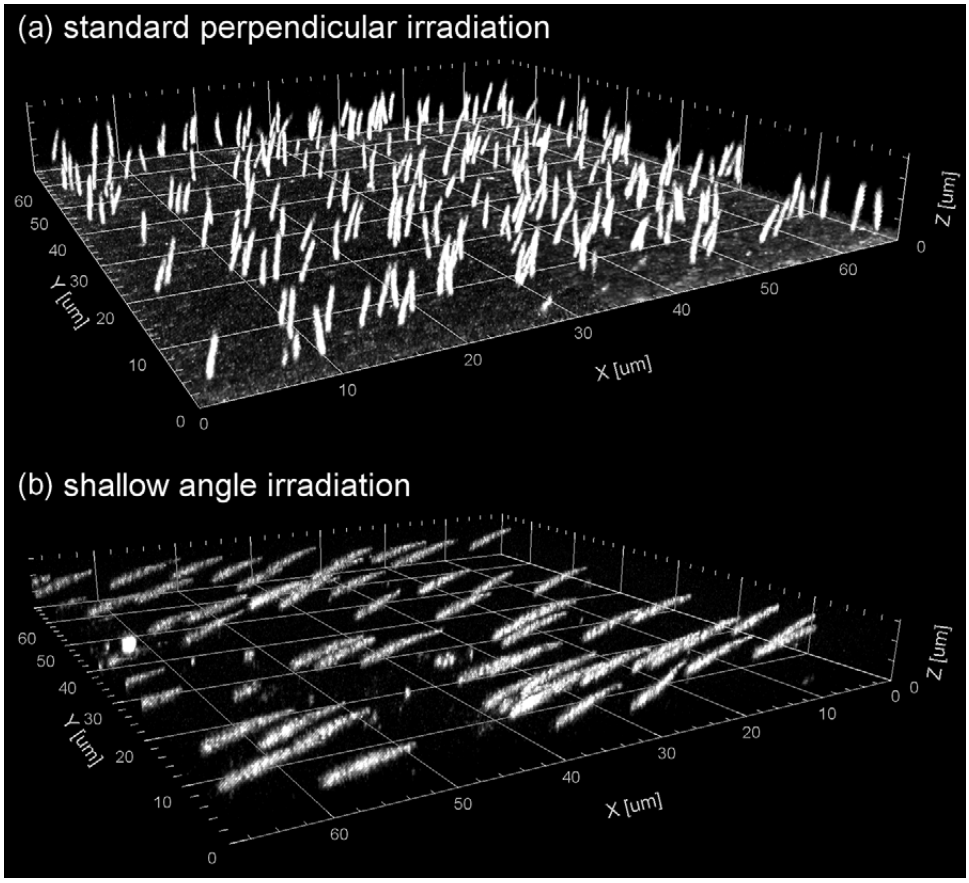

Figure 2. 3D image of α-particle tracks measured using FNTD: (**a**) for standard perpendicular irradiation with a corresponding dose of 1 Gy; (**b**) for angled irradiation after 50 traversals of the slit (using a 1 mm wide first collimating slit).

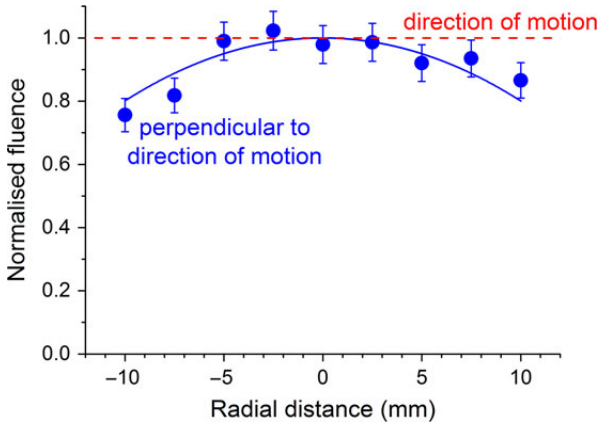

Figure 3. Variation in α-particle fluence across the sample dish perpendicular to the direction of motion measured using FNTD. (fitted solid line: $\Phi(r) = 1 - 0.00199\, r^2$). As a result of the dish travelling at a constant speed across the slit the fluence will be constant in the direction of motion (dashed line).

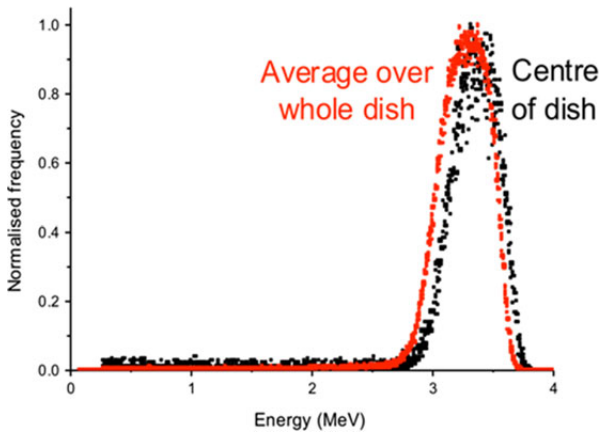

Figure 4. Measured energy spectra of the α-particles incident on the cells (after passing through the PET base of the sample dish).

fluence per traversal at the centre of the dish was $0.31 \pm 0.02 \times 10^{-3}\ \mu m^{-2}$ and to $2.1 \pm 0.2 \times 10^{-3}\ \mu m^{-2}$ for the 1.0 mm and 7.5 mm wide first collimator, respectively. The variation in α-particle fluence across the sample dish perpendicular to the direction of motion for shallow-angled irradiation after 50 traversals using a 1 mm wide first collimating slit is shown in Figure 3,

Table 1. Summary of -particle energy, fluence per traversal, incident dose rate and mean dose rate to a 5 µm cell monolayer (5.6 s per traversal) obtained using the 1 mm wide first collimator.

	Centre of dish
Peak energy	3.4 ± 0.5 MeV
Fluence per traversal	0.31 ± 0.03 × 10^{-3} µm^{-2}
Incident surface dose rate	0.19 ± 0.02 Gy min^{-1}
Incident LET	123 keV µm^{-1}
Mean dose rate (5 µm thick)	0.23 ± 0.02 Gy min^{-1}
Mean LET	152 keV µm^{-1}

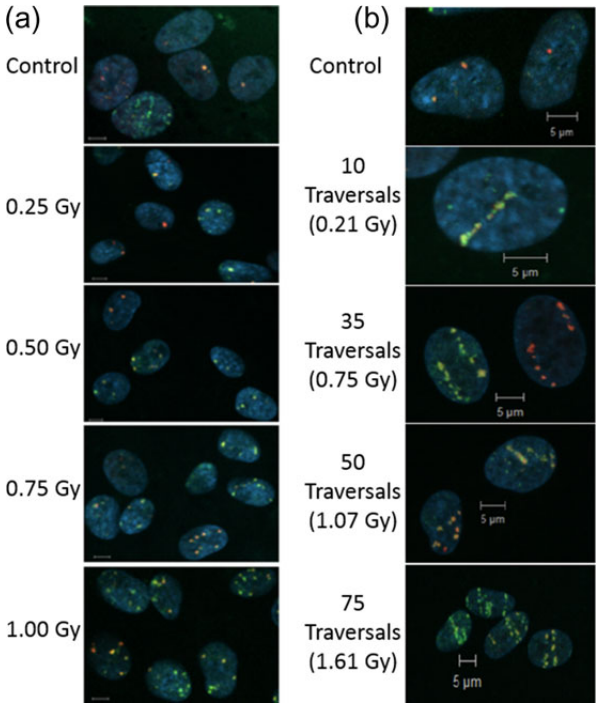

Figure 5. Induction of γH2AX (green) and 53BP1 foci (red) in the nucleus (blue) of MRC-5 cells induced following (**a**) perpendicular irradiation and (**b**) shallow-angled irradiation with α-particles (cell nuclei are labelled in blue using DAPI staining). Scale bar, 5 µm.

with the fitted normalised distribution given by the equation $f(x) = 1 - 0.00199\ x^2$. However, the fluence is constant in the direction of motion. In order to calculate the average fluence over the circular dish base (of radius, $r = 15$ mm). the distribution across the length of the static slit, $f(x)$, was integrated across the dish using the equation:

$$\int_{-r}^{r} \frac{2f(x)\sqrt{r^2 - x^2}\,dx}{\pi r^2} \qquad (2)$$

Therefore, the average fluence corresponds to 0.89 times the fluence at the centre of the dish.

The measured energy spectra of the α-particles incident on the cell monolayer (after passing through the PET base of the irradiation dish) at the centre of the dish had a peak energy of 3.4 MeV and a FWHM of 0.5 MeV (Figure 4). There is a slight reduction in energy when averaged over the majority of dish (represented by the 300 mm^2 active area of the surface barrier detector) with peak energy of 3.3 MeV (FWHM = 0.5 MeV) (Figure 4).

The incident dose rate at the centre of the dish for a 1 and 7.5 mm wide first collimator was 0.19 Gy min^{-1} and 1.28 Gy min^{-1}, respectively (Table 1). The corresponding mean dose rates were 0.23 Gy min^{-1} and 1.57 Gy min^{-1} for a 5 µm thick cell monolayer, respectively. A more accurate assessment of the dose rates across the dish can be made by including the variation in angle of incident, range straggling and the variation in cell geometry.

Visualisation of α-particle tracks

We exposed MRC-5 cells to both standard perpendicular or shallow-angled irradiations α-particles to validate that γH2AX and 53BP1 foci can be observed. As expected, the number of foci increases with increasing fluence. While with the perpendicular irradiations, it is difficult to resolve individual foci along the track, the shallow-angled irradiations clearly show multiple foci along the path of the α-particles traversing the nucleus (Figure 5). A number of the resulting foci-tracks do not appear to traverse the whole nucleus, however due to the angle of incidence of the particle, these typically represent tracks either entering the nucleus from below or exiting from the top.

CONCLUSIONS

To complement standard perpendicular α-particle irradiations, a new automated irradiation rig has been developed to expose mammalian cells in a 30 mm diameter dish to α-particles at shallow-angles (70° to the normal). The measured incident energy of the α-particles was 3.3 ± 0.5 MeV (LET = 120 keV µm^{-1}) at the centre of the dish for a 1 mm wide first collimator. This corresponded to an incident dose rate of 0.19 ± 0.02 Gy min^{-1} and a mean dose rate of 0.23 ± 0.02 Gy min^{-1} for 5 µm thick cell monolayer, with a mean LET of 154 keV µm^{-1}. The mean dose rate could be increased to 1.57 Gy min^{-1} if a 7 mm first collimator slit is used. Lower dose rates are achievable by reducing the size of the aperture in front of the ^{238}Pu source. The immunofluorescence studies performed clearly demonstrate the ability of these shallow-angled irradiations to resolve sites of damage along the track of the α-particle and therefore facilitating DNA repair studies. In addition to investigating the induction and repair of DSB, these techniques

can also be used to study the kinetics of recruitment and loss of DNA repair proteins in wild type and repair deficient cells. The use of live cell imaging of fluorescently tagged proteins can also be used to help shed light on the spatial dynamics of these breaks post exposure. Due to the high ionisation density along the path of the α-particle, it is still likely that not all DSB are resolved. Therefore, it would be interesting to use a super-resolution microscopy to explore the structure of the foci. In addition to DNA repair studies, the ability to irradiate a 30 mm diameter dish also enables the effect of cell geometry (with respect to the track) to be explored by comparing differences in biological response to shallow-angled α-particle exposure to and an identical dose delivered perpendicular to the cell monolayer.

FUNDING

The authors gratefully acknowledge funding from Medical Research Council Strategic Partnership (MC_PC_12004) for the CRUK/MRC Institute for Radiation Oncology.

REFERENCES

1. Elgqvist, J., Frost, S., Pouget, J. P. and Albertsson, P. *The potential and hurdles of targeted alpha therapy - clinical trials and beyond*. Front Oncol. **3**, 324 (2014).
2. International Commission on Radiological Protection. *Relative biological effectiveness (RBE), quality factor (Q), and radiation weighting factor (w(R))*. Ann. ICRP **33**, 1–117 (2003).
3. Barendsen, G. W. *Impairment of the proliferative capacity of human cells in culture by alpha-particles with differing linear-energy transfer*. Int. J. Radiat. Biol. **8**, 453–466 (1964).
4. Sorensen, B. S., Overgaard, J. and Bassler, N. *In vitro RBE-LET dependence for multiple particle types*. Acta Oncol. **50**, 757–762 (2011).
5. Tracy, B. L., Stevens, D. L., Goodhead, D. T. and Hill, M. A. *Variation in RBE for survival of V79-4 cells as a function of alpha-particle (helium ion) energy*. Radiat. Res. **184**, 33–45 (2015).
6. Thacker, J., Stretch, A. and Stephens, M. A. *Mutation and inactivation of cultured mammalian cells exposed to beams of accelerated heavy ions. II. Chinese hamster V79 cells*. Int. J. Radiat. Biol. **36**, 137–148 (2015).
7. Cox, R. and Masson, W. K. *Mutation and inactivation of cultured mammalian cells exposed to beams of accelerated heavy ions. III. Human diploid fibroblasts*. Int. J. Radiat. Biol. **36**, 149–160 (1979).
8. Miller, R. C., Marino, S. A., Brenner, D. J., Martin, S. G., Richards, M., Randers-Pehrson, G. and Hall, E. J. *The biological effectiveness of radon-progeny alpha particles. II. Oncogenic transformation as a function of linear energy transfer*. Radiat. Res. **142**, 54–60 (1995).
9. Goodhead, D. T. *Initial events in the cellular effects of ionizing radiations: clustered damage in DNA*. Int. J. Radiat. Biol. **65**, 7–17 (1994).
10. Hill, M. A. *Fishing for radiation quality: chromosome aberrations and the role of radiation track structure*. Radiat. Prot. Dosim. **166**, 295–301 (2015).
11. Nikjoo, H., Bolton, C. E., Watanabe, R., Terrissol, M., O'Neill, P. and Goodhead, D. T. *Modelling of DNA damage induced by energetic electrons (100 eV to 100 keV)*. Radiat. Prot. Dosim. **99**, 77–80 (2002).
12. Goodhead, D. T. *Energy deposition stochastics and track structure: what about the target?* Radiat. Prot. Dosim. **122**, 3–15 (2006).
13. deLara, C. M., Jenner, T. J., Townsend, K. M., Marsden, S. J. and O'Neill, P. *The effect of dimethyl sulfoxide on the induction of DNA double-strand breaks in V79-4 mammalian cells by alpha particles*. Radiat. Res. **144**, 43–49 (1995).
14. Paretzke, H. G. *Radiation track structure theory*. In: Kinetics of Nonhomologous Processes. Freeman, G. R., Ed. (New York: Wiley) pp. 88–169 (1987).
15. Friedland, W., Paretzke, H. G., Ballarini, F., Ottolenghi, A., Kreth, G. and Cremer, C. *First steps towards systems radiation biology studies concerned with DNA and chromosome structure within living cells*. Radiat. Environ. Biophys. **47**, 49–61 (2008).
16. Anderson, R. M., Stevens, D. L. and Goodhead, D. T. *M-FISH analysis shows that complex chromosome aberrations induced by alpha-particle tracks are cumulative products of localized rearrangements*. Proc. Natl Acad. Sci. USA **99**, 12167–12172 (2002).
17. Anderson, R. M., Stevens, D. L., Sumption, N. D., Townsend, K. M., Goodhead, D. T. and Hill, M. A. *Effect of linear energy transfer (LET) on the complexity of alpha-particle-induced chromosome aberrations in human CD34+ cells*. Radiat. Res. **167**, 541–550 (2007).
18. Goodhead, D. T., Bance, D. A., Stretch, A. and Wilkinson, R. E. *A versatile plutonium-238 irradiator for radiobiological studies with alpha-particles*. Int. J. Radiat. Biol. **59**, 195–210 (1991).
19. Neti, P. V. S. V., de Toledo, S. M., Perumal, V., Azzam, E. I. and Howell, R. W. *A multi-port low-fluence irradiator: fabrication, testing and benchmark radiobiological studies*. Radiat. Res. **161**, 732–738 (2004).
20. McFadden, C. H., Hallacy, T. M., Flint, D. B., Granville, D. A., Asaithamby, A., Sahoo, N., Akselrod, M. S. and Sawakuchi, G. O. *Time-lapse monitoring of DNA damage colocalized with particle tracks in single living cells*. Int. J. Radiat. Oncol. Biol. Phys. **96**, 221–227 (2016).
21. Ziegler, J. F. *Helium Stopping Powers and Ranges in all Elemental Matter.* (New York: Pergamon) (1977).
22. Ziegler, J. F., Biersack, J. P. and Ziegler, M. D. *SRIM—The Stopping and Range of Ions in Matter.* (Chester, Maryland, USA: SRIM Co) (2008).